Mass transfer and flooding phenomena in carbon dioxide electrolyzers

Baumgartner, L.M.

DOI
10.4233/uuid:a5c27498-55c7-4edb-b7b8-3f3ccf7b77c7

Publication date
2023

Document Version
Final published version

Citation (APA)
Baumgartner, L. M. (2023). *Mass transfer and flooding phenomena in carbon dioxide electrolyzers* (1 ed.). [Dissertation (TU Delft), Delft University of Technology]. https://doi.org/10.4233/uuid:a5c27498-55c7-4edb-b7b8-3f3ccf7b77c7

MASS TRANSFER AND FLOODING PHENOMENA

IN CARBON DIOXIDE ELECTROLYZERS

LORENZ MARTIN BAUMGARTNER

Propositions

accompanying the dissertation

MASS TRANSFER AND FLOODING PHENOMENA IN CARBON DIOXIDE ELECTROLYZERS

by

Lorenz Martin BAUMGARTNER

1. The scale-up of gas-fed CO_2 electrolyzers with flowing catholyte is limited by the stable pressure window of the gas diffusion electrode (this thesis, Chapter 2).
2. Woven gas diffusion electrodes can mitigate the effects of electrolyte flooding (this thesis, Chapter 3).
3. The chemical stability of most carbon-based gas diffusion electrodes is insufficient for an economical CO_2 electrolysis process (this thesis, Chapter 4).
4. For the field of CO_2 electrolysis, finding a stable gas diffusion electrode is more important than finding a highly active catalyst.
5. Automation in research is subject to the law of diminishing returns.
6. No preconceived research plan survives the encounter with reality.
7. Science finds the boundaries of what is possible. Engineering finds the boundaries of what is feasible.
8. Replacing highly scarce iridium as an anode material will be essential for a large scale implementation of CO_2 or PEM water electrolysis.
9. The high demand for renewables energies has the potential to fundamentally reshape the relationship between Europe and Northern Africa.
10. Societal trust in science ultimately depends on the belief that the future can be better than the present.

These propositions are regarded as opposable and defendable, and have been approved as such by the promotor Prof. dr. ir. C.R. Kleijn and the promotor Dr. ir. D.A. Vermaas.

MASS TRANSFER AND FLOODING PHENOMENA IN CARBON DIOXIDE ELECTROLYZERS

MASS TRANSFER AND FLOODING PHENOMENA IN CARBON DIOXIDE ELECTROLYZERS

Proefschrift

ter verkrijging van de graad van doctor
aan de Technische Universiteit Delft,
op gezag van de Rector Magnificus Prof.dr.ir. T.H.J.J. van der Hagen,
voorzitter van het College voor Promoties,
in het openbaar te verdedigen op
woensdag 21 april 2023 om 10:00 uur

door

Lorenz Martin BAUMGARTNER

Master of Science in Chemical Engineering,
Technische Universiteit München, Duitsland,
geboren te München, Duitsland.

This dissertation has been approved by

promotor: Prof.Dr.ir. C.R. Kleijn
promotor: Dr.ir. D.A. Vermaas

Composition of the doctoral committee:

Rector Magnificus,	chairman
Prof.Dr.ir. C.R. Kleijn,	Delft University of Technology, promotor
Dr.ir. D.A. Vermaas,	Delft University of Technology, promotor
Independent members:	
Dr. A. Forner-Cuenca	Eindhoven University of Technology, Netherlands
Prof.dr. T. Breugelmans	University of Antwerp, Belgium
Dr. V. Garbin	Delft University of Technology
Prof.dr.ir. J.T. Padding,	Delft University of Technology
Prof.dr.ir. W. de Jong,	Delft University of Technology

This project has received funding from the European Research Council (ERC) under the European Union's Horizon 2020 research and innovation programme (grant agreement No 852115).

Keywords: CO_2 reduction, electrochemistry, electrochemical engineering, gas diffusion electrode, bipolar membrane, pH imaging
Printed by: Proefschriftspecialist, Symon Spiersweg 4, 1506 RZ Zaandam, The Netherlands.
Front & Back: Design by Darius Siwek, 825 S. Windsor Boulevard, # 6, Los Angeles, CA 90005, United States.

ISBN 978-94-93330-16-0

An electronic version of this dissertation is available at
http://repository.tudelft.nl/.

To Caroline

CONTENTS

1

GENERAL INTRODUCTION

In recent years, the majority of countries have made ambitious pledges to decarbonize their economies within the next two decades as part of the Paris Agreement [1] or the Glasgow Climate Pact. [2] For example, the European Union has developed a vision to fully decarbonize the energy supply by maximizing the deployment of renewable energy sources by 2050, [3] which has the added benefit of becoming more self-sufficient.

1.1. WHAT LIMITS THE SUBSTITUTION OF FOSSIL FUELS?

The rapid substitution of fossil fuels through renewable energies in the key sectors electricity, industry, and transportation is complicated by major technological and economical challenges:

- Daily and seasonal fluctuations of renewable power sources
- Limited transmission capacity of the electrical power grid
- Insufficient energy capacity for electrical energy storage at large scale
- Insufficient energy density for electrical energy storage
- Limited availability of non-fossil carbon feedstocks for chemical production

For these reasons, our modern economies still rely heavily on fossil fuels (Figure 1.1). Luckily, many technologies are already starting to be employed that allow the further direct replacement of further fossil fuels with renewables.

The electricity sector of the US economy, for example, amounted to 38% of the countries energy consumption in 2018 (Figure 1.1). It still relies heavily on coal and gas power plants to meet the secondary energy demands of residential, commercial, and industrial sectors. However, the contribution from wind and solar has been steadily increasing over the last decades because technological innovation has allowed larger wind turbines

and solar photovolatic (PV) modules with higher efficiencies. According to a 2018 report from the International Renewable Energy Agency,[4] these improvements led to an electricity cost reduction of almost 75% for PV and about 25% for on-shore wind in the period of 2010 to 2017. Therefore, wind and solar energy sources can now compete with fossil fuel-fired power plants. However, the electrical infrastructure of most economies has insufficient transmission and storage capacity to completely replace coal and gas power plants.

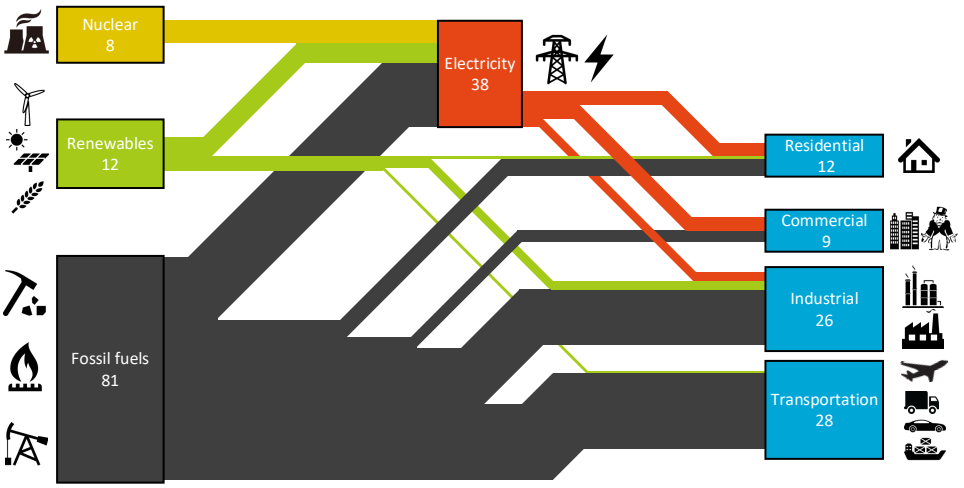

Figure 1.1: Sankey diagram of the estimated US energy consumption in 2018: 101 Quads.[5] 1 quad corresponds to 10^{15} British Thermal Units (BTU) or 1×10^{18} J.

The transportation sector was responsible for almost one third of the US energy consumption in 2018 (Figure 1.1). Luckily, many major car manufacturers have already started to phase out passenger vehicles and even trucks with internal combustion engine in favor of electrical vehicles.[6] If implemented at a large scale, this would make it possible to replace a large amount of gasoline and Diesel fuel required for the transportation sector. Unfortunately, the insufficient energy density of electrical batteries is a major obstacle to the electrification of the aviation and shipping subsectors. This means that without the possibility to recharge during long distance travel, it is unfeasible for airplanes and ships to carry the weight of the necessary batteries. Therefore, the aviation and shipping subsectors can not be easily electrified and will rely on energy-dense hydrocarbon fuels for the foreseeable future.

The industrial sector makes up more than a quarter of the energy consumption (Figure 1.1), which relies heavily on fossil fuels. While it might be possible in the near future to decarbonize energy-intensive industries, e.g., by developing a hydrogen process for steel making,[7] some industrial processes require fossil fuels as a carbon feedstock. For example, in 2016 the global production of the organic commodity chemical methanol (H_3COH) required 85 Mt of synthesis gas,[8] a mixture of H_2 and CO. This carbon feed-

stock is currently produced at industrial scale through steam reforming of CH_4 obtained from natural gas.

These examples highlight that the sustainable production of hydrocarbon fuels and chemicals will remain essential for the next decades.

1.2. PATHWAYS TO SUSTAINABLE HYDROCARBON PRODUCTION

One pathway for the sustainable production of synthesis gas requires expanding the natural carbon cycle through the cultivation, processing, and gasification of biomass.[9] For this route, plants convert CO_2 from the atmosphere to carbohydrates (e.g., sugars, cellulose, or lignin) through photosynthesis. The plants are harvested, dried, and gasified to synthesis gas, a central building block for a range of hydrocarbon products. A recent studies estimates that the global biomass production in 2050 could be extended to an energy potential of $160 - 650 \times 10^{18}$ J.[10] This is probably insufficient to meet the world's energy consumption, which is projected to reach 864×10^{18} J by 2050.[11] In addition, the large-scale implementation of biomass production raises concerns over biodiversity, water, and food security.[12]

Another pathway for sustainable hydrocarbon production is the establishment of an industrial carbon cycle (Figure 1.2). For this approach, large solar parks and wind farms would have to be constructed on non-arable land (e.g., deserts) and/or offshore to provide electrical power. This renewable power could then be used to capture CO_2 from industrial point sources,[13] directly from the atmosphere,[14] or perhaps the ocean.[15] Thermocatalytic[16,17] or electrochemical conversion[18,19] could then process the captured CO_2 to useful chemical intermediates such as CO, HCOOH, or C_2H_4. Well-established petrochemical processes (e.g., Fischer-Tropsch or methanol synthesis) would then enable the production of a wide range of fuels, organic chemicals, or plastics.

The case chemical methanol, for example, could be produced from CO_2 through a thermocatalytic or an electrochemical route. For both routes, the H_2 demand would be covered by water electrolysis. In the thermocatalytic route, CO_2 would exothermically react with H_2 to form H_3COH in a direct reaction ($CO_2 + 3H_2 \longleftrightarrow H_3COH + H_2O$; 250 °C, 20 bar). While thermocatalytic conversion of CO_2 to H_3COH is now a mature process that uses well-established Cu and Ni catalysts, it is projected to have a higher carbon footprint than the electrochemical route.[17,20]

In the electrochemical route, CO_2 could be directly converted to CO through electrochemical CO_2 reduction over an Ag catalyst ($CO_2 + 2e^- + 2H_2O \longrightarrow CO + 2OH^-$). Subsequently, CO would be converted with H_2 from water electrolysis in the exothermic methanol synthesis reaction ($CO + 2H_2 \longleftrightarrow H_3COH + H_2O$).[21] This emerging process has the potential to utilize electrical energy from renewables directly, which would reduce the H_2 demand of the overall process by one third.

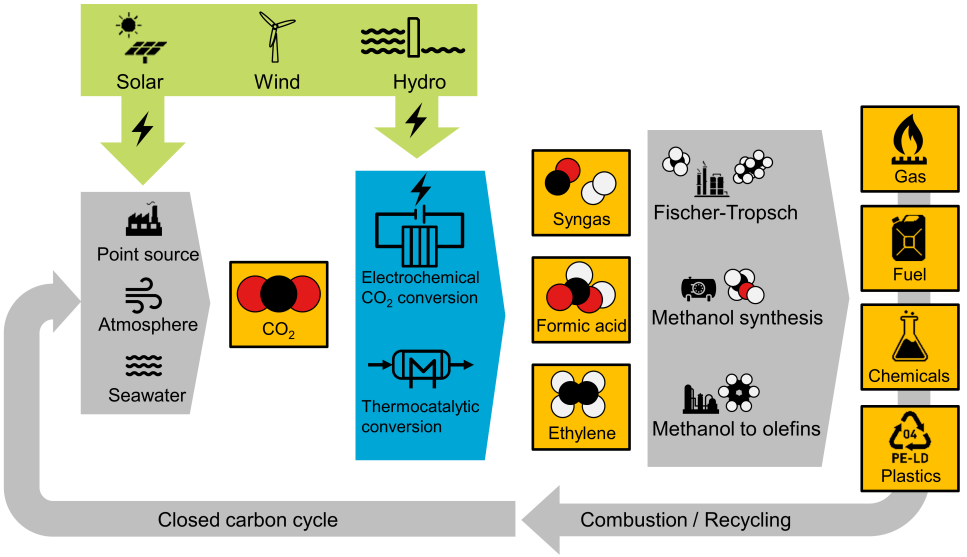

Figure 1.2: Sustainable hydrocarbon production through an industrial carbon cycle.

Ethylene, C_2H_4, is another bulk chemical that could be produced with electrochemical CO_2 reduction (Figure 1.2). It serves as a monomer for the commodity plastic polyethylene (PE). Conventionally, C_2H_4 is produced through the well established steam cracking process. This energy-intensive process is carried out at high temperatures (850 °C) and converts natural gas or naptha to C_2H_4.[22] With the direct electrochemical route, CO_2 would be reduced over a Cu catalyst at a much lower temperature (e.g., 25 °C) ($2CO_2 + 12e^- + 8H_2O \longrightarrow C_2H_4 + 12OH^-$).[19]

Besides the useful chemical intermediates C_2H_4 and CO, electrochemical CO_2 reduction can also produce formic acid (HCOOH). The estimated market values of these products varies significantly: The market for C_2H_4 is estimated at ≈ 160 billion USD, which is orders of magnitude larger than for the other possible products CO (≈ 5 billion USD) or HCOOH (≈ 0.5 billion USD).[23] This thesis explores the potentials and challenges of electrochemical CO_2 conversion to CO as this is the most mature process to date.[24]

1.3. CHALLENGES FOR ELECTROCHEMICAL CO_2 REDUCTION

Electrochemical CO_2 reduction (CO_2R) is a technology that is currently in the research stage and faces several challenges. Generally, CO_2R can produce a range of interesting target intermediates depending on the employed cathode catalyst (e.g., Ag: CO, Cu: C_2H_4, or Sn: HCOOH). CO_2R is usually carried out with aqueous electrolytes (Figure 1.3) and has a similar equilibrium potential as the hydrogen evolution reaction (HER).[25] This side reaction is typically undesired because it reduces the selectivity of the expended electrical current for the carbon products, the so-called Faradaic efficiency. As a result, the HER consumes additional energy relative to the produced carbon products and in-

creases the need for downstream separation. It is a key challenge, therefore, to minimize the HER by catalyst design and reaction engineering.[26]

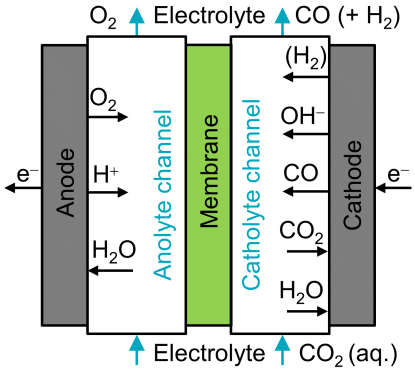

Figure 1.3: Schematic of a general CO_2 electrolysis cell. Anode: H_2O is converted to O_2 in the oxygen evolution reaction (OER). Cathode: CO_2 and H_2O are converted to reduced carbon products (e.g., CO) through electrochemical CO_2 reduction (CO_2R); H_2O can be reduced to H_2 in the competing hydrogen evolution reaction (HER).

In an electrolyzer, the electrochemical reaction on the electron-consuming cathode side has to be balanced with an electron-producing reaction on the anode side. For CO_2 electrolysis, the oxygen evolution reaction (OER) from water is the most interesting reaction because its feedstock is abundantly available (Figure 1.3). Depending on the pH value of the electrolyte employed, different anode materials are required,[23] which vary in their availability. For example, electrolyzers with alkaline electrolyte (e.g., KOH) on the anode side, the anolyte, can be operated with relatively abundant nickel-based anodes.[27] Electrolyzers with neutral or acidic pH, however, require iridium-based anodes to achieve a high stability and low overpotential.[28] Iridium, unfortunately, is one of the scarcest elements on earth.[29] For this reason, the design of an iridium-free CO_2 electrolyzer would be highly desirable.

Among the reaction systems for different target intermediates, the CO_2R to CO has reached the highest level of maturity. This process is also the focus of this thesis. According to techno-economical studies the following benchmarks have to be achieved before the process can become economically feasible:[19,24]

- Current density, j: $-200\,\mathrm{mA\,cm^{-2}}$ to $-500\,\mathrm{mA\,cm^{-2}}$
- Cell potential, E_{cell}: $\leq 3\,\mathrm{V}$ ($\hat{=}$ Energy Efficiency: $\geq 46\%$)[30]
- Faradaic efficiency for CO, FE_{CO}: $\geq 95\%$
- Stable performance over several years (e.g., ≥ 2 years $=\geq 17\,500\,\mathrm{h}$)
- Scalable electrolyzer design

To achieve these targets, the development of CO_2 electrolyzers has undergone several iterations in design.[31,32] In the most promising designs, catalyst-coated gas diffusion electrodes (GDE) serve as cathodes,[33] which are supplied with CO_2 from the gas side (Figure 1.4). This has enabled high Faradaic efficiency, FE, at high current density, j, by circumventing CO_2 mass transfer limitations in liquid-fed electrolyzers with CO_2-saturated electrolyte. Another improvement is the employment of porous anode materials (typically a nickel foam or iridium-coated titanium) in zero-gap configuration (Figure 1.4). This feature allows to decrease the cell potential by eliminating the gap between the anode and the membrane (Figure 1.3), thereby reducing the ohmic resistance of the anolyte.

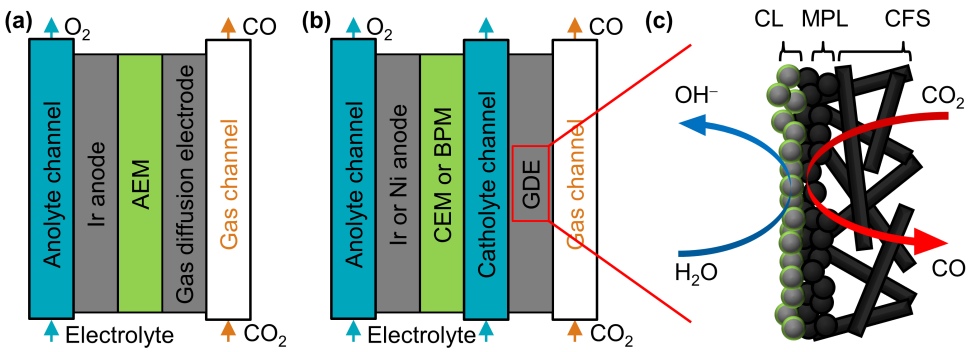

Figure 1.4: Schematics of gas-fed CO_2 electrolysis cells: (a) Membrane electrode assembly (MEA) type with anion exchange membrane (AEM) and iridium anode. (b) Flowing catholyte type with iridium or nickel anode combined with cation exchange membrane (CEM) or bipolar membrane (BPM), respectively. (c) Schematic of gas diffusion electrode (GDE) comprised of three layers: catalyst layer (CL); microporous layer (MPL); carbon fiber substrate (CFS).

1.3.1. CO_2 ELECTROLYZERS WITH MEMBRANE ELECTRODE ASSEMBLY

CO_2 electrolyzers with a membrane electrode assembly (MEA) also feature a zero-gap configuration on the cathode side (Figure 1.4 a). To date, one of the most advanced demonstrations of such a design has achieved $FE_{CO} = 80-90\%$ at $j = -500\,mA\,cm^{-2}$ and $E_{cell} = 3.2\,V$. In addition, the scale-up to an electrode area of $100\,cm^2$ has been demonstrated.[34] The design is also promising because it can be configured in multilayer cell stacks.[35] While the electrochemical performance and the scalability of this example are already close to meeting the previously mentioned benchmarks, the stability of the system has so far only been demonstrated for 500 h.[36]

MEA electrolyzers operate with anion exchange membranes (AEM), which allow the transfer of OH^- produced at the cathode to the anode.[34,37] Unfortunately, these membranes are not perfectly selective. For this reason, cations (e.g., Cs^+ or K^+) from the anolyte cross over to the gas channel, in which they can form carbonate salts by reacting with H_2O and CO_2. Because salt deposits can block the gas channel, special precautions have to be taken to prevent a buildup and ensure operational stability (e.g., periodic rinsing

of the gas channel).[38,39]

Another drawback of MEA electrolyzers (Figure 1.4 a) is the cross-over of (bi)carbonate anions to the anode side. These are formed at the cathode by the reaction of OH^- and CO_2. Because (bi)carbonate ions replace OH^- as the main ionic charge carrier and the OER at the anode produces H^+, the recirculated anolyte is acidified. Therefore, MEA electrolyzers with AEM require iridum-based anodes to ensure a stable cell operation.[23,34,40] Further, the cross-over of (bi)carbonate ions into the anolyte releases CO_2 at the anode. For this reason, the product gas at the anode side contains a significant amount of CO_2 (composition: 50 – 66 vol% CO_2, 50 – 33 vol% O_2),[41] which would probably have to be recovered to make the overall process economically feasible.

1.3.2. CO_2 ELECTROLYZERS WITH FLOWING CATHOLYTE

This thesis explores an alternative CO_2 electrolyzer design with a flowing catholyte (Figure 1.4 b). This type of system is compatible with cation exchange membranes (CEM) or bipolar membranes (BPM), which allow a significant reduction of CO_2 cross-over to the anode side.[40] In addition, the flowing catholyte allows a better control of the local reaction environment at the GDE (e.g. humidification or pH). This is because, in contrast to the MEA system, the mass transfer of ions does not only occur through diffusion and migration, but also through convection. Unfortunately, this benefit comes at the cost of additional ohmic losses by the catholyte gap, which lead to a higher E_{cell}.[19,23] This thesis investigates the mass transfer and flooding phenomena determining the performance of this electrolyzer design.

The cathode GDEs of gas-fed electrolyzers with flowing catholyte (Figure 1.4 b) are especially sensitive to the intrusion of electrolyte, which is called flooding. The mass transfer of CO_2 to the catalyst layer (CL) occurs through the pore network of the microporous layer (MPL) the carbon fiber substrate (CFS) (Figure 1.4 c). If the pore network is flooded with electrolyte, the gas diffusion can be strongly inhibited,[42] which can reduce the Faradaic efficiency achieved by the CO_2 electrolyzer. This phenomenon occurs if the differential pressure between liquid and gas phase becomes large enough to exceed the capillary pressure of the hydrophobic pores network. Preventing the flooding of GDEs is complicated through the following phenomena:

- Scale-up leads to differences in the hydrostatic and/or hydrodynamic pressure over the electrode[43]
- High current densities and cathode potentials lead to physical electrowetting[44]
- Physical electrowetting reduces the hydrophobicity of the GDE[44]
- (Electro-)chemical degradation reduces the hydrophobicity of the GDE[45]

The performance of CO_2 electrolyzers with a flowing catholyte also depends on which type of membrane is employed (CEM or BPM). For example, Haas *et al.*[46] presented a CO_2 electrolyzer with CEM that achieved $FE_{CO} = 60 – 90\%$ at $j = -300\,mA\,cm^{-2}$ and

E_{cell} = 6.0 V. It was demonstrated with an electrode size of 10 cm^2 and operated for ≥ 1200 h. However, this design requires the employment of iridium-based anodes because alkaline anolytes can not be used. This is because the CEM permits the exchange of protons and cations between the catholyte and anolyte.[47] As a consequence, the pH value of the electrolyte can only be stable if the anolyte is acidic (e.g. H_2SO_4)[46] or the anode and cathode share the same electrolyte (e.g., K_2SO_4 or $KHCO_3$).[46,48]

The employment of more abundant nickel-based anodes is possible in CO_2 electrolyzers with flowing catholyte and BPM.[49,50] This type of membrane consists of an AEM and a CEM layer. When a potential is applied across the membrane, the water splitting reaction ($H_2O \longrightarrow OH^- + H^+$) takes place at the interface between the two layers. If the AEM layer faces the anode and the CEM layer faces the cathode, the ions that are formed in the BPM can neutralize the OH^- and H^+ produced by the corresponding cathode and anode reactions. This allows to select the anolyte and catholyte indepdently while ensuring a stable pH on both sides of the cell. However, the additional potential required to drive the water splitting reaction increases E_{cell} compared to a system with a single CEM.[51,52]

For example, De Mot *et al.*[49] reported a BPM electrolyzer with a $KHCO_3$ catholyte and an electrode area of 16 cm^2. It achieved FE_{CO} = 70 – 90% at $j = -300\,mA\,cm^{-2}$. The E_{cell} was 8.2 V, which is more than twice as high compared to a MEA type electrolyzer (8.2 V vs. 3.2 V).[35] Chen *et al.*, in another example, where able to reduce E_{cell} below 5 V at $j = 300\,mA\,cm^{-2}$ by employing a K_2SO_4 catholyte and reducing the gap thickness.[50] Admittedly, the BPM-based CO_2 electrolyzers with flowing catholyte inhibit the CO_2 crossover, but the high operating voltage highlights that catholyte-containing electrolyzers require further optimization. Further, the Faradaic efficiency depends strongly on the local environment (e.g., pH, CO_2 concentration) at the GDE.[50] So far the understanding of this local environment is limited because it involves many phenomena (e.g., electrochemical reactions, homogenous reactions, convection, diffusion).

In conclusion, gas-fed CO_2 electrolyzers with flowing catholyte are interesting because they can reduce the cross-over of CO_2 to the anode side. More specifically, CO_2 electrolyzers with BPM allow the employment of more abundant nickel-bases anodes instead of scarce iridium-based anodes. However, this type of electrolyzer is less energy efficient compared to the catholyte-free MEA systems. Moreover, the direct contact of the GDE and the electrolyte make it difficult to scale up this electrolyzer type without flooding the GDE. In addition to mechanical flooding, the performance can be limited by the local reaction environment (e.g., pH, CO_2 concentration). The stability of cathode GDEs can be limited through reversible, physical electrowetting or irreversible, (electro-) chemical degradation. A better understanding of the mass transfer in the catholyte could allow an improved performance.

1.4. THESIS OUTLINE AND RESEARCH QUESTIONS

This thesis pursues the following research questions (RQ):

- RQ1: Can flooding due to pressure differences between the gas and liquid phase be suppressed by optimizing the structure of carbon-based GDEs? (Chapter 2)
- RQ2: How does the structure of carbon-based GDEs impact the Faradaic efficiency? (Chapter 2)
- RQ3: Does electrolyte flooding affect the Faradaic efficiency of carbon-based GDEs (Chapter 3)
- RQ4: Are carbon-based GDEs sufficiently chemically stable at current densities relevant for industrial applications? (Chapter 2 and Chapter 3)
- RQ5: How does electrowetting impact the performance of carbon-free, silver-based GDEs? (Chapter 4)
- RQ6: Are carbon-free, silver based GDEs sufficiently chemically stable at current densities relevant for industrial applications? (Chapter 4)
- RQ7: How do the process conditions of a BPM electrolyzer affect the Faradaic efficiency? (Chapter 5)
- RQ8: How do the process conditions of a BPM electrolyzer affect the local pH in the catholyte? (Chapter 5)

These research questions are addressed throughout the thesis with the following approaches. Chapter 2 examines the influence of the GDE microstructure on the flooding resistance and the mass transfer during electrochemical CO_2 reduction. To this end, a selection of seven commercial gas diffusion layers with different thicknesses (250 – 450 µm) and carbon fiber structures (paper, nonwoven, cloth) were investigated. Chapter 3 tests the electrochemical performance of these materials as a function of process parameters (current density, differential pressure). Further, the influence of electrowetting on the flooding resistance is quantified by measuring the liquid breakthrough pressure as a function of the cathode potential. Chapter 4 assesses the impact of electrowetting on the electrochemical CO_2 reduction performance of carbon-free, silver-based GDEs. In addition, their chemical stability is investigated by measuring changes to the chemical composition with XPS. Chapter 5 investigates how the process conditions of a BPM electrolyzer (current density, CO_2 saturation, and liquid flow rate) affect the Faradaic efficiency for CO and the local pH of the catholyte. The local pH of the catholyte was visualized with fluorescence lifetime imaging microscopy (FLIM).

1

REFERENCES

[1] J. Blau, *The Paris Agreement: climate change, solidarity, and human rights* (Springer, 2017).

[2] G. Hammond and M. Newborough, *Glasgow climate pact: a step on the way towards a lower carbon dioxide world,* in *Proceedings of the Institution of Civil Engineers-Civil Engineering*, Vol. 175 (Thomas Telford Ltd) pp. 8–8.

[3] *Going climate-neutral by 2050,* (2019), Publications Office of the European Union.

[4] A. Ilas, P. Ralon, A. Rodriguez, and M. Taylor, *Renewable Power Generation Costs in 2017* (International Renewable Energy Agency, Abu Dhabi, 2018).

[5] *Estimated US energy consumption in 2018,* (2019), https://flowcharts.llnl.gov/; consulted on 18.1.2020.

[6] P. Fayziyev, I. Ikromov, A. Abduraximov, and Q. Dehqonov, *Timeline: History of the electric car, trends and the future developments,* Eurasian Research Bulletin **6**, 89 (2022).

[7] A. Bhaskar, M. Assadi, and H. Nikpey Somehsaraei, *Decarbonization of the iron and steel industry with direct reduction of iron ore with green hydrogen,* Energies **13**, 758 (2020).

[8] G. Centi and S. Perathoner, *Chemistry and energy beyond fossil fuels. a perspective view on the role of syngas from waste sources,* Catalysis Today **342**, 4 (2020).

[9] A. Molino, S. Chianese, and D. Musmarra, *Biomass gasification technology: The state of the art overview,* Journal of Energy Chemistry **25**, 10 (2016).

[10] M. Hoogwijk, A. Faaij, B. Eickhout, B. De Vries, and W. Turkenburg, *Potential of biomass energy out to 2100, for four ipcc sres land-use scenarios,* Biomass and Bioenergy **29**, 225 (2005).

[11] J. L. Holechek, H. M. Geli, M. N. Sawalhah, and R. Valdez, *A global assessment: can renewable energy replace fossil fuels by 2050?* Sustainability **14**, 4792 (2022).

[12] A. Muscat, E. De Olde, I. J. de Boer, and R. Ripoll-Bosch, *The battle for biomass: A systematic review of food-feed-fuel competition,* Global Food Security **25**, 100330 (2020).

[13] S. Roussanaly, N. Berghout, T. Fout, M. Garcia, S. Gardarsdottir, S. M. Nazir, A. Ramirez, and E. S. Rubin, *Towards improved cost evaluation of carbon capture and storage from industry,* International Journal of Greenhouse Gas Control **106**, 103263 (2021).

[14] D. W. Keith, G. Holmes, D. S. Angelo, and K. Heidel, *A process for capturing CO_2 from the atmosphere,* Joule **2**, 1573 (2018).

[15] R. Sharifian, R. M. Wagterveld, I. A. Digdaya, C. Xiang, and D. A. Vermaas, *Electrochemical carbon dioxide capture to close the carbon cycle,* Energy & Environmental Science **14**, 781 (2021).

[16] J. Xiao, D. Mao, X. Guo, and J. Yu, *Effect of TiO_2, ZrO_2, and TiO_2–ZrO_2 on the performance of CuO–ZnO catalyst for CO_2 hydrogenation to methanol,* Applied Surface Science **338**, 146 (2015).

[17] H. Guzmán, F. Salomone, E. Batuecas, T. Tommasi, N. Russo, S. Bensaid, and S. Hernández, *How to make sustainable CO_2 conversion to methanol: Thermocatalytic versus electrocatalytic technology,* Chemical Engineering Journal , 127973 (2020).

[18] P. De Luna, C. Hahn, D. Higgins, S. A. Jaffer, T. F. Jaramillo, and E. H. Sargent, *What would it take for renewably powered electrosynthesis to displace petrochemical processes?* Science **364**, eaav3506 (2019).

[19] M. G. Kibria, J. P. Edwards, C. M. Gabardo, C.-T. Dinh, A. Seifitokaldani, D. Sinton, and E. H. Sargent, *Electrochemical CO_2 reduction into chemical feedstocks: From mechanistic electrocatalysis models to system design,* Advanced Materials **31**, 1807166 (2019).

[20] A. Zachopoulos and E. Heracleous, *Overcoming the equilibrium barriers of CO_2 hydrogenation to methanol via water sorption: A thermodynamic analysis,* Journal of CO_2 Utilization **21**, 360 (2017).

[21] W. A. Smith, T. Burdyny, D. A. Vermaas, and H. Geerlings, *Pathways to industrial-scale fuel out of thin air from CO_2 electrolysis,* Joule **3**, 1822 (2019).

[22] Y. Gao, L. Neal, D. Ding, W. Wu, C. Baroi, A. M. Gaffney, and F. Li, *Recent advances in intensified ethylene production—a review,* ACS Catalysis **9**, 8592 (2019).

[23] A. Vass, A. Kormanyos, Z. Kószó, B. Endrődi, and C. Janaky, *Anode catalysts in CO_2 electrolysis: Challenges and untapped opportunities,* ACS Catalysis **12**, 1037 (2022).

[24] R. I. Masel, Z. Liu, H. Yang, J. J. Kaczur, D. Carrillo, S. Ren, D. Salvatore, and C. P. Berlinguette, *An industrial perspective on catalysts for low-temperature CO_2 electrolysis,* Nature nanotechnology , 118–128 (2021).

[25] Y. I. Hori, *Electrochemical CO_2 reduction on metal electrodes,* in *Modern aspects of electrochemistry* (Springer, 2008) pp. 89–189.

[26] Y. Y. Birdja, E. Pérez-Gallent, M. C. Figueiredo, A. J. Göttle, F. Calle-Vallejo, and M. T. M. Koper, *Advances and challenges in understanding the electrocatalytic conversion of carbon dioxide to fuels,* Nature Energy **4**, 732 (2019).

[27] S. Hernandez, M. Amin Farkhondehfal, F. Sastre, M. Makkee, G. Saracco, and N. Russo, *Syngas production from electrochemical reduction of CO_2: current status and prospective implementation,* Green Chemistry **19**, 2326 (2017).

[28] C. C. McCrory, S. Jung, J. C. Peters, and T. F. Jaramillo, *Benchmarking heterogeneous electrocatalysts for the oxygen evolution reaction,* Journal of the American Chemical Society **135**, 16977 (2013).

[29] C. Minke, M. Suermann, B. Bensmann, and R. Hanke-Rauschenbach, *Is iridium demand a potential bottleneck in the realization of large-scale PEM water electrolysis?* international journal of hydrogen energy **46**, 23581 (2021).

[30] D. Salvatore and C. P. Berlinguette, *Voltage matters when reducing CO_2 in an electrochemical flow cell,* ACS Energy Letters **5**, 215 (2020).

[31] D. M. Weekes, D. A. Salvatore, A. Reyes, A. Huang, and C. P. Berlinguette, *Electrolytic CO_2 reduction in a flow cell,* Accounts of Chemical Research **51**, 910 (2018).

[32] B. Endrődi, G. Bencsik, F. Darvas, R. Jones, K. Rajeshwar, and C. Janáky, *Continuous-flow electroreduction of carbon dioxide,* Progress in Energy and Combustion Science **62**, 133 (2017).

[33] D. Higgins, C. Hahn, C. Xiang, T. F. Jaramillo, and A. Z. Weber, *Gas-diffusion electrodes for carbon dioxide reduction: A new paradigm,* ACS Energy Letters **4**, 317 (2019).

[34] B. Endrődi, E. Kecsenovity, A. Samu, T. Halmágyi, S. Rojas-Carbonell, L. Wang, Y. Yan, and C. Janáky, *High carbonate ion conductance of a robust PiperION membrane allows industrial current density and conversion in a zero-gap carbon dioxide electrolyzer cell,* Energy & Environmental Science , 4098 (2020).

[35] B. Endrődi, E. Kecsenovity, A. Samu, F. Darvas, R. V. Jones, V. Török, A. Danyi, and C. Janáky, *Multilayer electrolyzer stack converts carbon dioxide to gas products at high pressure with high efficiency,* ACS Energy Letters **4**, 1770 (2019).

[36] A. A. Samu, A. Kormányos, E. Kecsenovity, N. Szilágyi, B. Endrődi, and C. Janáky, *Intermittent operation of CO_2 electrolyzers at industrially relevant current densities,* ACS Energy Letters **7**, 1859 (2022).

[37] R. B. Kutz, Q. Chen, H. Yang, S. D. Sajjad, Z. Liu, and I. R. Masel, *Sustainion imidazolium-functionalized polymers for carbon dioxide electrolysis,* Energy Technology **5**, 929 (2017).

[38] B. De Mot, M. Ramdin, J. Hereijgers, T. J. Vlugt, and T. Breugelmans, *Direct water injection in catholyte-free zero-gap carbon dioxide electrolyzers,* ChemElectroChem **7**, 3839 (2020).

[39] B. Endrődi, A. Samu, E. Kecsenovity, T. Halmágyi, D. Sebők, and C. Janáky, *Operando cathode activation with alkali metal cations for high current density operation of water-fed zero-gap carbon dioxide electrolysers,* Nature Energy **6**, 439 (2021).

[40] M. Ma, S. Kim, I. Chorkendorff, and B. Seger, *Role of ion-selective membranes in the carbon balance for CO_2 electroreduction via gas diffusion electrode reactor designs,* Chemical Science **11**, 8854 (2020).

[41] G. O. Larrazábal, P. Strøm-Hansen, J. P. Heli, K. Zeiter, K. T. Therkildsen, I. Chorkendorff, and B. Seger, *Analysis of mass flows and membrane cross-over in CO_2 reduction at high current densities in an MEA-type electrolyzer,* ACS Applied Materials & Interfaces **11**, 41281 (2019).

[42] A. Z. Weber, *Improved modeling and understanding of diffusion-media wettability on polymer-electrolyte-fuel-cell performance,* Journal of Power Sources **195**, 5292 (2010).

[43] X.-L. WANG and S. KODA, *Scale-up and modeling of oxygen diffusion electrodes for chlorine-alkali electrolysis I. analysis of hydrostatic force balance and its effect on electrode performance,* Denki Kagaku Oyobi Kogyo Butsuri Kagaku **65**, 1002 (1997).

[44] B. De Mot, J. Hereijgers, M. Duarte, and T. Breugelmans, *Influence of flow and pressure distribution inside a gas diffusion electrode on the performance of a flow-by CO_2 electrolyzer,* Chemical Engineering Journal **378**, 122224 (2019).

[45] K. Yang, R. Kas, W. A. Smith, and T. Burdyny, *Role of the carbon-based gas diffusion layer on flooding in a gas diffusion electrode cell for electrochemical CO_2 reduction,* ACS Energy Letters **6**, 33 (2021).

[46] T. Haas, R. Krause, R. Weber, M. Demler, and G. Schmid, *Technical photosynthesis involving CO_2 electrolysis and fermentation,* Nature Catalysis **1**, 32 (2018).

[47] J.-B. Vennekötter, T. Scheuermann, R. Sengpiel, and M. Wessling, *The electrolyte matters: Stable systems for high rate electrochemical CO_2 reduction,* Journal of CO_2 Utilization **32**, 202 (2019).

[48] P. Jeanty, C. Scherer, E. Magori, K. Wiesner-Fleischer, O. Hinrichsen, and M. Fleischer, *Upscaling and continuous operation of electrochemical CO_2 to CO conversion in aqueous solutions on silver gas diffusion electrodes,* Journal of CO_2 Utilization **24**, 454 (2018).

[49] B. De Mot, J. Hereijgers, N. Daems, and T. Breugelmans, *Insight in the behavior of bipolar membrane equipped carbon dioxide electrolyzers at low electrolyte flowrates,* Chemical Engineering Journal , 131170 (2021).

[50] Y. Chen, A. Vise, W. E. Klein, F. C. Cetinbas, D. J. Myers, W. A. Smith, T. G. Deutsch, and K. C. Neyerlin, *A robust, scalable platform for the electrochemical conversion of CO_2 to formate: Identifying pathways to higher energy efficiencies,* ACS Energy Letters **5**, 1825 (2020).

[51] D. A. Vermaas and W. A. Smith, *Synergistic electrochemical CO_2 reduction and water oxidation with a bipolar membrane,* ACS Energy Letters **1**, 1143 (2016).

[52] M. A. Blommaert, D. Aili, R. A. Tufa, Q. Li, W. A. Smith, and D. A. Vermaas, *Insights and challenges for applying bipolar membranes in advanced electrochemical energy systems,* ACS Energy Letters , 2539 (2021).

2

Narrow Pressure Stability Window of Gas Diffusion Electrodes limits the Scale-up of CO_2 Electrolyzers

Electrochemical CO_2 reduction is a promising process to store intermittent renewable energy in the form of chemical bonds and to meet the demand for hydrocarbon chemicals without relying on fossil fuels. Researchers in the field have used gas diffusion electrodes (GDE) to supply CO_2 to the catalyst layer from the gas phase. This approach allows to bypass mass transfer limitations imposed by the limited solubility and diffusion of CO_2 in the liquid phase at a laboratory scale. However, at a larger scale, pressure differences across the porous gas diffusion layer can occur. This can lead to flooding and electrolyte breakthrough, which can decrease the performance. The aim of this study is to understand the effects of GDE structure on flooding behavior and CO_2 reduction performance. We approach the problem by preparing GDEs from commercial substrates with a range of structural parameters (carbon fiber structure, thickness, cracks). We then determined the liquid breakthrough pressure and measured the Faradaic efficiency for CO at an industrially relevant current density. We found that there is a trade-off between flooding resistance and mass transfer capabilities that limits the maximum GDE height of a flow-by electrolyzer. This trade-off depends strongly on the thickness and the structure of the carbon fiber substrate. We propose a design strategy for a hierarchically structured GDE, which might offer a pathway to an industrial scale by avoiding the trade-off between flooding resistance and CO_2 reduction performance.

This chapter has been published as "Narrow Pressure Stability Window of Gas Diffusion Electrodes Limits the Scale-Up of CO_2 Electrolyzers" by Lorenz M. Baumgartner, Christel I. Koopman, Antoni Forner-Cuenca, David A. Vermaas. *ACS Sustainable Chemistry & Engineering*, 2022, **14**, 4683-4693.

2.1. INTRODUCTION

The European Union has set the goal to become climate-neutral by 2050 in an attempt to limit the increase of average global temperature to 1.5 °C.[1] To meet the demand for hydrocarbon chemicals and fuels without relying on fossil feedstocks, the industrial and transport sectors will require new production processes that can be powered by intermittent wind and solar power. One possible pathway involves capturing CO_2 directly from the atmosphere[2] or the ocean[3] and converting it to useful chemical building blocks, such as C_2H_4, CO, or HCOOH, using electrochemical CO_2 reduction (CO_2R). These building blocks could then be further upgraded into plastics, fuels, or chemical intermediates using established chemical processes such as Fischer-Tropsch synthesis or methanol synthesis.[4,5]

The transfer of CO_2R from the lab scale (cm^2-size) to an industrial scale (m^2-size) requires a scalable reactor design that enables high current density and high Faradaic efficiency.[4] For illustration, reconverting the 1000 Mt of CO_2 emission of the EU transport sector in 2020[1] with a CO_2 electrolyzer operating at $-200\,mA\,cm^{-2}$ and a Faradaic efficiency of 85% would require a geometric electrode area of $80\,km^2$. To date, the largest CO_2 electrolyzers have an electrode area of only $100\,cm^2$.[6,7] To bridge this tremendous gap between the scale required to make an impact on climate change and the state of the art, researchers in the field of CO_2R have adopted carbon-based gas diffusion electrodes (GDE) from the mature field of polymer electrolyte fuel cells.[8] The adoption of this electrode type has been an important step to intensify the process by overcoming CO_2 mass transfer limitations in aqueous solutions. As a consequence, it is now possible to reach industrially relevant current densities of more than ($-200\,mA\,cm^{-2}$) while limiting the undesired hydrogen evolution reaction (HER).

In a typical GDE, gaseous reactants diffuse through the gas diffusion layer (GDL), which consists of the carbon fiber substrate (CFS) and the microporous layer (MPL). The CFS is impregnated with PTFE to increase the hydrophobicity. Typically, the fibers of the CFS have a size of $10\,\mu m$[9] or larger and are manufactured into unique microstructural arrangements using various mechanical methods, such as weaving or hydroentanglement. The MPL, a composite layer made out of carbon black and PTFE, plays an important role in keeping the CFS dry because its small, hydrophobic pores ($< 0.1\,\mu m$)[10] require high liquid overpressure to flood with liquid. This layer also provides electrical conductivity and support for the catalyst layer (CL).[8,11] Electrochemical reactions take place in the CL, which exchanges gaseous species through the pore network of the GDL and exchanges ionic species with the adjacent liquid/ionomer phase.[12]

Generally, the research on carbon-based GDEs has been geared towards fuel cell applications, where the produced water has to be drained through the GDL to the gas channel to prevent flooding of the GDE.[13] The flooding of the GDE, which is the saturation of the pores with liquid, is detrimental to the effective diffusivity.[14,15] In contrast to fuel cells, CO_2R does not produce water at the CL that has to be transported through the GDL. Therefore, a GDE design geared towards CO_2 electrolysis should support high mass transfer between the gas channel and the cathode CL to ensure the supply of gaseous re-

actants (CO_2, H_2O vapor) and the removal of gaseous products (CO, C_2H_4, or H_2). This GDE design, in addition, should prevent the intrusion of liquids to ensure a high resistance against electrolyte flooding. This requires understanding of the design of GDEs, which involves many adjustable parameters, e.g., the microstructure of the CFS (carbon paper, carbon cloth, nonwoven),[16,17] the thickness, or the composition of the different layers,[18,19] which all influence important properties like the electrical conductivity,[16] wettability[9,20] or diffusivity.[21]

Gas-fed CO_2 electrolyzers with flowing catholyte have demonstrated high current densities while maintaining a high Faradaic efficiency for the CO_2R reaction.[11,22–24] As the GDE is in direct contact with the liquid electrolyte, the supply of water molecules for the CO_2R reaction is no concern for this design. The flooding of the GDE with electrolyte, however, is a major practical challenge for scale-up because the separation of gas and liquid phase is being maintained only through the hydrophobic interfacial forces of the GDE. While it might be possible to control the differential pressure between gas and liquid to prevent flooding at a lab scale (height ≤ 10 cm)[25,26], it becomes increasingly difficult to maintain uniform conditions over the height of the electrode at a larger scale.[27,28] In large cells, or stacks of cells, hydrostatic pressure differences are much more significant and make (local) pressure differences between gas and liquid phase inevitable. These pressure differences will lead to the flooding of the GDE in the regions of the reactor in which the capillary pressure of the pores is exceeded and consequently limit the scalability. For example, Jeanty *et al.* investigated the scale-up of a reactor with flowing catholyte at a current density of 150 mA cm^{-2}. The Faradaic efficiency for CO, FE_{CO}, decreased from 66% to 53% after increasing the electrode area from 10 cm^2 to 100 cm^2. They attributed this decrease to the non-uniformity in reaction conditions due to GDE flooding and electrolyte breakthrough to the gas compartment.[7]

Gas-fed CO_2 electrolyzers with membrane electrode assemblies (MEA), feature a membrane that is in direct contact with the cathode GDE. This configuration creates a physical barrier between the electrolyte and the GDE. Although this reactor concept has demonstrated high current densities with high FE_{CO},[6,29] promising for scale-up and stacking,[30] an inherent challenge of the MEA design is supplying the right amount of H_2O to the cathode as a source of protons. For example, Berlinguette *et al.* showed that an insufficiently humidified CO_2 feed can lead to rapid decay of cell performance after only one hour of operation,[31] while an excess of H_2O at the cathode can also lead to performance decreases.[32] Hence, water management remains an issue in MEA-based CO_2 electrolyzers as well. Salt formation in gas channels is also frequently reported.[30] This phenomenon can be mitigated by periodically flooding the gas channel with water,[29,33] and therefore still requires a detailed understanding of the flooding mechanisms of GDEs.

While most CO_2 electrolysis research has been carried out at a scale of ≤ 10 cm^2 and repurposed GDLs from fuel cell applications, only a couple of studies focused on improving the GDE structure.[11,34,35] The scale-up of gas-fed CO_2 electrolyzers to a scale of m^2, however, requires the design of new materials that address the unique challenges of

CO_2R.

In this work, we investigate the effect of GDE structure on the CO_2R performance at commercially relevant current density in a gas-fed electrolyzer with a flowing catholyte. We investigate for the first time the effect of GDE structure on the resistance against electrolyte flooding/breakthrough due to pressure differences between the gas and the liquid phase, and how the structure impacts the formation of gaseous products in CO_2 electrolyzers. We deposited an Ag catalyst layer on a selection of commercial GDL materials with different CFS structures (paper, nonwoven, cloth) and thicknesses (250 – 450 µm). Additionally, we investigate how cracks in the MPL affect the flooding resistance and the mass transfer properties of a GDE. Our analysis helps researchers to select more suitable GDEs for their lab experiments using gas-fed CO_2 electrolyzers with MEA configuration or flowing catholyte configuration. We suggest a promising design strategy to improve carbon-based GDEs, which may be critical for the intensification and scale-up of electrochemical CO_2 reduction.

2.2. EXPERIMENTAL METHODS

We prepared GDEs from a selection of commercial GDL substrates. We characterized their physical properties and tested their electrochemical performance in a gas-fed CO_2 electrolyzer with flowing catholyte. More detailed descriptions are available in the supporting information (SI) of this chapter.

2.2.1. PREPARATION OF GDE SAMPLES

We have selected seven commercial GDL materials that varied in thickness and CFS structure (Table 2.1). Carbon papers are brittle materials, which are made of short carbon fiber fragments and carbonaceous binders.[36] The TGP-H carbon papers (Toray) have similar porosity, $\epsilon_{G,CFS}$, and tortuosity, $\tau_{G,CFS}$, for their CFS. Therefore, these materials allowed us to isolate the effects of CFS thickness, δ_{CFS} (190 – 370 µm). In comparison, the SGL carbon papers have a larger average pore radius, $\bar{d}_{pore}$, and a wider pore size distribution (PSD). This is also reflected by their higher porosity and lower tortuosity. The LT1400W (ELAT) is a flexible carbon cloth, which has been woven from carbon fiber bundles. The woven structure results in a bimodal PSD, which has large pores (85 µm) between the fiber bundles and small pores (10 µm) between individual fibers. The H23C6 (Freudenberg) has a nonwoven CFS structure and a crack-free MPL. The carbon fibers of this GDL have been partially entangled with high pressure water jets during the production process (hydroentanglement). This procedure gives the material flexibility and a dense packing, which results in a small average pore size with a narrow PSD (16 ± 16 µm). In conclusion, the studied GDLs exhibit the following trends from wide to narrow PSD: Cloth > SGL paper > Toray paper > Nonwoven (see SI, Figure 2.10).[17,37]

Table 2.1: Commercial GDL types with different CFS structures obtained from Fuel Cell Store (USA). The CFS of the Toray papers TGP-H-XX0 had been wet proofed with 8 – 9 wt% PTFE. They were supplied to us with a MPL composed of 33 – 35 wt% PTFE PTFE. The CFS of the SGL papers had been wet-proofed with 5 wt% PTFE; the MPL with 23 wt% PTFE. LT1400W and H23C6 had also been impregnated with PTFE, but no data were available on the exact contents. The thickness of the different layers, δ_i, was obtained from specification sheets issued by supplier and manufacturers. The mean pore diameter of the CFS, $\bar{d}_{pore}$, was reported by Parikh *et al.*.[17] The gas phase porosity, $\epsilon_{G,i}$, and tortuosity, $\tau_{G,i}$, were obtained from El-kharouf *et al.*.[16] Unavailable data is denoted as "-".

Material	TGP-H-060	TGP-H-090	TGP-H-120	SGL 22BB[a]	SGL 39BC[b]	LT1400W	H23C6[e]
Manufacturer	Toray	Toray	Toray	SGL	SGL	ELAT	Freudenberg
$\epsilon_{G,CFS+MPL}$ [16]	-	-	-	37%	53%	63%[c]	46%
$\tau_{G,CFS+MPL}$ [16]	-	-	-	2.9	1.9	-	5
$\delta_{G,CFS+MPL}$	250 µm	340 µm	430 µm	215 µm	325 µm	454 µm[c]	250 µm
Carbon fiber substrate (CFS) properties							
Structure	Paper	Paper	Paper	Paper	Paper	Cloth	Nonwoven
δ_{CFS}	190 µm	280 µm	370 µm	190 µm	300 µm	406 µm[d]	210 µm[f]
$\bar{d}_{pore}$ [17]	26 ± 20 µm	-	-	-	32 ± 30 µm	10, 85 µm[d]	16 ± 16 µm
$\epsilon_{G,CFS}$ [16]	63%	67%	62%	66%	71%	-	-
$\tau_{G,CFS}$ [16]	2.8	2.6	2.5	1.5	1.3	-	-
Microporous layer (MPL) properties							
δ_{MPL}	60 µm	60 µm	60 µm	25 µm	25 µm	48 µm	40 µm

[a] 22BB alternative names: 25BC, 29BB; CFS data for type without MPL: 25BA. [b] 39BC alternative names: 35BC, 39BB; CFS data for type without MPL: 35BA. [c] FuelCellsEtc GDL Comparison Table. [d] Bimodal pore size distribution with about 10 µm and 85 µm peak diameters; based on Nuvant ELAT Cloth.[37] [e] H23C6 alternative name: H2315 I2C6. [f] CFS thickness according to supplier data sheet for type without MPL: H2315.

The GDEs were prepared by depositing the CL with a custom-made automated airbrush coating system (see SI, Figure 2.9). The target catalyst loading was 1 mg Ag cm^{-1}. The solid composition was 80 wt% Ag and 20 wt% Nafion 521 ionomer. To prepare the sample, we cut the GDL to size, covered it with a 3 cm x 3 cm mask and fixed it to the heating plate (130 °C) of the system. To prepare the catalyst ink, we added 33 mg of Ag nanopowder (20 – 40 nm, 99.9%, Alfa Aesar), 2.1 mL of water, 2.1 mL of isopropyl alcohol, and 180 µL of Nafion D-521 dispersion (5 wt%, Alfa Aesar) into a glass vial. We homogenized the ink for 30 min in a sonication bath. Then we used the 2D-motorized stage to spray the ink evenly onto the MPL side of the GDL with an airbrush.

2.2.2. PHYSICAL GDE CHARACTERIZATION

The microstructure of each GDL was visualized with scanning electron microscopy (SEM) at three different locations of the CFS and MPL.

The wettability of the different GDE layers was quantified by measuring the static contact angle. For each sample, we deposited a 10 µL water droplet at five different locations of the surface. After recording an image, we extracted the contact angle with the image processing software ImageJ.

The flooding resistance of GDL and GDE was determined by observing the gas–liquid flow regime through a transparent flow cell as a function of differential pressure, Δp. We placed the sample in a flow cell (see SI, Figure 2.18). Then we pumped liquid into the liquid compartment. Water was used for the GDL samples; 1 M $KHCO_3$ was used for

the GDE samples. While gradually increasing the liquid backpressure and keeping the gas pressure constant, we observed the gas–liquid flow regime at the sample interface at both sides. We recorded Δp between gas and liquid compartment when a transition of the flow regime occurred (gas breakthrough, no breakthrough, liquid breakthrough). For more details on the exact procedure for the GDL and GDE samples, see the SI.

The CO_2 permeability was determined by measuring the pressure drop over the GDL as a function of the CO_2 flow rate. We installed the GDL in a flow cell (see SI, Figure 2.18 and forced the gas to flow through the sample by closing the gas outlet (see SI, Figure 2.20). We plotted the CO_2 flow rate against the recorded pressure drop according to Darcy's law[38] to determine the permeability constant, P_{CO_2}, from the slope of the resulting linear curve.

2.2.3. CO_2 ELECTROLYSIS PROCEDURE

The CO_2 reduction performance was measured with an automated electrolysis setup (Figure 2.1). We recirculated 1 M $KHCO_3$ through the anolyte and catholyte compartments with a peristaltic pump. The humidified CO_2 gas feed flowed through the gas compartment, whose backpressure was set by the cracking pressure of a check valve at the outlet. The liquid backpressure was controlled by electronic valves to obtain a flow-by regime (no breakthrough) when we applied a current density of $-200\,mA\,cm^{-2}$ to the cathode GDE. The product gases in the catholyte, anolyte and gas stream were collected in the headspace of the electrolyte reservoir. We recorded the flow rate (FR) of the product gas mixture with a mass flow meter (MFM). A gas chromatography system (GC) quantified the product gas concentration from three injections. We calculated the Faradaic efficiencies for the major products CO and H_2. The procedure is described in more detail in the SI. Preliminary experiments with a SGL 39BC GDE showed that the CO_2 reduction performance remained stable for at least 2 h, which is significantly longer than the short sampling period of 10 min required to carry out three GC injections (see SI, Section 2.5.9).

2.2.4. OVERALL O_2 MASS TRANSFER COEFFICIENT

The limiting overall O_2 mass transfer coefficient was measured as a proxy for the CO_2 mass transfer coefficient. We studied the O_2 flux induced by the oxygen reduction reaction (ORR) because it simplifies the analysis by avoiding the competing HER reaction (further discussion below). We installed the GDE in the flow cell (see SI, Figure 2.18) and supplied pressurized air as the gas feed (see SI, Figure 2.30). We carried out linear sweep voltammetry between 0 V and −2 V vs. SHE at a scan rate of $20\,mV\,s^{-1}$. We extracted the limiting current density for the ORR from these scans and used it to calculate the corresponding limiting overall mass transfer coefficient.

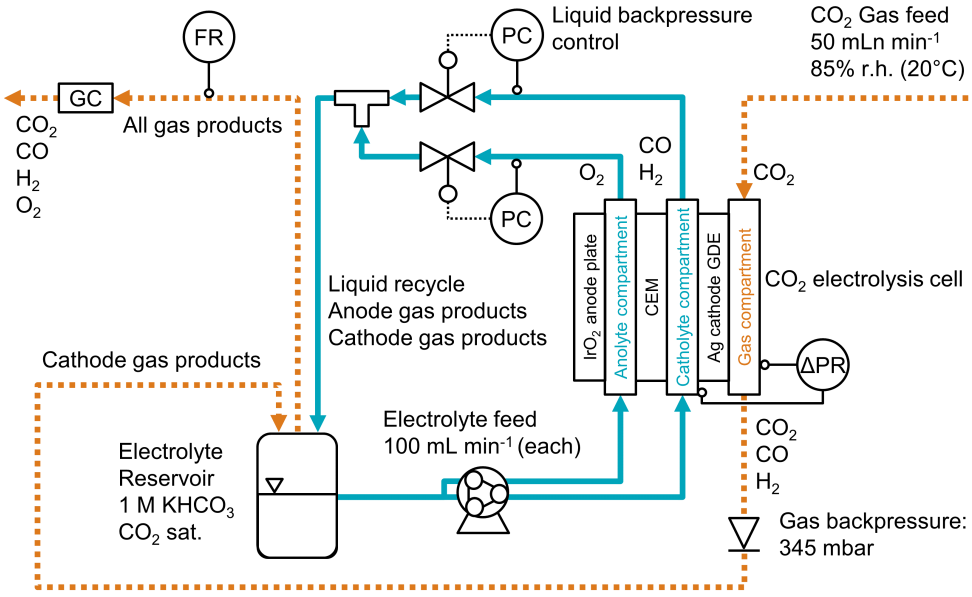

Figure 2.1: Process flow diagram for CO_2 electrolysis setup with differential pressure control. The anolyte and catholyte compartment were separated with a cation exchange membrane (CEM). The backpressure of both electrolyte streams was controlled (PC) before the two liquid streams were combined and recirculated. The Δp across the GDE was measured between the catholyte and gas compartment (ΔPR). The Faradaic efficiency was determined by recording the flow rate (FR) with a mass flow meter (MFM) and analyzing the gas composition by gas chromatography (GC).

2.3. RESULTS & DISCUSSION

Our study revealed a number of relationships between physical properties of the GDE materials and the resulting flooding resistance and electrochemical performance. More detailed results and all numerical values are available in the supporting information (SI).

2.3.1. STRUCTURE AND WETTABILITY DETERMINE FLOODING RESISTANCE

The SEM images illustrate the difference in microstructure between the materials (Figure 2.2). We arranged the materials according to the GDL thickness and the pore size distribution (PSD) of their CFS. The SGL carbon papers have a coarser structure than the Toray papers, which is in good agreement with the narrower PSD expected for Toray papers (see SI, Figure 2.10). The ELAT carbon cloth exhibits large pores between the fiber bundles. The nonwoven H23C6 has densely packed CFS with entangled fibers. Except for the H23C6, all GDLs show large cracks in the MPL with a size of tens of µm. Additional SEM images (see SI, Figure 2.12) let us estimate a CL thickness of 3.5 ± 0.2 µm. The primary Ag particles (79 ± 17 nm) formed larger agglomerates (200 – 1200 nm) embedded in a Nafion ionomer matrix (see SI, Figure 2.13).

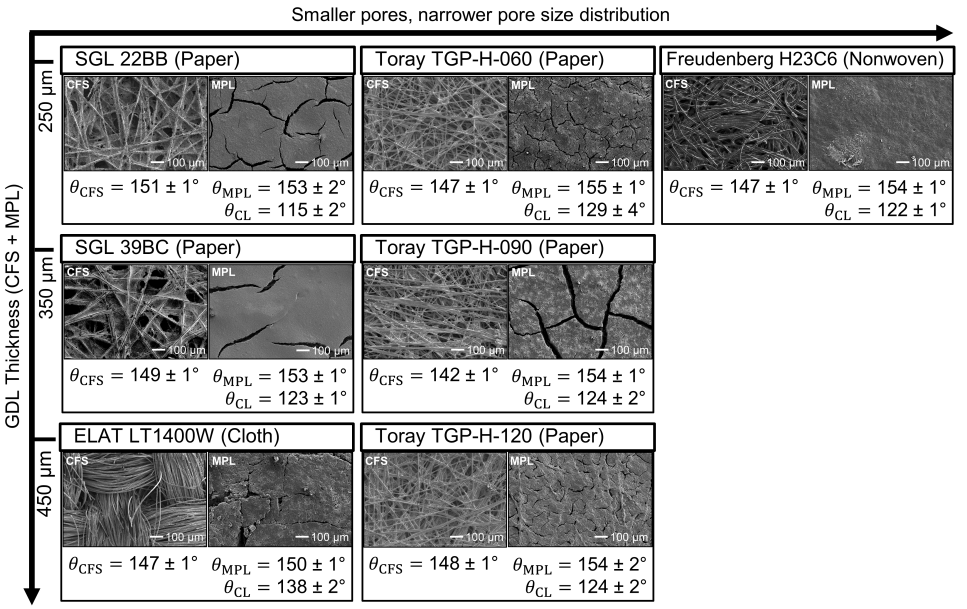

Figure 2.2: Microstructure and wettability results: SEM images of CFS and MPL at 100x magnification. Static contact angles, θ_i, of the carbon fiber substrate (CFS), microporous layer (MPL) and catalyst layer (CL). The presented contact angles are an average of five measurements at random locations ± the standard error.

The GDLs show little difference in their initial static contact angles (Figure 2.2). The CFS of all materials was highly hydrophobic (θ_{CFS} = 142 – 151°), which is in good agreement with literature.[18] The MPLs are even more hydrophobic (θ_{MPL} = 150 – 155°) because

their PTFE content is higher compared to the CFS. The higher PTFE content in the MPL of the Toray papers (33 – 35 wt%) compared to the SGL papers (23 wt%) does not seem to increase the contact angle significantly. This is consistent with studies in the literature reporting that the effect of PTFE content on the wettability levels off after a loading of 10 – 20 wt% is exceeded.[19,39] Nominally, the deposited CLs consist of 80 wt% Ag and 20 wt% Nafion. Because these components are more hydrophilic than carbon or PTFE,[40] the surface of this layer shows a lower contact angle (θ_{CL} = 115 – 138°). Note that the quantitative measurements of contact angles on rough surfaces are challenging (See SI for a detailed discussion). For example, rough surfaces can lead to an increase of the effective contact angle according to the Cassie-Baxter model.[41,42] This could explain why the LT1400W exhibits a higher θ_{CL} than the other materials.

We observed three different regimes of the two-phase flow at the GDE. These three flow regimes depend on the differential pressure between the liquid and the gas compartment, $\Delta p = p_L - p_G$: (i) Gas breakthrough occurs when Δp is below the threshold for gas breakthrough, Δp_G^* (flow-through). (ii) No breakthrough occurs when Δp is increased and the fluid phases are separated (flow-by).[26] (iii) Liquid breakthrough occurs when Δp exceeds the liquid breakthrough pressure, Δp_L^*, which is also called the percolation threshold.[43] Based on these flow regimes, we define the flow-by pressure window, $\Delta p^* = \Delta p_L^* - \Delta p_G^*$, as a metric for flooding resistance.

The flow-by pressure window, Δp^*, of most commercial GDL materials falls within a range of 40 – 80 mbar (Figure 2.3). This relatively low value implies that the scale-up of a flow-by electrolyzer would be limited to a height of about 41 – 81 cm. In practice, the height would have to be even smaller to make the process robust against variations in the material properties ($\sigma_{\Delta p^*} = \pm$ 14 mbar) and the limited accuracy of pressure control at the process level.

The application of the CL shifts the pressure window, Δp^*, to more negative values (Figure 2.3) without affecting the width significantly. This negative shift can be seen in the lower Δp_L^*, as the comparison between the upper limit of the pressure window of the GDL samples with the upper limit of the GDE samples shows. This phenomenon can be explained by the decrease of θ on the liquid side (Figure 2.2). According to the Young-Laplace equation (Figure 2.4 b), the higher hydrophilicity lowers the capillary pressure, p_C, which eases the flooding of pores in the GDE.

The flow-by pressure window, Δp^*, is an order of magnitude smaller for materials with cracks in the MPL (Figure 2.3). If no cracks are present (H23C6), the intruding liquid has to pass through the pores of the MPL. The pores of the MPL require a larger liquid pressure to be flooded because they are a lot smaller than the pores of the CFS (Figure 2.4). However, the largest pores determine the liquid breakthrough pressure, and cracks count as extremely large pores in the MPL. If cracks are present (all other GDEs), the MPL is bypassed and the liquid breakthrough pressure is determined by the pores of the CFS.

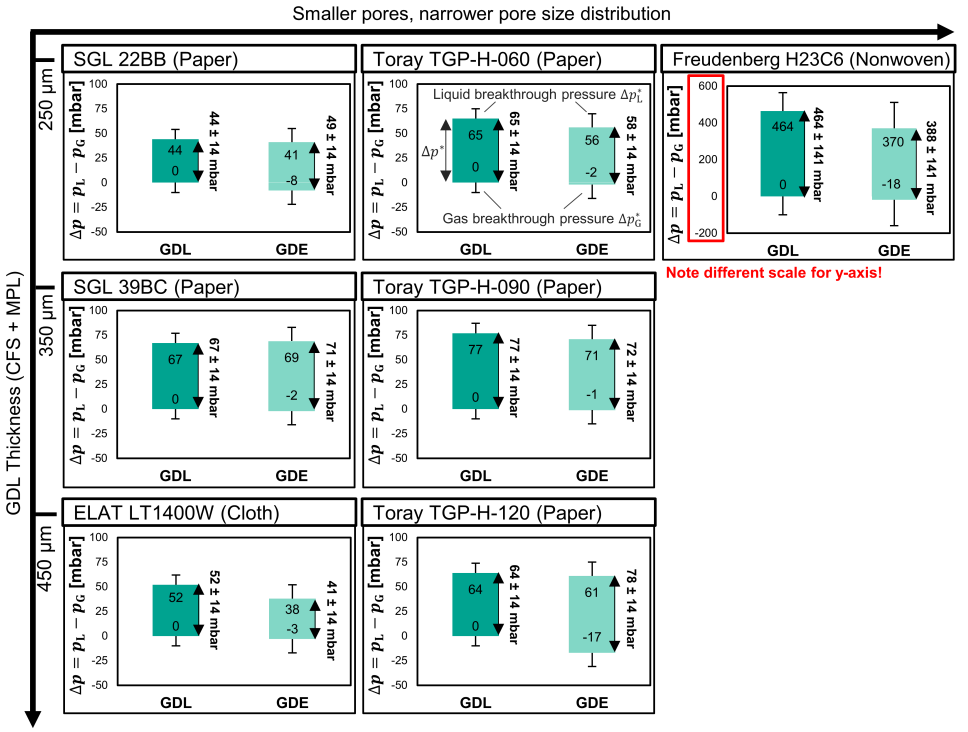

Figure 2.3: Flooding resistance results: Determination of flow-by pressure window, $\Delta p^* = \Delta p_L^* - \Delta p_G^*$, for uncoated GDL (MPL + CFS) and coated GDE (CL + MPL + CFS). Upper limit of bar chart: Liquid breakthrough pressure, Δp_L^*. Lower limit: Gas breakthrough pressure, Δp_G^*. The gas breakthrough pressure limit of the uncoated GDL samples was not measured; we assume that it was 0 mbar. The arrows next to the bar charts indicate the corresponding flow-by pressure window, Δp^*. The listed values are based on measurements of a single sample. For the breakthrough pressures, we estimated errors of $\sigma_{p_G^*} = \pm 10$ mbar and $\sigma_{p_L^*} = \pm 10$ mbar of all GDEs based on the work of Mortazavi *et al.* (except H23C6).[19] For H23C6, we estimated errors of $\sigma_{p_G^*} = \pm 100$ mbar and $\sigma_{p_L^*} = \pm 100$ mbar based on the work of Leonard *et al.*.[44] The error of the flow-by pressure window, $\sigma_{\Delta p^*}$, was estimated with the Gaussian error propagation: $\sigma^2_{\Delta p^*} = \sigma^2_{\Delta p_L^*} + \sigma^2_{\Delta p_G^*}$.

The two different percolation flow paths, with and without cracks in the MPL, are illustrated in Figure 2.5 a – b, using schematic pore network models.[45,46] Each network consists of pore bodies (circles) and throats (rectangles). The throats restrict fluid intrusion according to their capillary pressure, $p_{C,i}$. The spatial connectivity of the pores determines the percolation flow path and the liquid breakthrough pressure, Δp_L^*. For the material with the crack-free MPL (Figure 2.5 a), the narrow pores of the MPL prevent liquid intrusion into the gas-filled network until the high capillary pressure of $p_{C,4}$ is exceeded. For the material with cracks bypassing the MPL (Figure 2.5 b), Δp_L^* drops to $p_{C,2}$, which is the highest capillary pressure in flow path of the percolating liquid.

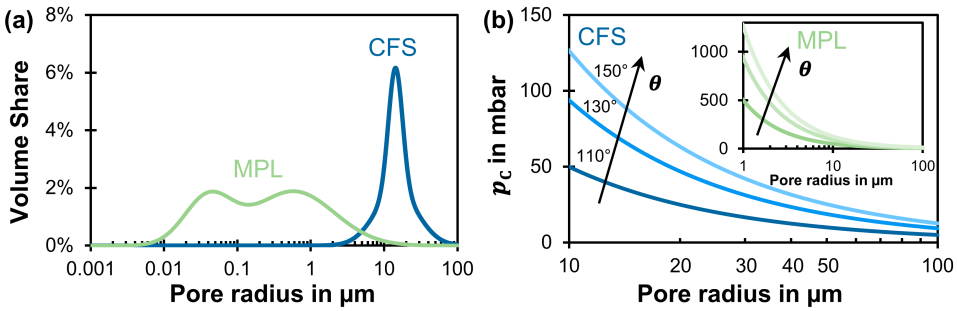

Figure 2.4: **(a)**: Typical pore size distribution of a SGL carbon paper with MPL. The y-axis shows the share of the total pore volume for a pore with radius r.[10] **(b)**: Capillary pressure, p_C, calculated with the Young-Laplace equation, $p_C = -2\gamma \cdot \cos\theta \cdot r^{-1}$, in which r is the cylindrical pore radius, θ is the wall contact angle (110°,130°, 150°), γ is the electrolyte surface tension (H_2O at 20 °C: $\gamma = 73\,mN\,m^{-1}$). The pore floods with liquid when the differential pressure acting on the pore exceeds the capillary pressure: $\Delta p = p_L - p_G \geq p_C$.

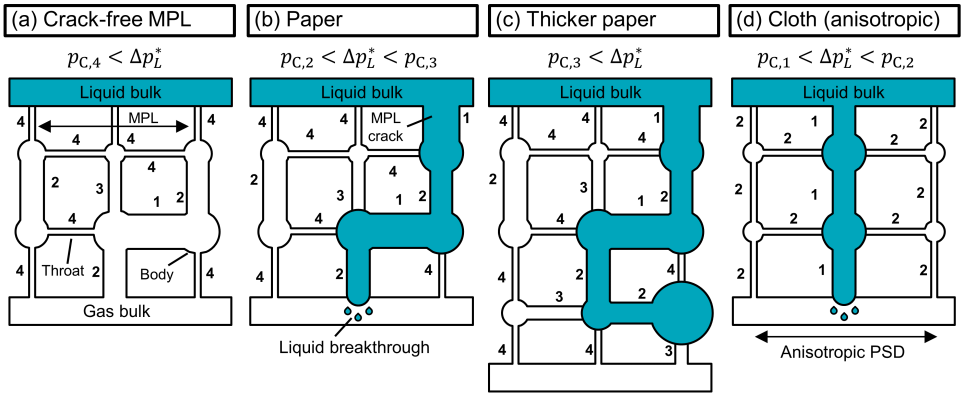

Figure 2.5: Schematic pore network models[45–47] representing different GDL materials. The spatial connectivity of the pores determines the percolation flow path and the liquid breakthrough pressure, Δp_L^*. The relative order of capillary pressures is: $p_{C,1} < p_{C,2} < p_{C,3} < p_{C,4}$. **(a)** Crack-free MPL: The network remains dry until the liquid exceeds the high capillary pressure of the MPL: $p_{C,4}$. **(b)** Carbon paper: The highest capillary pressure in the flow path, $p_{C,2}$, determines Δp_L^*. **(c)** Carbon paper with increased thickness: Compared with (b), the longer percolation pathway increases the probability of encountering pores with higher $p_{C,3}$. **(d)** Carbon cloth: The wide pore size distribution with anisotropic structure leads to a preferential breakthrough path along pores with low capillary pressure $p_{C,1}$. Adjacent pores with higher $p_{C,2}$ remain dry and allow gas diffusion.

The flow-by pressure window, Δp^*, of the GDE is also increased by a thicker CFS. This is illustrated by data of the SGL and Toray papers (Figure 2.3). For example, the Δp^* improves from 58 mbar for the thinnest Toray paper (TGP-H-060) to 78 mbar for the thickest (TGP-H-120). This trend is in good agreement with the liquid breakthrough pressures recorded by Mortazavi *et al.*, who explain that a thicker GDL has a higher probability to have small, hydrophobic pores in the percolation flow path.[19] We illustrate this phenomenon with the pore network model in Figure 2.5 b – c: The additional layer in the pore network of the thicker paper (Figure 2.5 c) increases the probability that the liquid

is stopped by a pore with $p_{C,3}$, which increases the liquid breakthrough pressure, Δp^*_L, without affecting the gas breakthrough pressure, Δp^*_G.

GDLs with broader pore size distributions exhibit a lower flooding resistance (Figure 2.3). This effect is most apparent for the LT1400W carbon cloth, which has a similar thickness as the TGP-H-120 carbon paper, but has a much smaller Δp^*: 41 mbar vs. 78 mbar. The effect of larger CFS pores is enhanced by the anisotropic PSD of the cloth: The large pores are located in between the fiber bundles and go all the way through the cloth, while the small pores are located inside of the fiber bundles. The large pores, therefore, offer a preferential percolation flow path, which bypasses smaller pores with higher capillary pressure (Figure 2.5 d). The effect of wider pore size distributions becomes clear—though to a lesser extent—by comparing the carbon papers SGL 22BB and TGP-H-060. Here, the SGL 22BB has a wider pore size distribution, which results in a lower Δp^* of 49 mbar compared to 58 mbar. We note that the Toray papers had a thicker MPL than the other GDL materials, which could convolute the effects of a narrower PSD and of a thicker MPL on the flooding resistance. We argue, however, that the properties of the CFS are more significant because the MPL offers little flooding resistance due to its large cracks. In summary, broader PSDs lead to a lower flooding resistance, however, they can also be advantageous because a large fraction of pores remains accessible for gas diffusion even if liquid breakthrough is occurring.[39]

2.3.2. MICROSTRUCTURE DETERMINES MASS TRANSFER AND CO_2 REDUCTION PERFORMANCE

As a mass transfer metric, the limiting current density for the CO_2 reduction is a valuable metric. However, the H23C6 was not stable during CO_2 electrolysis at the current density of $-200\,mA\,cm^{-2}$ (discussion further below). To isolate the mass transfer of the gaseous species from other factors (such as GDE stability), we measured the limiting overall O_2 mass transfer coefficient, k_{O_2}, in flow-by mode as a proxy for the CO_2 mass transfer. The CO_2R and the oxygen reduction reaction (ORR) are both subject to mass transfer limitations at sufficiently high current densities. The derived mass transfer metrics, however, can only be compared qualitatively between GDL substrates because the solubility and diffusivity of the two gases differ.

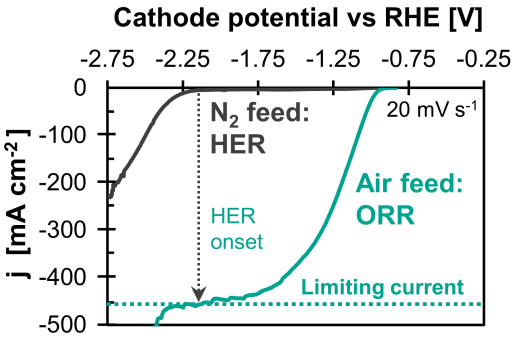

Figure 2.6: Limiting O_2 mass transfer as proxy for CO_2 mass transfer: Example LSV scan for SGL 39BC loaded with 1 mg Ag cm^{-1}. HER: hydrogen evolution reaction, ORR: oxygen reduction reaction: $O_2 + 2H_2O + 4e^- \longrightarrow 4OH^-$. The cathode potentials were corrected for the iR-drop between the reference electrode and the cathode. To reach sufficiently high currents with our potentiostat, we used 6 M KOH electrolyte due its high conductivity.

We determined k_{O_2} from the limiting current density of the oxygen reduction reaction (ORR) extracted from a LSV scan (Figure 2.6). This reaction is commonly performed with Ag-based GDEs for chlor-alkali electrolysis with oxygen depolarized cathodes.[48] The onset potential of the ORR is much higher (less negative) than for the competing HER, as the comparison of the LSV scan for an air feed (21 vol% O_2) with an N_2 feed illustrates. This leads to a distinct current density plateau at which the oxygen transfer to the CL determines the reaction rate. We used this limiting current density, therefore, to calculate the corresponding overall mass transfer coefficient, k_{O_2}. This metric describes the limiting transport of O_2 from the gas bulk, through the different GDE layers, to the surface of the catalyst (details of the data processing are explained Section 9 of the SI). The resulting values for k_{O_2} are presented together with the other mass transfer and electrolysis metrics in Figure 2.7.

Our mass transfer and electrolysis results suggest that convective mass transfer (permeation) might be of secondary importance for our electrolysis conditions (Figure 2.7). The CO_2 permeability constant, P_{CO_2}, showed a poor correlation with FE_{CO} or the limiting overall O_2 mass transfer coefficient, k_{O_2}. For example, we measured a lower P_{CO_2} for SGL 39BC in comparison with TGP-H-120, but the SGL 39BC exhibits a higher FE_{CO} and k_{O_2}. While a more quantitative analysis is precluded by the limited range of our P_{CO_2} data, it seems plausible, however, that the mass transfer occurs primarily by gas diffusion through the CFS and by a combination of gas and Knudsen diffusion through the MPL, as is the case in hydrogen fuel cells.[49]

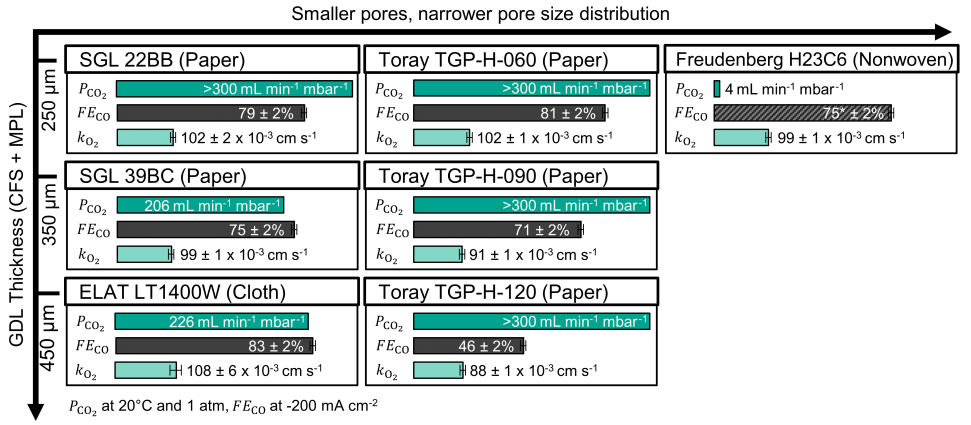

Figure 2.7: Mass transfer characterization results: Uncoated GDL samples (CFS+MPL): The CO_2 permeability constant, P_{CO_2}, of the Toray papers and SGL 22BB were out of range of our experimental setup (300 mL min^{-1} mbar^{-1}). GDE samples (flow-by mode): FE_{CO} at -200 mA cm^{-2}, k_{O_2} is the limiting overall O_2 mass transfer coefficient (proxy for CO_2 mass transfer). *Freudenberg H23C6: Unstable at -200 mA cm^{-2}. The $FE_{CO} = 75 \pm 2\%$ is a hypothetical value based on the data for SGL 39BC because the k_{O_2} of the two materials is equivalent.

An increase in GDL thickness limits the mass transfer significantly. This can be clearly seen by the trends of FE_{CO} (recorded at -200 mA cm^{-2}) for the SGL and Toray carbon papers (Figure 2.7). When comparing the thin TGP-H-060 with the thicker TGP-H-120, for example, the FE_{CO} drops from 81% to 46%. Kenis *et al.* reported a similar trend in their study on GDE structure.[11] We observe this decrease in FE_{CO} because the supply of CO_2 to the CL is restricted by the thicker CFS. The CO_2 diffusion rate, therefore, is unable to keep up with the electrical current, which leads to excess electrons being consumed by the competing HER.

In contrast, CFS structures with a broader PSD allow higher mass transfer rates. This is well illustrated by the data for LT1400W and TGP-H-120 (Figure 2.7). Both had a similar thickness, but the carbon cloth allowed a much better FE_{CO}. Another example that shows the effect of a broader PSD is the comparison of SGL 39BC vs. TGP-H-090. Again, the samples have a similar thickness, but the SGL 39BC showed a better FE_{CO} of 75% in comparison with 71% recorded for the TGP-H-090. The materials with broader PSD tend to have a higher porosity, $\epsilon_{G,CFS}$, and lower tortuosity, $\tau_{G,CFS}$ (Table 2.1). These properties improve the mass transfer coefficient through the CFS, $k_{CO_2,CFS}$, by increasing the effective diffusivity, D_{eff,CO_2}, according to (2.1).[50,51]

$$k_{CO_2,CFS} = \frac{D_{eff,CO_2}}{\delta_{CFS}} = \frac{\epsilon_{G,CFS}}{\tau^2_{G,CFS}} \frac{D_{CO_2}}{\delta_{CFS}} \tag{2.1}$$

Our results also indicate that a large resistance to mass transfer must lie in the CL. We come to this conclusion from decomposing the overall O_2 mass transfer coefficient, k_{O_2}. This empirical metric is an overall mass transfer coefficient that incorporates the se-

rial resistance over the different domains of the GDE (CFS, MPL, and CL). Figure 2.7 already reveals that k_{O_2} is not inversely proportional to the CFS thickness. If the mass transfer through the CFS were limiting, we would expect a relative mass transfer coefficient of about +100% for TGP-H-060 compared to TGP-H-120, as its porosity and tortuosity are similar (Table 2.1). The empirically determined k_{O_2}, however, shows only an increase of +16% ($0.102\,\mathrm{cm\,s^{-1}}$ vs. $0.088\,\mathrm{cm\,s^{-1}}$). This means that an additional resistance to mass transfer must be responsible for the smaller difference. We decomposed k_{O_2} for SGL 22BB in Table 2.8 by using characterization data from fuel cell research. Based on the data of Reshetenko *et al.*,[52] we estimated mass transfer coefficients of $k_{O_2,CFS} = 2.60\,\mathrm{cm\,s^{-1}}$, $k_{O_2,MPL} = 5.97\,\mathrm{cm\,s^{-1}}$, and $k_{O_2,CL} = 0.108\,\mathrm{cm\,s^{-1}}$. We note that $k_{O_2,MPL}$ has a higher value than $k_{O_2,CFS}$ because the MPL is an order of magnitude thinner than the CFS. The much lower value for $k_{O_2,CL}$ corresponds to the CL being responsible for 94% of the mass transfer resistance of this material (Table 2.10). The resistance of the CL is probably so high because it is flooded with electrolyte. The improvement of the CL resistance would, therefore, be an important topic for future research. We note that the mass transfer through the CL is probably lower for the ORR experiments compared to the CO_2R experiments. Due to the higher viscosity of 6 M KOH, the diffusivity of O_2 in this electrolyte ($0.7 \times 10^{-5}\,\mathrm{cm^2\,s^{-1}}$)[53] is 56% lower than the diffusivity of CO_2 in 1 M KHCO3 ($1.6 \times 10^{-5}\,\mathrm{cm^2\,s^{-1}}$)[54] at 25 °C. In addition, the solubility of O_2 in 6 M KOH (0.01 M)[53] is three times lower than the solubility of CO_2 in 1 M $KHCO_3$ (0.034 M).[54] Quantitative predictions, however, are difficult to make because the material values in the porous Nafion matrix of the CL are likely to differ from the corresponding values for bulk electrolytes.

The nonwoven H23C6 was unstable during CO_2 electrolysis at $-200\,\mathrm{mA\,cm^{-2}}$. At these conditions, the GDE lost its hydrophobicity and the gas compartment started to flood so that we were unable to measure a representative FE_{CO} (Figure 2.7). Similar behavior for this GDL material has been also reported in literature.[44,55] Yang *et al.*, for example, reported a degradation of the carbon when the cathode potential was more negative than −0.65 V vs. RHE.[55] We confirmed the hypothesis that the CFS degraded experimentally. After applying a current density of $-100\,\mathrm{mA\,cm^{-2}}$ at −1.2 V vs. RHE for 111 min, the θ_{CFS} dropped to $131 \pm 2°$ from its initial value of $147 \pm 1°$. We hypothesize that the poor stability of the Freudenberg H23C6 might be attributed to a larger number of oxygen groups at the surface of its carbon fibers relative to the other substrates (Freudenberg: 10 at% vs. SGL: < 1 at%).[56,57] These oxygen functionalities might facilitate the degradation of the surface by serving as active sites for the carbon surface oxidation.[58] The higher oxygen content probably originates from a lower degree of carbonization,[59,60] which likely also gives this material its high flexibility. A systematic study of the degradation mechanism of H23C6 would be an important contribution for future research.

The transport through MPL cracks seems to play a secondary role for the mass transport and Faradaic efficiency during electrolysis (Figure 2.7). If we compare the data for H23C6 and SGL 39BC, we find that the O_2 mass transfer coefficient of both samples was equivalent ($k_{O_2} = 0.99\,\mathrm{cm\,s^{-1}}$), although the P_{CO_2} was two orders of magnitude lower for the H23C6 due to the lack of cracks in the MPL. This result shows that the cracks in the MPL

do not have a significant impact on the mass transfer during electrolysis. It is likely the cracks are filled with electrolyte during electrolysis and the transport of CO_2 to the CL occurs through the gas-filled pore network of the MPL. Based on the equivalent values of k_{O_2} for these samples, we can also hypothesize that H23C6 would allow a $FE_{CO} = 75\%$ at $-200\,mA\,cm^{-2}$ if it were stable.

2.3.3. TRADE-OFF BETWEEN FLOODING RESISTANCE AND MASS TRANSFER LIMITS SCALABILITY

There seems to be an inevitable trade-off between the flooding resistance of the CFS at open circuit potential (OCP) and the mass transfer capabilities (Figure 2.8 a). GDEs with a broad PSD and/or with a thin CFS achieve the highest FE_{CO} at $-200\,mA\,cm^{-2}$. This presents a dilemma for building larger scale reactors because these same materials exhibited the lowest pressure window ($\Delta p^* < 50\,mbar$). For illustration, 50 mbar of hydrostatic pressure difference correspond to 51 cm cell height with an aqueous electrolyte in vertical orientation. Commercial alkaline electrolysis for H_2 production operates at a similar current density ($200 - 400\,mA\,cm^{-2}$), but commonly uses plate diameters of 100 – 200 cm, which implies a 4 – 32x larger production rate per cell compared to a 51 cm tall CO_2 electrolyzer operating at $200\,mA\,cm^{-2}$.[61] The smaller cell height of the CO_2 electrolyzer would, therefore, imply higher capital expenditures. Using a GDE with a thicker CFS and a narrower PSD would sacrifice in terms of mass transport rate. TGH-H-120, for example, exhibits a small gain in pressure stability ($\Delta p^* = 78\,mbar$), but in exchange FE_{CO} falls below 50%.

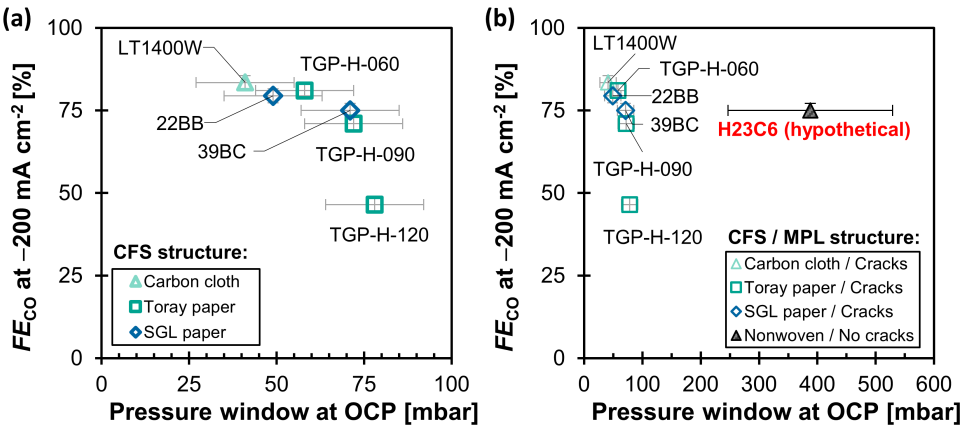

Figure 2.8: Trade-off between flooding resistance and CO_2 mass transfer: FE_{CO} at $-200\,mA\,cm^{-2}$ (flow-by mode) against the flow-by pressure window, Δp^*, recorded at open circuit potential (OCP). The shape and color of the markers indicate the CFS structure of each GDE. (a): Detailed view of materials with MPL cracks (b): Comparison of materials with and without MPL cracks (H23C6). The H23C6 marker represents a hypothetical value for FE_{CO} because this GDE type experienced a complete flooding of the gas channel at $-200\,mA\,cm^{-2}$.

It might be possible to avoid this trade-off between flooding resistance and mass transfer capabilities if the MPL is crack-free (Figure 2.8 b). As already established in the previous

section, the physical structure of the crack-free H23C6 allows mass transfer rates that should be able to provide a FE_{CO} of 75% at $-200\,mA\,cm^{-2}$, if it were electrochemically stable. This is remarkable because at the same time this material can also withstand gas–liquid differential pressures at OCP that would allow electrolysis cells with a height of more than 1 m. We hypothesize that the pressure window of the other GDEs could be greatly improved by curing the MPL cracks with a targeted application of a carbon black and PTFE mixture. Note that, although the crack-free H23C6 shows that large Δp^* are possible at OCP, the hydrophobicity (and thus Δp^*) decreases when a potential is applied during operation conditions due to electrowetting.[25] The effect of electrowetting on the flooding resistance and mass transfer is a topic for future work, and could shine light on the potential for other crack-free MPLs.

2.4. CONCLUSION

We have studied seven commercial GDLs with a range of structural parameters (CFS structure, CFS thickness, cracks in the MPL). The flooding behavior and mass transfer characteristics gave insight into the selection of suitable GDEs for CO_2 electrolyzers.

The carbon cloth (ELAT LT1400W) showed the highest mass transfer for gas–liquid CO_2 electrolysis operation, because the woven fiber bundles lead to an anisotropic PSD that has a broad (bimodal) distribution in the plane of the cloth, which allows high diffusivity. Carbon papers with thinner CFS (SGL 22BB, TGP-H-060) offer slightly lower mass transfer rates due to their narrower, more isotropic pore structure. Cloths and thin papers minimize the diffusional pathway at the cost of a low resistance against flooding through liquid–gas overpressure (< 50 mbar).

If CO_2 electrolyzers with flowing catholyte should be operated in flow-by mode, this low resistance against flooding in commercial GDLs poses serious limits on the scalability. All materials with acceptable Faradaic efficiency for CO_2R (> 50%) at $-200\,mA\,cm^{-2}$ suffer from a poor flooding resistance due to cracks in the MPL. Because of hydrostatic pressure differences between gas and liquid compartments, this poor flooding resistance would limit the maximum cell height to less than 51 cm if the electrolyzer should be operated in flow-by mode.

The only material with a crack-free MPL (H23C6) showed a very promising initial flooding resistance (> 200 cm), but degraded during CO_2 electrolysis. This degradation requires more comprehensive investigation because it remains unclear why the carbon-based GDEs differed in electrochemical stability. By using O_2 mass transfer as a proxy for CO_2 mass transfer, we were able to show that cracks in the MPL are not essential for high diffusion rates. The most significant resistance to mass transfer, however, was posed by the CL, which was probably flooded. Future research could optimize the performance by investigating the resistance in the CL in more detail.

The trade-off between flooding resistance and mass transfer capability has to be overcome before CO_2 electrolyzers can be constructed at an industrial scale. Our study implies that the layers of the ideal GDE have to be optimized for different objectives:

The CFS should be thin and feature a broad PSD to minimize the diffusional pathway. The MPL should be crack-free to protect the GDE from electrolyte flooding. Such a CO_2 electrolysis-geared GDE design might enable a GDE height larger than 100 cm for gas-fed electrolyzers with flowing catholyte. An alternative pathway to industrial CO_2 electrolysis is offered by MEA-based systems, which should be less complex to scale-up because their membrane constitutes a physical barrier against electrolyte flooding.

2.5. SUPPORTING INFORMATION

The digital version of the Supporting Information (SI) includes an Excel file with the values for all plotted data and all recorded experimental parameters for the CO_2 electrolysis experiments.

2.5.1. GDE PREPARATION

We prepared each GDE by depositing the CL with a custom-made automated airbrush coating system (Figure 2.9).

Sample preparation

We cut the GDL to size a size of 3.5 cm x 3.0 cm, dried it for 10 min at 120 °C, and weighed it in an airtight container (Kartell 034600 Polypropylene Weighing Bottles – 50 mL, Fisher Scientific). We then covered the sample with a 3 cm x 3 cm PTFE mask and fixed it to the heating plate (130 °C).

Ink preparation

An example for the ink specifications is given in Table 2.2. The target catalyst loading was 1 mg Ag cm^{-1}. We selected this common catalyst loading to simplify the comparison with other studies.[62] The solid composition was 80 wt% Ag and 20 wt% Nafion 521 ionomer. The Nafion binder content of 20 wt% was selected to match the optimized content determined by Duarte *et al.*.[26] To prepare the catalyst ink, we added 33 mg of Ag nanopowder (Aerodynamic particle size (APS): 20 – 40 nm, 99.9%, Alfa Aesar), 2.1 mL of de-ionized water, and 2.1 mL of isopropyl alcohol into a 10 mL glass vial. Then, we added 180 µL of Nafion D-521 dispersion (5 wt%, Alfa Aesar) to achieve an ink solid (Ag +Nafion) concentration of 0.01 g mL^{-1}. Note that we used an excess of ink to compensate for the loss of 30% ink during the deposition process. We homogenized the ink for 30 min in a sonication bath (USC500TH, VWR).

Table 2.2: Example for catalyst ink specifications.

Parameter	Unit	Value
Ag nanoparticle target loading	mg cm^{-2}	1.1
Expected deposition efficiency	-	30%
Spray-coated area	cm^2	9
Required catalyst mass	mg	33
Weighed catalyst mass	mg	33.4
Ink solid concentration	w/v in g mL^{-1}	0.01
Add H_2O:IPA (1:1) mixture	mL	4.175
Add Nafion solution (5wt%)	mL	0.180
Nafion content in catalyst layer	wt%	20

Deposition process

The ink was evenly sprayed onto the MPL side of the GDL sample with a Paasche Airbrush Set TG3 (Airbrush Services Almere, Netherlands) mounted on a custom made 2D-motorized stage (Figure 2.9).

Determination of catalyst loading

After the deposition process, we dried and weighed the coated sample for 10 min at 120 °C to determine the mass of the CL. An overview of the catalyst loading per sample is given in Table 2.3.

Table 2.3: Summary of Ag catalyst loading in mg cm^{-2} for samples used in experiments to determine the Faradaic efficiency for CO, FE_{CO}, and the overall O_2 mass transfer coefficient, k_{O_2}.

Experiment	TGP-H-060	TGP-H-090	TGP-H-120	SGL 22BB	SGL 39BC	LT1400W	H23C6
FE_{CO}	1.16	1.08	1.05	1.29	1.40	1.20	1.18
k_{O_2}	1.12	1.07	1.08	1.08	1.16	1.09	1.03

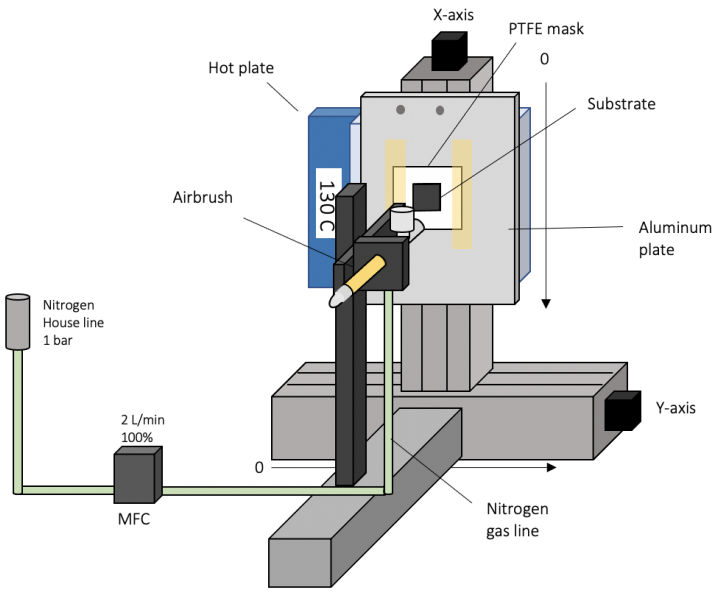

Figure 2.9: Catalyst layer deposition: Schematic of airbrush coating system.

2.5.2. QUALITATIVE PORE SIZE DISTRIBUTIONS OF GDLS

The studied GDLs exhibit the following trends from narrow to wide pore size distributions (PSD): Nonwoven < Toray paper < SGL paper, Cloth (Figure 2.10). Note that Figure 2.10 only shows the qualitative difference of the CFS types because we used different materials in this study. Forner-Cuenca *et al.* used materials without MPL and without PTFE wet-proofing. The Nuvant carbon cloth is of a different type than our LT1400W cloth.[37]

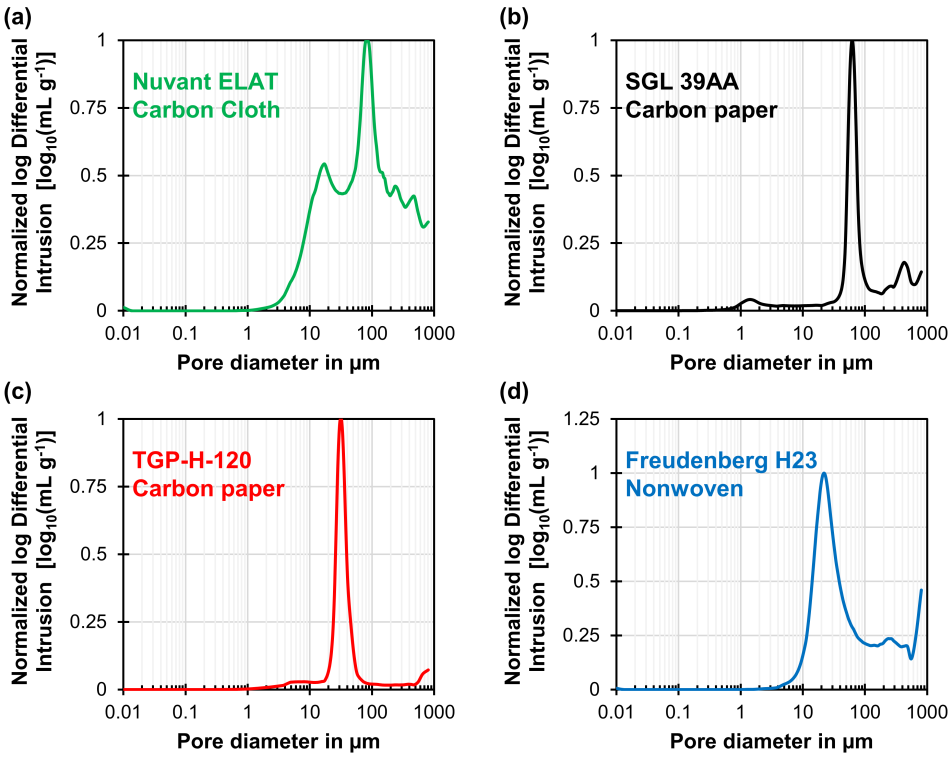

Figure 2.10: Qualitative comparison of the pore size distributions for the different carbon fiber substrate types. (a) ELAT carbon cloth (b) SGL carbon paper (c) Toray paper (d) Freudenberg Nonwoven. Note that the substrates shown here differ from our study because they were not impregnated with PTFE and do not have a MPL. The data is based on mercury intrusion porosimetry measurements from Forner-Cuenca *et al.*[37]

2.5.3. CHARACTERIZATION WITH SCANNING ELECTRON MICROSCOPY

The GDE microstructure was visualized with scanning electron microscopy (SEM). We used the instrument model JSM-6010LA (JEOL, Japan), which was equipped with a secondary electron imaging (SEI) detector for morphology and a backscattered electron (BEC) detector for elemental contrast imaging.

Catalyst layer (CL) characterization

We cut a Freudenberg H23C6 GDE sample with a surgical blade and looked at the edge with SEM (Figure 2.11). The SEI detector allowed to image the morphology at high resolutions. The BEC allowed us to identify the CL on top of the other layers. The brighter areas (Figure 2.11 c) indicate the fragments of the CL on the edge of the GDE. Because the CL consists of heavier Ag atoms and Nafion (sulfonated fluoropolymer), it appears brighter than the MPL and CFS. These two layers are less dense because they are composed of mostly carbon and < 20 wt% PTFE (fluoropolymer).

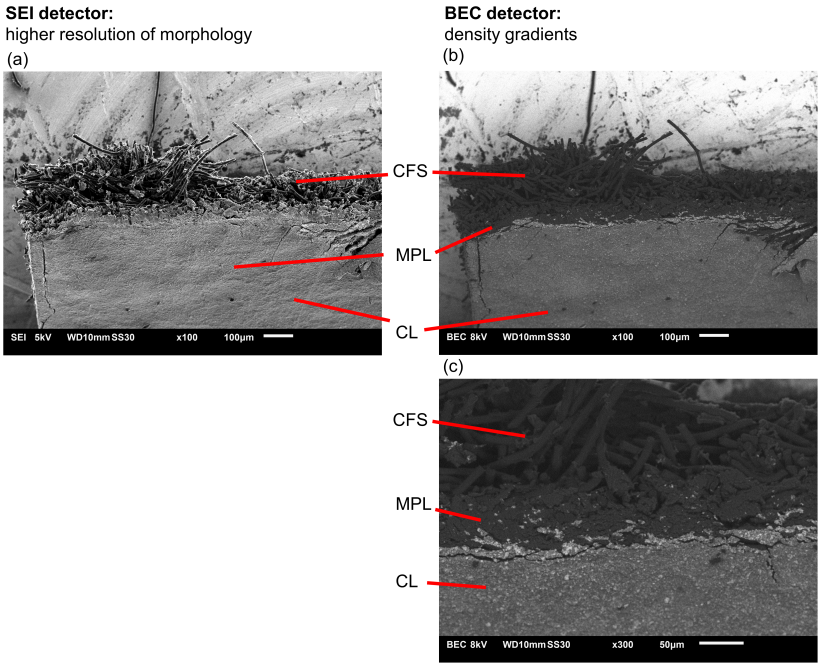

Figure 2.11: Exposed cross-section of GDE shows different layers: Carbon fiber substrate (CFS), microporous layer (MPL), catalyst layer (CL). **(a)** The secondary electron detector (SEI) shows the morphology at high resolution. **(b)** The backscattered electron detector (BEC) reveals density gradients, which allow the identifications of regions with differing elemental composition. **(c)** The density differences clearly distinguish the CL from the other layers.

Catalyst layer thickness

We determined the catalyst layer thickness by looking for a fragment of the CL lying on its side (Figure 2.12). The images recorded with SEI make it difficult to distinguish which particles belong to the CL (bottom row). The BEC detector let us locate a suitable fragment of the CL (top row). We measured the thickness of this fragment with ImageJ at 5 random locations. The average thickness is $3.5 \pm 0.2\,\mu m$.

Catalyst primary particle and agglomerate size

The BEC images of this CL fragment show that Ag particles are present in form of agglomerates and primary particles (bright spots in Figure 2.13). They are embedded in a Nafion matrix, which appear as a dark grey cloud in the BEC images. To estimate average Ag agglomerate size, we analyzed a sample set of 18 agglomerates from the BEC image with x12000 magnification (top left): The average diameter was $408 \pm 248\,nm$. The diameters were distributed over a wide range from 200 – 1200 nm. To estimate the average primary Ag particle size, we analyzed a sample set of 25 agglomerates from the BEC image with x20000 magnification (top middle): The average diameter was $79 \pm 17\,nm$. This estimate is a little bit higher than the nanoparticle size given by the supplier (20 – 40 nm).

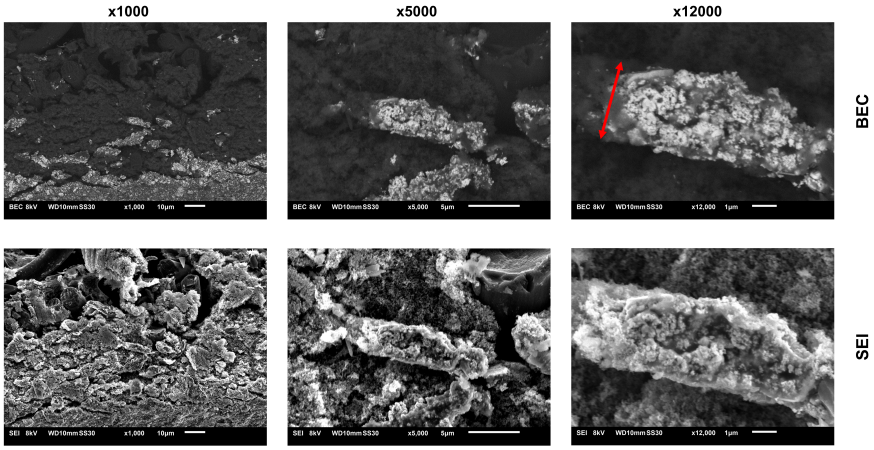

Figure 2.12: Estimation of catalyst layer (CL) thickness from the fragment lying on its side and facing the detector (top right). Average thickness at 5 random locations of this fragment: $3.5 \pm 0.2\,\mu m$.

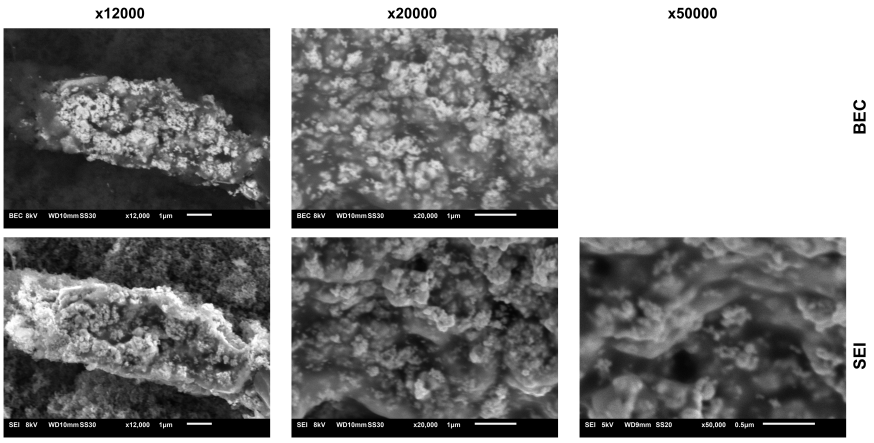

Figure 2.13: Estimation of primary Ag particles size ($79 \pm 17\,nm$) and Ag agglomerates size ($408 \pm 248\,nm$) embedded in Nafion.

2.5.4. STATIC CONTACT ANGLE AS METRIC FOR WETTABILITY

A table of the recorded contact angles can be found in the accompanying Excel file of the supporting information.

Wetting theory

The wettability or hydrophobicity of the pores in the GDL impacts the breakthrough pressure. For a simple cylindrical pore, the pressure equilibrium between the differential pressure, $\Delta p = p_L - p_G$, and the capillary pressure, p_C, is given by the Young-Laplace equation (2.2). The surface tension of the liquid is γ in $N\,m^{-1}$, the contact angle of the liquid with the pore wall is θ in °, and the pore radius is r in m. Hydrophilic pores ($0° < \theta < 90°$) draw in water and will have liquid breakthrough at any positive pressure. For water to break through hydrophobic pores ($90° < \theta < 180°$) work has to be done to overcome the surface energy. [63]

$$\Delta p = p_L - p_G = p_C = -2\gamma \cdot \cos\theta \cdot r^{-1} \tag{2.2}$$

The wettability is a measure of the ability of a liquid to adhere to a solid material , which is determined by the balance of surface tensions between the three phases (Figure 2.14). From an energy point of view, a system tries to minimize its energy and in this case that means minimizing the surface area between phases with unfavorable high surface tensions (γ in $J\,m^{-2}$). The surface tension can also be seen as a force per length (γ in $N\,m^{-1}$). That is, a force balance at the three phase interface explains the degree of wetting. The wettability of a material can be measured through the contact angle at this three phase interface. The contact angle, θ, is a result of the surface tension balance and is described by Young's law (2.3): [64]

$$\gamma_{lg}\cos\theta = \gamma_{sg} - \gamma_{sl}, \tag{2.3}$$

where γ_{sg} is the solid–gas surface tension, γ_{sl} is the solid–liquid surface tension, and γ_{lg} is the liquid–gas surface tension.

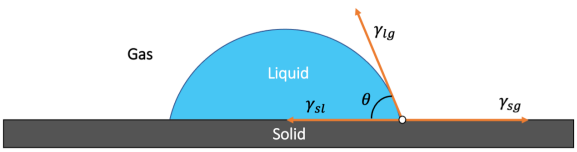

Figure 2.14: Static contact angle as a result of the force balance at the solid–liquid interface, following Young's law (2.3). Here, θ is the contact angle, γ_{sg} is the solid–gas surface tension, γ_{sl} is the solid–liquid surface tension, and γ_{lg} is the liquid–gas surface tension.

Again, GDL materials are slightly more complex due to their surface roughness and chemical heterogeneity. A GDL is often treated with a hydrophobic agent to increase hydrophobicity. Still, the material can contain a few hydrophilic pore voids. [65] The effect of this chemical heterogeneity on the wetting properties can be described with the empirical Cassie-Baxter model (2.4). The overall contact angle, θ^*, is determined by the fractions of surface area, f_1 and f_2, belonging to θ_1 and θ_2. The Cassie-Baxter model can also be applied to the effect of surface roughness, by assuming that air bubbles are entrapped inside the surface grooves. Thus, the liquid experiences a composite surface of the solid and the entrapped gas. This model allows for a rough surface to become more hydrophobic, even when the solid's intrinsic contact angle is lower than 90°. [64]

$$\cos\theta^* = f_1 \cdot \cos\theta_1 + f_2 \cdot \cos\theta_2 \tag{2.4}$$

The wetting of GDLs has been examined more extensively by other authors. [9,66,67] For example, Gurau *et al.* used the Washburn method to determine the internal contact angle. [20] Gostik *et al.* used the method of standard porosimetry the determine the volume of hydrophilic pores inside the GDL pore network. [65]

Static contact angle measurements
In our study, we measured the external, static contact angle according to the sessile drop technique to assess the wettability of our samples (Figure 2.15). We note that the rough surfaces also lead to the phenomenon of contact angle hysteresis, which would make a dynamic measurement with advancing and receding contact angle more appropriate. Further, this method does not measure internal surface properties, which should be most determining for the saturation characteristics of the GDEs. However, because the measurement of external, static contact angles provides a simple and convenient metric for the wettability, it has been used to study GDL characteristics in the past. [18,19]

The sample was placed on the sample support (Figure 2.15). We used a pipette to deposit a 10 µL water droplet on a random location of the surface. Then we recorded an image with the digital camera using the ThorCam software. This process was repeated five times per sample. The images were analyzed with ImageJ and the Contact angle plugin. The contact angle was determined by marking the outline of the interface and determining the elliptical contact angle with the manual point procedure function (Figure 2.16). An average angle elliptical angle, θ_E, was calculated from the angles $\theta_{E,L}$ and $\theta_{E,R}$. These angles arise at intersections of the left and right tangent lines to the ellipse with the solid interface line. The contact angle is then calculated as $\theta = 180° - \theta_E$.

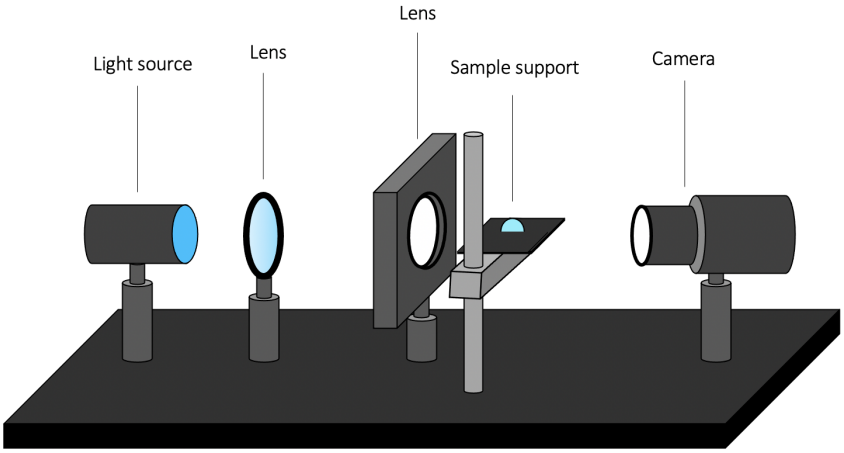

Figure 2.15: Static contact angle setup used to estimate the wettability of the GDE layers. The setup consist of a light source, two lenses, a sample support and a camera controlled by Thorcam.

Analyzed samples
We measured contact angles of the CFS and the MPL for each commercial GDL substrate. After applying the CL with the airbrush coater, we also analyzed the contact angles of the CL. To measure the static contact angle of the GDE samples after being used in CO_2 electrolysis, the samples were rinsed with water directly after the electrolysis experiment and left to dry in air for at least 2 days.

Post-electrolysis results
The run times for each sample are specified in the "FE" sheet of the Excel file. We observed a reduction in CL contact angle for all samples. This might be explained by the hydration of Nafion due to electrolyte contact. [63] Alternatively, residual carbonate salts could be responsible for the change in contact angle.

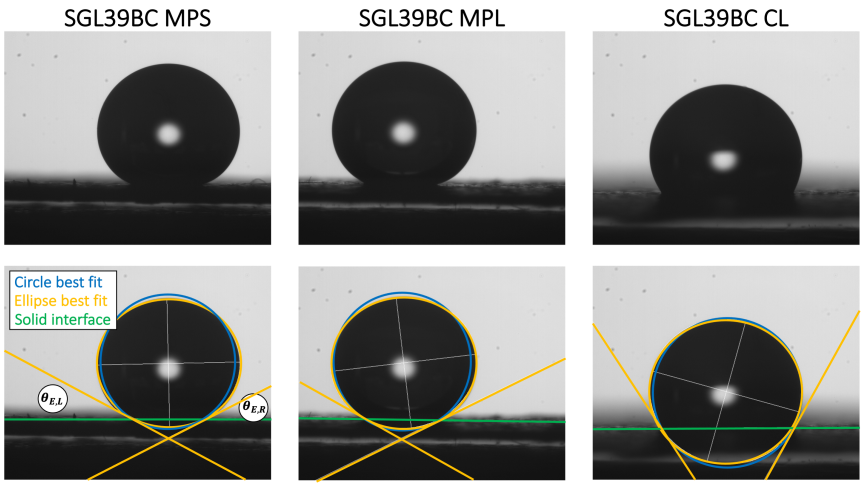

Figure 2.16: Static contact angle data processing example with SGL 39BC. The top images are the unprocessed images. The bottom images were processed using the contact angle function of ImageJ. The angles $\theta_{E,L}$ and $\theta_{E,R}$ arise at the intersection between the solid interface line and tangent of the ellipse.

The change in contact angle for the CFS due to electrolysis is not significant for all GDL samples except for H23C6. For H23C6, we carried out the experiment at $-100\,mA\,cm^{-2}$. After a run time of 30 min, θ_{CFS} changed by $-25 \pm 9°$. A similar current-dependent degradation rate was also reported by Leonard *et al.*.[44]

2.5.5. MEASUREMENT OF FLOODING RESISTANCE

The uncoated GDLs were characterized for their liquid breakthrough pressure in a 2-compartment cell prior to the electrolysis experiments. The flow-by pressure window, Δp^*, of the coated GDE samples was determined right before the electrolysis experiments were carried out in the 3-compartment cell.

H_2O breakthrough pressure for uncoated GDLs (CFS + MPL)

The measurement configuration to determine the liquid breakthrough pressure, Δp_L^*, with de-ionized water is shown in Figure 2.17 a. We installed the uncoated GDL sample (CFS + MPL) in the characterization cell (Figure 2.18 and Figure 2.19). The MPL was facing the liquid compartment of the cell leaving a cross-sectional area of 3.8 cm exposed. The sample was placed on a polypropylene mesh for mechanical support Figure 2.17 c. We set the liquid flow rate of the peristaltic pump to 1 mL$\,$min^{-1} to slowly fill and pressurize the liquid compartment for 15 min. The water was forced through the GDL because the outlet of the liquid compartment was closed. The breakthrough pressure, Δp^*, was determined by observing at which pressure the first droplet appeared at the GDL surface Figure 2.17 b. We used a mass flow controller (MFC) to supply 30 mLn min^{-1} of CO_2 gas through the gas inlet to remove permeated water from the gas compartment. The gas and the liquid left the cell together through the gas outlet. The pressure gradient across the sample was recorded with a Deltabar S differential pressure meter (Endress+Hauser, Switzerland). We performed these measurement with one sample per GDL model. For the SGL 39BC, we carried out one repeat experiment to estimate the random error.

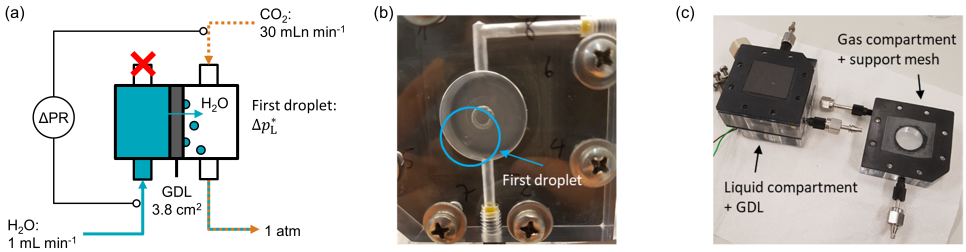

Figure 2.17: Experimental overview for liquid breakthrough measurements for uncoated GDL samples. **(a)**: Measurement configuration for H_2O breakthrough pressure Δp_L^*. **(b)**: Visual determination of liquid breakthrough pressure: The differential pressure was recorded when the first liquid droplet became visible on the GDL surface in the gas compartment. **(c)**: Disassembled characterization cell with GDL sample on top of liquid compartment and support mesh on gas compartment.

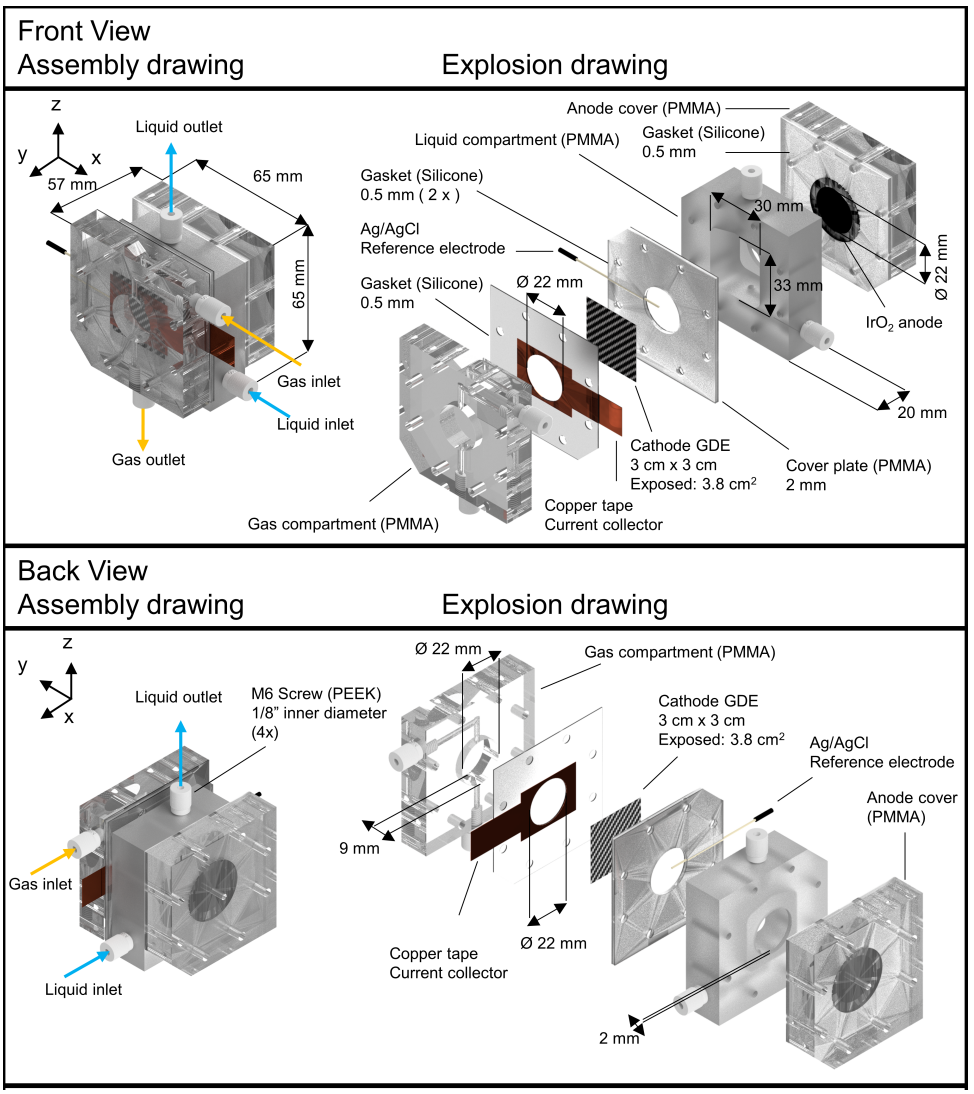

Figure 2.18: Characterization flow cell with two compartments: Assembly drawing. This cell was used to determine the liquid breakthrough pressure, Δp_L^*, the limiting overall O_2 mass transfer coefficient, k_{O_2}, and the CO_2 permeability constant, P_{CO_2}. PMMA stands for polymethyl methacrylat. PEEK stands for polyether ether ketone.

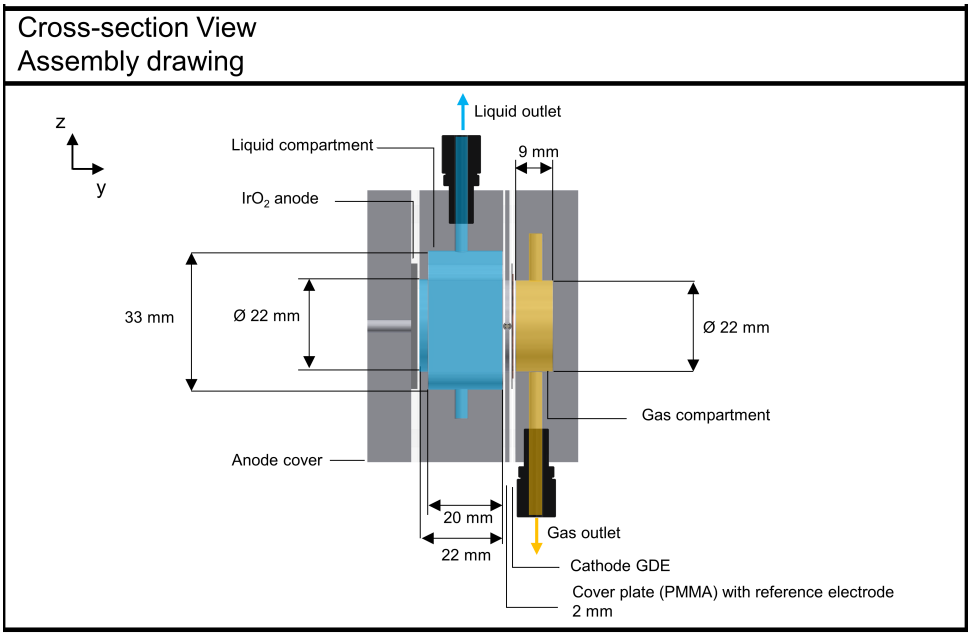

Figure 2.19: Characterization flow cell with two compartments: Cross-section view. This cell was used to determine the liquid breakthrough pressure, Δp_L^*, the limiting overall O_2 mass transfer coefficient, k_{O_2}, and the CO_2 permeability constant, P_{CO_2}.

Our recorded H_2O breakthrough pressures for the uncoated GDL (CFS + MPL) samples are listed in Table 2.4. We analyzed a second sample of SGL 39BC to get an estimate for the variability of the results. The two resulting values of 57 mbar and 67 mbar give an average breakthrough pressure of 62 mbar with a sample standard deviation of ±7 mbar. Because it was not feasible to carry out a large number of repeats for every GDL model, we estimate the random error based on similar studies we found in literature. A thorough study on liquid breakthrough pressure through polymer electrolyte fuel cell (PEFC) GDLs determined an error of about ±10 mbar for Toray papers. [19] We use this value as an estimate for all GDL models that have their breakthrough pressure in a similar order of magnitude (Toray paper, SGL paper, ELAT paper). For the Freudenberg H23C6, we use an estimate of ±100 mbar based on the study by Leonard *et al.* [44] We did not record the gas breakthrough pressure, Δp^*_G, for the uncoated samples, but we assume that this value is 0 mbar for all GDL types.

Table 2.4: Experimentally determined H_2O breakthrough pressure, Δp^*_L, and estimated standard error, $\sigma_{\Delta p^*_L}$, in mbar.

Experiment	TGP-H-060	TGP-H-090	TGP-H-120	SGL 22BB	SGL 39BC	LT1400W	H23C6
Sample 1	65	77	64	44	57	52	464
Sample 2	n.a.	n.a.	n.a.	n.a.	67	n.a.	n.a.
Mean Δp^*_L	65	77	64	44	62	52	464
$\sigma_{\Delta p^*_L}$	±10	±10	±10	±10	±10	±10	±100

Flow-by pressure window of the coated GDE

We measured the flow-by pressure window, Δp^*, of the GDE right before the CO_2 electrolysis experiments. For this purpose, the GDE was installed in the 3-compartment cell (Figure 2.22 – 2.24) and integrated into the electrolysis setup (Figure 2.25). The electrolyte reservoir was filled with 1 M $KHCO_3$ saturated with CO_2 and the liquid lines were primed. The pump was set to a liquid flow rate of 100 mL min^{-1} for each electrolyte channel. In its initial state, the reactor exhibited the breakthrough of feed gas because of the backpressure provided by the check valve at the outlet (345 mbar). The liquid back pressure was then slowly increased in increments of 10 mbar until a transition to the next flow regime occurred. The corresponding differential pressure Δp was noted. We recorded the transition between the following regimes:

- Gas breakthrough (Flow-through)
- No breakthrough (Flow-by)
- Liquid breakthrough

After these measurements, the liquid pressure was again reduced until gas breakthrough occurred. We used separate samples of the Freudenberg H23C6 for each of the experiments (Flow-by pressure window, −100 mA cm^{-2}). For all other GDLs, the same sample was used for all these experiments.

2.5.6. CO_2 PERMEABILITY FOR UNCOATED GDL (CFS + MPL)

The CO_2 permeability was characterized with the 2-compartment flow cell (Figure 2.18 and Figure 2.19) using the configuration shown in Figure 2.20. The gas was forced through the GDL from the CFS side by closing the gas and liquid outlet. We varied the gas flow rate from 0.1 to 1.4 L min^{-1} (20 °C) in steps of 0.1 L min^{-1}. Each flow rate step was held for 90 s to allow the system to reach a steady state. For the sample Freudenberg H23C6, the flow rate interval was 10 to 100 mL min^{-1} (20 °C) in steps of 10 mL min^{-1}. The pressure drop of the empty cell and the tubing was recorded and subtracted from the pressure drops recorded for each sample.

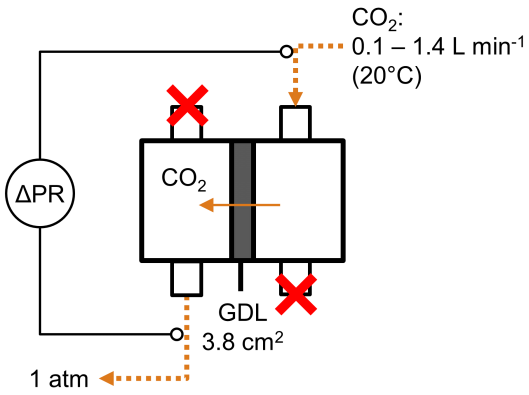

Figure 2.20: Configuration of 2-compartment characterization flow cell used to measure the CO_2 permeability.

We determined the permeability constant, P_{CO_2}, in mL min^{-1} bar^{-1} by plotting the volumetric flow rate, F, through the cross-sectional area, A, against the pressure drop across the sample, Δp, according to Darcy's law (2.5).[38] The sample thickness, δ, the dynamic viscosity, μ, the permeability, P' in m^2, and A are incorporated into the empirical permeability constant, P_{CO_2}.

$$F = \frac{P'}{\delta_{\text{CFS+MPL}}} \cdot \frac{A}{\mu} \cdot \Delta p = P_{CO_2} \cdot \Delta p \tag{2.5}$$

The resulting permeability curves are displayed in Figure 2.21. The permeability constant, P_{CO_2}, was determined from the slope of the curve and is listed in Table 2.5. The samples TGP-H-060, TGP-H-090, TGP-H-120, and SGL 22BB show a very similar pressure drop behavior, which is close to the 1 mbar resolution limit our equipment. Therefore, we can not distinguish the permeability constants of these samples and only give an estimate. In comparison to these samples, SGL 39BC and ELAT LT1400W have a lower permeability. We estimate a relative error of ±15% based on the resolution (1 mbar) relative to the measured range (6 mbar). In contrast, the slope of the Freudenberg H23C6 is much lower and the data is a lot less noisy. We estimated a relative error of ±5%.

Table 2.5: Experimentally determined CO2 permeability constants, P_{CO_2}, in mL min^{-1} bar^{-1}.

Material	TGP-H-060	TGP-H-090	TGP-H-120	SGL 22BB	SGL 39BC	LT1400W	H23C6
P_{CO_2}	> 300	> 300	> 300	> 300	206	226	4

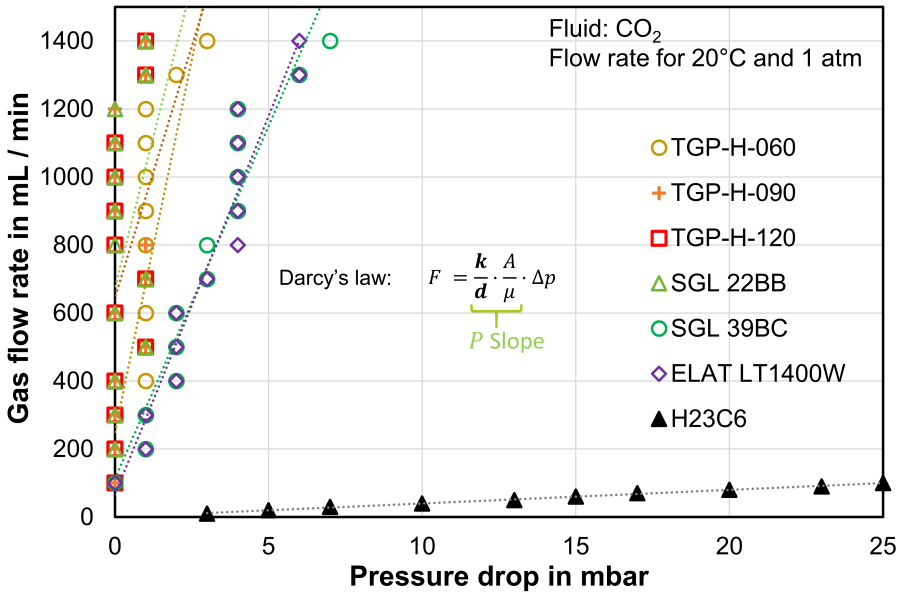

Figure 2.21: CO_2 permeability plots for uncoated GDL samples. The permeability constant, P_{CO_2}, is derived from the slope.

2.5.7. CO_2 ELECTROLYSIS EXPERIMENTS

The CO_2 mass transfer of the GDE materials was characterized with a 3-compartment electrolysis cell, which was integrated into an automated experimental setup.

ASSEMBLY OF THE 3-COMPARTMENT CO_2 ELECTROLYSIS CELL

The front view of the 3-compartment electrolysis cell is shown in Figure 2.22. The transparent body of the cell was machined out of poly methyl methacrylate (PMMA) by our workshop. This allowed the observation of the flow regime at the GDE during operation. The cell was connected to tubing with fittings made of poly ether ether ketone (PEEK), which were supplied by the IDEX corporation (Illinois, USA). The PMMA parts were sealed against each other with 0.5 mm silicone gasket (Eriks, Netherlands). The cation exchange membrane (Selemion CMV) was sandwiched between two gaskets. The differential pressure between the gas compartment and the catholyte compartment was measured directly inside the cell. For this purpose, the differential pressure meter was attached to the 1/16" outer diameter tubes, which were directly connected to the inside of the cell (Figure 2.22).

The back view of the 3-compartment electrolysis cell is shown in Figure 2.23. The GDE was connected to the potentiostat with a copper tape (Conrad, Netherlands), which served as current collector. We integrated an Ag/AgCl micro-reference electrode (Type: Leak free reference electrode; Supplier: Multi Channel Systems, Germany) into the center of the PMMA sheet that was next to the cathode GDE. The gap between cathode and tip of the reference electrode was 0.5 mm. The anode plate electrode was made of a titanium disk coated with an IrO_2 oxygen evolution catalyst (Magneto Special Anodes, Netherlands). We connected it to the potentiostat with a wire running to the back side of the disk through a hole in the anode cover.

Figure 2.24 shows the cross-section of the electrolysis flow cell. We choose an upward flow direction for the electrolytes to facilitate the removal of gas bubbles. The gas flows downward to remove any liquid from the gas compartment.

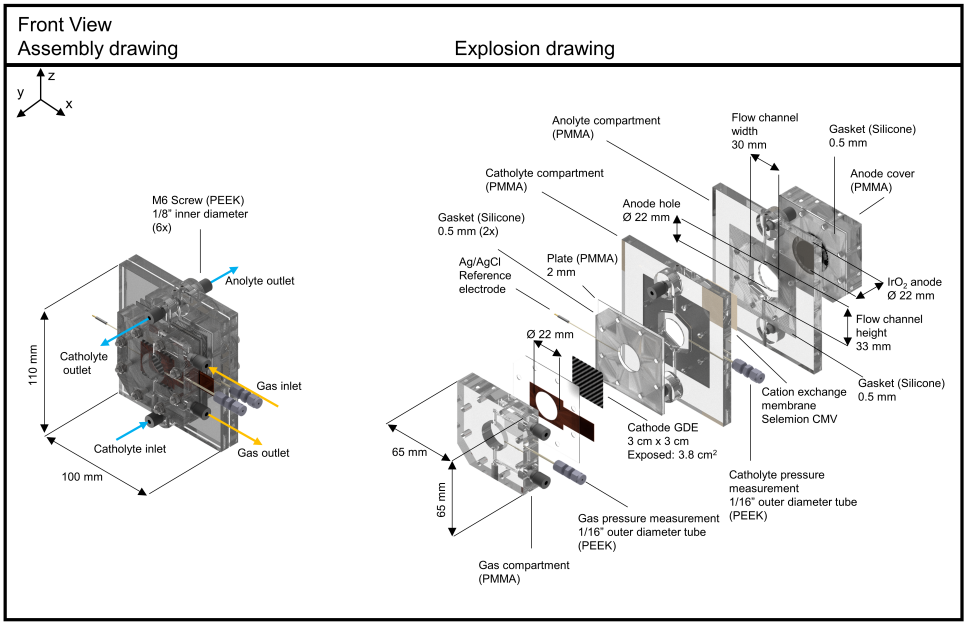

Figure 2.22: Front view of the 3-compartment electrolysis cell used to determine the flow-by pressure window pressure, Δp_L^*, at open circuit potential and the faradaic efficiency for CO, FE_{CO}, as a function of current density. PMMA stands for polymethyl methacrylat. PEEK stands for polyether ether ketone.

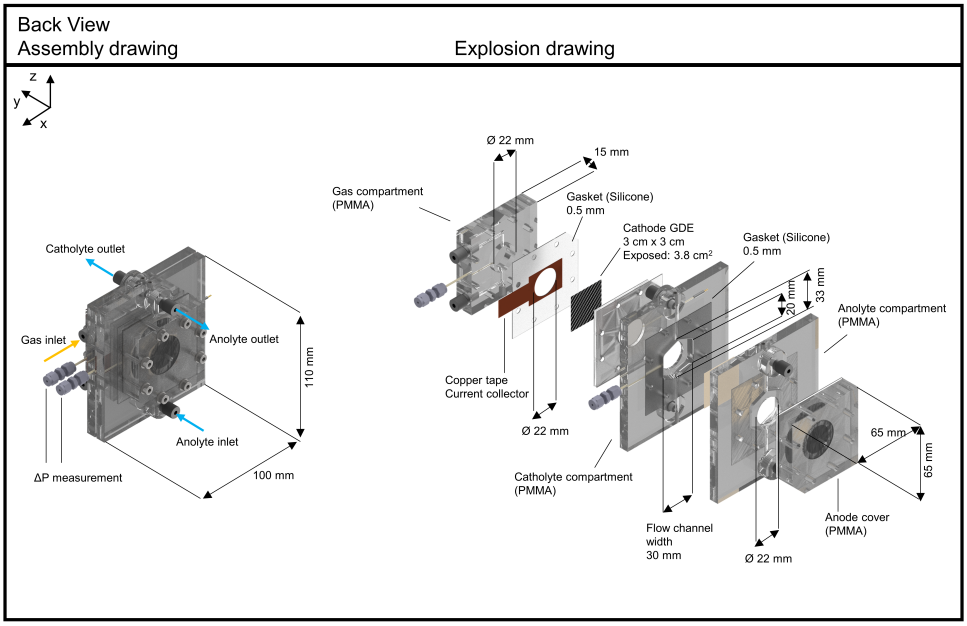

Figure 2.23: Back view of the 3-compartment electrolysis cell used to determine the flow-by pressure window pressure, Δp_L^*, at open circuit potential and the faradaic efficiency for CO, FE_{CO}, as a function of current density. PMMA stands for polymethyl methacrylat. PEEK stands for polyether ether ketone.

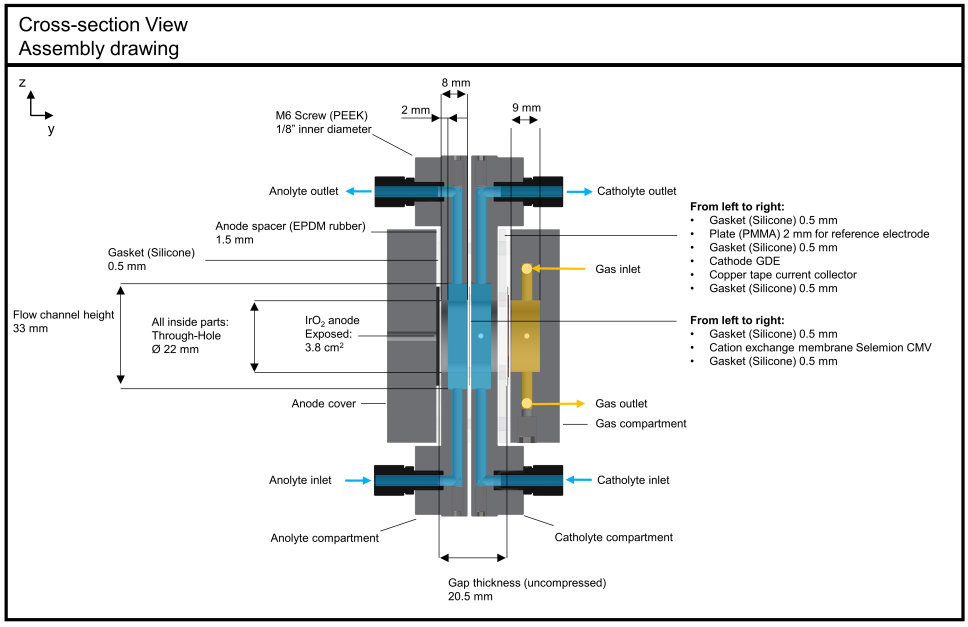

Figure 2.24: Cross-section of the 3-compartment electrolysis cell used to determine the flow-by pressure window pressure, Δp_L^*, at open circuit potential and the faradaic efficiency for CO, FE_{CO}, as a function of current density.

OPERATION OF THE CO_2 ELECTROLYSIS SETUP

The CO_2 reduction experiments were carried out with the electrolysis setup shown in Figure 2.25 and Figure 2.26. We used Labview (Version 2018, National Instruments) to record online data of the various sensors and to control the pump and the valves.

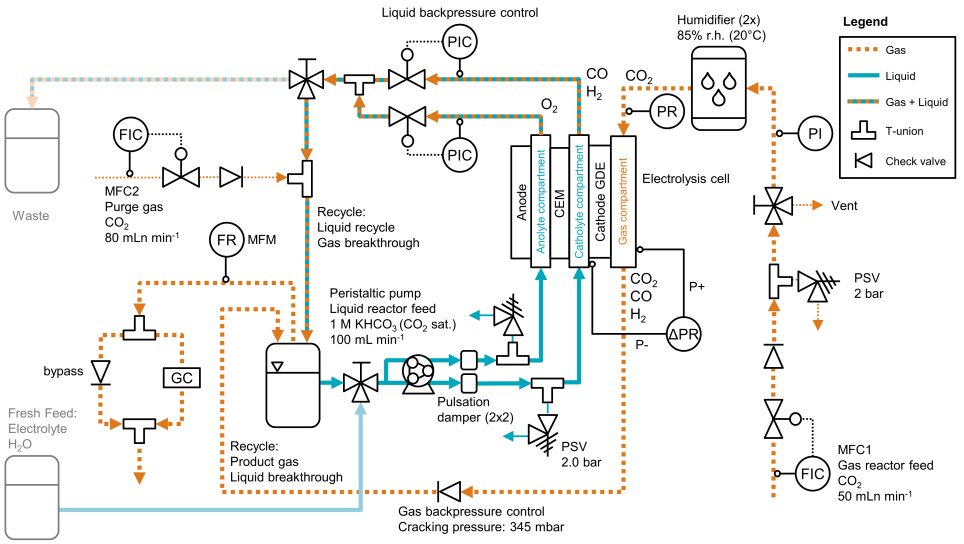

Figure 2.25: Extended process flow diagram for CO_2 electrolysis setup with different pressure control. The gas flow rates were controlled with mass flow controllers (MFC). Check valves were used to prevent the backflow of liquid into the MFCs. Pressure safety valves (PSV) were installed in line to prevent the unexpected buildup of pressure. The gas feed pressure was measured with an analog pressure indicator (PI) and recorded after the humidifiers (PR). The differential pressure between the gas and the catholyte compartment were recorded with a differential pressure meter (ΔPR). The anolyte and catholyte compartment were separated with a cation exchange membrane (CEM). The backpressure of both electrolyte streams was controlled (PIC) before both streams were combined and recirculated. The product gases were collected from all process streams and combined in the head space of the electrolyte reservoir. Their flow rate was recorded (FR) with a mass flow meter (MFM) and the composition analyzed with a gas chromatography system (GC) to calculate the Faradaic efficiency.

Gas feed flow path

The CO_2 feed gas was supplied from a CO_2 cylinder. The gas flow rate was controlled and measured with a mass flow controllers (MFC1) of the type F-201CV-500 from Bronkhorst (Netherlands). We passed the gas through two custom-made bubble columns (Figure 2.27 and Figure 2.28) in series to humidify the feed with water. The temperature and relative humidity of the gas feed was recorded after the humidification stage with a humidity sensor (Type: HC2A-S Hygroclip RV+T sensor; Supplier: Acin Instrumenten, Netherlands). The pressure of the gas feed was recorded with a Deltabar S pressure meter (Endress+Hauser, Switzerland). We used another Deltabar S to record the pressure difference between the gas compartment (positive terminal: P+) and the liquid compartment (negative terminal: P-). The backpressure of the gas outlet was set by a SS-CHS2-5 check valve (Swagelok, Netherlands) with a nominal cracking pressure of 345 mbar.

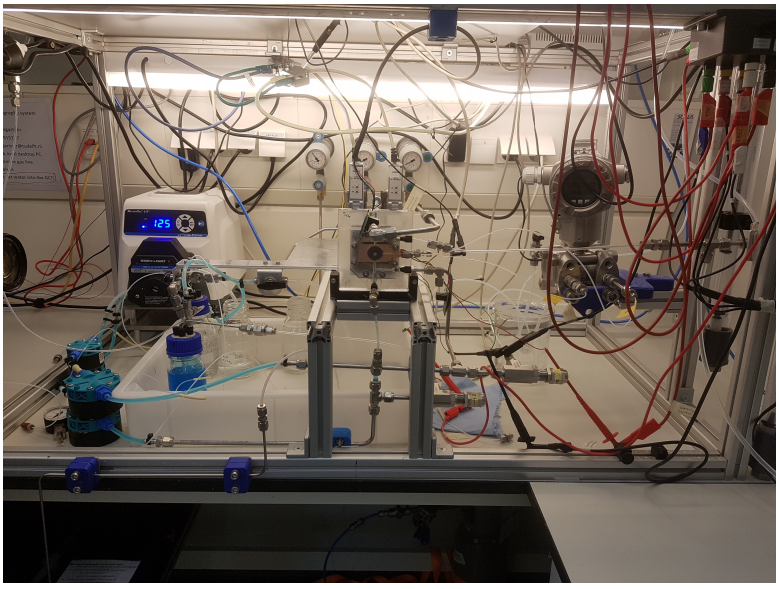

Figure 2.26: Picture of CO_2 electrolysis setup. The peristaltic pump is located on the left. The 3-compartment flow cell is in the center of the image.

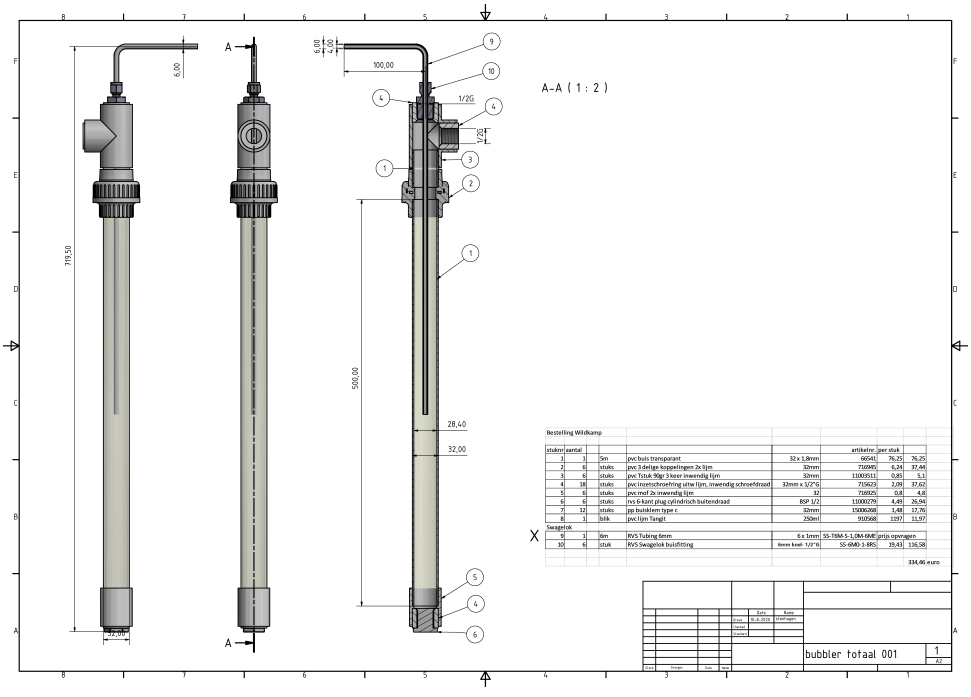

Figure 2.27: Technical drawing of the humidifier column. The units are in mm.

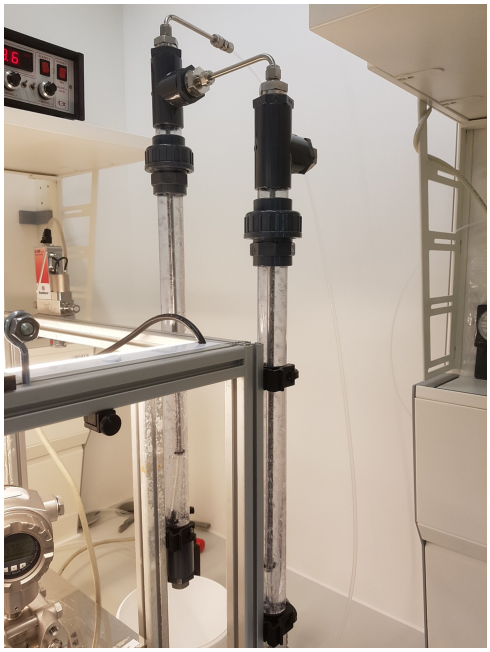

Figure 2.28: Two custom-made humidifier columns made from PVC pipes were used to humidify the CO_2 feed to 85% relative humidity (r.h.) at 20 °C.

Electrolyte flow path
The 1 M $KHCO_3$ electrolyte saturated with CO_2 was prepared by diluting concentrated KOH (50 wt%, analytical grade, Alfa Aesar) to 1 M KOH with de-ionized water. The CO_2 was bubbled through the solution to until the pH value was stable. The bulk pH of the electrolyte was measured prior to the experiments and is listed in the accompanying Excel file. The liquid lines and reactor was flushed before every experimental run. The electrolyte reservoir and liquid lines were filled with 100 mL fresh electrolyte. We used a peristaltic pump (Type: Masterflex L/S peristaltic pump; Supplier: Cole Parmer) to recirculate the electrolyte through the reactor and the liquid lines with a flow rate of 100 mL/min for the catholyte channel and for the anolyte channel each. Two pulsation dampers (Types: FPD 1.06, FPD 1.10; Supplier: KNF, Switzerland) reduced the pressure fluctuations caused by the pump.

We controlled the liquid back pressure of both channels with electronic control valves (Type: P-502C-6K0R; Supplier: Bronkhorst, Netherlands). After the experimental run, we collected a sample of the electrolyte to measure the formic acid content with HPLC. In addition to CO and H_2, formic acid has also been reported to form on Ag catalysts in small amounts.[68]

Product gas flow path
Unreacted CO_2 and product gases left the reactor through the gas outlet and entered the head space of the electrolyte reservoir. Product gases forming on the catholyte side (CO, H_2) and the anode side (O_2) were carried out of the reactor by the electrolyte stream. After the two electrolyte streams were recombined, we added a CO_2 purge gas stream to facilitate the transfer of product gases into the gas phase. The CO_2 purge gas stream further ensured that the electrolyte remained saturated with CO_2 during the experimental run. All the product gases were collected in the headspace of the electrolyte reservoir and passed through a mass flow meter (MFM) to record the flow rate (Type: F-111B-500; Supplier: Bronkhorst, Netherlands). The gas composition was analyzed with a gas chromatography system (Type: Compact GC 4.0; Supplier: Interscience, Netherlands).

Calculation of Faradaic efficiency

The Faradaic efficiency of gas species FE_i (H_2, CO) was calculated with the recorded current, I, Faraday's constant, F, the stoichiometric number of electrons exchanged, z_i, ($z_i = 2$ for H_2 and CO), the corrected MFM gas flux, $\dot{N}_{\mathrm{MFM}}$, and the gas concentration, C_i, using (2.6).

$$FE_i = \frac{z_i \cdot F \cdot C_i \cdot \dot{N}_{\mathrm{MFM}}}{I} \tag{2.6}$$

The simple gas conversion factors provided by the supplier of the MFM are listed in Table 2.6. We did not detect the components CH_4 or C_2H_4 in any of our product gas samples. Therefore, CO_2 is the only component that differs significantly from a conversion factor of 1 in our product mixture. This allows us to simplify the calculation of the mixture conversion factor K_{mix}.

Table 2.6: Single component gas conversion factors K_i for 20 °C and 1 atm provided by Bronkhorst General Manual Digital Instruments.

Component	K_i
H_2	1.01
N_2	1.00
O_2	0.98
CO_2	0.74
CO	1.00
CH_4	0.76
C_2H_4	0.6

We assume that the components N_2, H_2, O_2, are equivalent in their conversion factor to CO. We then developed a simple linear model using the Fluidat flow calculation tool (Bronkhorst, Netherlands). This tool allows to calculate K_{mix}, which converts the recorded gas flow, $\dot{N}_{\mathrm{MFM,nominal}}$, (MFM calibrated for 90 vol% CO_2, 5 vol% CO, 5 vol% H_2 at 10 bar (a) and 20 °C) to the corrected gas flow (actual product mixture at 0.1 bar (g) and 20 °C). The corrected MFM gas flux, $\dot{N}_{\mathrm{MFM}}$, is then calculated with (2.7). Our model assumes the product gas mixture is a two component mixture made up of CO_2 and CO (Figure 2.29).

$$\dot{N}_{\mathrm{MFM}} = \dot{N}_{\mathrm{MFM,nominal}} \cdot K_{\mathrm{mix}} \tag{2.7}$$

The mixture conversion factor, K_{mix}, is calculated with the regression formula (2.8) determined in Figure 2.29.

$$K_{\mathrm{mix}} = 1.291 - 0.2764 \cdot \frac{C_{CO_2}}{[\mathrm{vol\%}]} \tag{2.8}$$

We calculated the volumetric concentration of CO_2, C_{CO_2}, in vol% with (2.9).

$$C_{CO_2} = 100\ \mathrm{vol\%} - C_{CO} - C_{H_2} - C_{O_2} - C_{N_2} \tag{2.9}$$

The Faradaic efficiency values of the product gases CO and H_2 are listed in the accompanying Excel file in the sheet "FE" for all experiments.

We can estimate the Faradaic efficiency of formic acid, FE_{HCOOH}, with (2.10). We collected a sample of the electrolyte after electrolysis and analyzed it with HPLC to determine the concentration of formic acid, C_{HCOOH}, in $\mathrm{mol\,L^{-1}}$. The total passed charge, Q, was recorded by the potentiostat. The electrolyte volume $V_{\mathrm{electrolyte}}$ was about 60 mL for each experiment.

$$FE_{\mathrm{HCOOH}} = \frac{F \cdot C_{\mathrm{HCOOH}} \cdot V_{\mathrm{electrolyte}}}{Q} \tag{2.10}$$

The detailed values for all GDL samples are listed in the accompanying Excel file in the sheet "FE_Formic acid" for all experiments. We calculated a FE_{HCOOH} between 2% to 4% for our different materials samples. This roughly makes up the amount to complete the Faradaic efficiencies of H_2 and CO to 100%.

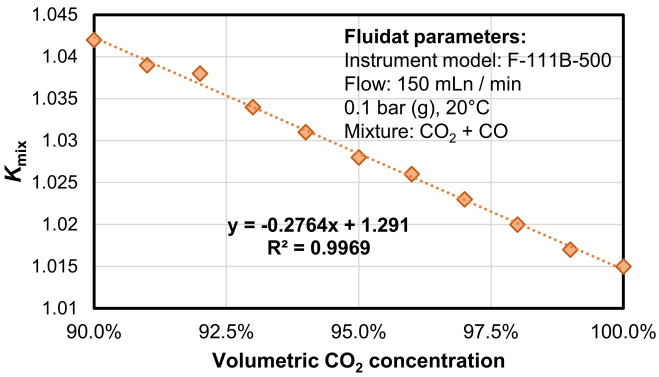

Figure 2.29: Determination of the mixture conversion factor, K_{mix}: The linear regression model to calculate K_{mix} is based on data points calculated with the Fluidat flow calculation tool (Bronkhorst, Netherlands). The model gas mixture consists of CO_2 and CO.

2.5.8. OVERALL O_2 MASS TRANSFER COEFFICIENT OF GDE

The overall O_2 mass transfer coefficient, k_{O_2}, was measured electrochemically with the configuration shown in Figure 2.30. At sufficiently high currents, the reduction at the cathode GDE becomes limited by the O_2 mass transfer through the GDE (Cathode reaction: $O_2 + 2H_2O + 4e^- \longrightarrow 4OH^-$). We placed the coated GDE samples (CFS + MPL + CL) in the characterization cell (Figure 2.18). The CL was facing the liquid compartment of the cell leaving a cross-sectional area of 3.8 cm^2 exposed. A titanium plate with a circular hole was used as a current collector. The plate was inserted between GDE and gas compartment. The Ag/AgCl micro-reference electrode was placed at a distance of 1 mm from the cathode surface. A Nickel plate with the same area as the cathode was used as counter electrode (Anode reaction: $4OH^- \longrightarrow O_2 + 2H_2O + 4e^-$).

Experimental procedure

During electrolysis measurements, the electrolyte (6 M KOH for high conductivity) was pumped through the liquid compartment at a flow rate of 20 mL min^{-1} and recirculated. Pressurized air from the house line was supplied at a flow rate of 40 mLn min^{-1} to the gas compartment. The backpressure of the gas outlet was set by a SS-CHS2-5 check valve (Swagelok, Netherlands) with a nominal cracking pressure of 345 mbar. The pressure controller of the liquid lines was used to balance the pressure between the gas and the liquid compartment until no gas or liquid breakthrough was observed. The gas pressure was recorded before starting the electrolysis process. We recorded a minimum of 3 linear sweep voltammetry (LSV) scans for each sample. The cathode potential was varied from 0 V to −2 V vs. SHE with a scan rate of 20 mV s^{-1}. We waited for 3 min between scans to give the system time to re-equilibrate. We carried out additional LSV scans with a N_2 gas feed to record the current of the competing hydrogen evolution reaction (Side reaction: $2H_2O + 2e^- \longrightarrow H_2 + 2OH^-$).

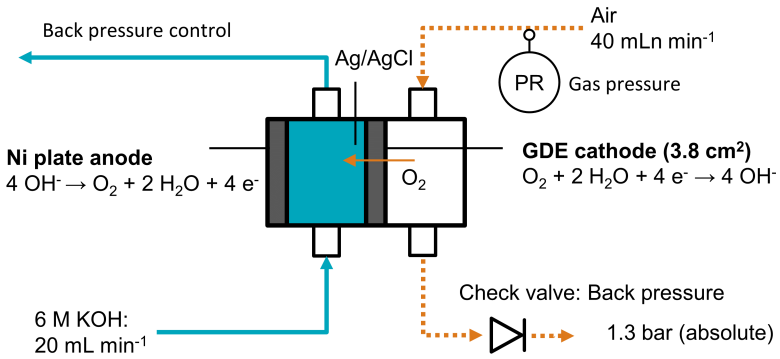

Figure 2.30: Configuration for limiting O_2 mass transfer measurement. The GDE cathode reduces O_2 at the catalyst surface to OH^- ions. The current is limited by the mass transfer rate of O_2 from the gas bulk through the GDL to the catalyst layer.

Calculation of overall O_2 mass transfer coefficient

To determine the overall O_2 mass transfer coefficient, k_{O_2}, for each GDE, the limiting current density, j_{lim} was extracted from the LSV scans according to Figure 2.31. The data processing parameters are listed in Table 2.7. We excluded the first two scans from our analysis because the recorded current curves drifted during the first scans. We also excluded scans with larger signal fluctuations caused by gas bubbles interfering with the measurement. The data processing is also described in the sheet "kO2" of the accompanying Excel file.

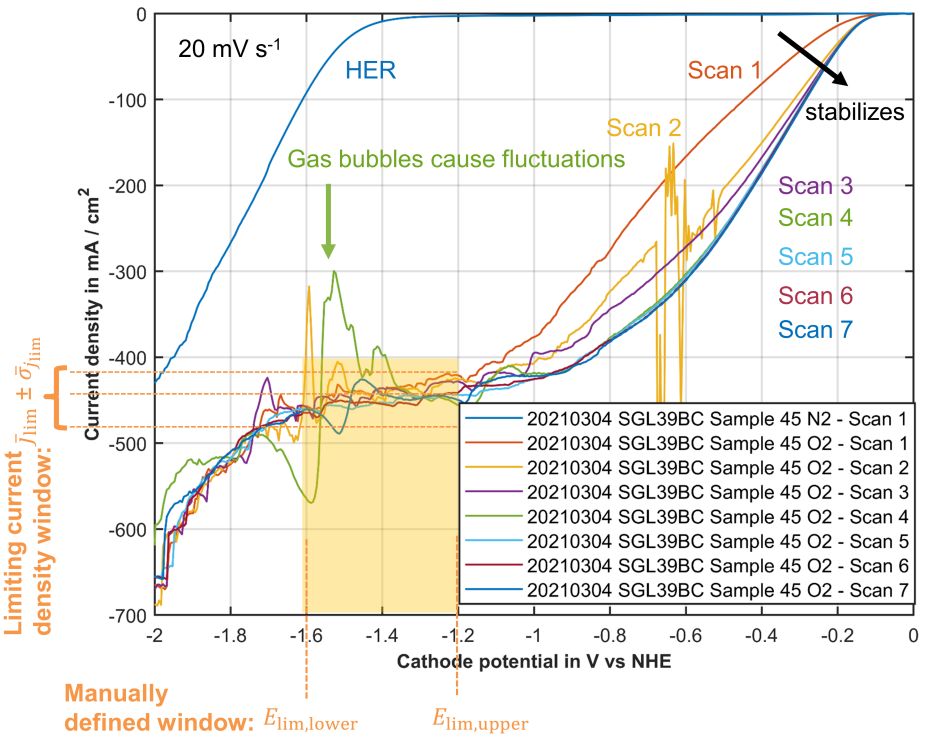

Figure 2.31: O_2 mass transfer coefficient raw data processing for SGL 39B determined by linear sweep voltammetry (LSV). The "O_2" scans 1-7 use an air feed at the cathode for the reduction of O_2 to OH^-. The scan with the N_2 gas feed shows the current of the hydrogen evolution reaction for comparison. The average limiting current density j_{lim} in $mA\,cm^{-2}$ and the sample standard deviation of the limiting current density $\sigma_{j_{lim}}$ was calculated for the limiting current plateau in the potential window between $E_{lim,lower}$ and $E_{lim,upper}$ in V vs. SHE. The first two scans and scans with large fluctuations were not included for calculation of the average limiting current densities.

We define the potential window of the limiting current plateau with the lower potential limit, $E_{lim,lower}$, and the upper potential limit, $E_{lim,upper}$, in V vs. SHE. The scan numbers (Scan #) included in current calculations are listed in Table 2.7. For each of these scans, we then determined the average limiting current, j_{lim}, in $mA\,cm^{-2}$ and its corresponding sample standard deviation, $\sigma_{j_{lim}}$, to consider the fluctuations in the current. Using j_{lim} and $\bar{\sigma}_{j_{lim}}$ of each scan, we then calculated the average limiting current density, $\bar{j}_{lim}$, and the standard error of the limiting current density, $\bar{\sigma}_{j_{lim}}$, for the GDE sample.

The limiting O_2 molar flux, $\dot{n}_{O_2,lim}$, in $mol\,cm^{-2}\,s^{-1}$ was calculated from $\bar{j}_{lim}$ with Faraday's law (2.11). Faraday's constant is $F = 96485\,C\,s^{-1}$ and the number of electrons exchanged in the reaction is $z = 4$.

$$\dot{n}_{O_2,\mathrm{lim}} = \frac{\bar{j}_{\mathrm{lim}}}{F \cdot z} \tag{2.11}$$

We assumed that the limiting O_2 flux, $\dot{n}_{O_2,\mathrm{lim}}$, is proportional to the overall O_2 mass transfer coefficient of the GDE, k_{O_2} in $\mathrm{cm\,s^{-1}}$, and the O_2 concentration gradient between the bulk of the gas compartment, $C_{O_2,\mathrm{bulk}}$, and the catalyst surface, $C_{O_2,\mathrm{Cat.}}$. We neglected concentration gradients in flow direction because the convective O_2 flux into the gas compartment was about 56% larger than the O_2 consumed in the reaction. By assuming that the O_2 concentration at the catalyst surface, $C_{O_2,\mathrm{Cat.}}$, dropped to 0 $\mathrm{mol\,cm^{-3}}$ when the current became limited, we calculated k_{O_2} with (2.12).

$$\dot{n}_{O_2,\mathrm{lim}} = k_{O_2} \cdot \Delta_{O_2} = k_{O_2} \cdot \left(C_{O_2,\mathrm{bulk}} - C_{O_2,\mathrm{Cat.}}\right) = k_{O_2} \cdot C_{O_2,\mathrm{bulk}} \tag{2.12}$$

We determined the bulk oxygen concentration, $C_{O_2,\mathrm{bulk}}$, with the ideal gas law (2.13). The ideal gas constant, R, has the value of 8.3145 $\mathrm{J\,mol^{-1}\,K^{-1}}$. We assumed the gas temperature, T, was equal to the ambient temperature of 20 °C. The partial pressure of oxygen, p_{O_2}, was calculated assuming a volumetric concentration of 21% of the recorded gas pressure, p_G, with (2.14).

$$C_{O_2,\mathrm{bulk}} = \frac{p_{O_2}}{RT} \tag{2.13}$$

$$p_{O_2} = p_G \cdot 21\% \tag{2.14}$$

Finally, the overall O_2 mass transfer coefficient of the GDE, k_{O_2} in $\mathrm{cm\,s^{-1}}$, can be calculated with (2.15) after substituting (2.14) and (2.13) into equation (2.12) and rearranging the factors. The random error of the mass transfer coefficient, $\sigma_{k_{O_2}}$, was also calculated using (2.15) by replacing the average $\bar{j}_{\mathrm{lim}}$ with the average sample standard deviation of the limiting current density, $\bar{\sigma}_{j_{\mathrm{lim}}}$.

$$k_{O_2} = \frac{C_{O_2,\mathrm{bulk}}}{\dot{n}_{O_2,\mathrm{lim}}} = \frac{21\% \cdot p_G \cdot F \cdot z}{R \cdot T \cdot \bar{j}_{\mathrm{lim}}} \tag{2.15}$$

The resulting overall mass transfer coefficients are displayed in Figure 2.32 and listed in Table 2.7.

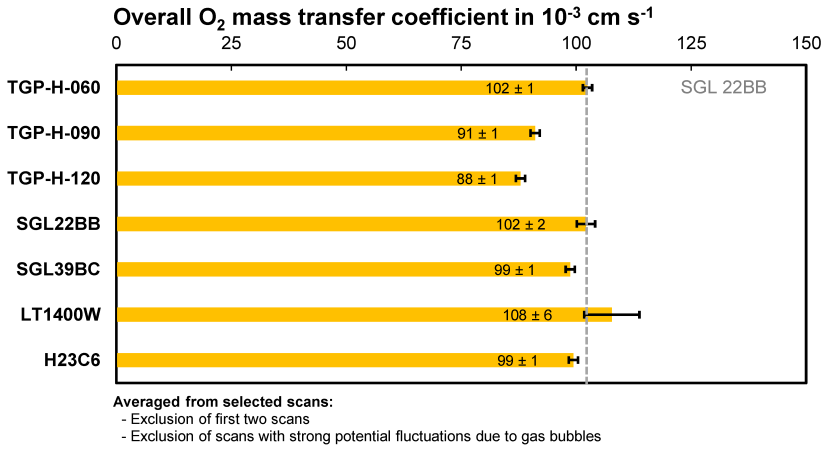

Figure 2.32: Resulting limiting overall O_2 mass transfer coefficients, k_{O_2}, determined with linear sweep voltammetry (LSV).

Table 2.7: Results and data processing overview for limiting overall O_2 mass transfer coefficients, k_{O_2}. The absolute pressure of the gas feed is p_G. The potential window of the limiting current density plateau is between the lower limit, $E_{lim,lower}$, and the upper limit, $E_{lim,upper}$. Scan numbers (#) used to determine average limiting current densities, $\bar{j}_{lim}$, and average sample standard deviations, $\bar{\sigma}_{j_{lim}}$. The limiting O_2 molar flux is $\dot{n}_{O_2,lim}$. The random error of the mass transfer coefficient is $\sigma_{k_{O_2}}$.

Material	Unit	TGP-H-060	TGP-H-090	TGP-H-120	SGL 22BB	SGL 39BC	LT1400W	H23C6
p_G	bar	1.290	1.533	1.242	1.344	1.370	1.280	1.264
$E_{lim,lower}$	V vs. SHE	-1.75	-1.80	-1.45	-1.80	-1.60	-1.50	-1.45
$E_{lim,upper}$	V vs. SHE	-1.30	-1.70	-1.15	-1.40	-1.20	-1.10	-1.20
Scan #	-	3, 4	3, 4, 5	3, 4, 5	3, 4	3, 5, 6, 7	3, 5	3, 4
$\bar{j}_{lim}$	$mA\,cm^{-2}$	-440	-464	-363	-456	-450	-459	-418
$\bar{\sigma}_{j_{lim}}$	$mA\,cm^{-2}$	±5	±8	±10	±13	±9	±33	±5
$\dot{n}_{O_2,lim}$	$10^{-6}\,mol\,cm^{-2}\,s^{-1}$	1.14	1.20	0.94	1.18	1.17	1.19	1.08
k_{O_2}	$cm\,s^{-1}$	0.102	0.091	0.088	0.102	0.099	0.108	0.099
$\sigma_{k_{O_2}}$	$cm\,s^{-1}$	±0.001	±0.001	±0.001	±0.002	±0.001	±0.006	±0.001

Decomposition of O_2 mass transfer coefficient for SGL 22BB

We can decompose the overall mass transfer coefficient of SGL 22BB by using characterization from the fuel cell research of Reshetenko *et al.*.[52,69] The overall mass transfer coefficient, k_i in $cm\,s^{-1}$, is a measure for the mass transfer rate from the bulk of the gas feed to the surface of the catalyst. It is the inverse of the overall resistance to mass transfer $R_{i,overall}$ (2.16).

$$\frac{1}{k_i} = R_{i,overall} \tag{2.16}$$

The overall resistance to mass transfer $R_{i,overall}$ can be broken down the into mass transfer resistances present in the different domains of the GDE (2.17).

$$R_{i,overall} = R_{i,CFS} + R_{i,MPL} + R_{i,CL} \tag{2.17}$$

The components of the resistance can also expressed as an inverse of their mass transfer coefficients (2.18).

$$\frac{1}{k_i} = \frac{1}{k_{i,m,CFS}} + \frac{1}{k_{i,K,MPL}} + \frac{1}{k_{i,K+film,CL}} \tag{2.18}$$

In the gas channel and the larger pores of the CFS, the transport takes place through molecular diffusion $(k_{i,m,CFS})$. In the small pores of the MPL, the transport can take place through molecular and Knudsen diffusion $(k_{i,K,MPL})$. Knudsen diffusion is a mechanism that dominates in small pores, in which the collisions of molecules with the pore walls are more frequent than the collisions of molecules with each other. In the CL, Knudsen diffusion takes place together with molecular diffusion through films of ionomer and electrolyte before reaching the catalyst surface $(k_{i,K+film,CL})$.[52]

Using (2.19) and (2.20), we can decompose the experimentally determined k_{O_2} of our SGL 22BB sample with an estimate for $k_{O_2,m,CFS}$ and $k_{O_2,K,MPL}$.

$$R_{O_2,overall} = R_{O_2,CFS} + R_{O_2,MPL} + R_{O_2,CL} \tag{2.19}$$

$$\frac{1}{k_{O_2}} = \frac{1}{k_{O_2,m,CFS}} + \frac{1}{k_{O_2,K,MPL}} + \frac{1}{k_{O_2,K+film,CL}} \tag{2.20}$$

Reshetenko *et al.* performed an experimental study of GDL materials for polymer electrolyte fuel cells that provides useful information for this analysis. They were able to break down the overall mass transfer coefficient, k_{O_2}, into mass transfer coefficients of the different GDE domains by using oxygen mixtures with different diluents.[52] Their study included the sample SGL 25BC, which is equivalent to the SGL 22BB of our study (Table 2.8).

Table 2.8: O_2 mass transfer coefficients recorded for SGL 25BC (equivalent to 22BB) taken from PEFC literature.[52] The measurements were carried out in N_2 media at a pressure of $p_0 = 1.5\,\text{bar}$ and a temperature of $T_0 = 60\,^\circ\text{C}$. The overall O_2 mass transfer coefficient through the all domains of the GDE, k_{O_2}, is broken down into the different domains k of the electrode (CFS, MPL, CL). The mass transfer resistances are given by the inverse of the individual mass transfer coefficients $R_k = 1/k_{O_2,k}$ from Table 2 of Reshetenko *et al.*.[52]

Domain k	CFS	MPL	CL	GDE
Transport	molecular	Knudsen	Knudsen + Film	overall
Symbol	$k_{O_2,\text{m,CFS}}$	$k_{O_2,\text{K,MPL}}$	$k_{O_2,\text{K+film,CL}}$	k_{O_2}
$k_{O_2,k}$	$2.82\,\text{cm}\,\text{s}^{-1}$	$6.36\,\text{cm}\,\text{s}^{-1}$	$1.65\,\text{cm}\,\text{s}^{-1}$	$0.89\,\text{cm}\,\text{s}^{-1}$
$R_{O_2,k} = 1/k_{O_2,k}$	$0.35\,\text{s}\,\text{cm}^{-1}$	$0.16\,\text{s}\,\text{cm}^{-1}$	$0.61\,\text{s}\,\text{cm}^{-1}$	$1.12\,\text{s}\,\text{cm}^{-1}$
$R_{O_2,k}/R_{O_2,\text{overall}}$	32%	14%	54%	100%

The data in Table 2.8 show us that the mass transfer resistance in the CFS of SGL 25BC is 32% of the overall mass transfer resistance, $R_{O_2,\text{overall}}$. We can adjust the mass transfer coefficients for the different conditions in the PEFC ($p_0 = 1.5\,\text{bar}$, $T_0 = 60\,^\circ\text{C}$) to our conditions ($p = 1.334\,\text{bar}$, $T = 20\,^\circ\text{C}$) with equation (2.21).[49] We replaced the binary diffusion coefficient $D_{i,k}$ of species i in (gas) medium k of this equation with the CFS mass transfer coefficient $k_{O_2,\text{m,CFS}}$. This gives us an estimate of the mass transfer coefficient through the CFS $k_{O_2,\text{K,MPL}}$ of our SGL 22BB sample Table 2.9.

$$D_{i,k}(T,p) = D_{i,k,0}\left(\frac{T}{T_0}\right)^{1.5}\left(\frac{p_0}{p}\right) \tag{2.21}$$

Because the Knudsen diffusion coefficient, $D_{O_2,\text{K}}$, is proportional to the square root of the temperature, $T^{0.5}$,[49] we can adjust its value for the different temperature with (2.22). The estimated Knudsen mass transfer coefficient for the MPL is given in Table 2.9.

$$k_{O_2,\text{K,MPL}}(T,p) = k_{O_2,\text{K,MPL},0}\left(\frac{T}{T_0}\right)^{1.5}\left(\frac{p_0}{p}\right) \tag{2.22}$$

Table 2.9: Adjustment of CFS mass transfer coefficient , $k_{O_2,\text{m,CFS}}$, and MPL mass transfer coefficient $k_{O_2,\text{K,MPL}}$ for temperature, T, and gas pressure ,p_G. These values for the SGL 22BB are based on the study of Reshetenko *et al.*.[52]

$k_{O_2,k}$	T	p_G	Value	Source / Comment
$k_{O_2,\text{m,CFS}}$	60 °C	1.5 bar	$2.82\,\text{cm}\,\text{s}^{-1}$	Table 2 of Reshetenko *et al.*.[52]
$k_{O_2,\text{m,CFS}}$	20 °C	1.334 bar	$2.60\,\text{cm}\,\text{s}^{-1}$	Previous line adjusted with (2.21)
$k_{O_2,\text{K,MPL}}$	60 °C		$6.36\,\text{cm}\,\text{s}^{-1}$	Table 2 of Reshetenko *et al.*.[52]
$k_{O_2,\text{K,MPL}}$	20 °C		$5.97\,\text{cm}\,\text{s}^{-1}$	Previous line adjusted with (2.22)

The contributions to the mass transfer resistance (Table 2.10) are then calculated with (2.19) and (2.20) . We neglected the contribution of gas diffusion in the MPL. The resistance of CL makes up 94% of the total resistance of the GDE. The large mass transfer resistance of the CL is probably caused by the flooding of this layer with electrolyte.

Table 2.10: Estimation of mass transfer resistance contributions of CFS, MPL, and CL for SGL 22BB at a pressure of p_G = 1.344 bar and a temperature of T = 20 °C. We assume that the listed transport mechanism is dominating the mass transfer in the corresponding domain k.

Domain k	CFS	MPL	CL	GDE
Transport	molecular	Knudsen	Knudsen + Film	overall
Symbol	$k_{O_2,m,CFS}$	$k_{O_2,K,MPL}$	$k_{O_2,K+film,CL}$	k_{O_2}
$k_{O_2,k}$	$2.60\,cm\,s^{-1}$	$5.97\,cm\,s^{-1}$	$0.108\,cm\,s^{-1}$	$0.102\,cm\,s^{-1}$
$R_{O_2,k} = 1/k_{O_2,k}$	$0.38\,s\,cm^{-1}$	$0.17\,s\,cm^{-1}$	$9.24\,s\,cm^{-1}$	$9.79\,s\,cm^{-1}$
$R_{O_2,k}/R_{O_2,overall}$	4%	2%	94%	100%

2.5.9. STABILITY TEST FOR CO_2 ELECTROLYSIS

We carried out a stability test for the electrochemical CO_2 reduction for 20 h. We used a GDE with a SGL 39BC substrate, which was loaded with a catalyst layer of 1.27 mg Ag cm^{-1} and 20 wt% Nafion. As this study was a preliminary experiment, the experimental setup varied slightly from the process flow diagram shown in Figure 2.25:

- We carried out the experiments in the 2-compartment cell (Figure 2.19)
- Due to the larger electrode distance of this cell, our potentiostat was only able to reach $-190\,mA\,cm^{-2}$
- Due to the membraneless configuration, the anode and cathode shared the same 1 M $KHCO_3$ electrolyte
- The electrolyte was supplied with a flow rate of $20\,mL\,min^{-1}$ instead of $100\,mL\,min^{-1}$
- The CO_2 feed flow rate was 30 mLn min^{-1} instead of 50 mLn min^{-1}
- The CO_2 purge was 50 mLn min^{-1} instead of 80 mLn min^{-1}
- A polypropylene mesh was placed on the gas side of the GDE for mechanical support
- The flow rate of the product gas mixture was determined with a bubble flow meter

More detailed data for each GC injection are provided in the "Stability" sheet of the Excel file. The results of the stability test are summarized in Figure 2.33.

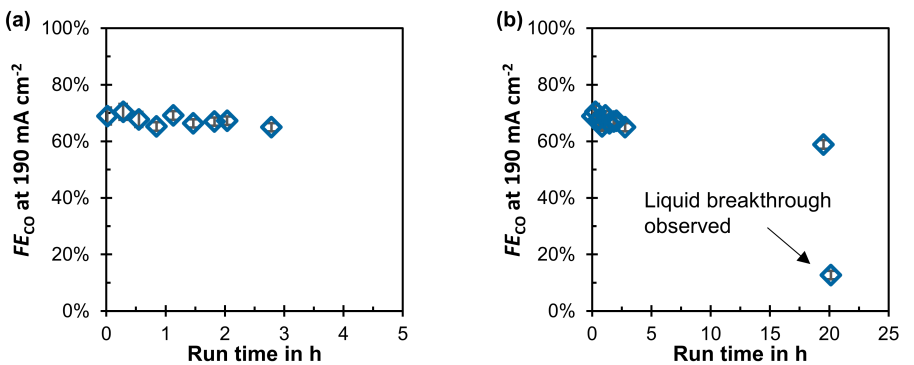

Figure 2.33: Results of stability test: Faradaic efficiency for CO at $-190\,mA\,cm^{-2}$ in flow-by mode. GDE material: SGL 39 BC coated with 1.27 mg $Ag cm^{-2}$ and 20 wt% Nafion. (a): First 3 h of the experiment. (b): Complete duration of experiment.

The Faradaic efficiency for CO, FE_{CO}, remained stable at 68% ± 1.5% over the first 2 h of the stability test (Figure 2.33 a). We note that this is lower than the corresponding value we measured during our mass transfer characterization experiments: We measured a FE_{CO} of 75% ± 2.1% at a current density of $-200\,mA\,cm^{-2}$ for SGL 39BC (Figure 2.7). This lower performance is probably due to differences in the experimental setup for the stability test. Based on the sufficient short-term stability over 2 h, we can assume that no significant loss of performance occurred during the short collection period (10 min) of the FE_{CO} data, which we used to compare the different GDL materials at $-200\,mA\,cm^{-2}$ (Figure 2.7).

The FE_{CO} declined slowly to a value of 59% ± 1.4% over a run time of 19.5 h (Figure 2.33 b). After 20 h, we suddenly observed GDE flooding and electrolyte breakthrough. This loss of stability could be explained by the following mechanisms (or a combination of both):

- Carbonate formation in the GDE: [44]
  - Electrolyte evaporates and increases the local salt concentration
  - Carbonate salts (K_2CO_3 or $KHCO_3$) precipitate in the pores of the GDE
  - The salt crystallites decrease the hydrophobicity of the pore surface
  - The capillary pressures of the pores are reduced and flooding occurs
- (Electro)-chemical degradation of the GDE: [55,70]
  - The very negative cathode potential (−1.9 V vs. SHE) and/or the high local pH in the CL degrade the carbon or even the PTFE of the GDL
  - The degraded carbon and/or PTFE has a lower hydrophobicity
  - The capillary pressures of the pores are reduced and flooding occurs

We observed the continuous formation of condensation on the outer wall of the gas compartment during the stability test (Figure 2.34 a). This observation makes the loss of hydrophobicity due to gradual carbonate formation in the GDE a plausible hypothesis. We suspect that the heat produced through the electrochemical reactions in the CL lead to an evaporation of water from the electrolyte. The water vapor must have then diffused through the GDE and oversaturated the already humidified gas stream in the gas compartment. The condensation occurred at the outer wall because this is the coldest point in the gas compartment.

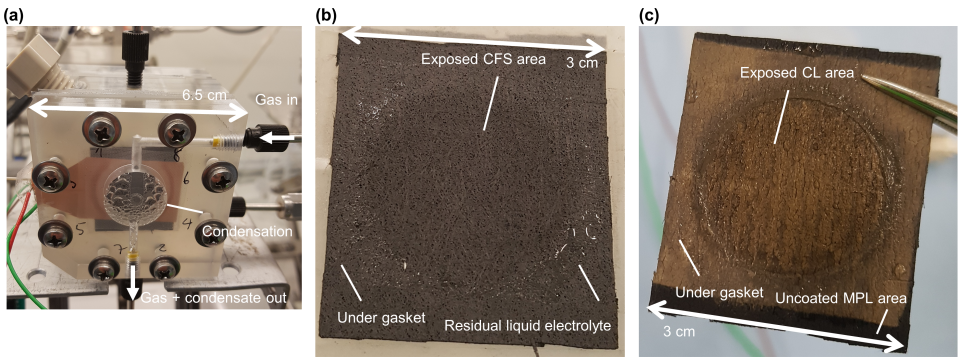

Figure 2.34: Pictures of stability test: **(a)**: Condensation during stability test **(b)**: Picture of CFS after 20 h stability test **(c)**: Picture of CL after 20 h stability test.

To test the hypothesis of carbonate salt formation, we disassembled the cell and inspected the CFS side (Figure 2.34 b) and the CL side of the GDE (Figure 2.34 c). The CFS appeared relatively dry and there were no salt deposits visible on the surface. Carbonate salt formation, however, could still be a possible degradation mechanism because the precipitation might have occurred inside the pores and not be visible from the outside.

To test the hypothesis of (electro-)chemical degradation, we measured the change in the static contact angle. We rinsed the spent sample with isopropyl alcohol to remove any residual electrolyte and let it dry in air. Our results show that the contact angle of the CFS decreased significantly due to the 20 h stability test at $-190\,mA\,cm^{-2}$ (Table 2.11). We can, therefore, assume that the (electro-)chemical degradation significantly limits the stability of carbon-based GDEs. The effects of this degradation mechanism on the surface chemistry should be investigated more systematically in a future study. It might be possible to mitigate this degradation mechanism by reducing the cathode overpotential through improved catalyst materials and lower mass transfer resistance in the CL.

Table 2.11: Contact angle change after stability test with SGL 39BC. CO_2 electrolysis was conducted for 20 h at $-190\,mA\,cm^{-2}$. Only one measurement was possible for the MPL of the spent sample because the uncoated area was limited in size.

Domain	Fresh sample	Spent sample
CFS	$149 \pm 1.0°$	$128 \pm 1.2°$
MPL	$153 \pm 0.8°$	133° (only one data point)
CL	$123 \pm 1.4°$	$109 \pm 5.4°$

2.6. ACKNOWLEDGEMENTS

We thank Christiaan Schinkel, Stefan ten Hagen, and Duco Bosma for their engineering support. This project has received funding from the European Research Council (ERC) under the European Union's Horizon 2020 research and innovation programme (grant agreement No 852115).

REFERENCES

[1] *Going climate-neutral by 2050,* (2019), Publications Office of the European Union.

[2] D. W. Keith, G. Holmes, D. S. Angelo, and K. Heidel, *A process for capturing CO_2 from the atmosphere,* Joule **2**, 1573 (2018).

[3] R. Sharifian, R. M. Wagterveld, I. A. Digdaya, C. Xiang, and D. A. Vermaas, *Electrochemical carbon dioxide capture to close the carbon cycle,* Energy & Environmental Science **14**, 781 (2021).

[4] M. G. Kibria, J. P. Edwards, C. M. Gabardo, C.-T. Dinh, A. Seifitokaldani, D. Sinton, and E. H. Sargent, *Electrochemical CO_2 reduction into chemical feedstocks: From mechanistic electrocatalysis models to system design,* Advanced Materials **31**, 1807166 (2019).

[5] P. De Luna, C. Hahn, D. Higgins, S. A. Jaffer, T. F. Jaramillo, and E. H. Sargent, *What would it take for renewably powered electrosynthesis to displace petrochemical processes?* Science **364**, eaav3506 (2019).

[6] B. Endrődi, E. Kecsenovity, A. Samu, T. Halmágyi, S. Rojas-Carbonell, L. Wang, Y. Yan, and C. Janáky, *High carbonate ion conductance of a robust PiperION membrane allows industrial current density and conversion in a zero-gap carbon dioxide electrolyzer cell,* Energy & Environmental Science , 4098 (2020).

[7] P. Jeanty, C. Scherer, E. Magori, K. Wiesner-Fleischer, O. Hinrichsen, and M. Fleischer, *Upscaling and continuous operation of electrochemical CO_2 to CO conversion in aqueous solutions on silver gas diffusion electrodes,* Journal of CO_2 Utilization **24**, 454 (2018).

[8] S. Park, J.-W. Lee, and B. N. Popov, *A review of gas diffusion layer in PEM fuel cells: Materials and designs,* International Journal of Hydrogen Energy **37**, 5850 (2012).

[9] D. L. Wood, C. Rulison, and R. L. Borup, *Surface properties of PEMFC gas diffusion layers,* Journal of The Electrochemical Society **157**, B195 (2010).

[10] D. Wood, J. Davey, P. Atanassov, and R. Borup, *PEMFC component characterization and its relationship to mass-transport overpotentials during long-term testing,* ECS Transactions **3**, 753 (2006).

[11] B. Kim, F. Hillman, M. Ariyoshi, S. Fujikawa, and P. J. Kenis, *Effects of composition of the micro porous layer and the substrate on performance in the electrochemical reduction of CO_2 to CO,* Journal of Power Sources **312**, 192 (2016).

[12] H.-R. M. Jhong, S. Ma, and P. J. Kenis, *Electrochemical conversion of CO_2 to useful chemicals: current status, remaining challenges, and future opportunities,* Current Opinion in Chemical Engineering **2**, 191 (2013).

[13] C. Simon, D. Kartouzian, D. Müller, F. Wilhelm, and H. A. Gasteiger, *Impact of microporous layer pore properties on liquid water transport in PEM fuel cells: Carbon black type and perforation,* Journal of The Electrochemical Society **164**, F1697 (2017).

[14] P. A. García-Salaberri, G. Hwang, M. Vera, A. Z. Weber, and J. T. Gostick, *Effective diffusivity in partially-saturated carbon-fiber gas diffusion layers: Effect of through-plane saturation distribution,* International Journal of Heat and Mass Transfer **86**, 319 (2015).

[15] A. Z. Weber, *Improved modeling and understanding of diffusion-media wettability on polymer-electrolyte-fuel-cell performance,* Journal of Power Sources **195**, 5292 (2010).

[16] A. El-kharouf, T. J. Mason, D. J. L. Brett, and B. G. Pollet, *Ex-situ characterisation of gas diffusion layers for proton exchange membrane fuel cells,* Journal of Power Sources **218**, 393 (2012).

[17] N. Parikh, J. Allen, and R. Yassar, *Microstructure of gas diffusion layers for PEM fuel cells,* Fuel Cells **12**, 382 (2012).

[18] M. Mortazavi and K. Tajiri, *Impact of gas diffusion layer properties on liquid water breakthrough pressure in polymer electrolyte fuel cell,* in *ASME 2013 11th International Conference on Fuel Cell Science, Engineering and Technology collocated with the ASME 2013 Heat Transfer Summer Conference and the ASME 2013 7th International Conference on Energy Sustainability* (American Society of Mechanical Engineers Digital Collection, 2013).

[19] M. Mortazavi and K. Tajiri, *Liquid water breakthrough pressure through gas diffusion layer of proton exchange membrane fuel cell,* International Journal of Hydrogen Energy **39**, 9409 (2014).

[20] V. Gurau, M. J. Bluemle, E. S. De Castro, Y.-M. Tsou, J. A. Mann, and T. A. Zawodzinski, *Characterization of transport properties in gas diffusion layers for proton exchange membrane fuel cells: 1. wettability (internal contact angle to water and surface energy of gdl fibers),* Journal of Power Sources **160**, 1156 (2006).

[21] J. M. Morgan and R. Datta, *Understanding the gas diffusion layer in proton exchange membrane fuel cells. I. how its structural characteristics affect diffusion and performance,* Journal of Power Sources **251**, 269 (2014).

[22] F. P. G. De Arquer, C.-T. Dinh, A. Ozden, J. Wicks, C. McCallum, A. R. Kirmani, D.-H. Nam, C. Gabardo, A. Seifitokaldani, and X. Wang, *CO_2 electrolysis to multicarbon products at activities greater than 1 A cm^{-1},* Science **367**, 661 (2020).

[23] Y. Chen, A. Vise, W. E. Klein, F. C. Cetinbas, D. J. Myers, W. A. Smith, T. G. Deutsch, and K. C. Neyerlin, *A robust, scalable platform for the electrochemical conversion of CO_2 to formate: Identifying pathways to higher energy efficiencies,* ACS Energy Letters **5**, 1825 (2020).

[24] B. De Mot, J. Hereijgers, N. Daems, and T. Breugelmans, *Insight in the behavior of bipolar membrane equipped carbon dioxide electrolyzers at low electrolyte flowrates,* Chemical Engineering Journal , 131170 (2021).

[25] B. De Mot, J. Hereijgers, M. Duarte, and T. Breugelmans, *Influence of flow and pressure distribution inside a gas diffusion electrode on the performance of a flow-by CO_2 electrolyzer,* Chemical Engineering Journal **378**, 122224 (2019).

[26] M. Duarte, B. De Mot, J. Hereijgers, and T. Breugelmans, *Electrochemical reduction of CO_2: Effect of convective CO_2 supply in gas diffusion electrodes,* ChemElectroChem **6**, 5596 (2019).

[27] G. Faita and F. Federico, *Electrolysis cell with gas diffusion electrode,* (2010), US Patent 7,670,472 B2.

[28] X.-L. WANG and S. KODA, *Scale-up and modeling of oxygen diffusion electrodes for chlorine-alkali electrolysis I. analysis of hydrostatic force balance and its effect on electrode performance,* Denki Kagaku Oyobi Kogyo Butsuri Kagaku **65**, 1002 (1997).

[29] B. De Mot, M. Ramdin, J. Hereijgers, T. J. Vlugt, and T. Breugelmans, *Direct water injection in catholyte-free zero-gap carbon dioxide electrolyzers,* ChemElectroChem **7**, 3839 (2020).

[30] B. Endrődi, E. Kecsenovity, A. Samu, F. Darvas, R. V. Jones, V. Török, A. Danyi, and C. Janáky, *Multilayer electrolyzer stack converts carbon dioxide to gas products at high pressure with high efficiency,* ACS Energy Letters **4**, 1770 (2019).

[31] D. A. Salvatore, D. M. Weekes, J. He, K. E. Dettelbach, Y. C. Li, T. E. Mallouk, and C. P. Berlinguette, *Electrolysis of gaseous CO_2 to CO in a flow cell with a bipolar membrane,* ACS Energy Letters **3**, 149 (2017).

[32] A. Reyes, R. P. Jansonius, B. A. W. Mowbray, Y. Cao, D. G. Wheeler, J. Chau, D. J. Dvorak, and C. P. Berlinguette, *Managing hydration at the cathode enables efficient CO_2 electrolysis at commercially relevant current densities,* ACS Energy Letters **5**, 1612 (2020).

[33] B. Endrődi, A. Samu, E. Kecsenovity, T. Halmágyi, D. Sebők, and C. Janáky, *Operando cathode activation with alkali metal cations for high current density operation of water-fed zero-gap carbon dioxide electrolysers,* Nature Energy **6**, 439 (2021).

[34] S. Ma, R. Luo, J. I. Gold, Z. Y. Aaron, B. Kim, and P. J. Kenis, *Carbon nanotube containing Ag catalyst layers for efficient and selective reduction of carbon dioxide,* Journal of Materials Chemistry A **4**, 8573 (2016).

[35] U. O. Nwabara, A. D. Hernandez, D. A. Henckel, X. Chen, E. R. Cofell, M. P. de Heer, S. Verma, A. A. Gewirth, and P. J. A. Kenis, *Binder-focused approaches to improve the stability of cathodes for CO_2 electroreduction,* ACS Applied Energy Materials (2021), 10.1021/acsaem.1c00715.

[36] R. W. Atkinson, Y. Garsany, B. D. Gould, K. E. Swider-Lyons, and I. V. Zenyuk, *The role of compressive stress on gas diffusion media morphology and fuel cell performance,* ACS Applied Energy Materials **1**, 191 (2018).

[37] A. Forner-Cuenca, E. E. Penn, A. M. Oliveira, and F. R. Brushett, *Exploring the role of electrode microstructure on the performance of non-aqueous redox flow batteries,* Journal of The Electrochemical Society **166**, A2230 (2019).

[38] Z. Zeng and R. Grigg, *A criterion for non-darcy flow in porous media,* Transport in Porous Media **63**, 57 (2006).

[39] J. Benziger, J. Nehlsen, D. Blackwell, T. Brennan, and J. Itescu, *Water flow in the gas diffusion layer of PEM fuel cells,* Journal of Membrane Science **261**, 98 (2005).

[40] S. Goswami, S. Klaus, and J. Benziger, *Wetting and absorption of water drops on nafion films,* Langmuir **24**, 8627 (2008).

[41] D. Quéré, *Rough ideas on wetting,* Physica A: Statistical Mechanics and its Applications **313**, 32 (2002).

[42] A. Forner-Cuenca, J. Biesdorf, A. Lamibrac, V. Manzi-Orezzoli, F. Büchi, L. Gubler, T. J. Schmidt, and P. Boillat, *Advanced water management in PEFCs: diffusion layers with patterned wettability II. measurement of capillary pressure characteristic with neutron and synchrotron imaging,* Journal of The Electrochemical Society **163**, F1038 (2016).

[43] J. T. Gostick, M. A. Ioannidis, M. W. Fowler, and M. D. Pritzker, *Wettability and capillary behavior of fibrous gas diffusion media for polymer electrolyte membrane fuel cells,* Journal of Power Sources **194**, 433 (2009).

[44] M. E. Leonard, L. E. Clarke, A. Forner-Cuenca, S. M. Brown, and F. R. Brushett, *Investigating electrode flooding in a flowing electrolyte, gas-fed carbon dioxide electrolyzer,* ChemSusChem **13**, 400 (2019).

[45] J. T. Gostick, M. A. Ioannidis, M. W. Fowler, and M. D. Pritzker, *Pore network modeling of fibrous gas diffusion layers for polymer electrolyte membrane fuel cells,* Journal of Power Sources **173**, 277 (2007).

[46] A. Lamibrac, J. Roth, M. Toulec, F. Marone, M. Stampanoni, and F. Büchi, *Characterization of liquid water saturation in gas diffusion layers by X-ray tomographic microscopy,* Journal of The Electrochemical Society **163**, F202 (2016).

[47] E. F. Medici, I. V. Zenyuk, D. Y. Parkinson, A. Z. Weber, and J. S. Allen, *Understanding water transport in polymer electrolyte fuel cells using coupled continuum and pore-network models,* Fuel Cells **16**, 725 (2016).

[48] I. Moussallem, J. Jörissen, U. Kunz, S. Pinnow, and T. Turek, *Chlor-alkali electrolysis with oxygen depolarized cathodes: history, present status and future prospects,* Journal of Applied Electrochemistry **38**, 1177 (2008).

[49] C.-Y. Wang, *Fundamental models for fuel cell engineering,* Chemical Reviews **104**, 4727 (2004).

[50] R. Krishna and J. A. Wesselingh, *The Maxwell-Stefan approach to mass transfer,* Chemical Engineering Science **52**, 861 (1997).

[51] N. Epstein, *On tortuosity and the tortuosity factor in flow and diffusion through porous media,* Chemical engineering science **44**, 777 (1989).

[52] T. Reshetenko and B. L. Ben, *Impact of a gas diffusion layer's structural and textural properties on oxygen mass transport resistance in the cathode and performance of proton exchange membrane fuel cells,* Electrochimica Acta **371**, 137752 (2021).

[53] R. E. Davis, G. L. Horvath, and C. W. Tobias, *The solubility and diffusion coefficient of oxygen in potassium hydroxide solutions,* Electrochimica Acta **12**, 287 (1967).

[54] N. Gupta, M. Gattrell, and B. MacDougall, *Calculation for the cathode surface concentrations in the electrochemical reduction of CO_2 in $KHCO_3$ solutions,* Journal of applied electrochemistry **36**, 161 (2006).

[55] K. Yang, R. Kas, W. A. Smith, and T. Burdyny, *Role of the carbon-based gas diffusion layer on flooding in a gas diffusion electrode cell for electrochemical CO_2 reduction,* ACS Energy Letters **6**, 33 (2021).

[56] V. Parry, G. Berthomé, and J.-C. Joud, *Wetting properties of gas diffusion layers: Application of the Cassie–Baxter and Wenzel equations,* Applied Surface Science **258**, 5619 (2012).

[57] O. Nibel, S. M. Taylor, A. Pătru, E. Fabbri, L. Gubler, and T. J. Schmidt, *Performance of different carbon electrode materials: Insights into stability and degradation under real vanadium redox flow battery operating conditions,* Journal of The Electrochemical Society **164**, A1608 (2017).

[58] Z. R. Yue, W. Jiang, L. Wang, S. D. Gardner, and C. U. Pittman, *Surface characterization of electrochemically oxidized carbon fibers,* Carbon **37**, 1785 (1999).

[59] M. Ji, C. Wang, Y. Bai, M. Yu, and Y. Wang, *Structural evolution of polyacrylonitrile precursor fibers during preoxidation and carbonization,* Polymer Bulletin **59**, 527 (2007).

[60] B. A. Newcomb, *Processing, structure, and properties of carbon fibers,* Composites Part A: Applied Science and Manufacturing **91**, 262 (2016).

[61] M. Lehner, R. Tichler, H. Steinmüller, and M. Koppe, *Power-to-gas: technology and business models* (Springer, 2014).

[62] B. Endrődi, G. Bencsik, F. Darvas, R. Jones, K. Rajeshwar, and C. Janáky, *Continuous-flow electroreduction of carbon dioxide,* Progress in Energy and Combustion Science **62**, 133 (2017).

[63] A. Z. Weber, R. M. Darling, and J. Newman, *Modeling two-phase behavior in PEFCs,* Journal of the Electrochemical Society **151**, A1715 (2004).

[64] P.-G. De Gennes, F. Brochard-Wyart, and D. Quéré, *Capillarity and wetting phenomena: drops, bubbles, pearls, waves* (Springer Science & Business Media, 2013).

[65] J. T. Gostick, M. W. Fowler, M. A. Ioannidis, M. D. Pritzker, Y. M. Volfkovich, and A. Sakars, *Capillary pressure and hydrophilic porosity in gas diffusion layers for polymer electrolyte fuel cells,* Journal of power sources **156**, 375 (2006).

[66] B. R. Friess and M. Hoorfar, *Measurement of internal wettability of gas diffusion porous media of proton exchange membrane fuel cells,* Journal of Power Sources **195**, 4736 (2010).

[67] S. Abbou, K. Tajiri, E. Medici, and J. S. Allen, *Characterization of water transport in PEMFC electrode using the washburn method,* ECS Transactions **80**, 87 (2017).

[68] Y. I. Hori, *Electrochemical CO_2 reduction on metal electrodes,* in *Modern aspects of electrochemistry* (Springer, 2008) pp. 89–189.

[69] T. V. Reshetenko and J. St-Pierre, *Separation method for oxygen mass transport coefficient in gas and ionomer phases in PEMFC GDE,* Journal of The Electrochemical Society **161**, F1089 (2014).

[70] G. Shapoval, A. Tomilov, A. Pud, and V. Vonsyatskii, *Electrochemical reductive destruction of polytetrafluoroethylene,* Theoretical and Experimental Chemistry **20**, 234 (1984).

3

When flooding is not Catastrophic – Woven Gas Diffusion Electrodes enable stable CO_2 Electrolysis

Electrochemical CO_2 reduction has the potential of using excess renewable electricity to produce hydrocarbon chemicals and fuels. Gas diffusion electrodes (GDE) allow to overcome limitations of CO_2 mass transfer, but are sensitive to flooding from (hydrostatic) pressure differences, which inhibits upscaling. We investigate the effect of the flooding behavior on the CO_2 reduction performance. Our study includes six commercial GDL materials with different microstructures (carbon cloth, carbon paper) and thicknesses, coated with Ag catalyst, and exposed to differential pressures corresponding to different flow regimes (gas breakthrough, flow-by, liquid breakthrough). We show that physical electrowetting further limits the flow-by regime at commercially relevant current densities (≥ -200 mA cm^{-2}), which reduced the Faradaic efficiency for CO (FE_{CO}) for most carbon papers. However, the carbon cloth GDE maintains its high CO_2 reduction performance despite being flooded with electrolyte due to its bimodal pore structure. Exposed to pressure differences equivalent to 100 cm height, the carbon cloth is able to sustain an average FE_{CO} of 69% at -200 mA cm^{-2}) even when liquid continuously breaks through. CO_2 electrolyzers with carbon cloth GDEs are therefore promising for scale-up because they enable high CO_2 reduction efficiency while tolerating a broad range of flow regimes.

This chapter has been published as "When Flooding is not Catastrophic – Woven Gas Diffusion Electrodes enable stable CO_2 electrolysis" by Lorenz M. Baumgartner, Christel I. Koopman, Antoni Forner-Cuenca, David A. Vermaas. *ACS Applied Energy Materials*, 2022, **5**, 15125-15135.

3.1. INTRODUCTION

Electrochemical CO_2 reduction (CO_2R) might be a key technology in our efforts to defossilize the chemical industry and transport sector with renewable electricity generated by wind or solar power.[1,2] This process could convert CO_2, which has been captured from point sources or directly from the atmosphere,[3–5] to useful chemical intermediates. Depending on the catalyst, common target intermediates include CO (Ag),[6,7] C_2H_4 (Cu),[8,9] or HCOOH (Sn).[10,11] Recently, the production of methanol and/or ethanol has been demonstrated with Cu_2O/ZnO catalysts[12,13] or metal–organic frameworks.[14–16] The conversion products could then be further upgraded to produce liquid hydrocarbon fuels or plastics aiming for a CO_2-neutral process.

Currently, a key challenge for the wide-scale adoption of CO_2R is designing an electrolyzer that can operate at high Faradaic efficiency, high current density, and low cell voltage. The reactor also has to be scalable and operate stably for ten thousands of hours. Liquid-fed electrolyzers suffer from CO_2 mass transfer limitations that lead to an increase in the undesired hydrogen evolution reaction (HER) at high current densities. To overcome this restriction, the field has introduced gas diffusion electrodes (GDEs), which allow the supply of CO_2 directly from the gas phase to the electrocatalytic interfaces. This development step has allowed high Faradaic efficiency at industrially relevant current densities ($\geq -200\,mA\,cm^{-2}$).[17,18]

GDEs have been successfully integrated into two major types of gas-fed CO_2 electrolyzers. In electrolyzers with membrane electrode assembly (MEA), the cathode GDE is in direct contact with a membrane. The GDE exchanges ions with the anode and a flowing electrolyte, which are on the other side of the membrane.[19–21] In electrolyzers with flowing catholyte, the GDE is in direct contact with an electrolyte. This electrolyte layer adds additional ohmic losses, but allows a better control of the ionic environment at the reaction interface.[8,10,22–24]

In a typical GDE, gaseous reagents transfer from the gas channel through the carbon fiber substrate (CFS) and the microporous layer (MPL) before reaching the catalyst layer (CL).[25,26] The CFS can have different microstructures (carbon paper, carbon cloth, nonwoven) and is typically impregnated with PTFE to provide wet-proofing. The MPL consists of carbon particles and PTFE. This layer plays an important role in controlling the intrusion of liquid into the GDL[27] and improves the electrical contact with the CL. The CL consists of catalyst particles in an ionomer matrix and requires ionic contact with the adjacent membrane or electrolyte.[18,28]

Many studies have found that the flooding of the GDE with electrolyte is a major challenge to maintaining high selectivity for CO_2R, especially at high current densities and larger electrolyzer scale. When flooding occurs, the electrolyte infiltrates the pore network, which reduces the effective diffusivity of the GDE and ultimately results in the flooding of the porous structure.[29,30] This phenomenon has been reported for both MEA-based and catholyte-based reactor configurations.

When focusing on CO_2 electrolyzers with flowing catholyte, the GDE can flood if the differential pressure between the liquid and the gas phase, $\Delta p = p_L - p_G$, exceeds the interfacial forces of the pore network. Therefore, the flooding behavior depends on the differential pressure,[31] but also on the wetting properties and microstructure.[32] The flooding behavior is made even more complex by electrowetting. This physical phenomenon reduces the hydrophobicity of a surface when an electrical potential is applied.[31,33,34]

While the effect of pressure differences across the GDE on the CO_2R performance has been receiving more attention recently,[31,35] its importance for scale-up has received limited attention.[33] At the same time, the scale-up of electrolyzers with a gas–liquid interface at the GDE inherently involves a non-uniform hydrostatic (and/or hydrodynamic) pressure balance.[36–38] The difference in density between the gas and the liquid phase leads to a variation in Δp, which can change the local flow regime along the GDE (Figure 3.1). In the flow-through regime,[35] gas breakthrough occurs because Δp is lower than the capillary forces of the pore network (ΔP1). In the flow-by regime, no breakthrough occurs as the pressure of the gas and the liquid phase are balanced (ΔP2). In the GDE flooding regime, Δp is sufficiently high to push electrolyte into the pore network and liquid breakthrough can occur (ΔP3).

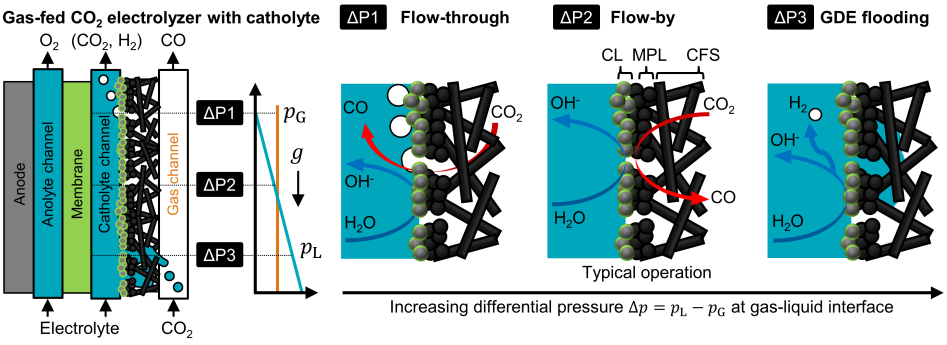

Figure 3.1: Flow regimes at the GDE of a gas-fed CO_2 electrolyzer with flowing catholyte. Hydrostatic (and/or hydrodynamic) pressure gradients along the liquid channel can lead to a pressure imbalance at the gas–liquid interface. **Flow-through regime (ΔP1)**: Gas overpressure leads to the breakthrough of CO_2 bubbles to the liquid phase. CO_2R occurs on sections of the catalyst layer (CL) that have sufficient contact with the electrolyte. **Flow-by regime (ΔP2)**: Interfacial forces keep the GDL dry at low pressure differences between gas and liquid phase. This ensures mass transfer of CO_2 through the carbon fiber substrate (CFS) and the microporous layer (MPL) to the CL. **GDE flooding regime (ΔP3)**: Liquid overpressure leads to the flooding of the GDL and breakthrough of electrolyte into the gas channel. The flooding of pores can reduce the transfer of CO_2 and favor the HER at the CL.

This raises the question how the flow regime at the GDE actually impacts the performance of the CO_2 electrolysis reaction. In this work, we study how the GDE structure and the operating conditions (cathode potential, differential pressure) affect the flooding behavior and performance of gas-fed CO_2 electrolyzer with flowing catholyte. We measured the Faradaic efficiency for CO with an electrolysis setup that allowed the control of the differential pressure across the GDE. For the first time, we show the impact of

electrowetting *in operando* at an industrially relevant current density ($-200\,mA\,cm^{-2}$). For this purpose, we applied an Ag catalyst layer to a selection of GDL substrates featuring different CFS microstructures (paper and cloth) and GDE thicknesses (250 – 450 µm).

We found that the cathode potential and GDE microstructure have a strong impact at which differential pressures the different GDE flow regimes occur. Our results suggest that large scale gas-fed CO_2 electrolyzers with flowing catholyte do not have to be operated with a flow-by regime over the entire electrode area. GDEs with a suitable structure allow robust CO_2 reduction despite flooding and electrolyte breakthrough as long as the gas channel can be drained at a sufficient rate. This insight offers a promising route to scale up CO_2 electrolyzers using currently available GDL materials.

3.2. EXPERIMENTAL METHODS

We prepared GDEs from a selection of commercial GDL substrates. We examined the gas–liquid flow regimes and electrochemical performance in a gas-fed CO_2 electrolysis cell with flowing catholyte. More detailed descriptions of the experimental procedures are available in the supporting information (SI).

The selection of commercial GDL materials was obtained from Fuel Cell Store (USA). We studied the effect of CFS thickness with a series of Toray carbon papers (TGP-H-060, 090, 120). We investigated the effect of pore size distribution (PSD) by comparing the Toray papers with SGL carbon papers (22BB, 39BC) and a carbon cloth (ELAT LT1400W). The CFS of all substrates had been wet-proofed with PTFE by the manufacturer. The microstructure was visualized with a scanning electron microscope (SEM).

The GDEs were prepared by coating the GDL substrate with an automated airbrush coating system (see SI of Chapter 2). The deposited CL had a target loading of 1 mg Ag cm^{-2} and a target composition of 80 wt% Ag nanoparticles and 20 wt% Nafion 521 ionomer. After cutting the GDL to size, we mounted the sample to the heating plate (130 °C) of the system and covered it with a 3 cm x 3 cm stencil. We prepared the ink by adding 33 mg of Ag nanopowder (20 – 40 nm, 99.9%, Alfa Aesar), 2.1 mL of deionized water, 2.1 mL of isopropyl alcohol, and 180 µL of Nafion D-521 dispersion (5 wt%, Alfa Aesar) into a glass vial. After homogenizing the ink for 30 min in a sonication bath, we used the airbrush and a 2D motorized stage to spray it evenly onto the MPL side of the GDL substrate.

We studied the effect of the different GDE flow regimes on the CO_2 reduction performance with the electrolysis setup shown in Figure 3.2 a. The humidified CO_2 feed was passed through the gas compartment of the flow cell. We used a gas–liquid phase sensor to estimate the volumetric fraction of electrolyte present in the product gas stream at the outlet of the flow cell. The back pressure was set by a check valve with a cracking pressure of 345 mbar. The peristaltic pump supplied the two liquid compartments with saturated 1 M $KHCO_3$.

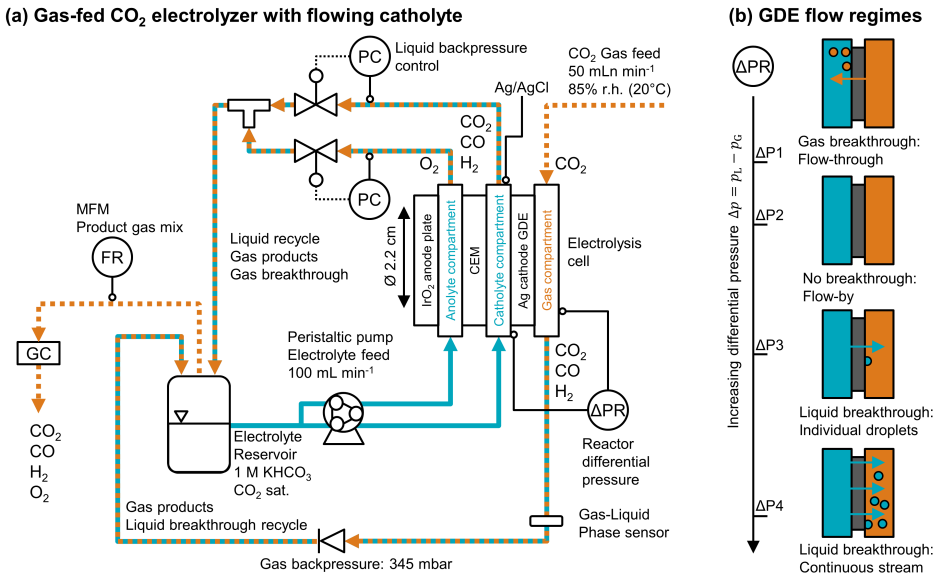

Figure 3.2: **(a)**: Process flow diagram of the CO_2 electrolysis setup with differential pressure, Δp, control. The anolyte and catholyte compartments were separated with a cation exchange membrane (CEM). The backpressure of both electrolyte streams was controlled (PC) before the two liquid streams were combined and recirculated. We directly measured Δp between the catholyte and gas compartment (ΔPR). The cathode potential was recorded with an Ag/AgCl reference electrode. The Faradic efficiency was determined by recording the flow rate (FR) with a mass flow meter (MFM) and analyzing the gas composition by gas chromatography (GC). **(b)**: Gas–liquid flow regimes observed at the GDE: **ΔP1**: Start of gas breakthrough (flow-through) and transition to separated flow, **ΔP2**: No gas or liquid breakthrough (flow-by): liquid and gas phase were separated, **ΔP3**: Individual liquid droplets form on the gas side and run down GDE, **ΔP4**: Continuous liquid stream through GDE.

We recorded the differential pressure between the gas and the catholyte compartment. Two electronic valves controlled the liquid back pressure. We collected the product gas mixture in the head space of the electrolyte reservoir and measured its flow rate with a mass flow meter. The composition was determined with gas chromatography (GC).

After inserting a dry GDE sample into the electrolysis cell, we increased the liquid backpressure until liquid breakthrough occurred. Through this initial flooding, we aimed to eliminate the effect of the residual liquid saturation, which causes differences between the first and subsequent flooding-drainage cycles (see SI, Figure 3.10).[29] We repeated the following steps for each current density (0, −10, −100, and −200 mA cm^{-2}): The liquid back pressure was reduced until gas breakthrough was observed, after which the galvanostatic control of the potentiostat was started.

We increased the liquid back pressure to control the differential pressure between the gas and liquid phase. This allowed us to establish the four characteristic flow regimes at the gas–liquid interface (Figure 3.2 b): (ΔP1) Start of gas flow-by (Slight gas breakthrough), (ΔP2) Flow-by (no breakthrough), (ΔP3) Individual droplets breaking through, and (ΔP4)

a continuous liquid stream breaking through. After the system was equilibrated for 6 min at each flow regime, we carried out three GC injections to determine the Faradaic efficiency for CO. Then the CO_2 electrolysis procedure was repeated at the next current density. An overview of the experimental sequence is shown in Figure 3.9 of the SI.

3.3. RESULTS & DISCUSSION

We investigated the interfacial phenomena at the gas–liquid interface and the CO_2 reduction performance for a selection of commercial GDL substrates. Supplementary results and the numerical values of all plotted data are included in the supporting information (SI).

3.3.1. PHYSICAL CHARACTERIZATION OF GDES

The microstructures of the different GDL materials are illustrated by SEM images (Figure 3.3). We arranged the materials in order of the CFS thickness, δ_{CFS}, and the average CFS pore size, $\bar{d}_{pore}$. Carbon papers are made of carbon fiber fragments that are held together by organic binders. This random lacing makes them spatially uniform in the in-plane direction of the material.[39] The Toray papers (TGP-H-060, 090, 120) have a CFS with a finer, unimodal pore size distribution (PSD) with small amounts of binder. The SGL papers (22BB and 39BC), in contrast, have a broader, unimodal PSD and a large amount of binder, which gives the CFS a coarser structure. The finer structure and narrower PSD of the Toray papers is also reflected in the smaller value of $\bar{d}_{pore}$ and its smaller standard deviation (Toray: $26 \pm 20\,\mu m$ vs. SGL: $32 \pm 30\,\mu m$).[40] The CFS of the LT1400W carbon cloth (ELAT) is woven from carbon fiber bundles without binder. This structure makes them anisotropic in the in-plane direction[39] and leads to a bimodal PSD, which has large pores between the fiber bundles ($\bar{d}_{pore} \approx 85\,\mu m$) and smaller pores ($\bar{d}_{pore} \approx 10\,\mu m$) between the individual carbon fibers.[41] The $\bar{d}_{pore}$ of the CFS, in conclusion, increased in the following order: Toray paper < SGL paper < Cloth.[41]

Although the MPL of our materials vary in thickness (Figure 3.3), we assume that the flooding properties will be mostly determined by the CFS because the large cracks in the MPL offers little flooding resistance.[32] The CFS and MPL of our substrates were impregnated with different amounts of PTFE (Figure 3.3). Literature studies show that the effect of PTFE content on wettability levels off after exceeding a certain loading threshold (e.g., 10 wt%).[42,43] We measured very similar static contact angles for all GDLs,[32] which suggests that differences in PTFE content should have little effect on the wettability.

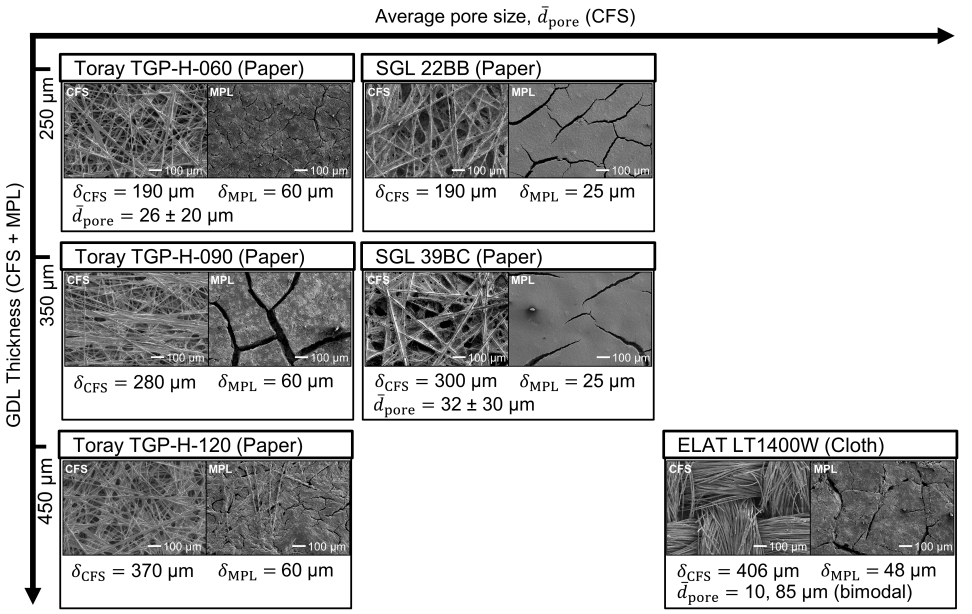

Figure 3.3: Microstructure and property data of commercial GDE substrates: Scanning electron microscope (SEM) images at 100x magnification. The thicknesses of the CFS, δ_{CFS}, was obtained from manufacturer and supplier data sheets. The layer thicknesses of ELAT LT1400W were provided by the FuelCellsEtc GDL Comparison table. The average diameter of the CFS pores, $\bar{d}_{pore}$, was obtained from Parikh *et al.* for the carbon paper and nonwoven GDLs.[40] The bimodal PSD of the carbon cloth is based on a ELAT Nuvant cloth.[41] Toray papers: the CFS was wet-proofed with 8 – 9 wt% PTFE; the MPL with 33 – 35 wt% PTFE. SGL papers: the CFS was wet-proofed with 5 wt% PTFE; the MPL with 23 wt%. The ELAT carbon cloth was also impregnated, but the PTFE content was unavailable.

3.3.2. PRESSURE FOR FLOW-BY REGIME DEPENDS ON MICROSTRUCTURE AND CATHODE POTENTIAL

From previous work, we know that breakthrough of gas or liquids depends on the differential pressure $\Delta p = p_L - p_G$.[32] However, those measurements were carried out at open circuit potential. When applying a potential to the cathode, it appears that the transition between the GDE flow regimes also depends on the cathode potential (Figure 3.4). We define the pressure zone, in which no gas or liquid breakthrough occurs, as the flow-by pressure window, Δp^*. It is indicated by the yellow shaded area.

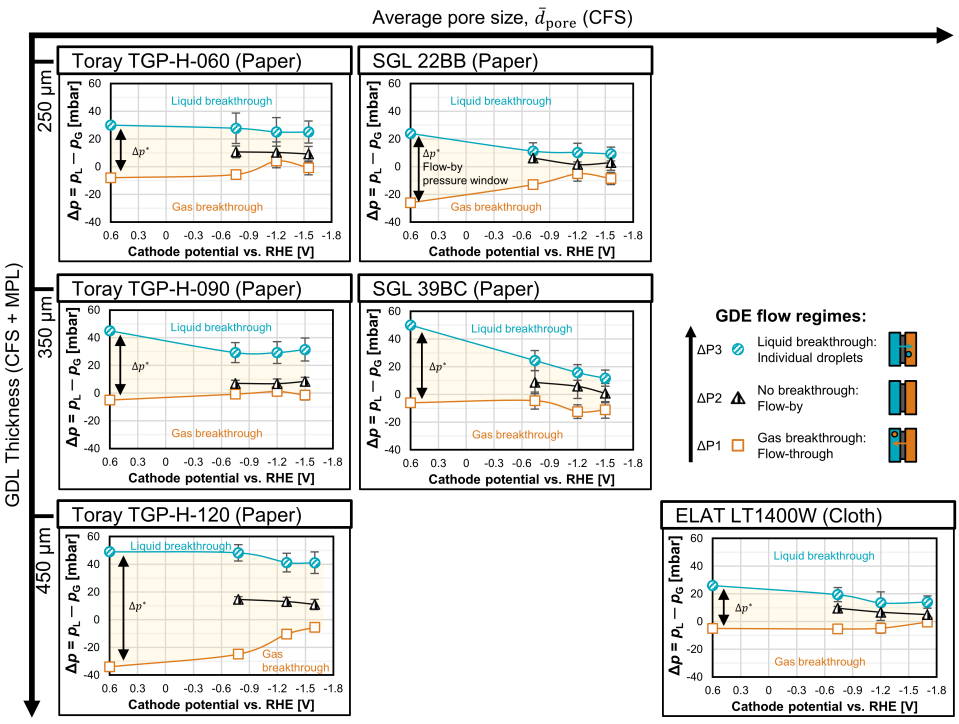

Figure 3.4: Development of the flow-by pressure window, Δp^*, as a function of GDE microstructure and the cathode potential. The cathode potential is plotted relative to the reversible hydrogen electrode (RHE) and was compensated for the iR-drop. The shaded yellow area between the curves for ΔP1 and ΔP3 indicates Δp^*. In the vertical direction, from bottom to top, the markers represent the observed GDE flow regimes: The square markers (□) indicate ΔP1, the pressure points at which gas breakthrough starts; the shaded triangle markers (△) indicate ΔP2, a series of pressure points in the flow-by regime; the shaded round markers (○) indicate ΔP3, the pressure points at which electrolyte breakthrough starts. In the horizontal direction, from left to right, she series of markers correspond to the current densities of 0, −10, −100, and −200 mA cm^{-2}. The error bars indicate the standard deviation of the Δp-fluctuation during the experiment. Smaller error bars are covered by the markers.

The Δp^* is the widest when no current is applied and the GDE is at open circuit potential, which is at approximately 0.6 V vs. RHE. Generally, we would expect a larger CFS thickness and a narrower pore size distribution (PSD) to widen Δp^*. The impact of structural

effects on Δp^* has been discussed in more detail in previous work.[32] For instance, TGP-H-120 has a larger CFS thickness than TGP-H-060 (370 µm vs. 190 µm), which results in a higher Δp^*: 83 mbar vs. 38 mbar (Figure 3.4). The effect of $\bar{d}_{\text{pore}}$ seems to depend on the type of GDL (paper or cloth) and/or the CFS thickness. While being similar in thickness, the carbon paper TGP-H-120 has a smaller $\bar{d}_{\text{pore}}$ than the carbon cloth LT1400W. This structural difference results in in a higher Δp^*: 83 mbar vs. 31 mbar. However, $\bar{d}_{\text{pore}}$ does not affect Δp^* for the thinner Toray and SGL carbon papers . Note that the data in Figure 3.4 constitute a worst case scenario for Δp^*, because they were recorded with wet GDEs, which exhibit a narrower Δp^* than initially dry GDEs (see SI, Figure 3.11).

The value of Δp^* decreases for all materials if the cathode potential is reduced below the open circuit potential (Figure 3.4). For example, the Δp^* of SGL 39BC drops by more than 50% from 56 mbar at open circuit potential ($\hat{=}$ 0 mA cm^{-2}) to 23 mbar at −1.5 V vs. RHE ($\hat{=}$ −200 mA cm^{-2}). The reduction in liquid breakthrough pressure is probably caused by reversible, physical electrowetting because we observed no permanent reduction in the static contact angle of the CFS after the CO_2 electrolysis.[32] The phenomenon of electrowetting reduces the hydrophobicity of an electrically charged surface because solvated ions are drawn into the electrical double layer.[34,44] It is remarkable, however, that we observed such a strong change in the breakthrough pressure. For example, according to the Young-Laplace equation[45], we would expect the contact angle of water in a pore with a radius of 10 µm to drop from 110° to 100° to explain a reduction in capillary pressure from 50 mbar to 25 mbar. To achieve such a drop in contact angle on a flat, dielectric PTFE surface, however, has been shown to require a potential of at least 50 V.[46]

A recent study of electrowetting on silver-based GDEs demonstrated that significant wettability changes occur at much lower potential differences (1 V) on bare metallic surfaces.[47] We therefore hypothesize that the electrowetting on our GDEs does not predominantly take place on the insulating PTFE, but instead takes place on uncoated carbon surfaces. The electrowetting behavior is also influenced by the heterogeneity and the rough surfaces inside the GDE's pores. Hydrophobic, insulating PTFE is dispersed on conductive carbon surfaces (e.g., carbon fibers). At open circuit potential, the electrolyte likely rests on top of the rough, dispersed PTFE in a Cassie-Baxter wetting state. As the electrical potential is changed, the electrolyte probably transitions to a Wenzel wetting state[34,48] by spreading along the uncoated, conductive carbon domains. The understanding of electrowetting in carbon-based GDEs could be greatly improved by future studies with *operando* synchrotron imaging.[47,49,50]

We would like to distinguish the reversible, physical electrowetting effect from irreversible (electro-)chemical degradation, which can decrease the contact angle of susceptible GDL materials like the Freudenberg H23C6 permanently.[32,51] This GDL substrate undergoes electrochemical degradation at cathode potentials below −0.65 V vs. RHE.[51] We hypothesize that the H23C6's carbon fibers are graphitized to a lower degree during manufacturing to make them more flexible, but this also reduces their chemical stability.[32]

We also observed the gas breakthrough threshold to shift to more positive Δp for the samples SGL 22BB, TGP-H-060, and TGP-H-120 (Figure 3.4). This is a curious phenomenon because we would expect the gas breakthrough pressure to remain constant as long as the pores remain hydrophobic and gas-filled. Starting at cathode potentials of −1.2 V vs. RHE, bubbles form at the liquid side of the CL. These bubbles might also displace electrolyte from previously wetted pores and thereby reduce the resistance against gas breakthrough (more positive Δp).

The potential-dependent contraction of Δp^* shows that it would be even more difficult to operate CO_2 electrolyzers in flow-by mode at a large scale when a significant current is applied. As the detrimental electrowetting effect reduces the resistance against electrolyte flooding, the cell height has to be limited to prevent electrolyte breakthrough due to hydrostatic pressure differences. Of the materials we studied (Figure 3.4), TGP-H-120 supports the widest flow-by pressure window of 47 mbar at −1.7 V vs. RHE ($\hat{=}$ −200 mA cm^{-2}). This pressure window would correspond to a cell height of about 48 cm, which is relatively modest in comparison with the height of commercial cells for alkaline electrolysis (100 – 200 cm)[52] or chlor-alkali electrolysis with an oxygen depolarized cathode (100 – 150 cm).[53,54]

3.3.3. LIQUID BREAKTHROUGH FLOW RATE DEPENDS PRIMARILY ON MICROSTRUCTURE

Having established that breakthrough seems inevitable for large scale GDEs operating between a liquid and a gas phase, the rate of breakthrough becomes a relevant metric. From a practical perspective, liquid breakthrough will be preferred over gas breakthrough, as the gas bubbles would cause additional ohmic resistances in the liquid compartment.[35] Therefore, we used a gas–liquid phase sensor at the gas compartment outlet to estimate the liquid breakthrough flow rate, F_L, when a current is applied (see SI, Figure 3.13).

The effect of differential pressure, Δp, and cathode potential on F_L is show in Figure 3.14 of the SI. Materials with a thicker CFS and smaller average CFS pore size, $\bar{d}_{pore}$ require a higher Δp to allow the same liquid breakthrough flow rate, F_L. The thinner TGP-H-060, for instance, requires an average Δp of 46 mbar to force a F_L of 6.3 mL min^{-1} cm^{-2} (see SI, Figure 3.14). The thicker TGP-H-090, in contrast, requires 58 mbar to achieve the same flow rate. This phenomenon can be explained by the higher hydrodynamic pressure drop imposed by the longer flow path through the thicker GDL. Similarly, the pressure drop is also increased by smaller $\bar{d}_{pore}$,[43] which is well illustrated by the comparison of the ELAT cloth with the TGP-H-120 paper. The larger pores of the cloth permits an average F_L of 5.1 mL min^{-1} cm^{-2} at 26 mbar, while the narrower pores of the carbon paper permit 3.6 mL min^{-1} cm^{-2} at 53 mbar (see SI, Figure 3.13).

The electrowetting effect does not seem to have a strong influence on the permeability, as F_L does not vary significantly as a function of the cathode potential for all GDE materials (see SI, Figure 3.14). This limited effect of electrowetting could mean that the

increasing wettability does not establish many new percolation pathways, but branches out the flooded pore volume inside of the network. From a hydrodynamic perspective, we can expect new pathways to only contribute marginally to the overall percolation flow because they have a smaller pore diameter than the already flooded pores. According to the Hagen-Poiseuille equation, the flow rate through a pore scales with the fourth power of the diameter ($F_{\mathrm{L,pore}} \propto d_{\mathrm{pore}}^4$). The relationship between the overall F_{L} and Δp is, therefore, mostly determined by the large pores in the percolation flow path, which are already flooded at higher (less negative) cathode potentials. Advanced imaging techniques, such as X-ray computed tomography,[55–57] would greatly enhance the understanding of these complex two-phase flow dynamics inside a GDE under operating conditions.

3.3.4. FARADAIC EFFICIENCY FOR CO DEPENDS ON MICROSTRUCTURE AND GDE FLOW REGIME

To assess the impact of gas and liquid breakthrough on the Faradaic efficiency for CO, FE_{CO}, we experimentally tested FE_{CO} for each GDE at different Δp, thereby inducing flow regimes of gas breakthrough, flow-by, or liquid breakthrough (Figure 3.5). For each current density curve, the different marker fillings indicate the flow regime with increasing differential pressure Δp: Empty marker (ΔP1): start of gas flow-through; first shaded marker (ΔP2): flow-by; second shaded marker (ΔP3): Individual liquid droplets breaking through; filled marker (ΔP4): Continuous liquid stream breaking through. We listed the cathode potential next to the legend for each current density curve because this potential showed little dependence on the Δp for most materials (see SI, Figure 3.15). The ELAT carbon cloth seems to be an exception to this because it deformed mechanically (see SI, Figure 3.18). We tested the stability of the GDEs by repeating the current density step of $-100\,\mathrm{mA\,cm^{-2}}$ for two substrates (see SI, Figure 3.16).

The highest FE_{CO} is achieved by materials with thinner CFS and/or larger $\bar{d}_{\mathrm{pore}}$, which allow higher transport rates of CO_2 at higher current densities (Figure 3.5). If the supply of electrons surpasses the diffusional flux of CO_2, the excess current is then shifted to the undesired HER. For example, TGP-H-060 has a thinner CFS than TGP-H-120 (190 µm vs. 370 µm) and thus exhibits a significantly higher FE_{CO} (81% vs. 46%) at $-200\,\mathrm{mA\,cm^{-2}}$ and ΔP1 (Figure 3.5). Similarly, the broader PSD of the LT1400W cloth in comparison with the TGP-H-120 paper results in a superior FE_{CO} (84% vs. 46%) at $-200\,\mathrm{mA\,cm^{-2}}$ and ΔP1 (Figure 3.5). The higher FE_{CO} achieved with thinner and/or coarser CFS structure (larger $\bar{d}_{\mathrm{pore}}$) was already known for the stable pressure window,[32] and is now also confirmed for breakthrough regimes. We note that the apparent effects of CFS thickness and CFS pore structure have to be treated with caution when comparing materials from Toray with materials from SGL or ELAT because there also differences in the MPL structure (Figure 3.3).

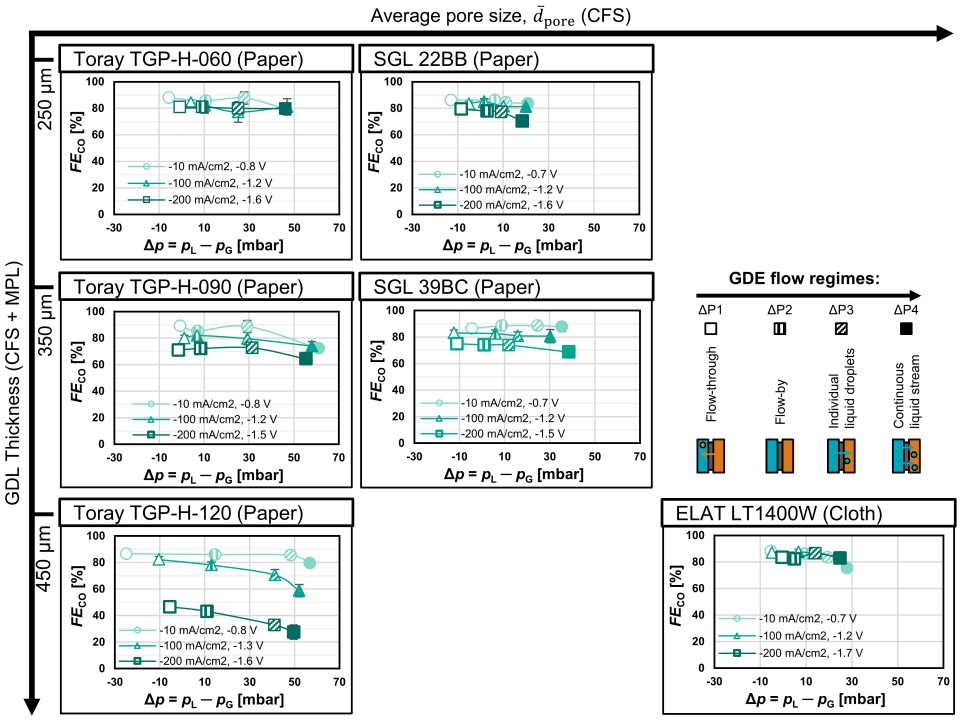

Figure 3.5: Faradaic efficiency for CO, FE_{CO}, as a function of differential pressure, Δp. The data series correspond to the current densities −10, −100, and −200 mA cm^{-2} from lighter to darker color. The corresponding cathode potential against the reversible hydrogen electrode (RHE) is given in the legend of each diagram. The marker filling indicates the GDE flow regime. The y-axis error represent the standard error for three consecutive GC injections. Smaller error bars are covered by the marker. The x-axis error bars were omitted here to make the representation of the other data more clear. These error bars are identical with the y-axis error bars in Figure 3.4.

The CO_2R performance generally drops with increasing Δp (Figure 3.5). For instance, the FE_{CO} at −200 mA cm^{-2} for SGL 39BC drops from 75% to 69% when Δp is increased from ΔP1 to ΔP4. The liquid saturation in the pore network of the GDE increases with Δp, which leads to a lower effective diffusivity for gaseous reactants.[29,30] This diminishes the mass transfer of CO_2 to the CL and reduces the rate of CO_2R in favor of the unwanted HER. The magnitude of this effect, however, depends strongly on the GDE structure.

The CO_2R performance of thicker carbon papers falls as a consequence of electrolyte intrusion (Figure 3.5). The thick TGP-H-120, for example, shows a drop in FE_{CO} from 46% to 27% at −200 mA cm^{-2} when the Δp is increased from ΔP1 to ΔP4. In contrast, the thin TGP-H-060 shows an insignificant drop in FE_{CO} from 81% to 80% for the same conditions. We can explain the different effects for thin and thick carbon papers with qualitative saturation curves[29] and schematic pore network models[32,57,58] (Figure 3.6). The connectivity of the pore bodies (circles) and throats (rectangles) determines the flow

path the intruding liquid follows. Each throat resists flooding up to its capillary pressure, $p_{C,i}$. We hypothesize that a thin paper becomes less saturated because the intruding liquid is drained at a lower liquid breakthrough pressure or percolation threshold, Δp_L^* or ΔP3 (Figure 3.6 a). This prevents the liquid from branching out extensively inside the pore network and lets the thin paper maintain a higher residual gas saturation, S_G^0, when Δp is increased further.

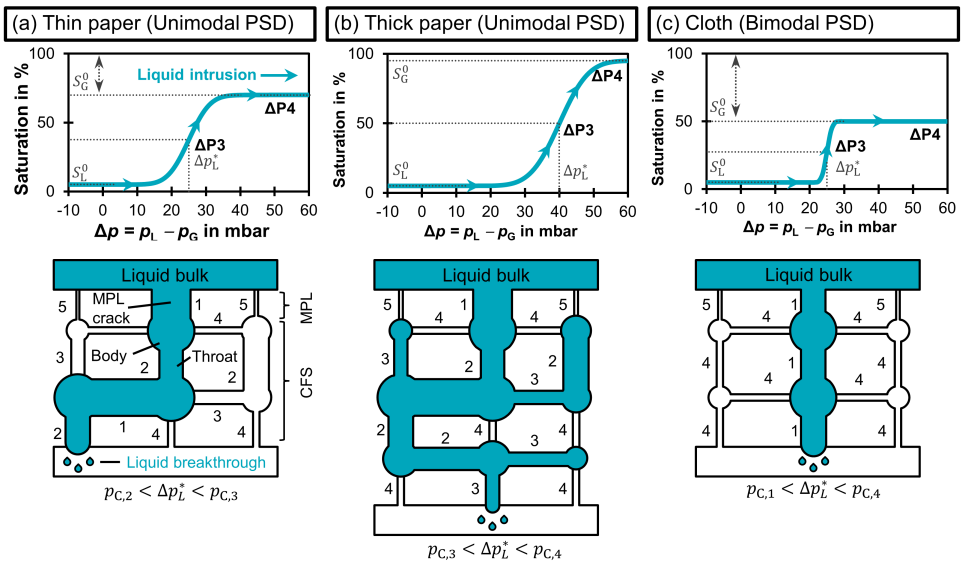

Figure 3.6: Saturation behavior of different CFS structures. The hypothetical saturation curves show how the liquid intrusion changes the saturation level. The curves start at their residual liquid saturation, S_L^0, as the GDEs were pre-wetted. As Δp is increased, the saturation ultimately reaches the full effective saturation, at which the residual gas saturation, S_G^0, remains unflooded.[29,59] The schematic pore networks[32,57,58] explain the difference in saturation at the percolation threshold (ΔP3). The spatial connectivity of the pores determines the percolation flow path and the liquid breakthrough pressure, Δp_L^*. The relative order of capillary pressures is: $p_{C,1} < p_{C,2} < p_{C,3} < p_{C,4} < p_{C,5}$. Cracks allow the liquid to bypass the pores with high capillary pressure $(p_{C,5})$ of the MPL. **(a)** Thin paper: The intruding liquid has to overcome $p_{C,2}$ and takes a relatively straight path through the material. **(b)** Thick paper: The additional layer increases Δp_L^* by adding a pore with $p_{C,3}$ to the flow path. This allows the liquid to branch out more and reach a higher saturation. **(c)** Cloth: The liquid follows a direct flow path along pores with the $p_{C,1}$. No branching occurs because the Δp is too low to flood adjacent pores. This leads to high S_G^0.

A thick paper, in comparison, has a higher Δp_L^* because the longer flow path has a higher probability of including a throat with a high capillary pressure.[42] Figure 3.6 b illustrates this effect with the additional layer of the thick paper, which adds a throat with $p_{C,3}$ to the flow path. We think that the additional thickness leads to stronger branching out of the liquid in two ways. First, the higher Δp_L^* allows pores with higher $p_{C,i}$ to be flooded. Second, the longer percolation flow path increases the probability of the liquid to be in contact with pores that can be flooded. Thus, there are less uninterrupted flow paths in the gas phase, which reduces the effective diffusivity and leads to a lower FE_{CO} with

increasing Δp.

The high CO_2R performance of the LT1400W carbon cloth is only minimally affected by electrolyte intrusion (Figure 3.5). This can be seen by the insignificant reduction of FE_{CO} from 84% to 83% at $-200\,mA\,cm^{-2}$ when comparing ΔP1 to ΔP4. This behavior can be attributed to the bimodal pore size distribution of the cloth which preferentially drains the electrolyte through the large pores between the fiber bundles[43] and leaves the adjacent smaller pores available for gas diffusion (Figure 3.6 c). We therefore hypothesize that the carbon cloth has the highest S_G^0 of the investigated materials, which allows high CO_2 transport even if liquid breakthrough is occurring.

The modest impact of breakthrough of gas or liquid on the FE_{CO} — at least for materials bimodal pore structures or thin CFS — has a large practical meaning, as it suggest that large scale operation of CO_2 electrolyzers is still possible at good selectivity, accepting breakthrough of gas or liquid. To further investigate this implication, we conducted a more stringent performance test to evaluate how well a GDE based on ELAT LT1400W would perform inside a cell with a height $\geq 100\,cm$. We varied Δp from -6 to $+109$ mbar, which resulted in a mixed flow regime along the GDE and an average FE_{CO} of 69% (Figure 3.7 a). More details on this experiments are available in Section 3.5.7 of the SI.

The cloth GDE allows robust CO_2 reduction for at least 125 h at current densities close to $-200\,mA\,cm^{-2}$ despite experiencing continuous breakthrough due to a liquid overpressure Δp around 100 mbar. The Faradaic efficiency for CO remains between 55% – 60%. (Figure 3.7 b). The dips and slight decrease in FE_{CO} were caused by oxygen crossover (after stopping the purge gas) and interruptions in the control software, while the flooding does not seem to change the Faradaic efficiency significantly over time (see SI, Figure 3.20).

We hypothesize that the robust CO_2 reduction is enabled by the bimodal pore structure of the cloth, which separates the transport pathways of the gas and electrolyte phase (Figure 3.7 c). Electrolyte breakthrough must occur through cracks in the MPL and large pores between the fiber bundles of the cloth ($d_{pore} \approx 85\,\mu m$).[41] The smaller pores within the fiber bundles ($d_{pore} \approx 10\,\mu m$) remained gas-filled and allow the CL to exchange CO_2 and CO with the gas channel (Figure 3.7 c). Using the capillary pressure equation provided by Wood *et al.*,[60] we can estimate that Δp would need to exceed 138 mbar before these small pores are also filled with electrolyte.

Based on the promising performance of the cloth GDE, we believe that GDEs with a bimodal PSD are able to maintain sufficient gas transport for CO_2 electrolysis at high current densities even for continuous liquid breakthrough. Compared to operating at lower overpressure, the Faradaic efficiency is only slightly compromised (Figure 3.7 a). We propose a CO_2 electrolyzer design, which should be scalable to an electrode height of at least 100 cm (Figure 3.7 d). The percolated catholyte is collected and separated from the product gas stream inside the catholyte reservoir.

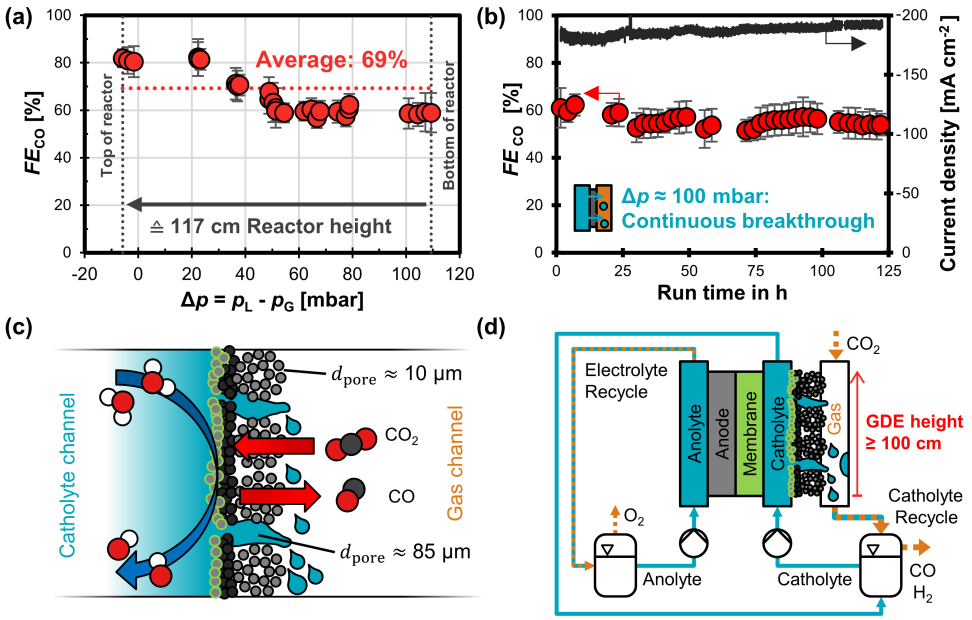

Figure 3.7: CO_2R performance test of ELAT LT1400W carbon cloth GDE: **(a)** Faradaic efficiency for CO, FE_{CO}, as a function of differential pressure, Δp. The cell potential was constant at 10 V (Potentiostat limit). The current density was between −180 to −200 mA cm^{-2}. The average FE_{CO} was determined by integrating FE_{CO} numerically over the Δp range. **(b)** Robust CO_2 electrolysis despite continuous catholyte breakthrough: Δp ranged from 80 to 120 mbar. The cell potential was constant at 10 V. The current density was between −180 to −193 mA cm^{-2}. **(c)** Transport mechanisms inside flooded cloth GDE cloth: CO_2 and gaseous products (CO, H_2) can diffuse through the dry, small pores inside the fiber bundles. Liquid electrolyte can pass through the large pores between the fiber bundles. **(d)** Proposed scalable CO_2 electrolyzer design: The cloth GDE allows robust CO_2 conversion despite electrode breakthrough in lower sections of the cell. More detailed data on all experiments available in Section 3.5.7 of the SI.

Compared to MEA-based CO_2 electrolyzers with anion exchange membranes,[20,61] the use of a catholyte layer in our proposed design would act as a buffer between the membrane and the catalyst. This would allow the utilization of e.g. a bipolar membrane, which could reduce CO_2 crossover[10,61,62] and allow the deployment of a non-precious anode made from nickel.[10,24,63] Although the catholyte channel introduces additional ohmic resistance, it allows a better control of the local reaction environment at high current densities[8,24] in comparison to MEA electrolyzers, in which the water management at the membrane[64] and the cathode[65] or salt formation in the gas channel[66,67] can hinder performance. From a practical perspective, the reactor (Figure 3.7 d) has to be fed with a sufficiently high electrolyte flow rate to ensure it does not run dry. Liquid breakthrough rinses the GDE[33] and the gas channel, which limits salt deposition from carbonate scaling.

3.4. CONCLUSION

We have studied how structural parameters (CFS structure, CFS thickness, CFS pore size) and process parameters (differential pressure, cathode potential) influence the scalability of gas-fed CO_2 electrolyzers with flowing catholyte. The scale-up of an electrolyzer operating in a flow-by regime is not viable with currently available commercial GDL materials. The relatively low capillary pressure and electrowetting make it difficult to keep the fluid phases separated at industrially relevant current densities ($\geq -200\,\mathrm{mA\,cm^{-2}}$). A thick carbon paper with a small average CFS pore size (Toray TGP-H-120) achieved the widest flow-by pressure window of 47 mbar, which corresponds to a relatively modest electrode height of 48 cm. The same structure, however, leads to a poor diffusivity in the GDL, which limits FE_{CO} to less than 46%.

Instead, we propose the scale-up of an electrolyzer with a carbon cloth GDE, which can tolerate GDE flooding and electrolyte breakthrough. We found that a carbon cloth (ELAT LT1400W) allowed the highest FE_{CO} of 84% at $-200\,\mathrm{mA\,cm^{-2}}$. The bimodal pore size distribution allows this GDE to maintain a high effective diffusivity at higher liquid overpressures. The intruding electrolyte preferentially floods the large pores between the fiber bundles and is drained before it can flood the smaller pores inside of the bundles. This ensures that a significant share of the GDL pores remain available for gas diffusion despite electrolyte flooding. We demonstrated that this material allows stable CO production with $FE_{CO} \geq 55\%$ over at least 125 h despite high liquid overpressures of 100 mbar. This promising electrolyzer design would therefore enable a cell height of at least 100 cm and operate at an estimated average FE_{CO} of 69% at $-200\,\mathrm{mA\,cm^{-2}}$.

3.5. SUPPORTING INFORMATION

The digital version of the Supporting Information (SI) includes an Excel file with the values for all plotted data and all recorded experimental parameters for the CO_2 electrolysis experiments.

3.5.1. GDE PREPARATION

We prepared each GDE by depositing the CL with a tailor-made automated airbrush coating system (Figure 2.9). The GDE coating procedure and samples are identical with Chapter 2.

3.5.2. CHARACTERIZATION WITH SEM

The GDE microstructure was visualized with a JSM-6010LA scanning electron microscope (SEM) (JEOL, Japan). The instrument was equipped with a secondary electron imaging (SEI) detector for morphology and a backscattered electron composition (BEC) detector for elemental contrast imaging. We characterized the CL with SEM images in Chapter 2. We estimate a thickness of $3.5 \pm 0.2\,\mu m$. The CL consisted of a Nafion ionomer matrix with larger Ag agglomerates (200 – 1200 nm) embedded. The agglomerates were formed by smaller primary Ag particles ($79 \pm 17\,nm$).

3.5.3. QUALITATIVE COMPARISON OF PORE SIZE DISTRIBUTION

The studied GDLs exhibit the following trends from narrow to wide pore size distributions (PSD): Toray paper < SGL paper, Cloth (Figure 3.8). We ranked the carbon cloth according to its larger pores because these are relevant for the flooding resistance. While not all PSD data were available for this specific set of materials, we leverage measurements on substrates from the same set of materials which are expected to results in minor influences on the PSD (Figure 3.8). Forner-Cuenca *et al.* used materials without MPL and without PTFE wetproofing. The Nuvant carbon cloth is of a different type than our LT1400W cloth.[41] Additional characterization data of all used GDE are available in the SI of our recent publication.[32]

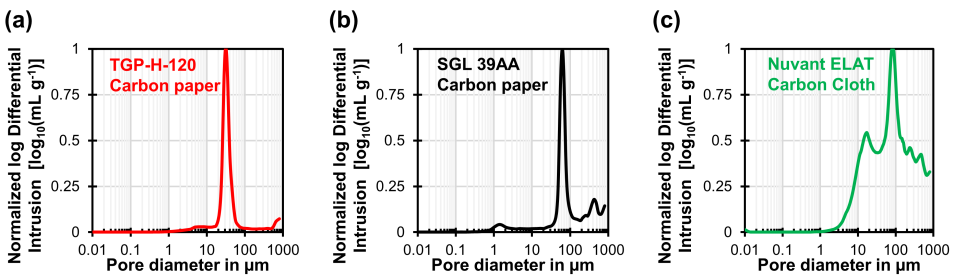

Figure 3.8: Qualitative comparison of the pore size distributions for the different carbon fiber substrate types. **(a)** ELAT carbon cloth **(b)** SGL carbon paper **(c)** Toray paper. Note that the substrates shown here differ from our study because they were not impregnated with PTFE and do not have a MPL. The data is based on mercury intrusion porosimetry measurements from Forner-Cuenca *et al.*.[41]

3.5.4. ASSEMBLY OF 3-COMPARTMENT CO_2 ELECTROLYSIS CELL

The GDEs were installed in a 3-compartment cell (Figure 2.22). The assembly of the cell is described in Section 2.5.7.

3.5.5. ENGINEERING OF THE CO_2 ELECTROLYSIS SETUP

The CO_2 reduction experiments were carried out with the electrolysis setup shown in Figure 2.25. We used Labview (Version 2018, National Instruments) to record online data of the various sensors and to control the pump and the electronic valves. Section 2.5.7 of Chapter 2 explains the engineering of the CO_2 electrolysis setup in detail.

3.5.6. CO_2 ELECTROLYSIS WITH VARYING CURRENT DENSITY AND DIFFERENTIAL PRESSURE

The following section contains more detailed descriptions of the methods and data processing for our CO_2 electrolysis experiments with varying current density and differential pressure for our six GDL materials. The sheet "CO2 electrolysis" in the accompanying Excel document of the online article includes detailed values for all process parameters and resulting Faradaic efficiencies for H_2 and CO.

OVERVIEW OF EXPERIMENTAL SEQUENCE FOR GDE TESTING

The overview of the experimental sequence is presented in Figure 3.9. After installing the GDE in the electrolysis cell, we pre-flooded the GDE samples. During this procedure, we measured the flow-by pressure window, Δp^*, of the initially dry GDE by stepping the pressure up from ΔP1 to ΔP3 and recording the Δp at which the GDE flow regime changed. Then, we measured the Δp^* of the now wetted GDE by reducing the pressure back down to ΔP3 and recording when the liquid breakthrough ceased (ΔP3 of wet GDE) and when the gas breakthrough started (ΔP1).

Second, we carried out the CO_2 electrolysis run with the current densities −10, −100, and −200 mA cm^{-2} at the different flow regimes ΔP1, ΔP2, ΔP3, and ΔP4 (Figure 3.9). Typically, the setting of each ΔP took less than 10 min. After the process parameters were set, we waited for 6 min so the system could equilibrate. We then carried out three GC injections.

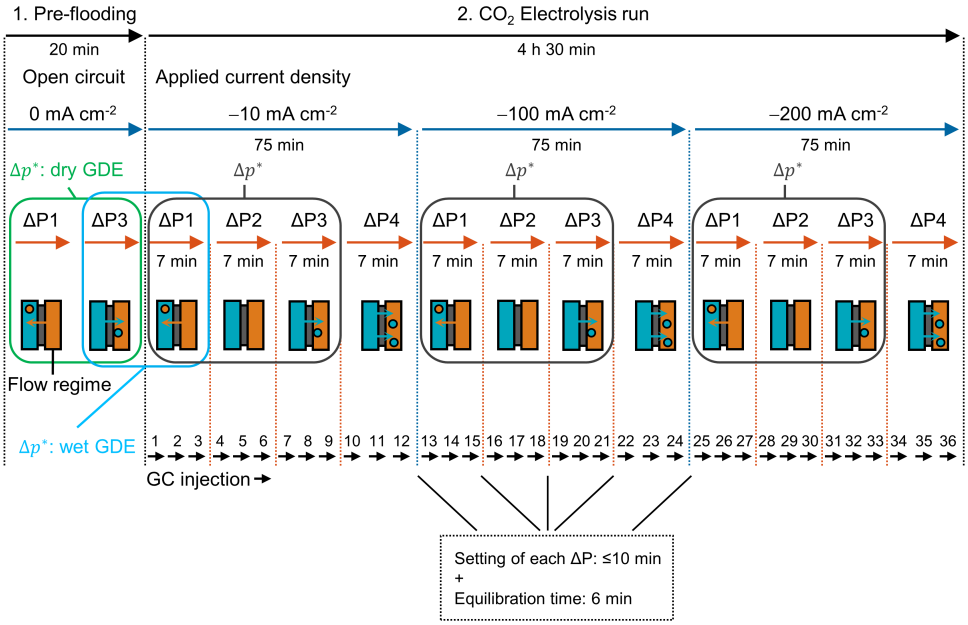

Figure 3.9: Overview of experimental sequence for GDE testing. 1. Pre-flooding and measurement of the flow-by pressure windows, Δp^*, for the initially dry GDE and the pre-wetted GDE. 2. CO_2 electrolysis run with the current densities −10, −100, and −200 mA cm^{-2}. During each current density step, we adjusted the liquid backpressure to set the four characteristic flow regimes at the GDE interface: (ΔP1) Transition from flow-through to flow-by, (ΔP2) Flow-by (no breakthrough), (ΔP3) Individual droplets breaking through, and (ΔP4): Continuous liquid stream breaking through. The setting of the pressure points took less than 10 min. For each parameter set of current density and GDE flow regime, we let the system equilibrate for 6 min before carrying out three GC injections.

FLOW-BY PRESSURE WINDOW OF GDL, DRY GDE, AND WET GDE

We pre-flooded the GDEs before carrying out the CO_2 electrolysis run (Figure 3.9) to take the differences in flooding behavior of a dry GDE and a wet GDE into account. This ensures that the effects of the cathode potential on Δp^* the CO_2 electrolysis run are isolated from the effect of residual liquid saturation, S_L^0. The flooding behavior of porous gas diffusion media can be characterized by a capillary pressure curve (Figure 3.10). Typically, the flooding of hydrophobic pores with a non-wetting fluid requires higher capillary pressures when it is carried out the first time (Dry GDE) in comparison to subsequent flooding cycles (Wet GDE). This phenomenon can be explained through residual water being present in the network, which reduces the mechanical work necessary to force water into the hydrophobic pores during subsequent cycles. [29,68]

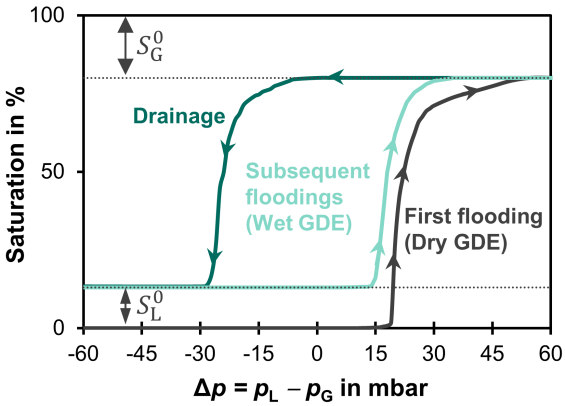

Figure 3.10: Qualitative capillary pressure curves for first flooding (Dry GDE) and subsequent flooding cycles (Wet GDE). The liquid saturation increases with increasing liquid pressure until it reaches the residual gas saturation, S_G^0. Reducing the liquid pressure leads to a drainage of the pore volume and a reduction of the liquid saturation down to the residual liquid saturation, S_L^0. [29] Adapted from Figure 11 of Gostik *et al.*. [68]

The flow-by pressure window Δp^* of the wet GDE constitutes a worst case assumption for the flooding resistance of a GDL material (Figure 3.11). In comparison with the uncoated GDL, the deposition of the CL reduces the liquid breakthrough pressure Δp_L^* because the CL consists of the more hydrophilic materials silver and Nafion. [32] The pre-flooding shifts Δp_L^* of the initially dry GDEs to even more negative values and leads to a narrower Δp^* for most samples (wet GDE).

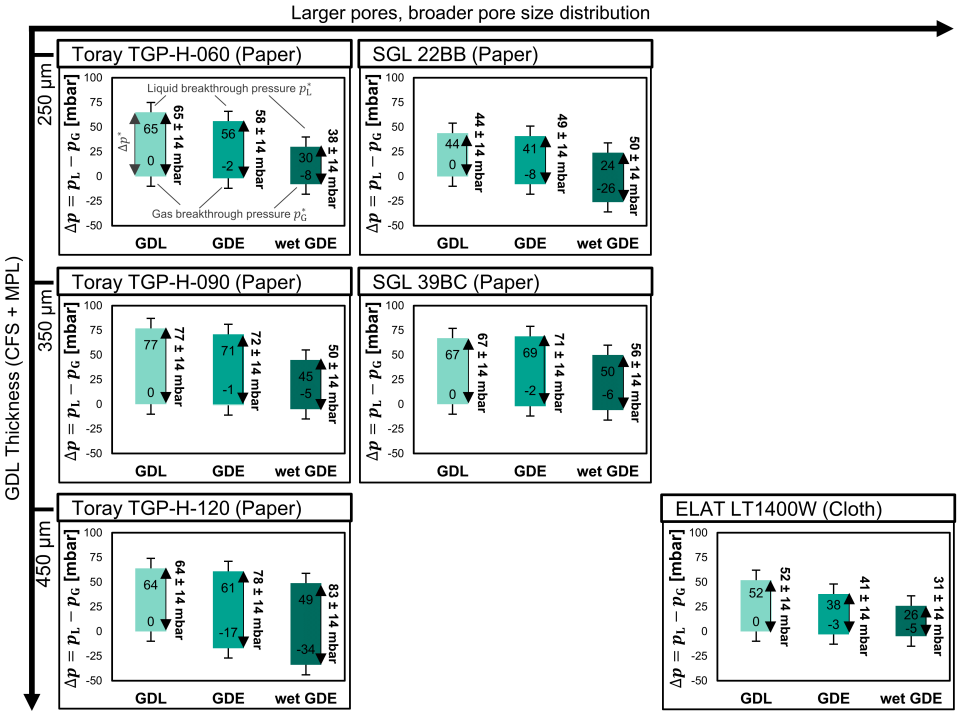

Figure 3.11: Change of the flooding resistance due to application of CL and pre-flooding of the GDE. Determination of flow-by pressure window (at open circuit), $\Delta p^* = \Delta p_L^* - \Delta p_G^*$, for uncoated GDL (MPL + CFS), coated GDE (CL + MPL + CFS), and pre-flooded/wet GDE. Upper limit of bar chart: Liquid breakthrough pressure, Δp_L^*. Lower limit: Gas breakthrough pressure, Δp_G^*. The gas breakthrough pressure limit of the uncoated GDL samples was not measured; we assume that it was 0 mbar. The arrows next to the bar charts indicate the corresponding flow-by pressure window, Δp^*. The GDL data and (dry) GDE data are identical with the data of our previous publication.[32] The listed values for the wet GDE are based on measurements of a single sample. For the breakthrough pressures, we estimated errors of $\sigma_{p_G^*} = \pm 10$ mbar and $\sigma_{p_L^*} = \pm 10$ mbar of all GDEs based on the work of Mortazavi *et al.*[42] The error of the flow-by pressure window, Δp^*, was estimated with the Gaussian error propagation.

LIQUID BREAKTHROUGH DEPENDS ON DIFFERENTIAL PRESSURE AND CURRENT DENSITY

We calculated the liquid breakthrough flow rate, F_L, with a mass balance around the gas compartment and with the data of the gas–liquid phase sensor attached to the outlet of the gas compartment (Figure 3.12).

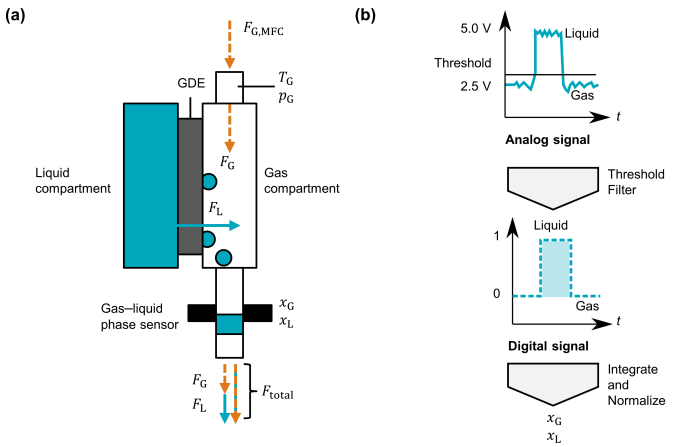

Figure 3.12: Determination of liquid breakthrough flow rate, F_L, with a mass balance around the gas compartment. The gas feed flow rate at normal conditions is $F_{G,MFC}$. The feed gas has the pressure p_G, the temperature T_G, and the volumetric flow rate F_G at the reactor inlet. The total two-phase flow rate is F_{total}. The volumetric gas and liquid fractions are x_G and x_L. (b) Measurement of x_G and x_L with the gas–liquid sensor at the gas compartment outlet.

Electrolyte that broke through the GDE left through the tubing at the bottom of the reactor (Figure 3.12 a). The two-phase flow in the outlet tube consists of liquid electrolyte and the product gas of the reactor. The volumetric gas fraction, x_G, and the volumetric liquid fraction, x_L, add up to 100% (3.1). The volumetric gas flow rate, F_G, and the volumetric liquid flow rate, F_L, add up to the total volumetric flow rate, F_{total}, in $mL\,min^{-1}$ (3.2). The value of F_G and F_{total} are connected through x_G (3.3).

$$1 = x_G + x_L \tag{3.1}$$

$$F_{total} = F_G + F_L \tag{3.2}$$

$$F_G = F_{total} \cdot x_G \tag{3.3}$$

We can solve the equation system for the desired F_L by bringing F_L to the left side of (3.2). We then substitute F_{total} with (3.3) and exclude F_G to receive (3.4). The values of F_G and x_G are available through experimental data.

$$F_L = F_{total} - F_G = \frac{F_G}{x_G} - F_G = F_G\left(\frac{1}{x_G} - 1\right) \tag{3.4}$$

The gas flow rate, F_G, in the outlet tube is determined from the gas feed flow rate, $F_{G,MFC}$. We can assume the $F_{G,MFC}$ changes little while passing through the reactor because CO_2 is supplied in large excess. The CO_2R reaction would have little effect on the volumetric flow rate because each converted molecule of CO_2 is replaced with a molecule of CO. We assume that the HER does not contribute to F_G because we observed the formation of hydrogen bubbles at the liquid side of the CL. Any evolved hydrogen, therefore, should leave the reactor through the liquid outlet instead of the gas outlet.

The feed flow rate, $F_{G,MFC}$, has a value of 50 mLn min^{-1} (normal conditions: 0 °C, 1.013 bar (a)). We adjusted this flow rate to the conditions in the reactor with the ideal gas equation. We assumed that the gas temperature, T_G, remained constant at the feed temperature of 20 °C. The gas pressure, p_G, was measured with the gas sensor in front of the reactor. The data are available in the accompanying Excel sheet.

The volumetric gas fraction, x_G, in the outlet tube can be estimated from the phase sensor data (Figure 3.12 b). A liquid slug that passes through the sensor, causes a peak in the analog output voltage. We converted the analog data signals to digital data signals by applying a threshold filter. A value of 0 for the digital data indicates that gas is present at the sensor; a value of 1 indicates that liquid is present. We integrated the sensor data for each experimental setting (current density step and differential pressure) to determine the averaged value of x_G.

The measured F_L determined with (3.4) was corrected with a non-linear calibration curve (Figure 3.13). This was necessary because the actual and the measured F_L start deviating from each other at higher flow rates. This deviation can be attributed to a number of phenomena:

- The data acquisition rate of 20 Hz limits the signal's time resolution
- The liquid slugs deviate from an ideal cylinder shape. This makes the slug volume calculation inaccurate.
- The two-phase flow is less steady at high flow rates.

For these reasons, the error starts increasing at higher flow rates, which makes it more difficult to distinguish higher flow rates from each other. At low flow rates, for example, we calculate a measured F_L of 2.9 mL min^{-1} cm^{-2} (3.4), which corresponds to an actual flow rate of 2.8 ± 0.2 mL min^{-1} cm^{-2}. If we compare this to a higher flow rate of 15.9 mL min^{-1} cm^{-2}, this then corresponds to 10.0 ± 3.9 mL min^{-1} cm^{-2}.

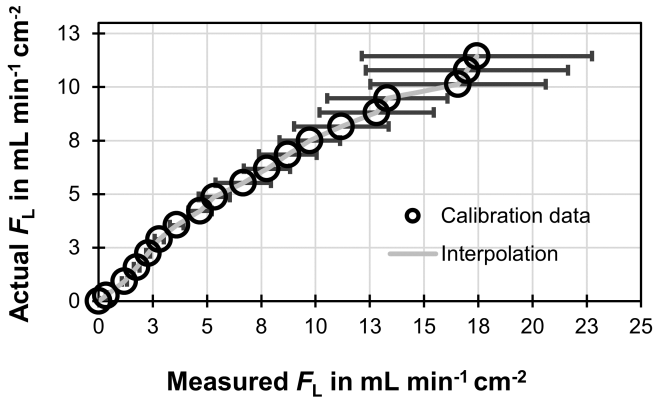

Figure 3.13: Gas–liquid sensor calibration of the liquid breakthrough flow rate, F_L. The measured F_L was determined with the sensors and calibrated against the actual liquid flow rate. The markers represent the average measured F_L, the error bars represent the standard error determined through three independent calibration runs. The data acquisition rate of the sensor was 20 Hz. We used a linear interpolation between the data points to correct all data from the CO_2 electrolysis experiments.

Our values for F_L are a bit larger, but in a similar order of magnitude as in the study on the flooding behavior of SGL 39BC reported by Mot *et al.* (Table 3.1).[31] A possible explanation for the different values for F_L might be the different techniques used to measure Δp. De Mot *et al.* determined Δp by comparing the pressure of the gas and the liquid inlet line. This measurement technique exaggerates the Δp between the gas and the liquid compartment because it neglects the hydrodynamic pressure drops in the gas and in the liquid feed lines. The reported F_L, therefore, might correspond to a lower value of Δp than 30 mbar. The resulting F_L is shown in Figure 3.14 for the different materials in dependence of differential pressure, Δp, and cathode potential.

Table 3.1: Comparison of liquid breakthrough flow rates with literature.

Data set	De Mot et al.[31]	This work
Electrode parameters		
CL composition	70 wt% Sn, 30 wt% Nafion	80 wt% Ag, 20 wt% Nafion
CL loading	0.75 mg Sn cm^{-2}	1 mg Ag cm^{-2}
GDL substrate	SGL 39BC	SGL 39BC
Electrode area	16 cm^2	3.8 cm^2
Process parameters		
Current density	$-100\,mA\,cm^{-2}$	$-100\,mA\,cm^{-2}$
Δp	30 mbar	30 mbar
Δp measurement technique	between inlets	between compartments
Resulting liquid breakthrough flow rate		
F_L	$0.1\,mL\,min^{-1}\,cm^{-2}$	$0.9 \pm 0.12\,mL\,min^{-1}\,cm^{-2}$
F_L measurement technique	weighing	inline gas–liquid sensor

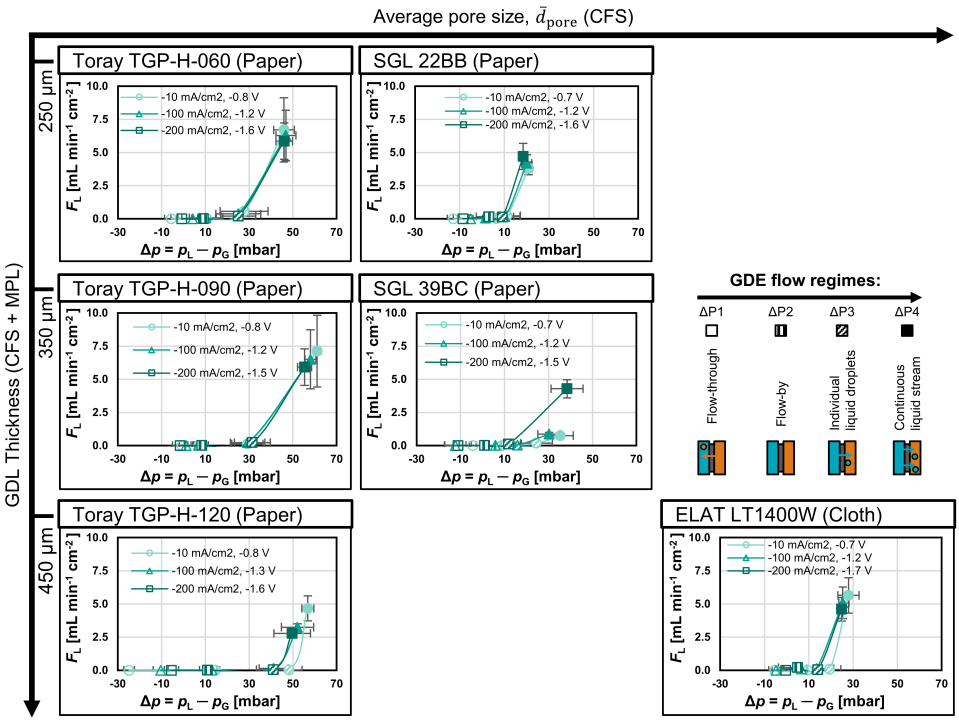

Figure 3.14: Liquid breakthrough flow rates F_L as a function of differential pressure Δp. The series of markers corresponds to the current densities -10, -100, and $-200\,\mathrm{mA\,cm^{-2}}$. The y-axis error bars represent the estimated error of the calibration curve (Figure 3.13). The x-axis error bars represent the sample standard deviation of the recorded differential pressure. The transition from individual liquid droplets to a continuous liquid breaking through occurred around $1\,\mathrm{mL\,min^{-1}\,cm^{-2}}$.

CATHODE POTENTIAL DEPENDS ON DIFFERENTIAL PRESSURE AND CURRENT DENSITY

The cathode potentials, E_{Cathode}, recorded during the CO_2 electrolysis experiments with varying current density and differential pressure are shown in Figure 3.15.

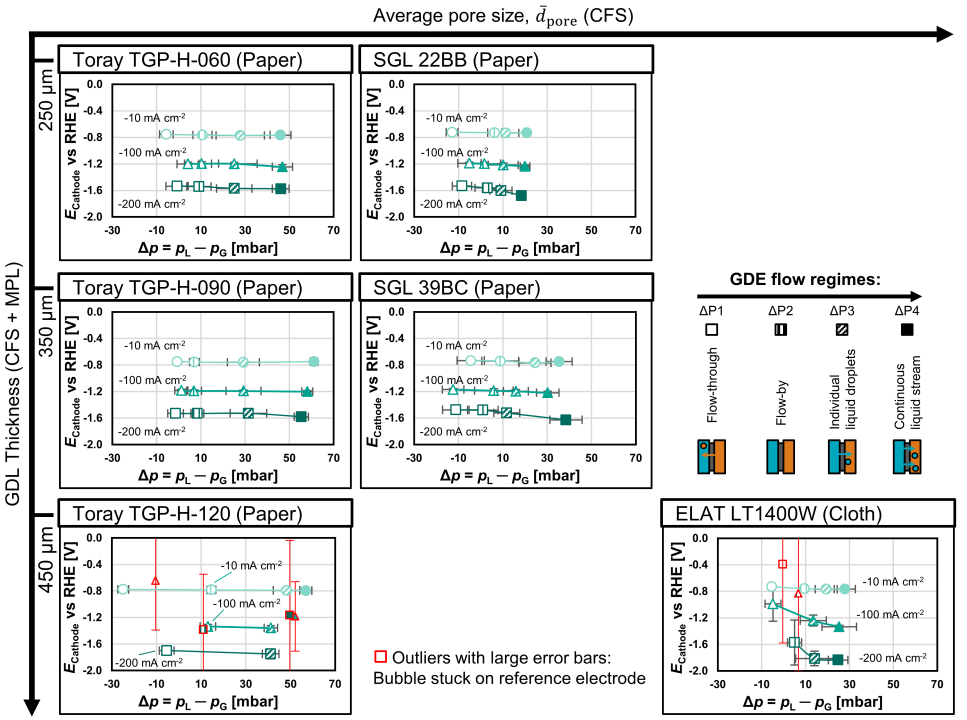

Figure 3.15: Cathode potential, E_{Cathode}, as a function of differential pressure, Δp. The data series correspond to the current densities -10 (○), -100 (△), and $-200\,\text{mA}\,\text{cm}^{-2}$ (□) from lighter to darker color. The marker filling indicates the GDE flow regime. The y-axis error bars represent the sample standard deviation of the recorded potential. Some measurements of TGP-H-120 and LT1400W suffered from high fluctuations in the cathode potential due to gas bubbles blocking the reference electrode. The marker outline of these outliers is marked in red. The x-axis error bars represent the sample standard deviation of the recorded Δp.

With increasing current density, E_{Cathode} increases due to the electrochemical overpotential of the CO_2R and the HER taking place. For most materials, E_{Cathode}, does not depend strongly on Δp. For the ELAT LT1400W carbon cloth, however, the potential becomes more negative with increasing Δp. At a current density of $-200\,\text{mA}\,\text{cm}^{-2}$, for example, E_{Cathode} drops from -1.57 V vs. RHE at +5 mbar to -1.83 V vs. RHE at +25 mbar. We think this phenomenon can be explained by the flexibility of the cloth, which makes it deform at higher liquid overpressures. This mechanical deformation then increases the distance between the reference electrode and the cathode, which leads to an uncompensated ohmic resistance. The other materials are less flexible because the binder in the carbon paper makes them rigid. We discuss this effect in more detail in the next section (Figure 3.18).

STABILITY DURING CO_2 ELECTROLYSIS WITH VARYING DIFFERENTIAL PRESSURES

The electrochemical performance of GDEs can decrease over time due to mechanisms like catalyst leaching or deactivation, salt formation, and/or loss of GDE hydrophobicity. We tested the stability of our GDE materials to ensure their performance was sufficiently stable during the 4.5 h of our main CO_2 electrolysis run. In a previous publication, we showed that the GDE based on SGL 39BC did not show any significant loss in the Faradaic efficiency for CO, FE_{CO}, over a run time of 2 h at a current density of $-190\,mA\,cm^{-2}$.[32] In this publication, we present additional results for GDEs based on TGP-H-060 and TGP-H-120. We tested the stability of these GDEs by repeating the experiments with the parameter set of $\Delta P1$ and $-100\,mA\,cm^{-2}$ after completing the main CO_2 electrolysis run (Figure 3.16).

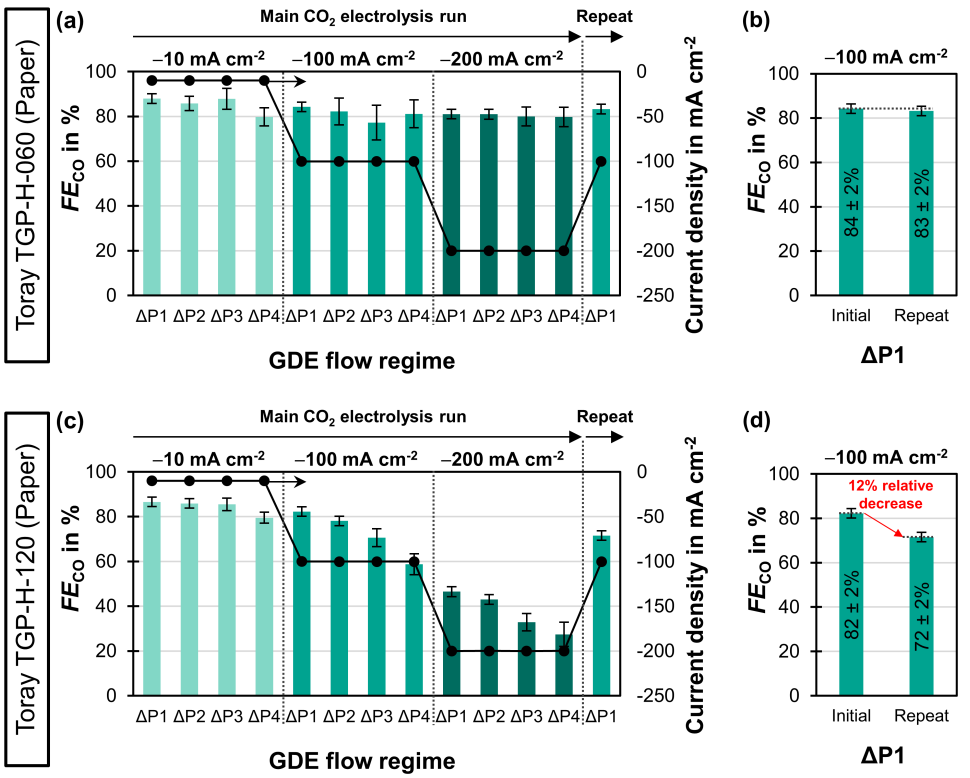

Figure 3.16: Stability test with TGP-H-060 and TGP-H-120 carbon papers. After the main CO_2 electrolysis run (duration of 4.5 h), we repeated the parameter set of $\Delta P1$ and $-100\,mA\,cm^{-2}$ (duration of 7 min). TGP-H-060: **(a)** Faradaic efficiency, FE_{CO}, for all parameter sets (combination of current density and GDE flow regime Δp) of the main CO2 electrolysis run and the repeated experiment. **(b)** Comparison of FE_{CO} at $\Delta P1$ and $-100\,mA\,cm^{-2}$ between main run (initial) and repeat experiment. TGP-H-120: **(c)** FE_{CO} for all parameter sets of the main CO_2 electrolysis run and the repeat experiment. **(d)** Comparison between main run (initial) and repeat experiment.

For TGP-H-060, the comparison of the initial FE_{CO} recorded at $\Delta P1$ and $-100\,mA\,cm^{-2}$ shows no significant reduction in CO_2 reduction performance (Figure 3.16 b). In contrast, TGP-H-120 showed a slight performance loss during the 4.5 h electrolysis run. This can be seen in the drop of FE_{CO} from 82% for the initial experiment to 72% for the repeat experiment (Figure 3.16 d), which corresponds to a relative decrease of 12%. These results implies that the effect of the GDE flow regime is partially convoluted with this loss in performance, especially at the highest current density.

A possible explanation for the deactivation of the GDE could be the leaching of Ag from the catalyst layer into the electrolyte. Another explanation could be the contamination of the cathode GDE with other metals, which catalyze the HER reaction, such as Fe or Ni. [69] We used ICP-OES to measure the concentrations of metal ions in the electrolyte after the electrolysis procedure to test these hypotheses (Table 3.2).

Table 3.2: Leaching and contamination study: Metal concentrations in 1 M $KHCO_3$ electrolyte determined with ICP-OES. Detection limit: 0.01 mg L^{-1}.

Experiment	Run time	Ag	Fe	Ni
Blank	0 h	$< 0.01\,mg\,L^{-1}$	$0.02\,mg\,L^{-1}$	$< 0.01\,mg\,L^{-1}$
TGP-H-060	4.5 h + 0.5 h	$< 0.01\,mg\,L^{-1}$	$0.08\,mg\,L^{-1}$	$0.09\,mg\,L^{-1}$
TGP-H-120	4.5 h + 0.5 h	$< 0.01\,mg\,L^{-1}$	$0.14\,mg\,L^{-1}$	$0.11\,mg\,L^{-1}$

The leaching of Ag probably does not significantly contribute to the performance decrease of the GDE. Our data shows that Ag concentration in the electrolyte remained below the detection limit (Table 3.2). This means that in the worst case, there might be up to 0.01 mg Ag L^{-1} in the 60 mL of electrolyte. We can estimate that this would correspond up to 0.016% of the Ag on the GDE being leached, which has an area of 3.8 cm^2 and a loading of 1 mg cm^{-2}. The leaching of Ag seems an unlikely explanation for the deactivation, however, because we would expect the leaching rates and the resulting deactivation to be similar for the two GDE samples. This is evidently not the case because TGP-H-120 exhibited a stronger performance decrease than TGP-H-060 (Figure 3.16 d).

The contamination with Fe or Ni, similarly, also seems an unlikely explanation for the degradation because it can not explain the difference between the two samples. We measured a slight increase in the Fe and Ni concentrations compared to the blank sample (Table 3.2). These contaminants likely originate from the contact of the electrolyte with the tubes, fittings, and valves made from stainless steel (Grade 316). We did not detect any Fe or Ni on the surface of the TGP-H-060 sample with XPS (results not shown).

Another possible explanation for the loss of CO_2 reduction performance of TGP-H-120 could be the (electro-) chemical degradation of the CFS, which is associated with HER and can lead to a loss of hydrophobicity (lower contact angle). [51] This phenomenon could have led to additional flooding of the GDE and a decrease in CO_2 diffusivity. However, we did not measure any significant change of the contact angle due to the CO_2 electrolysis run to support this hypothesis (Table 3.3).

Table 3.3: Comparison of the CFS static contact angle, θ_{CFS}, ± the standard error before electrolysis and after CO_2 electrolysis run. The data was originally published in our previous publication. [32]

Experiment	θ_{CFS} before	θ_{CFS} after
TGP-H-060	147 ± 1.0	148 ± 0.6
TGP-H-120	148 ± 0.4	149 ± 0.4

The performance loss of TGP-H-120 (Figure 3.16) might be due to a change inside of the pore network. The residual liquid saturation might have increased over the course of the experiment due to salt formation or loss of hydrophobicity inside of the pores. Precipitated salt could have also blocked pores. These phenomena might have decreased the CO_2 diffusion for the repeat experiment. This kind of deactivation mechanism could be investigated with X-ray tomographic microscopy [27,55] in future studies.

3.5.7. CO_2 ELECTROLYSIS PERFORMANCE TEST WITH CARBON CLOTH

We conducted a performance test of the carbon cloth GDE for 120 h with a Δp of up to 120 mbar. This test should be able to estimate the local performance at the bottom of a CO_2 electrolyzer, which is subject to a hydrostatic pressure difference between catholyte and gas phase. At this high liquid overpressure, electrolyte breaks through the GDE continuously. We used the sample GDE sample based on the ELAT LT1400W carbon cloth that we previously tested in our CO_2 electrolysis run with varying Δp and current density (Section 3.5.6). We used a check valve with a cracking pressure of 69 mbar at the outlet of the gas compartment. The complete data set is available in the sheet "ELAT flow through run" in the accompanying Excel file.

FARADAIC EFFICIENCY AND CATHODE POTENTIAL DEPENDS ON DIFFERENTIAL PRESSURE

To determine the average FE_{CO} over the height of a reactor with mixed flow regime (Figure 3.17 a), we varied Δp from −6 mbar to 109 mbar while the potentiostat was set to a galvanostatic current density step of $-200\,mA\,cm^{-2}$. The FE_{CO} ranged from 80% to 60% over the different flow regimes (flow-by to continuous liquid breakthrough). The data points in the flow-by regime (Δp = −6 mbar) correspond to the top of a hypothetical reactor; the data points with continuous liquid flow-through (Δp = 109 mbar) correspond to the bottom of a hypothetical reactor. We determined the weighted average FE_{CO} of 69% by integrating the FE_{CO} over the corresponding range of Δp. The calculations are included in the sheet "Average FE_CO cloth" of the Excel file.

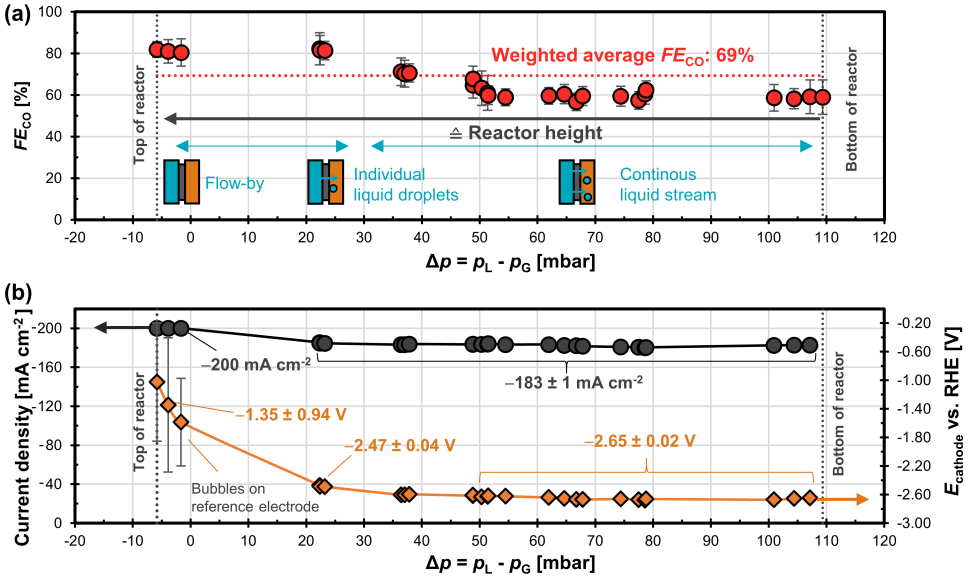

Figure 3.17: **(a)** Larger version of Figure 3.7 a: Faradaic efficiency for CO, FE_{CO}, as a function of differential pressure, Δp. The cell potential was constant at 10 V (Potentiostat limit). The average FE_{CO} was determined by integrating FE_{CO} numerically over the Δp range. The blue arrows below the FE_{CO} data points indicate the GDE flow regime. **(b)** Current density (left axis) and cathode potential, $E_{cathode}$, as a function of Δp. The large error bars of the first three data points were caused by bubble formation between the cathode surface and the reference electrode.

While we were able to reach the current density set point of $-200\,mA\,cm^{-2}$ in the flow-by regime, the potentiostat only achieved $-183\,mA\,cm^{-2}$ at higher Δp (Figure 3.17). The current density was limited because the cathode potential increased significantly beyond $\Delta p \geq 22$ mbar, which let the potentiostat reach the cell potential limit of 10 V. It is important to understand the source of this increased cathode overpotential to improve the energy efficiency of the process.

The decreasing $E_{cathode}$ (Figure 3.17 b) might impact FE_{CO} in addition to the effects of Δp. According to a kinetic study of an Ag electrocatalyst in $KHCO_3$ by Jaramillo *et al.*,[70] higher cathode overpotentials can favor the kinetics of HER. Therefore, it is possible that the decreasing $E_{cathode}$ changes the relative kinetics of the CO_2R and HER. These kinetic effects are convoluted with mass transfer limitation effects at high current density making it difficult to assess their relative importance. The data in Figure 3.17 suggest that there is no significant correlation between $E_{cathode}$ and FE_{CO} for the investigated GDE. For example, FE_{CO} remains constant while $E_{cathode}$ drops from -1.35 V to -2.47 V ($\Delta p = -5$ mbar vs. $\Delta p = 23$ mbar). Further, the drop in FE_{CO} from 71% to 61% occurs without a change in $E_{cathode}$ ($\Delta p = 36$ mbar vs. $\Delta p = 51$ mbar). Therefore, we can assume that FE_{CO} depends predominantly on the CO_2 mass transfer, which is a function of Δp and the saturation behavior of the GDE's pore network.

The decrease in cathode potential is caused by the deformation of the flexible carbon cloth through liquid overpressure. The cathode potential was measured with an Ag/AgCl micro-reference electrode, which was placed with a gap of 0.5 mm from the GDE surface (Figure 3.18 a). The cathode potential was compensated for the ohmic resistance arising in this small gap. We observed that the carbon cloth bulged at higher Δp due to the mechanical pressure from the liquid side (Figure 3.18 b). The bulging increased the gap between the cathode and the reference electrode, which introduced an uncompensated potential drop (Figure 3.18 c). The effect of this increased gap on the apparent cathode potential is substantial because of the low electrolyte conductivity of $\kappa = 0.077\,S\,cm^{-1}$ (Figure 3.18 d).[71] For example, the gap of 4 mm would increase the apparent cathode potential by 0.95 V at $-183\,mA\,cm^{-2}$. Therefore, the mechanical deformation can explain the more negative cathode potential observed at higher values for Δp in Figure 3.15 and Figure 3.17. While the bulging of the cloth GDE introduces a systematic error into measured cathode potential of our lab experiments, this phenomenon does not inherently limit the energy efficiency of this material for application. The flexible cloth can be supported mechanically with a rigid mesh and/or a gas flow field, which also serves as a current collector.

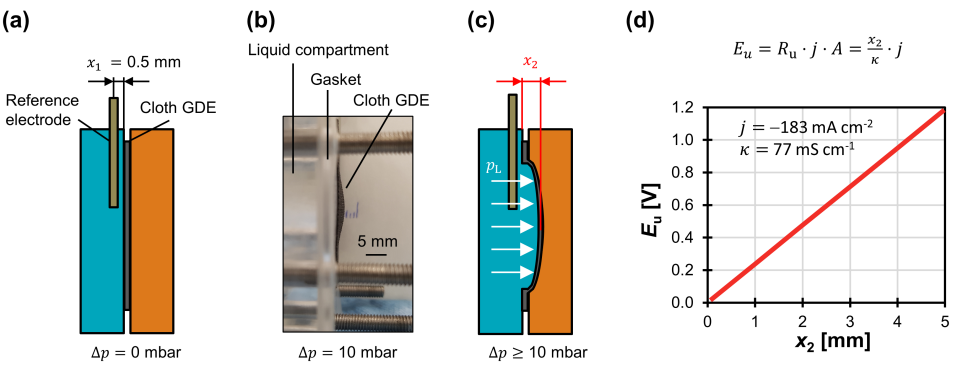

Figure 3.18: Cloth deformation increases apparent cathode overpotential. **(a)** At $\Delta p = 0$ mbar, the ohmic resistance arising in the 0.5 mm gap between cathode GDE and the micro-reference electrode is compensated. **(b)** Disassembled cell after imposing a liquid overpressure of $\Delta p = 10$ mbar: The cloth bulged by about 2 mm. **(c)** Liquid overpressures introduce an unknown additional gap, x_2, between the reference electrode and the cathode. **(d)** Uncompensated potential, E_u, as a function of the additional gap width, x_2. The 1 M $KHCO_3$ had ionic conductivity, conductivity of $\kappa = 0.077\,S\,cm^{-1}$.[71]

PERFORMANCE TEST WITH CONTINUOUS LIQUID BREAKTHROUGH

To carry out the more stringent CO_2 performance test (Figure 3.7 b), the potentiostat was set to a galvanostatic current density step of $-200\,mA\,cm^{-2}$ continuously for 125 h. We were, however, only able to reach a current density of $-180\,mA\,cm^{-2}$ to $-193\,mA\,cm^{-2}$ because of the cell potential limit of 10 V (Figure 3.19). The Δp ranged from 80 to 100 mbar, which is discussed further below (Figure 3.21).

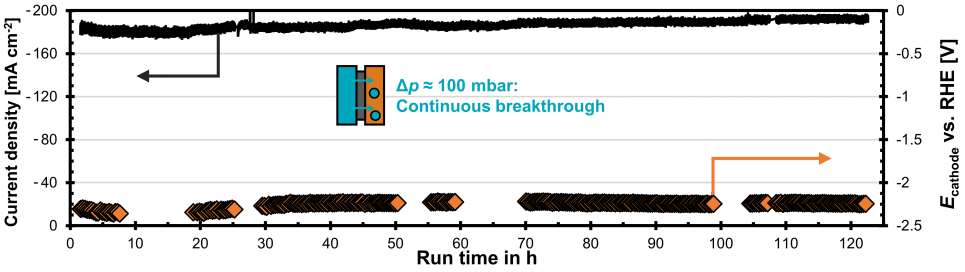

Figure 3.19: CO_2R performance test of ELAT LT1400W carbon cloth GDE exhibiting continuous catholyte breakthrough: Δp ranged from 80 to 120 mbar: Current density (left axis) and cathode potential, $E_{cathode}$, over the run time.

The FE_{CO} remained stable at $60 \pm 4.5\%$ for 10 h (Figure 3.20 a). We had to depressurize and restart the electrolysis system three times because of technical issues (Labview program crashed, had to switch to new CO_2 tank). These restarts had a negative effect on FE_{CO}. It is unclear to us why it took the FE_{CO} several hours to re-stabilize to a steady state value because it only took several minutes to re-pressurize the electrolyzer after a restart. We highlighted the data points for which the system was still re-stabilizing.

The system was operating at an average FE_{CO} of $55 \pm 6.8\%$ at the end of the performance test (Figure 3.20 a). We hypothesize that this reduction in performance was not due to a change in the GDE, but due to the reduction of the purge flow rate during the run (Figure 3.20 c), which lead to an increased crossover of gaseous products within the system. The errors in Faradaic efficiency increase after 20 h run time because the reduction of the purge flow rate lead to a stronger fluctuation of the product gas flow rate measured at the mass flow meter.

We can support this crossover hypothesis by comparing the Faradaic efficiency for the cathode reactions (CO_2R and H_2; Figure 3.20 b) with the anode side reactions (OER; Figure 3.20 c). For the first 20 h of the electrolysis run, the CO_2 purge flow rate was 80 mLn min^{-1} (Figure 3.20 c). During this time the combined Faradaic efficiency on the cathode side, FE_{CO+H_2}, add up to an average of $83 \pm 6.5\%$ (Figure 3.20 b). The Faradic efficiency on the anode side, FE_{O_2}, has an average value of $95\% \pm 4.6\%$. The FE probably does not reach 100% because a part of the product gases (O_2, CO, H_2) remains dissolved in the electrolyte and is then feed to the "wrong" electrode by the pump. This way, for example, a part of the O_2 produced at the anode could remain dissolved in the electrolyte and be feed to the cathode, where the oxygen reduction reaction (ORR) can take place ($O_2 + 4e^- \longrightarrow 4OH^-$).[37] Because this reaction would consume part of the current at the cathode, the FE_{CO+H_2} would be lower than 100%.

After the 25 h we reduced the CO_2 purge flow rate to 10 mLn min^{-1} to reduce the CO_2 consumption from the supply tank (Figure 3.20 c). This reduced purge flow increased the crossover of gaseous products in the system because dissolved product gases were being removed from the electrolyte bottle less effectively. As a consequence, the deficits in FE increased for both electrodes. On the cathode side, FE_{CO+H_2} dropped from an average of $83 \pm 6.5\%$ to $78 \pm 8.9\%$ (Figure 3.20 b). On the anode side, FE_{O_2} dropped from $95 \pm 6.5\%$ to $87 \pm 6.3\%$ (Figure 3.20 b). We argue, therefore, this product gas crossover is a primary reason for the reduction in FE_{CO} from 60% to 55% over the course of the experiment (Figure 3.20 a). No other gaseous products were detected with the gas chromatography system (CH_4, C_2H_4, or C_2H_6).

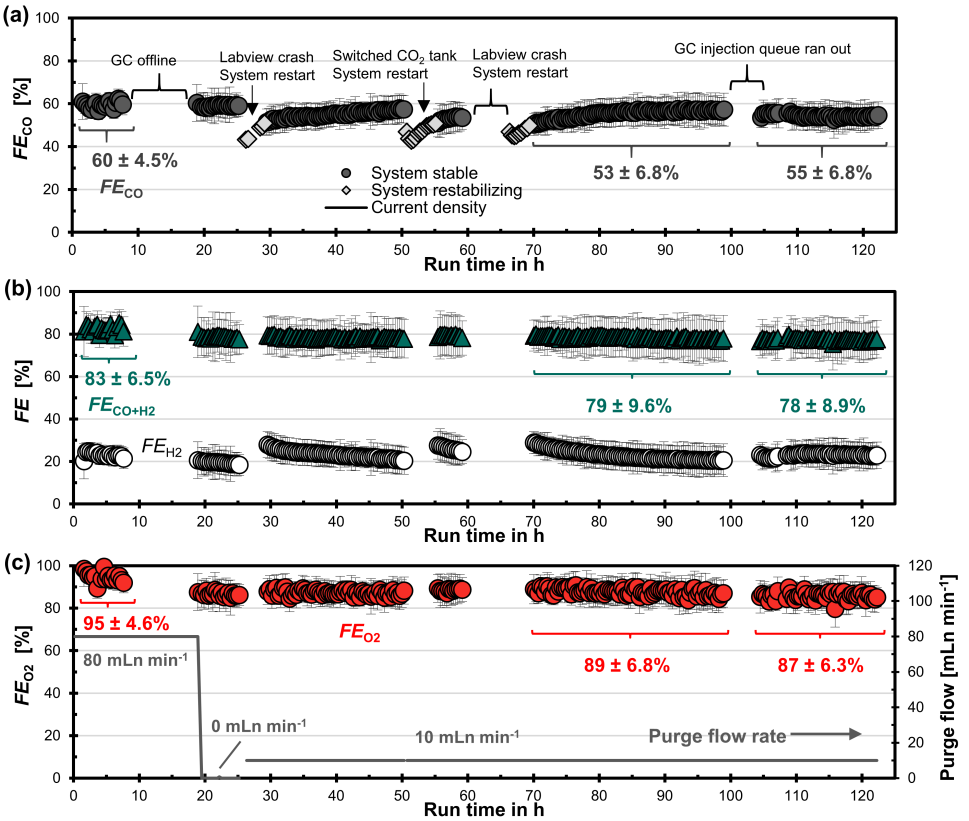

Figure 3.20: **(a)** Faradaic efficiency for CO, FE_{CO}, (left y-axis) and current density (right y-axis) over the run time. No GC data is available for the periods when the GC was idle or when we had to restart the system. The electrolysis system required several hours to re-stabilize the FE_{CO} values after each restart. These non-representative data points are highlighted with grey diamond markers (◇). **(b)** Combined Faradaic efficiency for CO and H_2, FE_{CO+H_2}, and FE_{H_2}, over the run time. **(c)** Faradic efficiency for O_2, FE_{O_2}, and CO_2 purge flow rate over run time.

We analyzed a sample of the electrolyte after the run with HPLC to determine any liquid products. The average Faradaic efficiency for formic acid was 0.3%. We detected trace amounts of acetic acid. No ethanol was detected. It is not clear to us why the FE deficit is not the same for both electrodes. The electrolyte pH after the experiment was 7.55, which is slightly higher than the initial pH of 7.41 (20 °C).

For the first 10 h of the experiment, we kept the setpoint of the liquid backpressure, $p_{L,back}$, constant at 750 mbar (Figure 3.21 a). The gas feed pressure, p_G, fell steadily during this time. This resulted in a drift in the differential pressure across the GDE, Δp, from 50 mbar to 80 mbar. We adjusted $p_{L,back}$ for the last 100 h of the experiment to stabilize the drifting Δp at 100 mbar (Figure 3.21 b). The falling p_G seems to have little effect on the FE_{CO} (Figure 3.20 a).

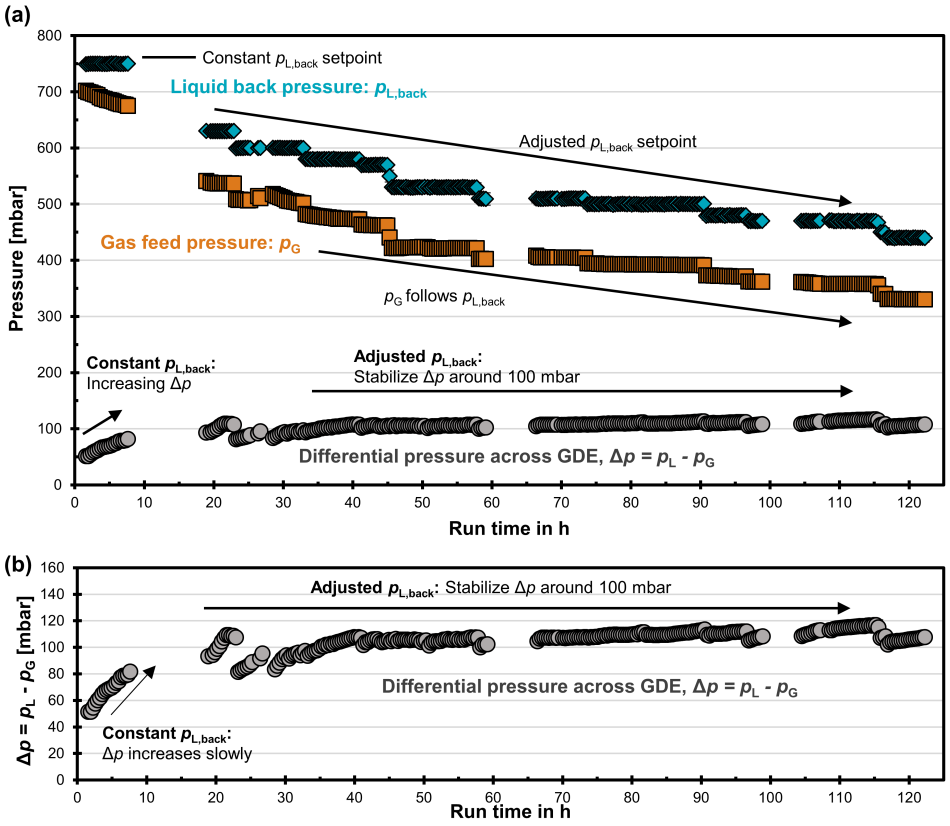

Figure 3.21: **(a)** Liquid backpressure, $p_{L,back}$, at the control valve, gas feed pressure, p_G, and differential pressure across GDE, Δp, over the run time. **(b)** Detail view of Δp over the run time.

The drifting Δp (Figure 3.21) could be explained by a reduction in the liquid permeability over the course of the experiment. This might be due to carbonate salt formation or mechanical deformation of the GDE, which blocks some pores. A reduction in liquid permeability would have reduced the liquid breakthrough flow rate at a constant $p_{L,back}$, which then would have also reduced p_G. We can expect the p_G to fall in this situation because a lower combined liquid and gas flow rate (Figure 3.12) has to be forced through the check valve at the outlet of the gas compartment, which results in a lower pressure drop. Unfortunately, the exact liquid breakthrough flow rate is unknown because it exceeded the range of our gas–liquid phase sensor (Figure 3.13).

POST-ELECTROLYSIS CHARACTERIZATION

After electrolysis, we rinsed the GDE with IPA and dried it to perform additional characterization. The SEI and BEC images (x100) show the presence of large salt crystals, which have a diameter of 10 – 50 µm (Table 3.4). They appear in medium grey scale in the BEC images because they have a higher density than the carbon background and a lower density than the Ag particles of the CL (small white dots). These crystals are carbonate salts which precipitate due to the alkaline environment at the cathode.[72,73] They are even more clearly visible at higher magnifications (Table 3.5).

Table 3.4: Salt formation on ELAT LT1400W GDE: Scanning electron microscope images of the catalyst layer after the 125 h performance test at different magnifications (x100 – x500). **Left**: Secondary electron imaging (SEI) for morphology, **Right**: Back scattered electron composition (BEC) detector for elemental contrast imaging. Dark grey domains in the BEC images indicate the carbon-rich MPL and carbon fibers. Medium grey domains indicate carbonate salt crystals. Light grey domains indicate dispersed Ag nanoparticles in a Nafion matrix.

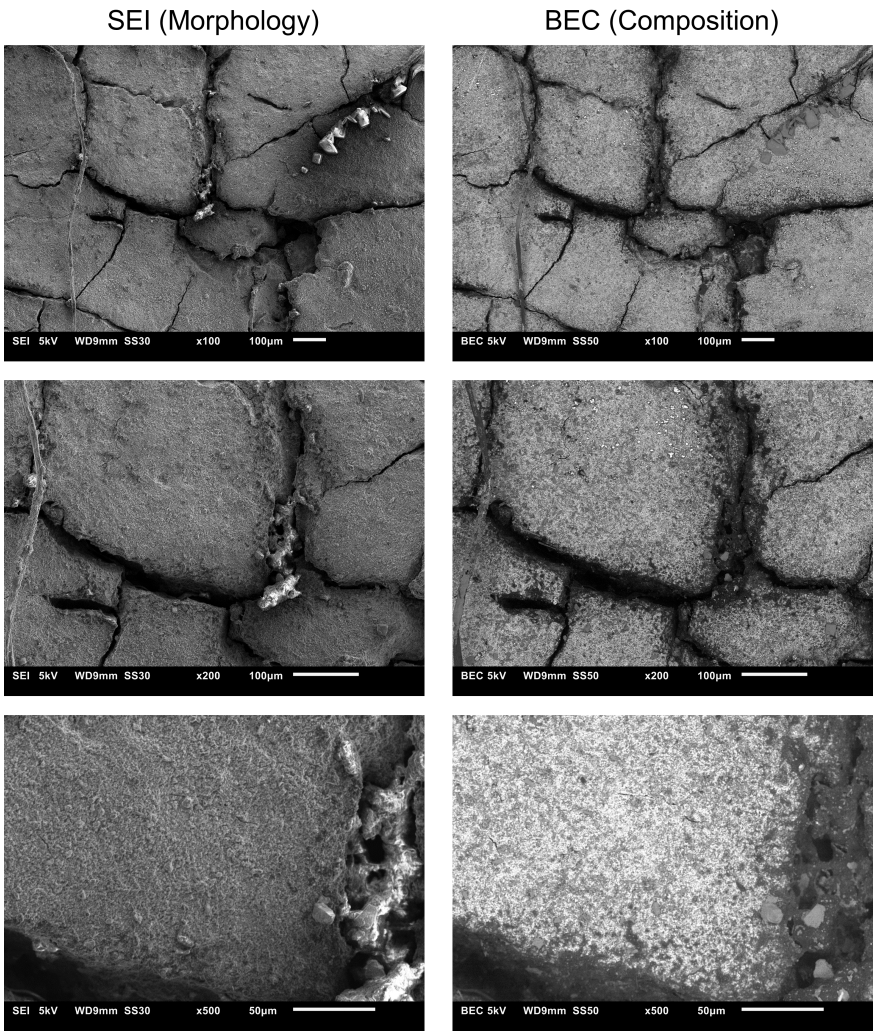

We can assume that the carbonate formation on the CL (Table 3.5) has a detrimental effect on the CO_2R performance because it reduces the active area of the CL. It is unclear, however, if the salt formation leads to a slow decrease in FE_{CO} over time or if its effect stabilizes after an equilibration period. During such a period, the salt formation could have reached an equilibrium state, in which the rate of nucleation and growth of crystals equals the rate of dissolution and/or detachment.

Table 3.5: Salt formation on ELAT LT1400W GDE: Scanning electron microscope images of the catalyst layer after the 125 h performance test at different magnifications (x1000 – x5000). **Left**: Secondary electron imaging (SEI) for morphology, **Right**: Back scattered electron composition (BEC) detector for elemental contrast imaging. Dark grey domains in the BEC images indicate the carbon-rich MPL and carbon fibers. Medium grey domains indicate carbonate salt crystals. Light grey domains indicate dispersed Ag nanoparticles in a Nafion matrix.

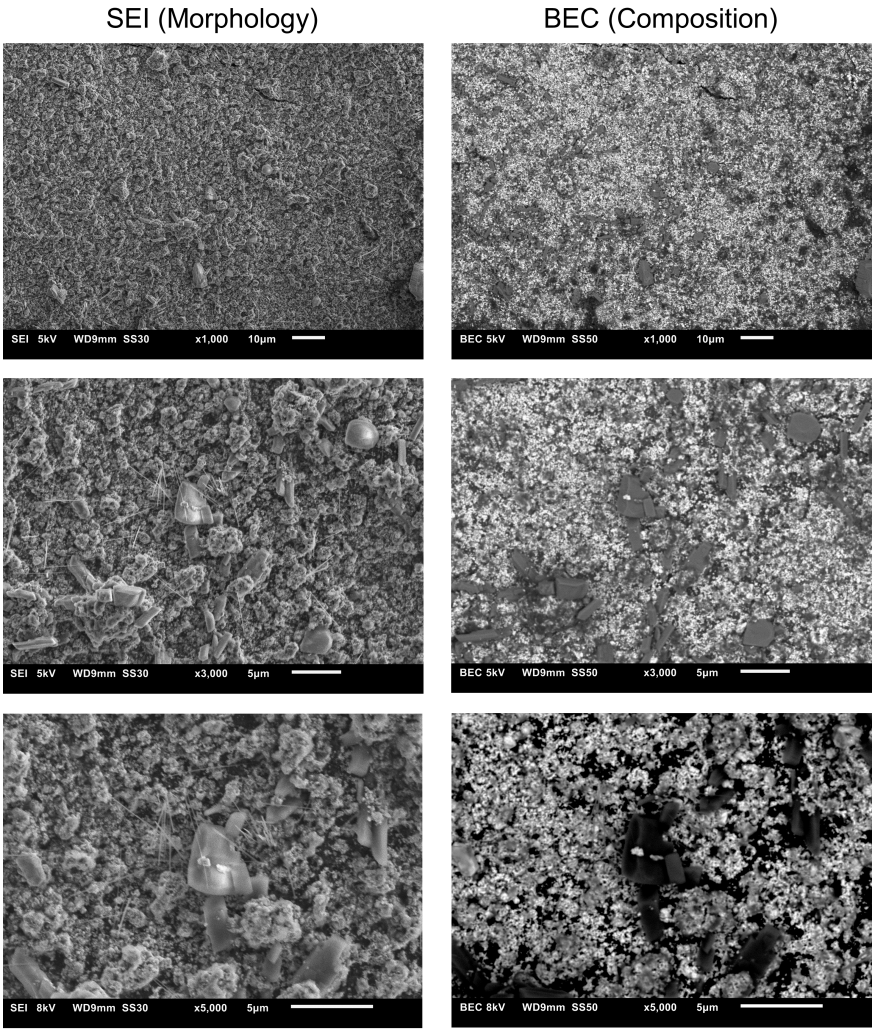

We also observed precipitates in the shape of scales on fibers of the CFS (Table 3.6), which have a higher density than the carbon fibers according to the BEC images. These precipitates are probably also carbonate salts.

Table 3.6: Salt formation on ELAT LT1400W GDE: Scanning electron microscope images of the carbon fiber substrate after the 125 h performance test at different magnifications (x100 – x500). **Left**: Secondary electron imaging (SEI) for morphology, **Right**: Back scattered electron composition (BEC) detector for elemental contrast imaging.

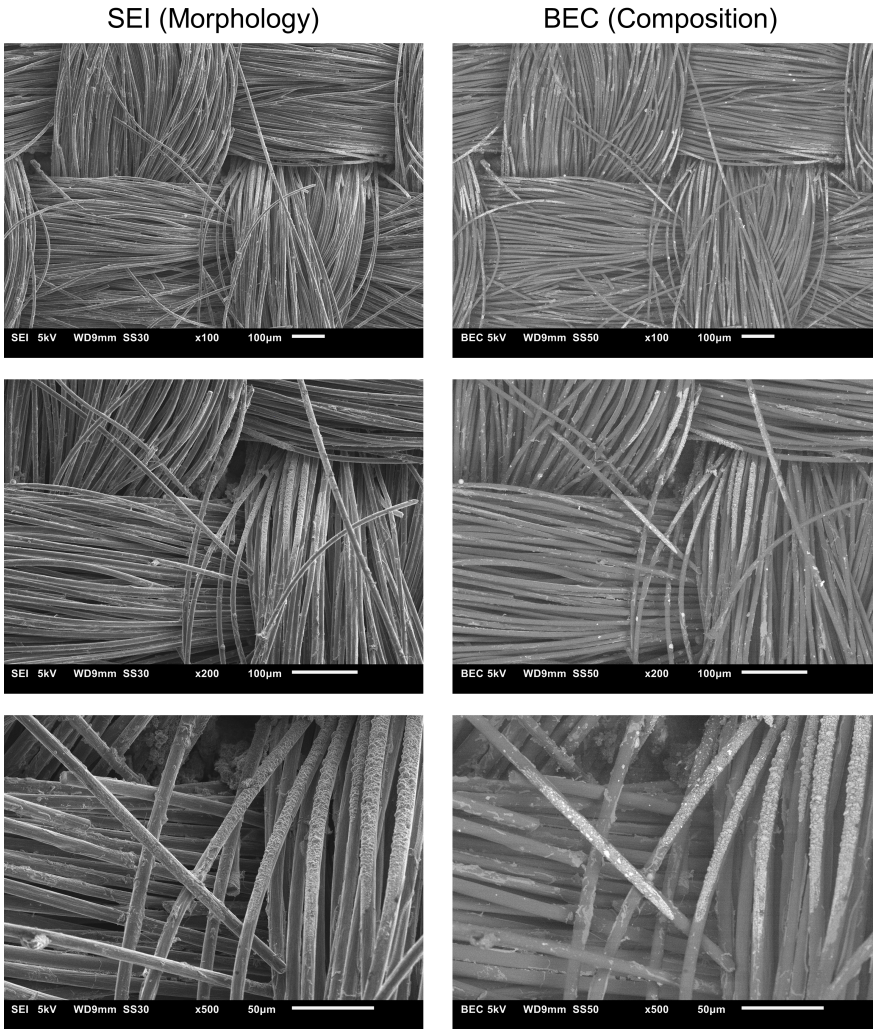

We measured the static contact angle to assess how much the salt formation affected the wettability. While θ_{CFS} did not change significantly after 4.5 h of CO_2 electrolysis , it decreased slightly from 147° (fresh CFS) to 140° after 125 h (Table 3.7). This reduction could be caused by the hygroscopic properties of the salts formed on the carbon fibers. The θ_{CL} seems to have fallen from 138° to 78° degrees after the 4.5 h experiment, but then increased again to 102° after the 125 h experiment. The later increase in observed contact angle could be explained by an increase in CL roughness due salt formation and/or mechanical deformation, which can lead to an enhancement of the observed contact angle according to the Cassie-Baxter model. [45]

Table 3.7: ELAT LT1400W after 125 h performance test: Static contact angles θ_i ± standard error of different layers i.

Layer	Fresh GDE [32]	After 4.5 h(Figure 3.9) [32]	After 125 (Figure 3.20)
θ_{CFS}	$147 \pm 0.8°$	$150 \pm 1.8°$	$140 \pm 0.9°$
θ_{MPL}	$150 \pm 1.4°$	-	-
θ_{CL}	$138 \pm 1.7°$	$78 \pm 4.1°$	$102 \pm 3.8°$

The carbonate formation on the CFS (Table 3.6) could also decrease the FE_{CO} over time (Figure 3.20) because a lower θ_{CFS} could lead to a decrease in effective diffusivity of CO_2. It is, however, possible that the internal pore surfaces remain unaffected because the precipitation seems to be mostly present on the external surface.

It is difficult to quantify any mechanical deformation because defects were already present in the fresh MPL (Table 3.8). For this reason, it is unclear if the cracks present after 125 h of liquid flow-through were already present before or were created through the mechanical pressure of the liquid.

Table 3.8: Scanning electron microscope images of ELAT LT1400W defects: Comparison of MPL cracks in fresh MPL and CL after 125 h of liquid flow-through.

Fresh MPL (uncoated)	CL after 125 h
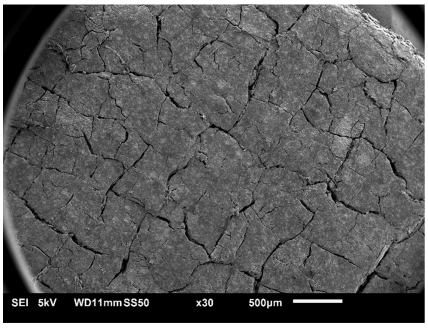	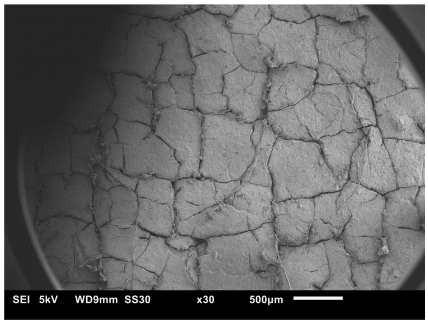

The Ag nanoparticles in the catalyst layer were highly stable during the 125 h performance test because they do not seem to have changed in size (Table 3.9). This finding indicates that the Nafion matrix of the CL can effectively prevent aging and/or agglomeration during sustained electrolysis conditions. We complemented the SEM characterization with X-ray diffraction (XRD) measurements. The XRD characterization shows no significant increase in the crystallite size obtained for the peak corresponding to the (111) crystal plane, $L_{(111)}$, estimated with the Scherrer evaluation (Figure 3.22). This supports the claim that the Ag nanoparticles were highly stable during our experiment.

Table 3.9: BEC images of Ag nanoparticles in Nafion matrix of the catalyst layer (CL): **Left**: Ag nanoparticles in fragments of fresh CL.[32] **Right**: Ag nanoparticles on front face of CL after 125 h performance test.

Ag nanoparticles in fresh CL	Ag nanoparticles in CL after 125 h
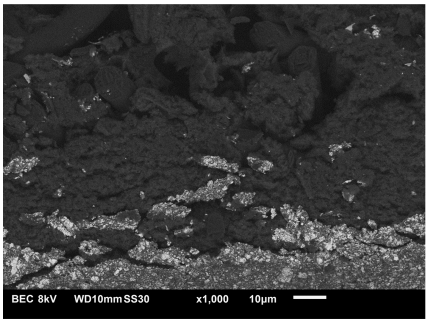	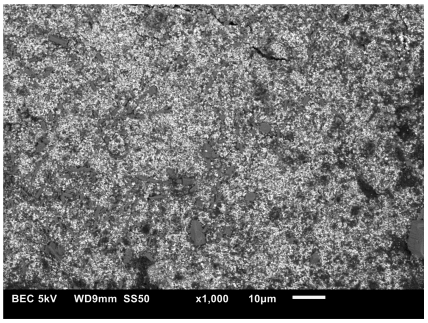
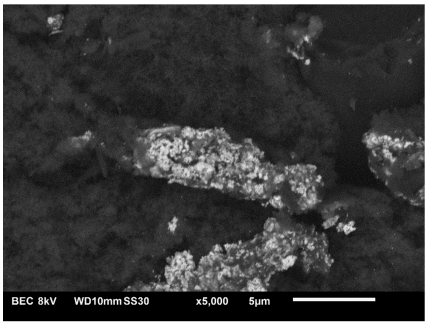	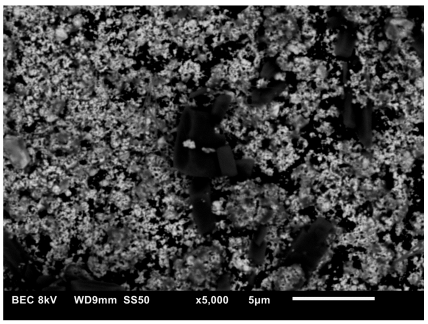

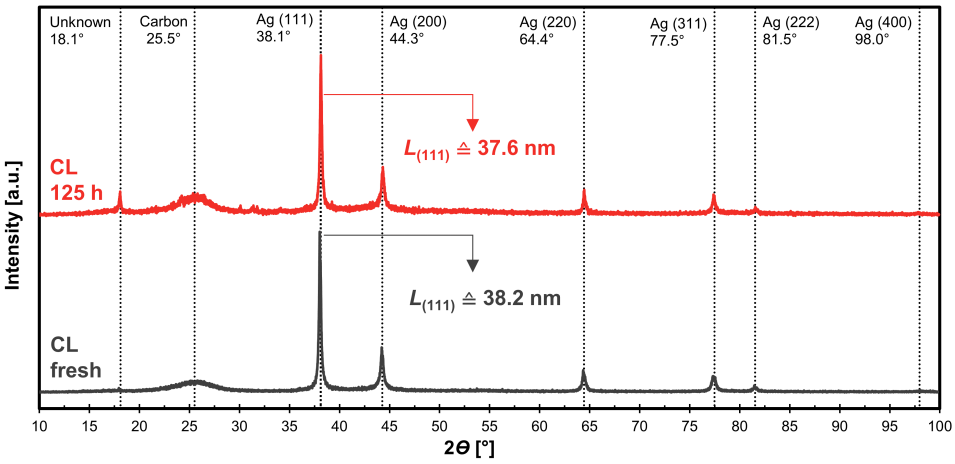

Figure 3.22: X-ray diffractograms for fresh catalyst layer (CL) and for CL after 125 h of electrolysis at $-183\,\mathrm{mA\,cm^{-2}}$ obtained with a Bruker D8 Advance diffractometer. X-ray source (40 kV, 25 mA): Cu tube with characteristic wavelengths of K_{α_1} (100) = 1.5406 Å and K_{α_2} (100) = 1.544 39 Å. Position sensitive detector: Lynxeye. The sample was analyzed in the Bragg-Brentano geometry with a step size of 0.01° and an acquisition time of 0.1 s. The sample was illuminated with a divergence slit setting of 5 mm. The diffractograms were processed with DiffracSuite EVA (5.1) software. We corrected the XRD patterns for the K_{α_2} radiation and carried out a sample height correction. The Powder Diffraction File©(PDF)-2004 database of the International Centre for Diffraction Data powder diffraction file was used for peak assignment. The Scherrer evaluation was used to determine the crystallite size, $L_{(111)}$, corresponding to the (111) plane.

Further, we can assume that there is no significant leaching of Ag into the electrolyte because the concentration of Ag in the electrolyte remained below the detection limit of the ICP-OES analysis (Table 3.10). We detected small concentration of Fe and Ni in the electrolyte. These metals must have leached into the electrolyte from stainless steel parts (Type 316 stainless steel) in the flow path. In theory, these metals could electrodeposit on the cathode and have negative impact on the Faradaic efficiency for CO_2R because they catalyze the HER. [69] For this reason electrolyzers should be designed without any stainless steel parts in the flow path to avoid any contamination.

Table 3.10: Leaching and contamination study: Metal concentrations in 1 M $KHCO_3$ electrolyte determined with ICP-OES. Detection limit: 0.01 mgL^{-1}.

Experiment	Ag	Fe	Ni
0 h (Blank)	< 0.01 mgL^{-1}	0.02 mgL^{-1}	< 0.01 mgL^{-1}
125 h	< 0.01 mgL^{-1}	0.57 mgL^{-1}	0.26 mgL^{-1}

CAPILLARY PRESSURE CALCULATION WITH OWENS-WENDT MODEL

We use (3.5) to estimate a capillary pressure of p_C = 138 mbar necessary to fill the space within the fiber bundles with electrolyte. It is a modified version of the Young-Laplace equation, which takes the internal contact angle and the heterogeneous GDL surface according to the Owens-Wendt model into account. [60] We approximate the properties of the wetting electrolyte with the properties of pure water. We estimate the radius of the water surface, r_{H_2O}, between the individual carbon fibers with 5 µm. The surface tension of water at 20 °C is σ_{H_2O} = 0.073 Nm^{-1}. The dispersive energy component ($\sigma^D_{H_2O}$ = 0.019 Jm^{-2}) and the overall surface energy (γ_{sub} = 0.020 Jm^{-2}) were taken from Table II from Wood *et al.*. [60] Note that the sign of p_C is negative because the surface tension of water exceeds the term for the attractive forces of the surface. This means that the surface is not wetted spontaneously and is hydrophobic.

$$p_C = \frac{4}{r_{H_2O}} \left(\sqrt{\sigma^D_{H_2O} \cdot \gamma_{sub}} - \frac{\sigma_{H_2O}}{2} \right) = -138\,\text{mbar} \tag{3.5}$$

3.6. ACKNOWLEDGEMENTS

We thank Christiaan Schinkel, Stefan ten Hagen, and Duco Bosma for their engineering support. This project has received funding from the European Research Council (ERC) under the European Union's Horizon 2020 research and innovation programme (grant agreement No 852115).

REFERENCES

[1] R. I. Masel, Z. Liu, H. Yang, J. J. Kaczur, D. Carrillo, S. Ren, D. Salvatore, and C. P. Berlinguette, *An industrial perspective on catalysts for low-temperature CO_2 electrolysis,* Nature nanotechnology , 118–128 (2021).

[2] A. Somoza-Tornos, O. J. Guerra, A. M. Crow, W. A. Smith, and B.-M. Hodge, *Process modeling, techno-economic assessment, and life cycle assessment of the electrochemical reduction of CO_2: a review,* iScience **24**, 102813 (2021).

[3] R. Sharifian, R. M. Wagterveld, I. A. Digdaya, C. Xiang, and D. A. Vermaas, *Electrochemical carbon dioxide capture to close the carbon cycle,* Energy & Environmental Science **14**, 781 (2021).

[4] A. Muroyama, A. Patru, and L. Gubler, *CO_2 separation and transport via electrochemical methods,* Journal of the Electrochemical Society (2020).

[5] W. A. Smith, T. Burdyny, D. A. Vermaas, and H. Geerlings, *Pathways to industrial-scale fuel out of thin air from CO_2 electrolysis,* Joule **3**, 1822 (2019).

[6] A. A. Samu, A. Kormányos, E. Kecsenovity, N. Szilágyi, B. Endrődi, and C. Janáky, *Intermittent operation of CO_2 electrolyzers at industrially relevant current densities,* ACS Energy Letters **7**, 1859 (2022).

[7] B. Endrődi, G. Bencsik, F. Darvas, R. Jones, K. Rajeshwar, and C. Janáky, *Continuous-flow electroreduction of carbon dioxide,* Progress in Energy and Combustion Science **62**, 133 (2017).

[8] F. P. G. De Arquer, C.-T. Dinh, A. Ozden, J. Wicks, C. McCallum, A. R. Kirmani, D.-H. Nam, C. Gabardo, A. Seifitokaldani, and X. Wang, *CO_2 electrolysis to multicarbon products at activities greater than 1 A cm^{-1},* Science **367**, 661 (2020).

[9] I. Merino-Garcia, J. Albo, and A. Irabien, *Tailoring gas-phase CO_2 electroreduction selectivity to hydrocarbons at cu nanoparticles,* Nanotechnology **29**, 014001 (2017).

[10] B. De Mot, J. Hereijgers, N. Daems, and T. Breugelmans, *Insight in the behavior of bipolar membrane equipped carbon dioxide electrolyzers at low electrolyte flowrates,* Chemical Engineering Journal , 131170 (2021).

[11] H. Yang, J. J. Kaczur, S. D. Sajjad, and R. I. Masel, *Electrochemical conversion of CO_2 to formic acid utilizing sustainion™ membranes,* Journal of CO_2 Utilization **20**, 208 (2017).

[12] J. Albo, G. Beobide, P. Castaño, and A. Irabien, *Methanol electrosynthesis from CO_2 at Cu_2O/ZnO prompted by pyridine-based aqueous solutions,* Journal of CO_2 Utilization **18**, 164 (2017).

[13] J. Albo and A. Irabien, *Cu_2O-loaded gas diffusion electrodes for the continuous electrochemical reduction of CO_2 to methanol,* Journal of Catalysis **343**, 232 (2016).

[14] J. Albo, M. Perfecto-Irigaray, G. Beobide, and A. Irabien, *Cu/Bi metal-organic framework-based systems for an enhanced electrochemical transformation of CO_2 to alcohols,* Journal of CO_2 Utilization **33**, 157 (2019).

[15] M. Perfecto-Irigaray, J. Albo, G. Beobide, O. Castillo, A. Irabien, and S. Pérez-Yáñez, *Synthesis of heterometallic metal–organic frameworks and their performance as electrocatalyst for CO_2 reduction,* RSC Advances **8**, 21092 (2018).

[16] J. Albo, D. Vallejo, G. Beobide, O. Castillo, P. Castaño, and A. Irabien, *Copper-based metal–organic porous materials for CO_2 electrocatalytic reduction to alcohols,* ChemSusChem **10**, 1100 (2017).

[17] D. Higgins, C. Hahn, C. Xiang, T. F. Jaramillo, and A. Z. Weber, *Gas-diffusion electrodes for carbon dioxide reduction: A new paradigm,* ACS Energy Letters **4**, 317 (2019).

[18] S. Hernandez-Aldave and E. Andreoli, *Fundamentals of gas diffusion electrodes and electrolysers for carbon dioxide utilisation: Challenges and opportunities,* Catalysts **10**, 713 (2020).

[19] R. B. Kutz, Q. Chen, H. Yang, S. D. Sajjad, Z. Liu, and I. R. Masel, *Sustainion imidazolium-functionalized polymers for carbon dioxide electrolysis,* Energy Technology **5**, 929 (2017).

[20] B. Endrődi, E. Kecsenovity, A. Samu, F. Darvas, R. V. Jones, V. Török, A. Danyi, and C. Janáky, *Multilayer electrolyzer stack converts carbon dioxide to gas products at high pressure with high efficiency,* ACS Energy Letters **4**, 1770 (2019).

[21] D. A. Salvatore, D. M. Weekes, J. He, K. E. Dettelbach, Y. C. Li, T. E. Mallouk, and C. P. Berlinguette, *Electrolysis of gaseous CO_2 to CO in a flow cell with a bipolar membrane,* ACS Energy Letters **3**, 149 (2017).

[22] S. Verma, X. Lu, S. Ma, R. I. Masel, and P. J. Kenis, *The effect of electrolyte composition on the electroreduction of CO_2 to CO on Ag based gas diffusion electrodes,* Physical Chemistry Chemical Physics **18**, 7075 (2016).

[23] M. R. Thorson, K. I. Siil, and P. J. Kenis, *Effect of cations on the electrochemical conversion of CO_2 to CO,* Journal of the Electrochemical Society **160**, F69 (2013).

[24] Y. Chen, A. Vise, W. E. Klein, F. C. Cetinbas, D. J. Myers, W. A. Smith, T. G. Deutsch, and K. C. Neyerlin, *A robust, scalable platform for the electrochemical conversion of CO_2 to formate: Identifying pathways to higher energy efficiencies,* ACS Energy Letters **5**, 1825 (2020).

[25] A. El-kharouf, T. J. Mason, D. J. L. Brett, and B. G. Pollet, *Ex-situ characterisation of gas diffusion layers for proton exchange membrane fuel cells,* Journal of Power Sources **218**, 393 (2012).

[26] B. Kim, F. Hillman, M. Ariyoshi, S. Fujikawa, and P. J. Kenis, *Effects of composition of the micro porous layer and the substrate on performance in the electrochemical reduction of CO_2 to CO,* Journal of Power Sources **312**, 192 (2016).

[27] A. Lamibrac, J. Roth, M. Toulec, F. Marone, M. Stampanoni, and F. Büchi, *Characterization of liquid water saturation in gas diffusion layers by X-ray tomographic microscopy,* Journal of The Electrochemical Society **163**, F202 (2016).

[28] S. Park, J.-W. Lee, and B. N. Popov, *A review of gas diffusion layer in PEM fuel cells: Materials and designs,* International Journal of Hydrogen Energy **37**, 5850 (2012).

[29] A. Z. Weber, *Improved modeling and understanding of diffusion-media wettability on polymer-electrolyte-fuel-cell performance,* Journal of Power Sources **195**, 5292 (2010).

[30] P. A. García-Salaberri, G. Hwang, M. Vera, A. Z. Weber, and J. T. Gostick, *Effective diffusivity in partially-saturated carbon-fiber gas diffusion layers: Effect of through-plane saturation distribution,* International Journal of Heat and Mass Transfer **86**, 319 (2015).

[31] B. De Mot, J. Hereijgers, M. Duarte, and T. Breugelmans, *Influence of flow and pressure distribution inside a gas diffusion electrode on the performance of a flow-by CO_2 electrolyzer,* Chemical Engineering Journal **378**, 122224 (2019).

[32] L. M. Baumgartner, C. I. Koopman, A. Forner-Cuenca, and D. A. Vermaas, *Narrow pressure stability window of gas diffusion electrodes limits the scale-up of CO_2 electrolyzers,* ACS Sustainable Chemistry & Engineering **10**, 4683 (2022).

[33] P. Jeanty, C. Scherer, E. Magori, K. Wiesner-Fleischer, O. Hinrichsen, and M. Fleischer, *Upscaling and continuous operation of electrochemical CO_2 to CO conversion in aqueous solutions on silver gas diffusion electrodes,* Journal of CO_2 Utilization **24**, 454 (2018).

[34] M. Li, M. N. Idros, Y. Wu, T. Burdyny, S. Garg, X. S. Zhao, G. Wang, and T. E. Rufford, *The role of electrode wettability in electrochemical reduction of carbon dioxide,* Journal of Materials Chemistry A (2021), 10.1039/D1TA03636J.

[35] M. Duarte, B. De Mot, J. Hereijgers, and T. Breugelmans, *Electrochemical reduction of CO_2: Effect of convective CO_2 supply in gas diffusion electrodes,* ChemElectroChem **6**, 5596 (2019).

[36] X.-L. WANG and S. KODA, *Scale-up and modeling of oxygen diffusion electrodes for chlorine-alkali electrolysis I. analysis of hydrostatic force balance and its effect on electrode performance,* Denki Kagaku Oyobi Kogyo Butsuri Kagaku **65**, 1002 (1997).

[37] I. Moussallem, J. Jörissen, U. Kunz, S. Pinnow, and T. Turek, *Chlor-alkali electrolysis with oxygen depolarized cathodes: history, present status and future prospects,* Journal of Applied Electrochemistry **38**, 1177 (2008).

[38] F. Kubannek, T. Turek, and U. Krewer, *Modeling oxygen gas diffusion electrodes for various technical applications,* Chemie Ingenieur Technik **91**, 720 (2019).

[39] S. Litster and N. Djilali, *Two-phase transport in porous gas diffusion electrodes,* Developments in Heat Transfer **19**, 175 (2005).

[40] N. Parikh, J. Allen, and R. Yassar, *Microstructure of gas diffusion layers for PEM fuel cells,* Fuel Cells **12**, 382 (2012).

[41] A. Forner-Cuenca, E. E. Penn, A. M. Oliveira, and F. R. Brushett, *Exploring the role of electrode microstructure on the performance of non-aqueous redox flow batteries,* Journal of The Electrochemical Society **166**, A2230 (2019).

[42] M. Mortazavi and K. Tajiri, *Liquid water breakthrough pressure through gas diffusion layer of proton exchange membrane fuel cell,* International Journal of Hydrogen Energy **39**, 9409 (2014).

[43] J. Benziger, J. Nehlsen, D. Blackwell, T. Brennan, and J. Itescu, *Water flow in the gas diffusion layer of PEM fuel cells,* Journal of Membrane Science **261**, 98 (2005).

[44] L. Yeo and H.-C. Chang, *Electrowetting,* in *Encyclopedia of Microfluidics and Nanofluidics*, edited by D. Li (Springer US, Boston, MA, 2008) pp. 600–606.

[45] D. Quéré, *Rough ideas on wetting,* Physica A: Statistical Mechanics and its Applications **313**, 32 (2002).

[46] A. Quinn, R. Sedev, and J. Ralston, *Contact angle saturation in electrowetting,* The Journal of Physical Chemistry B **109**, 6268 (2005).

[47] F. Bienen, M. C. Paulisch, T. Mager, J. Osiewacz, M. Nazari, M. Osenberg, B. Ellendorff, T. Turek, U. Nieken, and I. Manke, *Investigating the electrowetting of silver-based gas-diffusion electrodes during oxygen reduction reaction with electrochemical and optical methods,* Electrochemical Science Advances , e2100158 (2022).

[48] E. D. Laird, R. K. Bose, H. Qi, K. K. S. Lau, and C. Y. Li, *Electric field-induced, reversible lotus-to-rose transition in nanohybrid shish kebab paper with hierarchical roughness,* ACS Applied Materials & Interfaces **5**, 12089 (2013).

[49] H. Hoffmann, M. C. Paulisch, M. Gebhard, J. Osiewacz, M. Kutter, A. Hilger, T. Arlt, N. Kardjilov, B. Ellendorff, F. Beckmann, H. Markötter, M. Luik, T. Turek, I. Manke, and C. Roth, *Development of a modular operando cell for X-ray imaging of strongly absorbing silver-based gas diffusion electrodes,* Journal of The Electrochemical Society **169**, 044508 (2022).

[50] D. Franzen, M. C. Paulisch, B. Ellendorff, I. Manke, and T. Turek, *Spatially resolved model of oxygen reduction reaction in silver-based porous gas-diffusion electrodes based on operando measurements,* Electrochimica Acta **375**, 137976 (2021).

[51] K. Yang, R. Kas, W. A. Smith, and T. Burdyny, *Role of the carbon-based gas diffusion layer on flooding in a gas diffusion electrode cell for electrochemical CO_2 reduction,* ACS Energy Letters **6**, 33 (2021).

[52] M. Lehner, R. Tichler, H. Steinmüller, and M. Koppe, *Power-to-gas: technology and business models* (Springer, 2014).

[53] G. Faita and F. Federico, *Electrolysis cell with gas diffusion electrode,* (2010), US Patent 7,670,472 B2.

[54] N. Chavan, S. Pinnow, G. Polcyn, and T. Turek, *Non-isothermal model for an industrial chlor-alkali cell with oxygen-depolarized cathode,* Journal of Applied Electrochemistry **45**, 899–912 (2015).

[55] I. V. Zenyuk, D. Y. Parkinson, G. Hwang, and A. Z. Weber, *Probing water distribution in compressed fuel-cell gas-diffusion layers using X-ray computed tomography,* Electrochemistry Communications **53**, 24 (2015).

[56] W. Yoshimune, S. Kato, and S. Yamaguchi, *Multi-scale pore morphologies of a compressed gas diffusion layer for polymer electrolyte fuel cells,* International Journal of Heat and Mass Transfer **152**, 119537 (2020).

[57] E. F. Medici, I. V. Zenyuk, D. Y. Parkinson, A. Z. Weber, and J. S. Allen, *Understanding water transport in polymer electrolyte fuel cells using coupled continuum and pore-network models,* Fuel Cells **16**, 725 (2016).

[58] J. T. Gostick, M. A. Ioannidis, M. W. Fowler, and M. D. Pritzker, *Pore network modeling of fibrous gas diffusion layers for polymer electrolyte membrane fuel cells,* Journal of Power Sources **173**, 277 (2007).

[59] A. Z. Weber, R. M. Darling, and J. Newman, *Modeling two-phase behavior in PEFCs,* Journal of the Electrochemical Society **151**, A1715 (2004).

[60] D. L. Wood, C. Rulison, and R. L. Borup, *Surface properties of PEMFC gas diffusion layers,* Journal of The Electrochemical Society **157**, B195 (2010).

[61] B. Endrődi, E. Kecsenovity, A. Samu, T. Halmágyi, S. Rojas-Carbonell, L. Wang, Y. Yan, and C. Janáky, *High carbonate ion conductance of a robust PiperION membrane allows industrial current density and conversion in a zero-gap carbon dioxide electrolyzer cell,* Energy & Environmental Science , 4098 (2020).

[62] G. O. Larrazábal, P. Strøm-Hansen, J. P. Heli, K. Zeiter, K. T. Therkildsen, I. Chorkendorff, and B. Seger, *Analysis of mass flows and membrane cross-over in CO_2 reduction at high current densities in an MEA-type electrolyzer,* ACS Applied Materials & Interfaces **11**, 41281 (2019).

[63] R. A. Tufa, M. A. Blommaert, D. Chanda, Q. Li, D. A. Vermaas, and D. Aili, *Bipolar membrane and interface materials for electrochemical energy systems,* ACS Applied Energy Materials **4**, 7419 (2021).

[64] H. W. Shafaque, C. Lee, K. F. Fahy, J. K. Lee, J. M. LaManna, E. Baltic, D. S. Hussey, D. L. Jacobson, and A. Bazylak, *Boosting membrane hydration for high current densities in membrane electrode assembly CO_2 electrolysis,* ACS Applied Materials & Interfaces **12**, 54585 (2020).

[65] A. Reyes, R. P. Jansonius, B. A. W. Mowbray, Y. Cao, D. G. Wheeler, J. Chau, D. J. Dvorak, and C. P. Berlinguette, *Managing hydration at the cathode enables efficient CO_2 electrolysis at commercially relevant current densities,* ACS Energy Letters **5**, 1612 (2020).

[66] B. Endrődi, A. Samu, E. Kecsenovity, T. Halmágyi, D. Sebők, and C. Janáky, *Operando cathode activation with alkali metal cations for high current density operation of water-fed zero-gap carbon dioxide electrolysers,* Nature Energy **6**, 439 (2021).

[67] B. De Mot, M. Ramdin, J. Hereijgers, T. J. Vlugt, and T. Breugelmans, *Direct water injection in catholyte-free zero-gap carbon dioxide electrolyzers,* ChemElectroChem **7**, 3839 (2020).

[68] J. T. Gostick, M. A. Ioannidis, M. W. Fowler, and M. D. Pritzker, *Wettability and capillary behavior of fibrous gas diffusion media for polymer electrolyte membrane fuel cells,* Journal of Power Sources **194**, 433 (2009).

[69] Y. I. Hori, *Electrochemical CO_2 reduction on metal electrodes,* in *Modern aspects of electrochemistry* (Springer, 2008) pp. 89–189.

[70] T. Hatsukade, K. P. Kuhl, E. R. Cave, D. N. Abram, and T. F. Jaramillo, *Insights into the electrocatalytic reduction of CO_2 on metallic silver surfaces,* Physical Chemistry Chemical Physics **16**, 13814 (2014).

[71] T. Burdyny and W. A. Smith, *CO_2 reduction on gas-diffusion electrodes and why catalytic performance must be assessed at commercially-relevant conditions,* Energy & Environmental Science (2019), 10.1039/C8EE03134G.

[72] U. O. Nwabara, A. D. Hernandez, D. A. Henckel, X. Chen, E. R. Cofell, M. P. de Heer, S. Verma, A. A. Gewirth, and P. J. A. Kenis, *Binder-focused approaches to improve the stability of cathodes for CO_2 electroreduction,* ACS Applied Energy Materials (2021), 10.1021/acsaem.1c00715.

[73] E. R. Cofell, U. O. Nwabara, S. S. Bhargava, D. E. Henckel, and P. J. A. Kenis, *Investigation of electrolyte-dependent carbonate formation on gas diffusion electrodes for CO_2 electrolysis,* ACS Applied Materials & Interfaces **13**, 15132 (2021).

4

Electrowetting Limits Electrochemical CO_2 Reduction in Silver-based Gas Diffusion Electrodes

CO_2 electrolysis might be a key process to utilize intermittent renewable electricity for the sustainable production of hydrocarbon chemicals without relying on fossil fuels. Commonly used carbon-based gas diffusion electrodes (GDEs) enable high Faradaic efficiencies for the desired carbon products at high current densities, but have limited stability. In this study, we explore the adaption of a silver-based GDE from a Chlor-alkali electrolysis process as a cathode for gas-fed CO_2 electrolysis. We determine the impact of electrowetting on the electrochemical performance by analyzing the Faradaic efficiency for CO at industrially relevant current density. In addition, we assessed the chemical stability of the GDE with XPS and XRD characterization. The characterization of used GDEs reveals a potential-dependent degradation, which can be explained through chemical PTFE degradation and/or physical erosion of PTFE through the restructuring of the silver surface. Our results further suggest that electrowetting-induced flooding limits the Faradaic efficiency for CO in the short term. We propose a design strategy that could mitigate the effect of electrowetting for the silver-based GDEs and enable CO_2 electrolysis with high performance.

This chapter has been submitted under the title "Electrowetting Limits CO_2 Reduction in carbon-free Gas Diffusion Electrodes" by Lorenz M. Baumgartner, Andrey Goryachev, Christel I. Koopman, David Franzen, Barbara Ellendorff, Thomas Turek, and David A. Vermaas to *RCS Energy Advances* and is currently under revision.

4.1. INTRODUCTION

Electrochemical CO_2 reduction (CO_2R) could utilize excess wind and solar power to allow the sustainable production of hydrocarbon chemicals, fuels, or plastics.[1,2] If combined with CO_2 capture from the atmosphere[3,4] or the ocean,[5] this process could be independent of fossil feedstocks and contribute to the goal of the Glasgow Climate Pact to limit the increase in global temperature to 1.5 °C.[6]

Captured CO_2 can be converted electrochemically with a CO_2 electrolyzer. Depending on the catalyst employed at the cathode, CO_2R can yield a range of chemical products (Ag: CO; Sn: HCOOH; Cu: C_2H_4). Despite suitable catalysts being available, CO_2R can still suffer from poor Faradaic efficiency due to mass transfer limitations. If the supply of CO_2 to the catalyst cannot match the applied current density, the competing hydrogen evolution reaction (HER) takes place.[7] While the production of CO on Ag has the highest maturity among the different CO_2R routes, the process for CO production still has to be further optimized to meet a number of key industrial criteria:[8]

- Current density, j: -200 to $-500\,mA\,cm^{-2}$
- Faradaic efficiency, FE_{CO}: > 95%
- Catalyst activity: $100\,A\,g^{-1}$
- Stability: > 10 000 h

High j_{CO_2R} has become feasible through the introduction of gas diffusion electrodes (GDEs). By avoiding mass transfer limitations imposed by the limited solubility and diffusivity of CO_2 in aqueous electrolytes,[9–11] GDEs suppress the unwanted HER and allow high FE for C1[12–14] and C2 products.[15–17] Typically, GDEs for CO_2R consist of a catalyst layer (CL), coated on top of a gas diffusion layer (GDL). The CL provides a reaction interface, at which gaseous reactants get in contact with the catalyst surface and the electrolyte. Catalysts are typically employed in the form of nanoparticles[18] with typical loadings of $1\,mg\,cm^{-2}$,[19] which allows specific catalyst activities of $> 200\,A\,g^{-1}$. The GDL is typically treated with PTFE to prevent electrolyte intrusion and ensure free pore space for gas transport. The majority of studies utilizes commercial, carbon-based GDL materials adapted from hydrogen fuel cell research.[20,21]

To date, only a limited long-term stability has been reported for carbon-based GDEs. CO_2 electrolyzers with membrane electrode assembly (MEA) have achieved j_{CO_2R} values of $\geq -200\,mA\,cm^{-2}$ and $FE_{CO} \geq 90\%$ for up to 1000 h (Table 4.1).[14] More commonly, however, much shorter lifetimes than this are reported because insufficient hydration management leads to rapid electrode drying[22] or carbonate salt formation in the gas channels.[23–25] Even shorter lifetimes have been reported for CO_2 electrolyzers with a catholyte buffer (Table 4.1). Similar problems with GDE stability are also known from fuel cell applications, in which carbon and PTFE can degrade significantly after 100 h of operation at target current densities, which leads to a loss of hydrophobicity. In turn, the pore network of the GDL becomes more flooded with liquid, which reduces the performance by inhibiting the gas transport.[26]

Table 4.1: Stability of GDEs in electrolyzers. Carbon-based GDEs typically consist of a catalyst layer deposited on a commercial gas diffusion layer (Catalyst / GDL). In MEA reactors, a membrane separates the GDE from the electrolyte. The silver-based GDE from Covestro (oxygen depolarized cathode) consists of Ag particles (92 – 98 wt%) and PTFE (2 – 8 wt%) on a Ag mesh support.[27,28] The current density is j. The reaction temperature is T.

Process	Gas diffusion electrode	j mA cm^{-2}	T °C	Electrolyte	Lifetime h
Carbon-based GDEs (direct electrolyte contact)					
CO_2R: CO	Ag + Nafion / ELAT LT1400W cloth[29]	−185	20	1 M $KHCO_3$	> 120
CO_2R: CO	Ag + Nafion / SGL 39BC[30]	−190	20	1 M $KHCO_3$	≤ 20
CO_2R: HCOOH	Sn + Carbon + PTFE / SGL 35BC[31]	−200	20	1 M $KHCO_3$	> 5
CO_2R: C_2H_4	Cu / Freudenberg (unspecified)[16]	−320	20	7 M KOH	< 1
CO_2R: CO	Ag / Freudenberg H23C6[32]	−196	20	1 M KOH	< 0.25
Carbon-based GDEs (MEA)					
CO_2R: CO	Ag + Sustainion / SGL 35BC[14]	−200	20	10 mM $KHCO_3$	> 1000
CO_2R: CO	Ag + Nafion / Carbon felt[22]	−100	20	1 M NaOH	< 2
Silver-based GDEs (direct electrolyte contact)					
ORR	Ag + Carbon + PTFE / Ag mesh[33]	−300	80	32 wt% NaOH	> 28800
CO_2R: CO	Covestro[34]	−300	30	0.4 M K_2SO_4 + 1.5 M $KHCO_3$	> 1200
CO_2R: CO	Covestro GDE[35]	−150	20	0.4 M K_2SO_4	> 840

The lifetime of carbon-based GDEs in CO_2 electrolyzers depends on the chemical stability of the GDL substrate. As chemical degradation reduces the hydrophobicity of the pore network, electrolyte breakthrough occurs at lower differential pressure between liquid and gas phase,[36] which limits the flow-by regime in scaled-up electrolyzers.[29] The reported lifetime of carbon-based GDEs differs between materials types (Table 4.1). Nonwoven GDLs from Freudenberg exhibit especially short lifetimes of less than 1 h (Table 4.1).[16,30,32] Yang *et al.* demonstrated the flooding of a Freudenberg GDL started when the cathode potential was set below −0.65 V vs. RHE. XPS measurements indicated a degradation of the CFS, which showed a reduction of C–F bonds and an increase in oxygen content.[37] In contrast, carbon papers manufactured by SGL seem to be more stable (Table 4.1). For example, we recently demonstrated the operation of a SGL carbon paper at −190 mA cm^{-2} for 20 h until flooding occurred. Post-electrolysis characterization revealed that the static contact angle of the CFS had dropped from initially 149° to 128° after electrolysis.[30] A woven carbon cloth from ELAT showed a very promising performance, as it was stable for at least 120 h and allowed more than 50% FE_{CO} despite flooding (Table 4.1).[29]

The adoption of oxygen depolarized cathodes (ODC) for the CO_2R process might help avoid the limitations of carbon-based GDLs altogether.[38] ODCs are silver-based GDEs, which have been employed in industrial chlor-alkali electrolysis for many years. Typically, they consist of a current collector mesh with a porous layer of Ag and PTFE (sometimes also carbon), which allows O_2 transfer to reaction zone. There, the oxygen reduction reaction (ORR) is carried out at 80 – 90 °C with 30 – 35 wt% NaOH electrolytes.[39–41] Silver-based GDEs have been shown to be stable for ten thousands of hours in these harsh chemical conditions (Table 4.1).[33] The long-term stability of such ODCs (> 10 000 h)

is limited by the restructuring of Ag, the degradation of PTFE,[42] or the degradation of carbon.[40] Recently, ODCs have also been successfully employed for up to 1200 h in CO_2 electrolyzers with flowing catholyte (Table 4.1).[34,35]

As ODCs consist of less carbonaceous materials, which can be more susceptible to chemical degradation (Table 4.1), they have the potential to ensure a better long term stability than carbon-based GDEs. The baseline flooding resistance of GDEs depends on material properties, such as pore structure or PTFE treatment.[43,44] It is also affected by the effect of electrowetting,[45–47] which describes the physical phenomenon of surfaces becoming more hydrophilic under potential bias. This has important implications for the flooding behavior of porous GDEs, because the internal contact angles of the pore network are reduced as the electrode is charged during electrolysis.

To the best of our knowledge, only a limited number of publications have investigated the application of silver-based GDEs for CO_2R. At the same time, the commercial, silver-based GDE for the chlor-alkali process (Covestro) shows promising performance and stability for CO_2R,[34,35] as this electrode could overcome the stability issues of carbon-based GDEs and silver is a common catalyst for CO_2R. Unfortunately, the GDE from Covestro is proprietary, which means that limited public characterization data is available.[27,28] A recent experimental–modeling study has revealed that the CO_2R efficiency of these GDEs becomes strongly limited by CO_2 mass transfer at higher j.[48]

In our previous work, we developed our own silver-based GDE, which have been optimized for ORR[43,44] and characterized with advanced imaging techniques (e.g., X-ray tomography, *operando* X-ray radiography)[46,47] Hoffmann *et al.* performed CO_2R with these electrodes and varied the cathode potential between −0.7 and −1 V vs. RHE. By studying the electrolyte intrusion operando with synchrotron imaging, they showed that a content of 97 wt% Ag (3 wt% PTFE) allowed the highest current density.[49]

In this work, we study the CO_2R performance of silver-based GDEs by assessing the chemical stability and analyzing the Faradaic efficiency for CO at industrially relevant current density (−200 mA cm^{-2}). We conducted experiments with a silver-based GDE (97 wt% Ag) and a typical carbon-based GDE made with a SGL 39BC substrate to allow a direct comparison between these two electrodes types. Our study assesses the impact of electrowetting on the CO_2R performance of silver-based GDEs. In addition, the used electrodes were characterized with XPS and XRD to measure changes to the chemical composition. We propose a design approach that could mitigate the effect of electrowetting for the silver-based GDEs and enable CO_2 electrolysis with high performance.

4.2. EXPERIMENTAL METHODS

The electrode preparation, physical characterization, and electrochemical experiments are described in more detail in the supporting information (SI).

4.2.1. ELECTRODE PREPARATION

Preparation of the silver-based GDE

The silver-based GDEs were prepared by spray deposition.[44] A suspension was mixed from 30 g Ag particles, 50 g of a solution with 1 wt% hydroxymethyl cellulose, 40 g water to adjust the viscosity, and 1.5 g of a dispersion with 59 wt% PTFE. A silver gauze was used as a current collector. It was fixed in a frame and placed on a heating plate (100 °C) to facilitate the drying process. Then, the suspension was deposited onto the gauze in 80 homogeneous layers with an airbrush. The composition of the deposited layer was 97 wt% Ag and 3 wt% PTFE. The target Ag loading was 160 mg cm^{-2}. The coated sample was hot-pressed at 130 °C and 15 MPa for 5 min. Subsequently, we placed the GDE in an air oven at 330 °C for 15 min to form pores by burning out methylcellulose and to sinter the Ag and PTFE.

Preparation of the carbon-based GDE

The carbon-based GDEs were prepared by depositing a silver catalyst layer on a commercial carbon-based GDL with a spray deposition process.[30] The ink suspension for the catalyst layer was mixed from 33 mg Ag nanopowder, 2.1 mL water, 2.1 mL propan-2-ol, and 180 µL of a 5 wt% Nafion D-521 dispersion. The mixture was homogenized in a sonication bath for 30 min. The GDL substrate (SGL 39 BC, SGL Carbon) was placed on a heating table (130 °C) equipped with a 2D-motorized stage. The ink was evenly sprayed onto the MPL side with an airbrush. The target composition of the deposited catalyst layer was 80 wt% Ag and 20 wt% Nafion. The target Ag loading was 1 mg cm^{-2}.

4.3. ELECTRODE CHARACTERIZATION

The static contact angle was measured with the sessile drop method.[50] We recorded images of 10 µL water droplets at five different locations of the sample. The contact angle was extracted with the image processing software ImageJ (see SI, Figure 4.8).[51]

The liquid breakthrough pressure (at open circuit potential) was measured by placing the sample in a transparent flow cell and pumping water into the liquid compartment (see Chapter 2, Figure 2.18). By closing off the liquid outlet, water was forced to break through the porous sample. We recorded the differential pressure at which the first droplet appeared on the gas side (see Chapter 2, Figure 2.17).

The convective mass transfer was analyzed by studying the CO_2 permeability. After installing the sample in a flow cell, we passed CO_2 through the material at different flow rates and measured the pressure drop (see SI, Figure 4.9). By plotting the flow rate against the pressure drop, we derived the permeability constant from the slope according to Darcy's law.[52]

The diffusive mass transfer was evaluated by determining the limiting overall O_2 mass transfer coefficient. We use this metric as a proxy for the CO_2 mass transfer coefficient.[30] The GDE was placed in a flow cell with 6 M KOH in the liquid compartment. We flowed air through the gas compartment and measured the gas pressure (see Chapter 2, Figure 2.30). We carried out a linear sweep voltammetry (LSV) scan for the ORR. The value of k_{O_2} was derived from the plateau current density (see SI, Figure 4.10).

Scanning electron microscopy (SEM) was carried out with a JSM-6010LA microscope (JEOL, Japan) at an acceleration voltage of 5 kV. The images were recorded with a secondary electron imaging (SEI) and a back-scattered electron composition (BEC) detector.

X-ray diffraction (XRD) patterns were obtained using a Bruker D8 Advance diffractometer equipped with a Co anode (λ(Kα) = 1.7889 Å, 35 kV, 40 mA) and a Lynxeye position-sensitive detector. The diffractograms were acquired in the Bragg-Brentano geometry with a step size of 0.02° and an acquisition time of 4 s. A motorised varied-divergent slit (V6) and constant rotation of the holder (30 RPM) were applied. The diffractograms were processed in DiffracSuite.EVA (v.5.1) software. The Scherrer equation was used to evaluate changes to the crystallite size.[53]

X-ray photoelectron spectroscopy (XPS) measurements were carried out on a K-Alpha XPS spectrometer (Thermo Scientific), equipped with a small-spot (400 µm) monochromatic X-ray source (Al Kα= 1486.6 eV). Core level spectra were recorded with a pass energy of 50 eV. Low energy Ar^+ ions were used to compensate surface charging. CasaXPS software was used for data processing. The spectra were normalized on the C 1s binding energy (BE) of the adventitious carbon (284.8 eV). XPS depth profiles were recorded on the same spectrometer. Ar^+-sputtering was done at 3 kV with time steps of 60 s.

4.4. CO_2 ELECTROLYSIS PROCEDURE

The CO_2 reduction performance was determined with an automated setup (Figure 4.1). The cathode GDEs were installed in a 2-compartment flow cell (see Chapter 2, Figure 2.18). A mass flow controller (MFC1) supplied the CO_2 feed at a flow rate of 50 mLn min^{-1}. The CO_2 was humidified to 85% relative humidity at 20 °C in two bubble columns and fed into the gas compartment (see Chapter 2, Figure 2.28). The backpressure of the gas was set by the cracking pressure of a check valve. The 1 M $KHCO_3$ electrolyte was recirculated with a peristaltic pump. The liquid backpressure was controlled with an electronic control valve to set the flow-by regime at the GDE. After passing through the flow cell, the liquid stream was mixed with a purge gas, which was supplied at a flow rate of 80 mLn min^{-1}, in order to facilitate the transfer of the product gases into the headspace of the electrolyte reservoir. From there, the product gas mixture passed to the gas chromatography (GC) system. The flow rate was measured with a mass flow meter (MFM).

We performed a series of current density steps ranging from −10 to −200 mA cm^{-2}. For each step, we carried out at least two GC injections to determine the Faradic efficiency for CO and H_2 (see SI, Figure 4.12). The cathode potential was recorded with an Ag/AgCl micro-reference electrode and corrected for the ohmic resistance of the electrolyte. Unless indicated otherwise, all reported potentials are given in the reversible hydrogen electrode (RHE) scale.

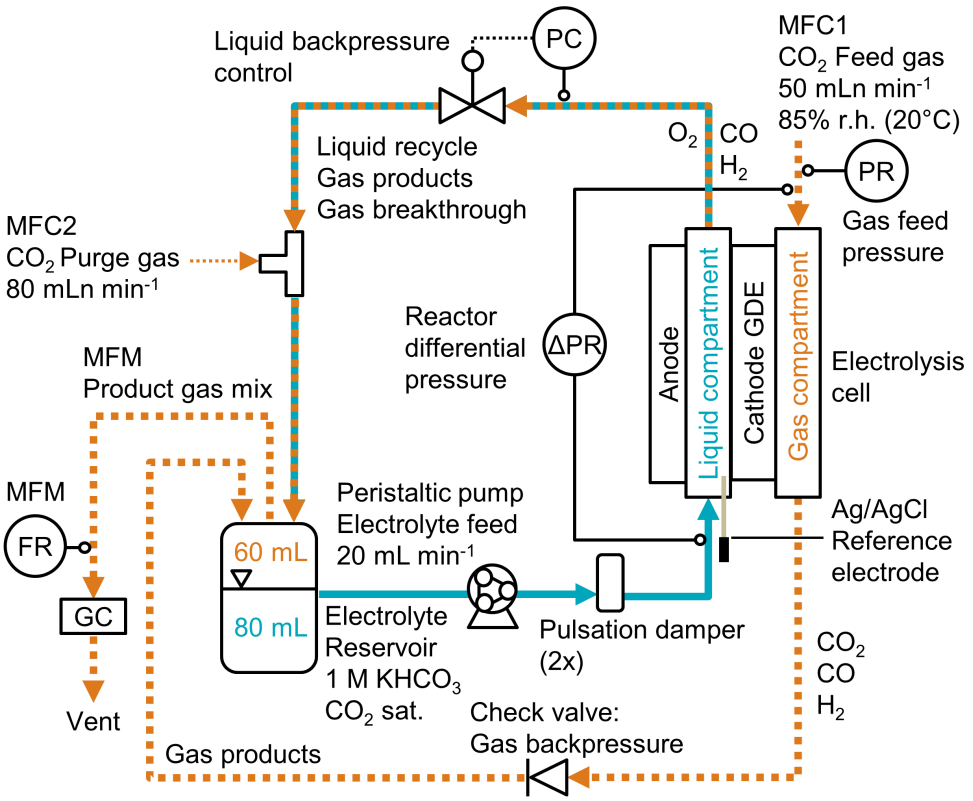

Figure 4.1: Process flow diagram for CO_2 electrolysis setup. The backpressure of the electrolyte stream was controlled (PC) before it was mixed with the purge gas and recirculated. The differential pressure, Δp^*, across the GDE was measured between the catholyte and gas compartment (ΔPR). The faradic efficiency was determined by recording the product gas flow rate (FR) with a mass flow meter (MFM) and analyzing the gas composition by gas chromatography (GC).

4.5. RESULTS & DISCUSSION

The prepared GDE samples were characterized and their CO_2 reduction performance assessed with galvanostatic measurements. The chemical stability of the GDEs was assessed by additional characterization after the electrolysis experiments. Supplementary results and the numerical values of all plotted data are included in the supporting information (SI).

4.5.1. ELECTRODE CHARACTERIZATION

The silver-based GDE consists of the sintered Ag-PTFE composite forming a uniform layer around the current collector mesh (see SI, Figure 4.13).[44] Both sides of the GDE exhibit a static contact angle of $\theta = 141°$ at open circuit (Figure 4.2). The material is more hydrophobic compared to a flat silver surface ($\theta_{Ag} = 95°$)[54] because of the 3 wt% PTFE binder ($\theta_{PTFE} = 122°$).[55] In addition, the sintered GDE has a rough surface which allows gas pockets to enhance the contact angle according to the Cassie-Baxter model.[50] An overview of all measured contact angles is given in Table 4.4 (see SI).

The carbon-based GDE is made up of the catalyst layer (CL), which is coated on top of the GDL (Figure 4.2). The GDL has two components: the microporous layer (MPL) and the carbon fiber substrate (CFS). The MPL consists of carbon black and PTFE particles, which give it a high contact angle ($\theta_{MPL} = 153°$). The CFS is comprised of graphitized carbon fibers, which have been impregnated with PTFE ($\theta_{CFS} = 149°$). We note that our static contact angles have a mostly qualitative meaning as they do not capture the effects of contact angle hysteresis on rough surfaces or the internal contact angle,[56] which are critical to quantify the flooding behavior of the pore network.

The silver-based GDE has a more than 20x higher liquid breakthrough pressure at open circuit, Δp_L^*, than the carbon-based GDE (Figure 4.2: 1410 vs. 67 mbar). This high resistance against liquid intrusion is due to the unimodal pore structure with a small average diameter of $\bar{d}_{pore} = 0.8\,\mu m$,[44] In contrast, the carbon-based GDL exhibits a much lower Δp_L^*. As the MPL commonly features large cracks due to the manufacturing process (see SI, Figure 4.15), this layers adds little flooding resistance despite the high θ_{MPL} and small pore size.[30,36] Instead, Δp_L^* is mostly determined by the properties of the CFS, whose pores are much larger ($\bar{d}_{pore} = 32\,\mu m$)[57] and consequently exhibit a much lower capillary pressure.

The high Δp_L^* of the silver-based GDE is very promising for scale-up because it determines how well the GDE could maintain the separation of gas and liquid phase at a large scale. For illustration, a Δp_L^* of 1.4 bar corresponds to resisting the hydrostatic pressure of an aqueous electrolyte in a 14 m tall cell, which is an order of magnitude larger than the height of commercial cells for alkaline electrolysis (1 – 2 m)[58] or chlor-alkali electrolysis (1 – 1.5 m).[59,60] However, the flooding resistance also has to be assessed under operating conditions because electrowetting can reduce the hydrophobicity and thereby decrease Δp_L^*.[29,36]

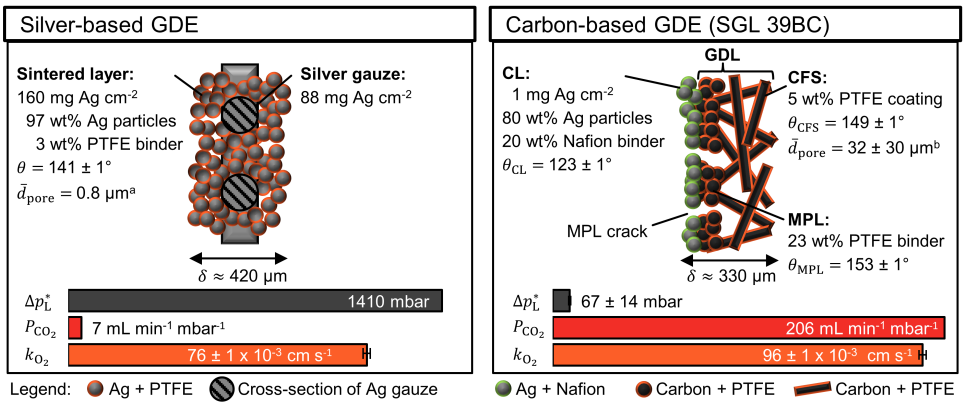

Figure 4.2: Physical properties of silver-based GDE and carbon-based GDE (GDL: SGL 39BC carbon paper). The static contact angle, θ, ± its standard error were calculated from five or more measurements. [a]The average pore diameter, $\bar{d}_{pore}$, was obtained from Franzen *et al.*[44] for the silver-based GDE. [b]The $\bar{d}_{pore}$ of the SGL 39BC's carbon fiber substrate (CFS) was obtained from Parikh *et al.*.[57] The total thickness of the GDE is δ. The liquid breakthrough pressure is Δp_L^*. The CO_2 permeability constant is P_{CO_2}. The limiting overall O_2 mass transfer coefficient is, k_{O_2}, (proxy for CO_2 mass transfer). Its error bars indicate the standard deviation of the limiting currents. More detailed characterization data are available in the SI.

The mass transfer between the gas bulk and the reaction zone can occur through convection and/or diffusion. The silver-based GDE has a 30x smaller capacity for convective mass transfer compared to the carbon-based GDE, which is quantified with the CO_2 permeability constant, P_{CO_2} (Figure 4.2): 7 vs. 206 mL min^{-1} mbar^{-1}. According to the Hagen-Poiseuille equation ($F_{G,pore} \propto d_{pore}^4$), the flow rate through a pore scales with the fourth power of the diameter. We can therefore expect the silver-based GDE's small pores to result in a lower P_{CO_2}. In contrast, the carbon-based GDE has relatively large CFS pores and large cracks allowing a large portion of the gas flow to bypass the small pores of the MPL. As proposed in a previous study, we can expect diffusion to be the dominating mass transfer mechanism in the flow-by regime.[30] For this reason, the lower P_{CO_2} of the silver-based GDE should not hamper the CO_2 reduction performance significantly.

The silver-based GDE has a 20% lower capacity for diffusive mass transfer, k_{O_2} (Figure 4.2: 76 vs. 96 × 10^{-3} cm s^{-1}). We quantified this capacity with the limiting overall O_2 mass transfer coefficient, k_{O_2}, which serves as a proxy for the experimentally less accessible limiting CO_2 mass transfer coefficient.[30] The lower diffusive mass transport for the silver-based GDE is explained by its higher thickness and smaller pore size, which lead to a longer, more tortuous diffusion pathway compared to its carbon-based counterpart. It may be beneficial to reduce the thickness of the GDE by using a thinner current collector gauze and depositing fewer layers of silver and PTFE.

4.5.2. CO_2 ELECTROLYSIS: ELECTROWETTING INHIBITS PERFORMANCE

The silver-based GDE has a similar CO_2 reduction performance at $-100\,mA\,cm^{-2}$ as the carbon-based GDE (Figure 4.3). At $-200\,mA\,cm^{-2}$ its FE_{CO} becomes significantly lower compared to the carbon-based GDE (35 vs. 86%). Based on the relative diffusivities of the characterization results, we would expect the silver-based GDE to achieve a proportionally lower FE_{CO} of 69%. Because this is not the case, however, we hypothesize that the additional performance drop is caused by the observed electrolyte flooding. Flooding fills empty pores with liquid and decreases the effective diffusivity of the porous GDE. As a consequence, the CO_2 mass transfer falls below the supply of electrons, so that the HER takes place instead of the CO_2R. The cathode potential, $E_{Cath.}$, probably becomes more negative compared to the carbon-based GDE because evolving hydrogen gas bubbles increase the ohmic resistance ($-1.4\,V$ vs. RHE compared to $-1.7\,V$ vs. RHE). We can further investigate this inferior performance by comparing the short-term stability.

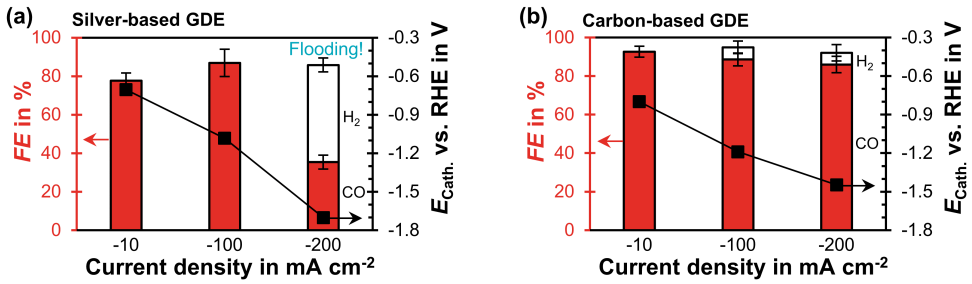

Figure 4.3: CO_2 reduction performance in flow-by regime at steady state: The Faradaic efficiency, FE, for CO or H_2 is plotted as a function of current density on the left y-axis. The error bars represent the estimated standard errors. The cathode potential, $E_{Cath.}$, against the reversible hydrogen electrode (RHE) is plotted on the right y-axis. The potential was corrected for the ohmic potential drop between the reference electrode and the cathode. (a) Silver-based GDE: Each data point represents an average calculated from two GC injections. Flooding occurred after 10 min at $-200\,mA\,cm^{-2}$. The two injections were taken 30 min later. (b) Carbon-based GDE: Each data point is based on three GC injections. The data is taken from a previous publication.[29]

The silver-based GDE does not allow stable CO_2R at $-200\,mA\,cm^{-2}$ and has a much lower FE_{CO} compared to the carbon-based GDE (Figure 4.4 a vs. c). First droplets of electrolyte appear on the gas side of the GDE 10 min after the current density is applied and the cathode potential drops below $-1.3\,V$. This suggests that the initially high flooding resistance is lost due to electrowetting. As the run proceeds, the FE_{CO} declines steadily while the electrolyte droplets increase in size and start to dry out. After a run time of 40 min, (bi)carbonate salts start forming on the surface of the GDE (see SI, Figure 4.16).

We carried out another electrolysis run with the silver-based GDE at $-50\,mA\,cm^{-2}$ in an attempt to mitigate the electrowetting-induced flooding with a less negative cathode potential (Figure 4.4 b). FE_{CO} declines more slowly as the initial $E_{Cath.}$ is less negative compared to the $-200\,mA\,cm^{-2}$ run ($-1.0\,V$ compared to $-1.3\,V$). This slower flooding is in agreement with X-ray imaging studies, which report that the speed of electrolyte intrusion is potential-dependent.[45,47] Ultimately, however, the CO_2R performance is also

not stable at −1.0 V because the flooding leads to salt formation on the gas side.

Our results (Figure 4.4) raise the question why electrowetting leads to a more detrimental flooding for the silver-based than for the carbon-based GDE. Electrowetting spreads an electrolyte more strongly on bare, conductive surfaces (e.g., silver, carbon) than on surfaces that are covered with a dielectric insulator (e.g., PTFE).[47,61] We hypothesize that the carbon-based GDE's higher PTFE content (MPL: 23 wt%, CFS: 5 wt%) covers bare carbon surfaces more effectively, which leads to a stronger insulation against electrowetting. In contrast, the PTFE in the silver-based GDE has a lower concentration (3 wt%) and is distributed heterogeneously throughout the pore network.[46,47] This structure probably allows the electrolyte to transition from a non-wetting Cassie-Baxter state to a wetting Wenzel state, when the potential is decreased sufficiently.[61,62] This means that the electrolyte does not rest on the dispersed PTFE, but spreads along the bare silver surfaces through electrowetting.[47]

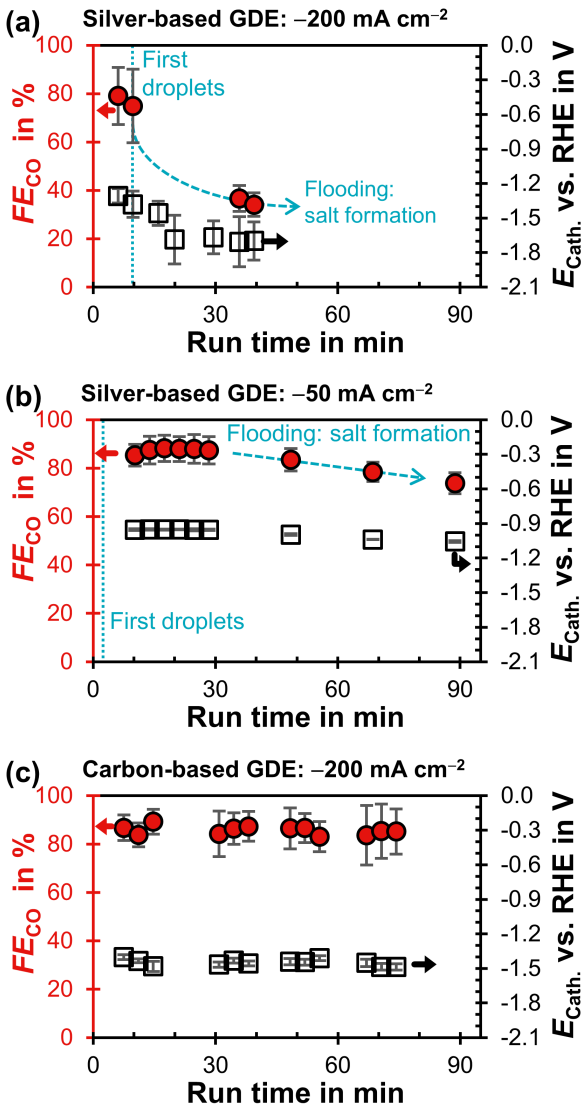

Figure 4.4: Faradaic efficiency for CO, FE_{CO}, as a function of run time after starting the potentiostat. The iR-compensated cathode potential, $E_{Cath.}$, against the reversible hydrogen electrode (RHE) is plotted on the right y-axis. Every data point represents a single GC injection. The error bars represent the estimated standard error. (a) Silver-based GDE at $-200\,mA\,cm^{-2}$. (b) Silver-based GDE at $-50\,mA\,cm^{-2}$. (c) Carbon-based GDE (GDL: SGL 39BC) at $-200\,mA\,cm^{-2}$.[29]

Electrowetting leads to a poor performance for CO_2R with the silver-based GDE (Figure 4.4). This is interesting because electrowetting and electrolyte breakthrough also occur during ORR, but they do not seem to have such a detrimental effect for this reaction. [43,45] We hypothesize that the flooding due to electrowetting is stronger for the CO_2R because this reaction requires more negative cathode potentials compared to the ORR (Figure 4.5). Therefore, the electrolyte saturates the pore network to a higher extent and the supply of CO_2 is severely limited.

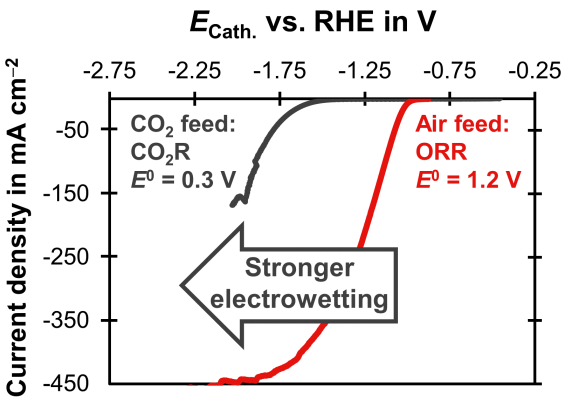

Figure 4.5: Linear sweep voltammetry scans comparing CO_2R and ORR on a carbon-based GDE with a loading of 1 mg Ag cm^{-2} on the basis of a SGL 39BC GDL. The current density is plotted as a function of the cathode potential, $E_{Cath.}$. The potential was corrected for the ohmic potential drop between the reference electrode and the cathode. The experiments were conducted at 20 °C with a scan rate of 20 mV s^{-1}. The CO_2R experiment was carried out in 1 M $KHCO_3$ (pH = 7.5) with a CO_2 gas feed. The equilibrium potential of E^0 = 0.3 V vs. RHE, was obtained from Jouny *et al.*. [63] The ORR experiment used 6 M KOH (pH = 14.8) and an air gas feed. The equilibrium potential of E^0 = 1.2 V vs. RHE was obtained from Mousallem *et al.*. [39]

The effect of electrowetting could probably be mitigated by changing the GDE structure. Our silver-based GDE had a relatively low PTFE content (3 wt%), which leads to a poor performance because the electrolyte wets a large part of the pore network and blocks gas transport. In contrast, a GDE with a higher PTFE content (8 wt%) was shown to successfully retard the intrusion of electrolyte, [49] but also performed poorly because the PTFE prevents the wetting of catalyst area and reduces the amount of open pore space available for gas diffusion. [44] Therefore, we propose to fabricate the GDE from two layers with varying PTFE content. The (I) reaction layer should have a relatively low PTFE content ($\leq$ 3 wt%) and would provide a large wetted catalyst surface for the CO_2R reaction. The (II) diffusion layer should have a relatively high PTFE content ($\geq$ 6 wt%) to make it more resilient against electrowetting and ensure the transport of CO_2 from the gas bulk to the reaction layer.

4.5.3. POST ELECTROLYSIS CHARACTERIZATION: PTFE DEGRADATION OCCURS AT HIGH OVERPOTENTIAL

In addition to reversible electrowetting, the GDE can also experience a permanent loss of hydrophobicity through chemical reactions, which also has a negative impact on performance and is detrimental to the long-term stability. After CO_2 electrolysis, we rinsed the electrodes with water to remove carbonate salts. We then measured the static contact angle and analyzed chemical changes with SEM, XPS, and XRD.

The XPS analysis of the GDE surface shows no clear change in Ag oxidation state (see SI, Figure 4.21), in line with the applied cathodic potentials. The XRD diffractograms of fresh and used GDEs show a single cubic phase of Ag^0 with no variation of crystalline parameters (see SI, Figure 4.18). These results indicate that the surface did not oxidize and that the crystallite size of Ag particles did not change by CO_2R.

Elemental contrast imaging with SEM/BEC suggests that the amount of surface PTFE was reduced by the electrolysis at $-200\,mA\,cm^{-2}$ (Figure 4.6). Particularly, the silver backbone of a fresh GDE was covered with finely dispersed PTFE particles, in contrast to the large silver clusters emerged at the surface of the spent sample. The morphology change of spent GDEs was also reflected in a significant reduction of θ (Figure 4.6: 111° vs. 141°), which is in line with the observed removal of hydrophobic PTFE domains from the electrode surface. We hypothesize that the removal of PTFE is caused by chemical degradation and/or physical erosion due to restructuring of the silver surface.

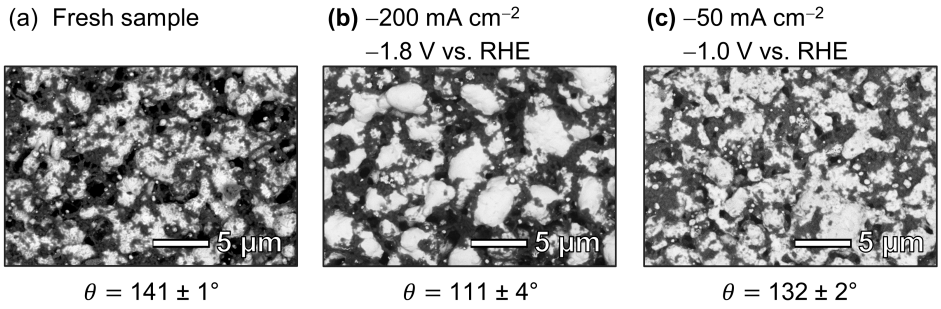

Figure 4.6: SEM images and static contact angle, θ, of silver-based GDEs: Elemental contrast images were recorded with the BEC detector of the SEM (Light grey domains: Ag, Dark grey domains: PTFE). The average θ ± the standard error were determined with the sessile drop method. (a) Fresh GDE sample. (b) After electrolysis at $-200\,mA\,cm^{-2}$ for 84 min with an initial cathode potential of −1.8 V vs. RHE (potential stabilized at −1.4 V vs. RHE). Additional SEM images are available in Figure 4.19 (see SI).

The XPS survey reveals that the loss of hydrophobicity is accompanied by a change in surface chemistry. The electrolysis reduced the fluorine concentration from 58 at.% vs. 40 at.%, while the carbon concentration increased from 36 at.% vs. 49 at.% (Table 4.2). Further, the chemical state of carbon changes as the fraction of C–R bonds increases at the cost of C–F bonds (Table 4.2). These results support the hypothesis that PTFE undergoes reductive electrochemical degradation. According to Shapoval *et al.*,[64] this

mechanism takes place below the cathode potential threshold of −1.3 V vs. RHE (see SI, Figure 4.24). In its course, fluoride is eliminated from the PTFE polymer chain[64] and carbonaceous decomposition products are left behind.[42,64]

The slight increase in the atomic concentration of oxygen and the fraction of CO_x bonds (Table 4.2) is probably caused by residual potassium (bi-)carbonate salts. The presence of these salts was confirmed by the small amount of potassium in the XPS signal of the used sample (see SI, Table 4.7 and Figure 4.22).

Table 4.2: XPS measurements of silver-based GDEs: Assessment of elemental composition and the chemical state of carbon (CF_2: C–F bonds in PTFE; COX: COR, CO, COOR; CR: C–H or C–C bonds. C–X: all carbon bonds). (a) Fresh GDE sample. (b) After electrolysis at $-200\,mA\,cm^{-2}$ for 84 min with an initial cathode potential of −1.8 V vs. RHE (stabilized at −1.4 V vs. RHE). (c) After electrolysis at $-50\,mA\,cm^{-2}$ for 89 min with cathode potential of −1.0 V vs. RHE. The analyzed area was facing the electrolyte during electrolysis.

Sample	(a) Fresh sample	(b) $-200\,mA\,cm^{-2}$ −1.8 V vs. RHE	(c) $-50\,mA\,cm^{-2}$ −1.0 V vs. RHE
Elemental surface composition			
F	58 at.%	40 at.%	51 at.%
C	36 at.%	49 at.%	35 at.%
Ag	4 at.%	4 at.%	6 at.%
O	1 at.%	6 at.%	4 at.%
Relative fraction of carbon bonds			
CF_2 / C–X	84%	45%	76%
CO_x / C–X	4%	7%	4%
CR / C–X	13%	48%	20%

XPS depth profile analysis shows a uniform reduction of 14 at.% in fluorine content along the surface profiled after electrolysis (Figure 4.7 a). As a consequence, the relative concentration of Ag increases by an average of 11 at.% along the depth profile. The relative carbon content increases only slightly by 4 at.% along the profile (Figure 4.7 c). These findings agree with the hypothesis that electrochemical degradation eliminates fluoride from the PTFE polymer chain and leaves behind carbonaceous degradation products.[42,64]

In addition, the normalized Ag distribution of the used sample is shifted towards the surface (Figure 4.7 e), which might be due to the migration of Ag and/or the removal of PTFE close to the top surface. This phenomenon could be explained by a potential-induced restructuring of the Ag surface,[27,42] which might cause the PTFE to loose adhesion and fall off. Such a restructuring would be in agreement with the smoother Ag surfaces observed in the SEM images (Figure 4.6). We can therefore conclude that physical erosion of PTFE due to Ag restructuring probably takes place in parallel to chemical degradation.

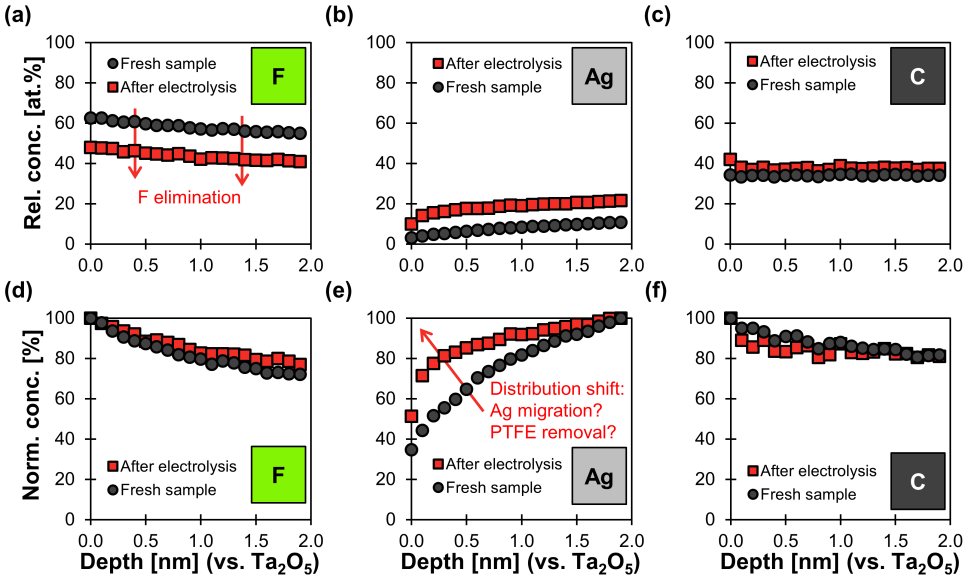

Figure 4.7: XPS depth profiles of fresh silver-based GDE and spent sample after electrolysis. Electrolysis was performed at $-200\,\mathrm{mA\,cm^{-2}}$ for 84 min with an initial cathode potential of $-1.8\,\mathrm{V}$ vs. RHE (stabilized at $-1.4\,\mathrm{V}$ vs. RHE). The x-axis shows the depth profile calibrated against a Ta_2O_5 standard sputtered with Ar^+ ions. (a) – (c): The y-axis shows the relative atomic concentrations of F, Ag, and C (other elements were not considered in this analysis mode). This means that the three elements together make up 100 at.% in this plot. (d) – (e): The y-axis shows the normalized concentrations for each elements along the profile. This means that the depth with the highest atomic concentration along the profile determines the 100% value in the normalized concentration plot.

The silver-based GDE that was operated at $-50\,mA\,cm^{-2}$ and a cathode potential of $-1.0\,V$ also underwent chemical changes. The XPS analysis shows that the surface concentration of fluorine is lower than for the fresh sample (Table 4.2: 58 at.% vs. 51 at.%). The fraction of CF_2 bonds drops from 84% to 76% (Table 4.2). These changes to the surface chemistry are accompanied by a reduction of θ from $141 \pm 1°$ to $132 \pm 2°$ compared to the fresh sample (Figure 4.6). However, the SEM images suggest that the silver matrix remains covered with dispersed PTFE (Figure 4.6). The XPS depth profiles vary little compared to a fresh sample (see SI, Figure 4.23). These results show that the degradation of the GDE is less significant at $-1.0\,V$ ($-50\,mA\,cm^{-2}$) compared to the GDE that was operating at $-1.8\,V$ ($-200\,mA\,cm^{-2}$).

It is noteworthy that the degradation of PTFE also seems to take place below the reported potential threshold of $-1.3\,V$ vs. RHE.[64] A possible explanation for this inconsistency might be that the difference in solvent affects the elimination of fluoride from the polymer chain. Shapoval *et al.*[64] studied PTFE degradation in anhydrous DMF, while our electrolyte was aqueous $KHCO_3$. Other interesting questions for future study are how fast the degradation occurs over time and if the mechanism only depends on the cathode potential or also on the total charge passed through the GDE.

Our silver-based GDEs underwent chemical degradation after less than 1.5 h of CO_2 electrolysis. Long-term CO_2 electrolysis was successfully performed for more than 1200 h by Haas *et al.* with the silver-based GDEs from Covestro.[34] These electrodes were characterized after electrolysis, which revealed a restructuring of the silver surface. Further, Raman microscopy showed a shift in signal from PTFE to carbon,[27] which is probably a sign of PTFE degradation at the surface. This example suggests that silver-based GDEs can tolerate some chemical degradation during long-term CO_2 electrolysis. A possible explanation for this tolerance might be that the removal and degradation of PTFE occurs primarily close to the surface while leaving the internal pores less affected. Nonetheless, it is critical that the sintered silver backbone retains its morphology and pore size to ensure stable long-term operation.

4.6. CONCLUSION

We have investigated the adoption of a silver-based GDE for electrochemical CO_2 reduction (CO_2R), which was originally developed for the oxygen reduction reaction (ORR) in the chlor-alkali process. The GDE experienced an unstable FE_{CO} at cathode potentials beyond $-1.0\,V$ vs. RHE ($-50\,mA\,cm^{-2}$) due to physical electrowetting. Electrowetting reduces the hydrophobicity of the porous GDE, which blocks gas diffusion paths by electrolyte flooding and (bi)carbonate salt formation. Exposing the GDE to potentials of $-1.8\,V$ vs. RHE ($-200\,mA\,cm^{-2}$) for $< 90\,min$ resulted in a partial degradation and removal of PTFE from the GDE. This might suggest a limited long-term stability of these electrodes, but it was not possible to quantify the effect on the FE_{CO}.

These results show that our silver-based GDEs require further improvement before they can enable CO_2 electrolysis with high performance. We propose to reduce the thickness of the GDE to increase the CO_2 mass transfer rates. A lower thickness might also lower

the cathode overpotential, which would reduce the extent of electrowetting and PTFE degradation. In addition, we suggest to separate the two core functions of the GDE into two layers with different PTFE contents to mitigate electrowetting. The first layer faces the electrolyte and should have a relatively low PTFE content (≤ 3 wt%) to provide a large wetted catalyst surface for the CO_2R reaction. The second layer faces the gas compartment and should have a relatively high PTFE content (≥ 6 wt%) . This would make it more resilient against electrowetting and thereby ensure that the CO_2 diffusion pathways remain dry. This two-layer design might be able to limit the effects of electrowetting and enable the long-term CO_2 electrolysis with a high FE_{CO}.

4.7. SUPPORTING INFORMATION

The digital version of the Supporting Information (SI) includes an Excel file with the values for all plotted data and all recorded experimental parameters for the CO_2 electrolysis experiments.

4.7.1. METHODS

GDE PREPARATION

We prepared three silver-based GDEs samples and one carbon-based GDE sample for all experiments.

Preparation of the silver-based GDEs

The silver-based GDEs were prepared by spray deposition.[44] The components of the ink suspension were added together in the following order:

- 30 g Ag particles (SF9ED, Ferro GmbH)
- 50 g methyl cellulose solution with 1 wt% hydroxymethyl cellulose (WALOCEL™ MKX 70000 PP 01)
- 40 g water to adjust the viscosity
- 1.5 g PTFE dispersion (TF 5060GZ, 3 M™ Dyneon™: 59 wt% PTFE, 8 wt% surfactant)

A silver gauze was used as current collector (40936 Silver gauze, 80 mesh, 115 µm diameter wire, 99.9% metal basis, Alfa Aesar). The area weight of the gauze was 88 mg Ag cm^{-2}. We fixed the current collector in a frame and placed it on a heating plate (100 °C) to facilitate the drying process. Then, the suspension was deposited onto the gauze in 80 homogeneous layers using an airbrush (Evolution, 0.6 mm pin hole, Harder & Steenbeck). The composition of the deposited layer was 97 wt% Ag and 3 wt% PTFE. The target Ag loading was 160 mg cm^{-2}. We hot-pressed the coated sample at (130 °C) and 15 MPa for 5 min (LaboPress P200S, Vogt, Germany). Subsequently, the GDE was placed in an air oven at (330 °C) for 15 min to form pores by burning out methylcellulose and to sinter the Ag and PTFE.

Preparation of the carbon-based GDEs

The carbon-based GDEs were prepared by depositing a catalyst layer on a commercial carbon-based GDL with a spray deposition process.[30] We mixed the ink for the catalyst layer in the following order:

- 33 mg Ag nanopowder (Aerodynamic particle size: 20 – 40 nm, 99.9% metal basis, Alfa Aesar)
- 2.1 mL water
- 2.1 mL propan-2-ol
- 180 µL of Nafion D-521 dispersion (5 wt%, Alfa Aesar)

The target composition of the deposited catalyst layer was 80 wt% Ag and 20 wt% Nafion. The Nafion binder content of 20 wt% was selected to match the optimized content determined by Duarte *et al.*.[65] The target Ag loading was 1 mg cm^{-2}. This common catalyst loading was selected to simplify the comparison with other studies.[19] The concentration of solids (Ag + Nafion) in the ink was 0.01 g mL^{-1}. Note that we used an excess of ink to compensate for the loss of 30% ink during the deposition process. We homogenized the ink in a sonication bath for 30 min (USC500TH, VWR). We cut the GDL (SGL 39BC, SGL Carbon) to a size of 3.5 cm x 3 cm, dried it for 10 min at 120 °C, and weighed it in an airtight container (Kartell 034600 Polypropylene Weighing Bottles – 50 mL, Fisher Scientific). The sample was then covered with a 3 cm x 3 cm PTFE mask and fixed to the heating plate (130 °C) of the 2D-motorized stage. We sprayed the ink evenly onto the MPL side with an airbrush (Paasche TG3, Airbrush Services Almere, Netherlands). The sample was dried at 120 °C for 10 min and weighed after the deposition to determine the Ag loading.

Sample overview

Table 4.3 summarizes the different samples used for the experiments of this publication. The carbon-based GDE samples are identical with the sample from our previous work.[29,30]

Table 4.3: Sample overview for silver-based and carbon-based GDEs. The total thickness δ of the silver-based GDEs was determined with a thickness gauge. The δ of the carbon-based GDEs is based on the manufacturer data and our own estimation of the catalyst layer thickness (3.5 µm).[30]

Sample ID	GDE base	Loading mg Ag cm^{-2}	δ µm	Used in Figure	Determined metrics
Ag 114-1	Silver	254	419	4.2,4.9	θ, Δp_L^*, P_{CO_2})
Ag 114-2	Silver	236	390	4.3 a, 4.4 a, 4.16	FE_{CO}
Ag 114-3	Silver	249	413	4.2, 4.6, 4.7 , 4.17 – 4.19, 4.21 – 4.23	k_{O_2}, FE_{CO}, θ
Ag 178-1	Silver	269	416	4.19, 4.23	FE_{CO}, θ
45	Carbon	1.2	330	4.2, 4.5	k_{O_2}, θ
47	Carbon	1.3	330	4.3 b, 4.4 c	FE_{CO}

ASSEMBLY OF THE 2-COMPARTMENT CO_2 ELECTROLYSIS CELL

The GDE samples were installed in the membraneless, 2-compartment flow cell (Figure 2.18) described in Chapter 2. [30]

ELECTRODE CHARACTERIZATION

The silver- and carbon-based GDEs were characterized with various methods before and after electrolysis.

Scanning electron microscope (SEM): Microstructure investigation

The GDE microstructure was visualized with a JSM-6010LA SEM (JEOL, Japan). The morphology was investigated with a secondary electron imaging (SEI) detector at an acceleration voltage of 5 kV and an electron beam spot size of 30. The elemental contrast was imaged with a backscattered electron composition (BEC) detector operated at 5 kV and a spot size of 35.

Sessile drop contact angle: Wettability assessment

We described the relevant wetting theory and experimental method in more detail in a previous publication. [30] The wettability of (external) surfaces was quantified with the sessile drop method. We recorded images of a 10 µL water droplet at five different locations of the sample (Figure 4.8 a and b). The static contact was extracted with the image processing software ImageJ and the Contact angle plugin. The contact angle was determined by marking the outline of the droplet and the intersection with the solid interface manually. An ellipse was fit to the outline of the droplet (Figure 4.8 c and d). The left and right ellipse angle, $\theta_{E,L}$ and $\theta_{E,R}$, were determined from the intersection of the ellipse tangents with the line of the solid interface. They are used to calculate the average ellipse angle, θ_E. The static contact angle, θ, is calculated with $180° - \theta = \theta_{E,L}$. The averaged θ for each sample is listed in Table 4.4. The complete list of contact angles can be found in the accompanying Excel file of the online version.

Table 4.4: Static contact angle, θ, average ± the corresponding standard error for at least five measurement locations on silver- and carbon-based GDEs.

Samples	θ
Before electrolysis	
Silver-based GDE (Sample Ag 114-1)	$141 \pm 4.3°$
Carbon-based GDE (Sample 45) – CFS	$149 \pm 1.1°$
Carbon-based GDE (Sample 45) – MPL	$153 \pm 0.9°$
Carbon-based GDE (Sample 45) – CL	$123 \pm 1.5°$
After electrolysis	
Silver-based GDE (Sample Ag 114-3: $-200\,mA\,cm^{-2}$)	$111 \pm 4.3°$
Silver-based GDE (Sample Ag 178-1: $-50\,mA\,cm^{-2}$)	$132 \pm 1.9°$

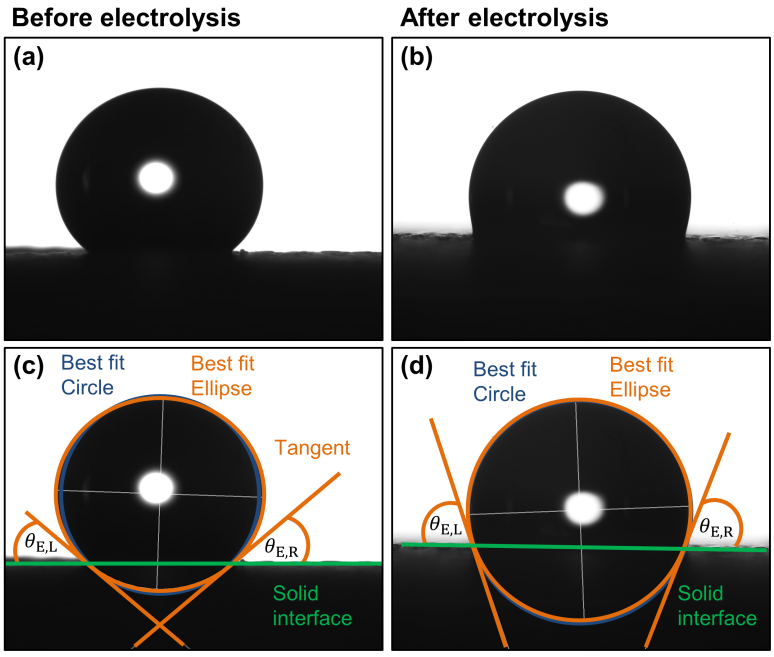

Figure 4.8: Data analysis example for static contact angle, θ, with sessile drop technique. (a) and (b): Raw data images. (c) and (d): Corresponding data processing images generated with ImageJ and the contact angle plugin. The angles $\theta_{E,L}$ and $\theta_{E,R}$ arise between the intersection of the tangents of the ellipse and the solid interface line. They are used to calculate the average ellipse angle, θ_E. The value of θ is calculated with $180° - \theta = \theta_{E,L}$.

Liquid breakthrough pressure: Flooding resistance
To measure the liquid breakthrough pressure at open circuit, Δp_L^*, the sample was installed in the 2-compartment flow cell (see Chapter 2, Figure 2.18). We closed off the outlet of the liquid compartment (see Chapter 2, Figure 2.17 a) and filled the compartment with water at a flow rate of 1 mL min^{-1}. We determined Δp_L^* by recording the differential pressure between the gas and liquid compartment when the first water droplet appeared at the surface of the sample (see Chapter 2, Figure 2.17 b). For the carbon-based GDE, two samples of uncoated SGL 39BC gas diffusion layers were used to determine the average Δp_L^*. The data for this material was reported in our previous publication. [30]

CO_2 Permeability constant: Convective mass transfer
To measure the CO_2 permeability constant, P_{CO_2}, the sample was installed in the 2-compartment flow cell (see Chapter 2, Figure 2.18). We supplied CO_2 at different flow rates and recorded the pressure drop across the sample (Figure 4.9 a). The gas was forced through the sample by closing off the outlet of both compartments. The values for P_{CO_2} were determined from the linear slope of the resulting pressure drop curve Figure 4.9 b according to Darcy's law. [30,52] We used an uncoated carbon-based GDL for the SGL 39BC sample. [30]

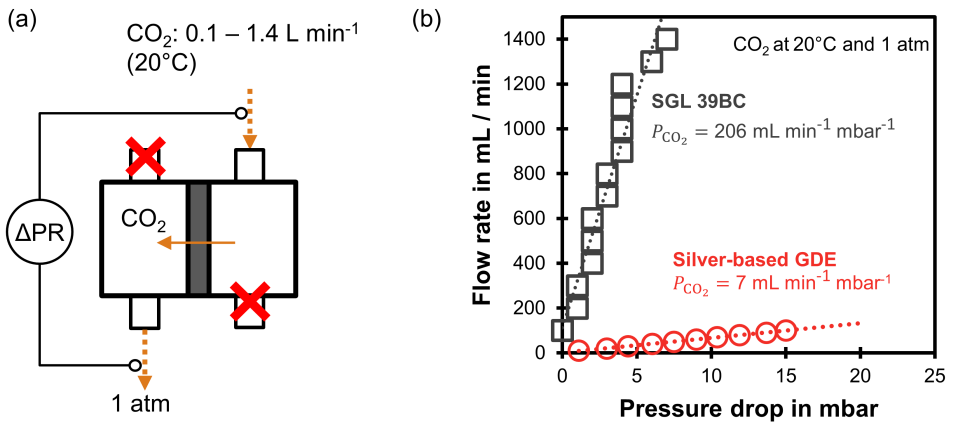

Figure 4.9: Convective mass transfer capacity: (a) Flow chart for measurement of CO_2 permeability constant, P_{CO_2}. (b) Resulting pressure drop curves to determine P_{CO_2} from the linear slope.

Limiting overall O_2 mass transfer coefficient: Diffusive mass transfer
We measured the limiting overall O_2 mass transfer coefficient, k_{O_2}, with the electrochemical procedure described in Chapter 2. [30] The oxygen from an air feed is reduced to hydroxide ions at the cathode GDE according to the oxygen reduction reaction (ORR) (see Chapter 2, Figure 2.30). A Nickel plate served as a counter electrode. We used 6 M KOH as the electrolyte due to its high conductivity. We balanced the pressure between the gas and the liquid compartment to achieve a flow-by regime, in which the transfer of O_2 from the gas bulk to the catalyst layer occurs primarily through diffusion. The cathode potential was recorded with a Ag/AgCl micro-reference electrode.

We performed linear sweep voltammetry from 0 V to −2 V vs. SHE with a scan rate of 20 mV s^{-1}. The limiting current density, j_{lim}, was derived from the plateau region of the scan, at which the ORR was limited by oxygen diffusion through the GDE (Figure 4.10). We only used a single scan to determine j_{lim} because the flooding due to electrowetting might influence on consecutive scans. The calculations to determine k_{O_2} are described in Chapter 2. The resulting k_{O_2} and all other numerical values of various calculation steps are listed in Table 4.5.

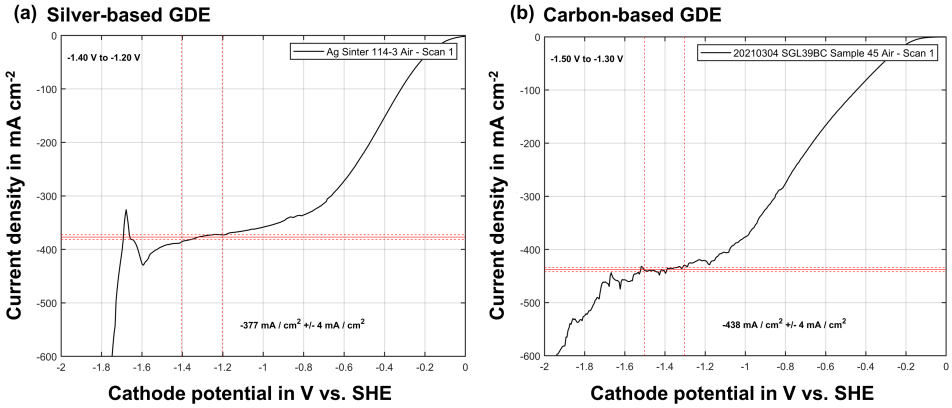

Figure 4.10: Limiting overall O_2 mass transfer coefficient: linear sweep voltammetry scans to determine the limiting current density plateau. The scan rate was $20\,\mathrm{mV\,s^{-1}}$. The limiting current density, j_{lim}, ± and its standard deviation $\sigma_{j_{\mathrm{lim}}}$ are indicated by the red horizontal lines within the manually determined potential window marked with the red vertical lines. (a) Silver-based GDE. (b) Carbon-based GDE.

Table 4.5: Data processing overview for limiting overall O_2 mass transfer coefficients, k_{O_2}. The absolute pressure of the gas feed is p_{G}. The potential window of the limiting current density plateau is between the lower limit, $E_{\mathrm{lim,lower}}$, and the upper limit, $E_{\mathrm{lim,upper}}$. The limiting current density is j_{lim} and its sample standard deviation is $\sigma_{j_{\mathrm{lim}}}$. The limiting O_2 molar flux is $\dot{n}_{O_2,\mathrm{lim}}$. The random error of the mass transfer coefficient is $\sigma_{k_{O_2}}$.

GDE	Unit	TGP-H-060	TGP-H-090
p_{G}	bar	1.49	1.37
$E_{\mathrm{lim,lower}}$	V vs. SHE	−1.4	−1.5
$E_{\mathrm{lim,upper}}$	V vs. SHE	−1.2	−1.3
j_{lim}	$\mathrm{mA\,cm^{-2}}$	−377	−464
$\sigma_{j_{\mathrm{lim}}}$	$\mathrm{mA\,cm^{-2}}$	±4	±4
$\dot{n}_{O_2,\mathrm{lim}}$	$10^{-6}\,\mathrm{mol\,cm^{-2}\,s^{-1}}$	0.98	1.13
k_{O_2}	$\mathrm{cm\,s^{-1}}$	0.076	0.096
$\sigma_{k_{O_2}}$	$\mathrm{cm\,s^{-1}}$	±0.001	±0.001

CO_2 ELECTROLYSIS EXPERIMENTS

Engineering of the CO_2 electrolysis setup

The CO_2 reduction experiments were carried out with the electrolysis setup shown in Figure 4.11. We used Labview (Version 2018, National Instruments) to record online data of the various sensors and to control the pump and the electronic valves.

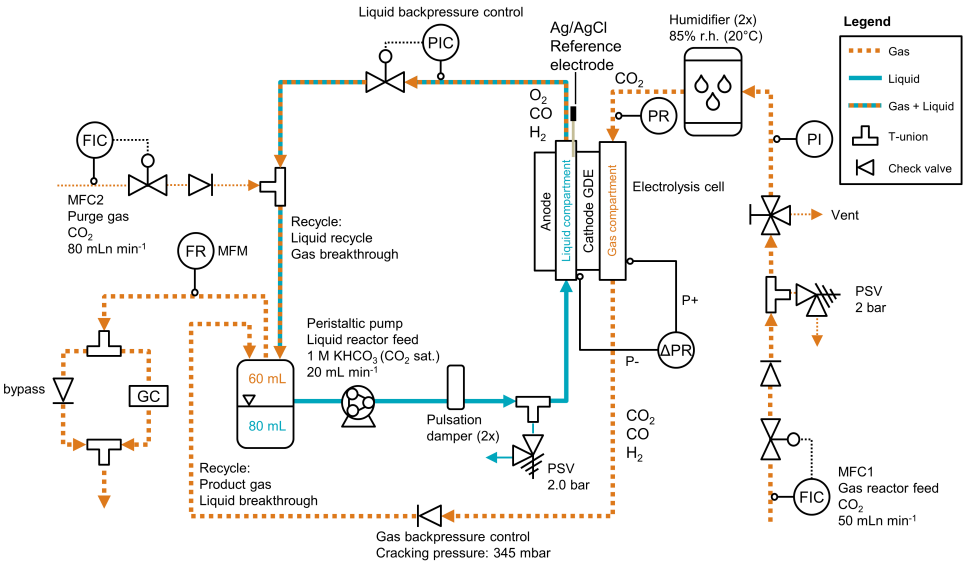

Figure 4.11: Extended process flow diagram for CO_2 electrolysis setup with differential pressure control. The gas flow rates were controlled with mass flow controllers (MFC). Check valves were used to prevent the backflow of liquid into the MFCs. Pressure safety valves (PSV) were installed in line to prevent the unexpected buildup of pressure. The gas feed pressure was measured with an analog pressure indicator (PI) and recorded after the humidifiers (PR). The differential pressure between the gas and the catholyte compartment was recorded with a differential pressure meter (ΔPR). The backpressure of the electrolyte stream was controlled with an electronic control valve (PIC). The product gases were collected from all process streams and combined in the head space of the electrolyte reservoir. Their combined flow rate was recorded (FR) with a mass flow meter (MFM) and the composition analyzed with a gas chromatography system (GC) to calculate the Faradaic efficiency.

Gas feed flow path

The CO_2 feed gas was supplied from a CO_2 cylinder. The gas flow rate was controlled and measured with a mass flow controller (MFC1) of the type F-201CV-500 from Bronkhorst (Netherlands). We passed the gas through two custom-made bubble columns in series to humidify the feed with water vapor (see Chapter 2, Figure 2.27 and Figure 2.28). The temperature and relative humidity of the gas feed was recorded after the humidification stage with a humidity sensor (Type: HC2A-S Hygroclip RV+T sensor; Supplier: Acin Instrumenten, Netherlands). The pressure of the gas feed was recorded with a Deltabar S pressure meter (Endress+Hauser, Switzerland). We used another Deltabar S to record the pressure difference between the gas compartment (positive terminal: P+) and the liquid compartment (negative terminal: P−). The backpressure of the gas outlet was set by a SS-CHS2-5 check valve (Swagelok, Netherlands) with a nominal cracking pressure of 345 mbar.

Electrolyte flow path

The 1 M $KHCO_3$ electrolyte saturated with CO_2 was prepared by diluting concentrated KOH (50 wt%, analytical grade, Alfa Aesar) to 1 M KOH. The CO_2 was bubbled through the solution until the pH value was stable. The bulk pH of the electrolyte was measured prior to the experiments and is listed in the accompanying Excel file

of the online version. The liquid lines and reactor were flushed before every experimental run. The electrolyte reservoir and liquid lines were filled with fresh electrolyte. We used a peristaltic pump (Type: Masterflex L/S peristaltic pump; Supplier: Cole Parmer) to recirculate the electrolyte through the reactor and the liquid lines with a flow rate of 20 mL min^{-1}. Two pulsation dampers (Types: FPD 1.06, FPD 1.10; Supplier: KNF, Switzerland) reduced the pressure fluctuations caused by the pump. We controlled the liquid back pressure with an electronic control valve (Type: P-502C-6K0R; Supplier: Bronkhorst, Netherlands).

Product gas flow path

Unreacted CO_2 and product gases left the reactor through the gas outlet and entered the head space of the electrolyte reservoir. Product gases forming on the catholyte side (CO, H_2) and the anode side (O_2) were carried out of the reactor by the electrolyte stream. We added a CO_2 purge gas stream to facilitate the transfer of product gases into the gas phase. The CO_2 purge gas stream further ensured that the electrolyte remained saturated with CO_2 during the experimental run. All the product gases were collected in the headspace of the electrolyte reservoir and passed through a mass flow meter (MFM) to record the flow rate (Type: F-111B-500; Supplier: Bronkhorst, Netherlands). The gas composition was analyzed with a gas chromatography system (Type: Compact GC 4.0; Supplier: Interscience, Netherlands).

Calculation of Faradaic efficiency

The calculation of the Faradaic efficiency is described in Chapter 2.

Experimental timeline for CO_2 reduction performance with current density steps
We measured the Faradaic efficiency and cathode potential for the silver-based GDE (Sample Ag 114-2) at three different current density steps (Figure 4.12). After installing the flow cell into the experimental setup and priming the fluid lines, we increased the liquid backpressure to achieve a flow-by regime at the GDE. We waited for 6 min after the start of each current density step (-10, -100, $-200\,mA\,cm^{-2}$) so the system could reach a steady state. For the first two current densities, we collected three GC injections. We carried out additional GC injections at $-200\,mA\,cm^{-2}$ to assess the effect of the observed flooding. The accompanying Excel sheet of the online version lists the exact GC injection times. The sheet also includes all measured process parameters, such as current density or fluid flow rates, and the resulting performance metrics like the Faradaic efficiency and electrical potentials.

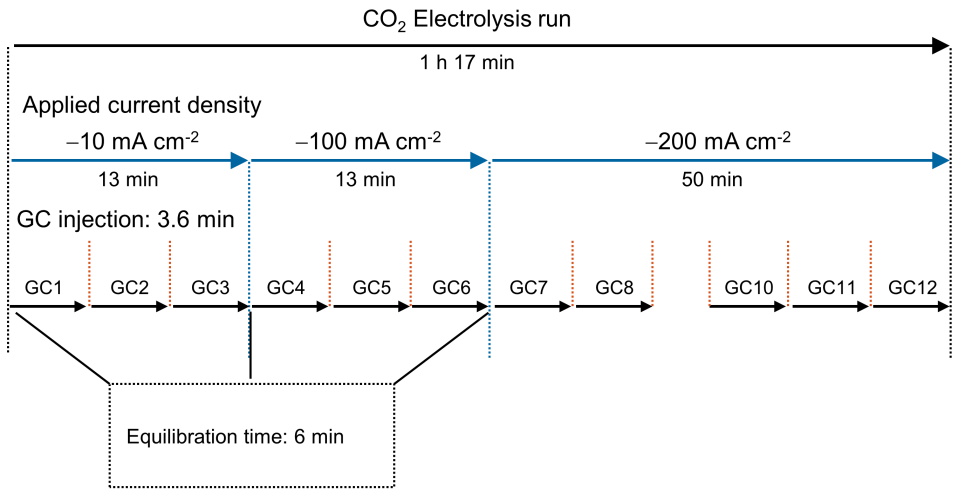

Figure 4.12: Experimental timeline of CO_2 electrolysis performance test with current density steps. After setting the potentiostat and balancing the pressure between liquid and gas compartment, we let the system equilibrate for 6 min. Then carried out at least three GC injections before continuing to the next current density step.

4.7.2. SUPPLEMENTARY RESULTS AND DISCUSSION

This section presents additional results for the SEM imaging, CO_2 performance test, and assessment of chemical changes to the electrodes after electrolysis.

MICROSTRUCTURE INVESTIGATION (SEM)

The Ag-based GDE exhibits circular patterns at low magnifications between 30x and 200x (Figure 4.13). These are created by the current collector gauze, which lies underneath the sintered coating. Larger pores with a diameter of up to 40 µm are visible in depressions at the surface, however, closer inspection revealed that these do not extend through the entire thickness of the electrode.

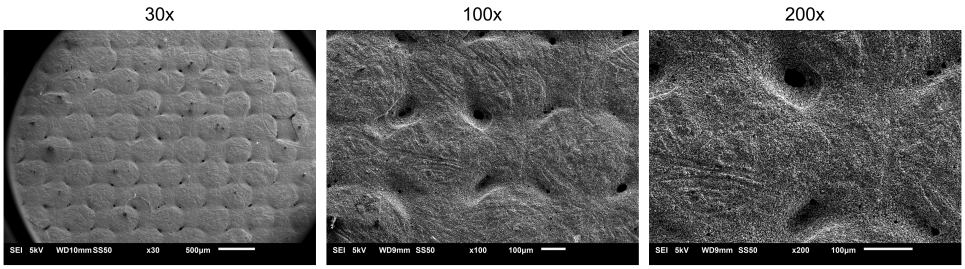

Figure 4.13: Structure of the silver-based GDE. The images were recorded with the secondary electron imaging (SEI) detector of the SEM at an acceleration voltage of 5 kV at magnifications 30x, 100x, and 200x.

At magnifications between 500x and 5000x, the structure of the sintered PTFE and silver particles becomes visible (Figure 4.14). Primary silver particles have a diameter in the range of 1 – 5 µm. They are sintered together to form a porous structure, which is visualized by the light grey domains in the BEC images. The dark domains indicate the PTFE, which is dispersed over the electrode surface.

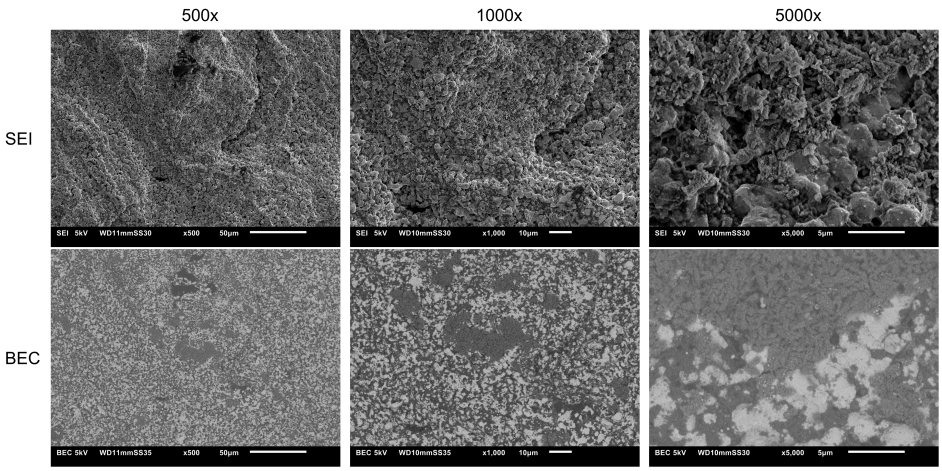

Figure 4.14: Structure of the Ag-based GDE's PTFE. Top: Secondary electron imaging (SEI) for morphology. Bottom: back-scattered electron composition (BEC) detector imaging of the corresponding SEI image for elemental contrast. All images were recorded with an acceleration voltage of 5 kV.

The carbon fiber substrate (CFS) of the carbon-based GDE has large pores between the PTFE-coated carbon fibers (Figure 4.15). The microporous layer (MPL) has many cracks and defects, which form during the manufacturing process. After spray-coating the catalyst layer (CL) on top of the MPL, dispersed silver particles are visible at the surface. The cracks of the MPL are not filled by the coating process.

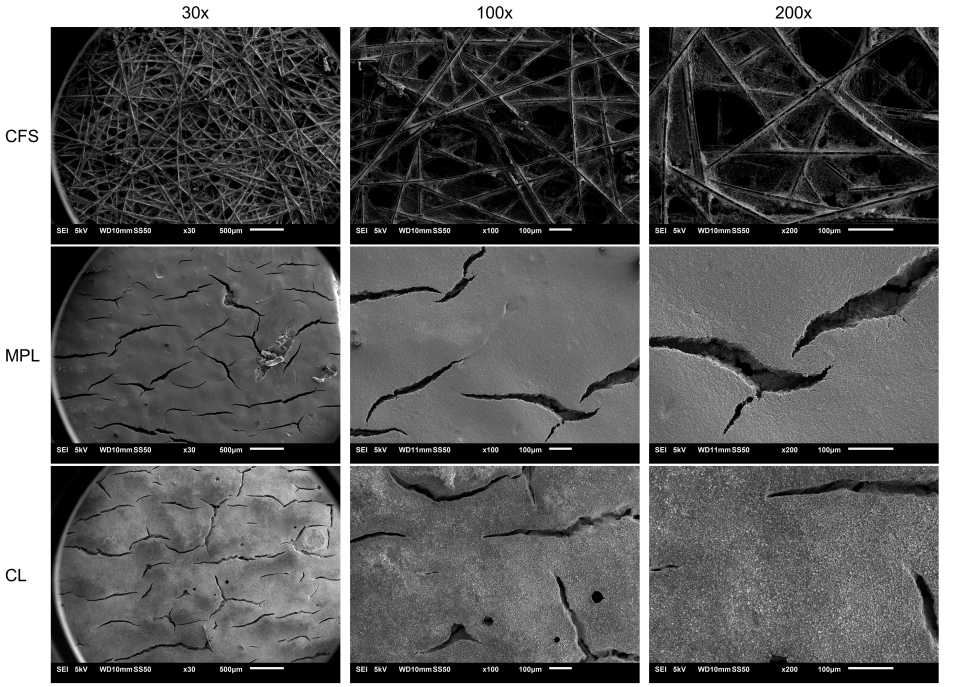

Figure 4.15: Morphology of the carbon-based GDE (SGL 39BC). The images of the carbon fiber substrate (CFS), the microporous layer (MPL), and the catalyst layer (CL) were recorded with the secondary electron imaging (SEI) detector of the SEM at an acceleration voltage of 5 kV at magnifications 30x, 100x, and 200x.

CO_2 REDUCTION PERFORMANCE WITH CURRENT DENSITY STEPS: FLOODING AND SALT FORMATION

We observed the breakthrough of electrolyte during the CO_2 electrolysis experiment with sample Ag 114-2 (Figure 4.4 a). First droplets started appearing at the gas side of the GDE about 10 min after applying a current density of $-200\,mA\,cm^{-2}$ ($-1.3\,V$ vs. RHE) (Figure 4.16 a). Over the course of the experiment, the droplets coalesced into larger drops and started to dry out (Figure 4.16 b). After disassembling the cell, potassium (bi)carbonate salt was present at the gas side of the GDE (Figure 4.16 c).

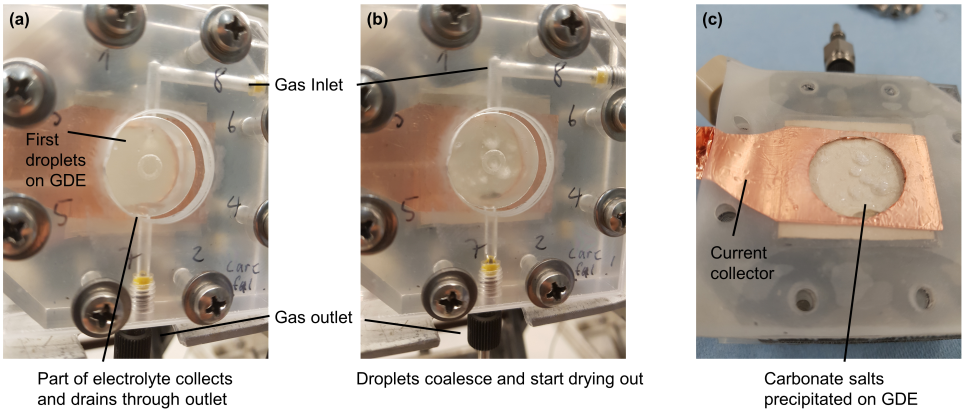

Figure 4.16: CO_2 electrolysis with silver-based GDE at $-200\,mA\,cm^{-2}$: electrolyte breakthrough and salt formation. (a) First electrolyte droplets start breaking through to the gas side of GDE. (b) Potassium (bi)carbonate salt starts precipitating after 40 min. (c) After disassembling: Gas side of GDE is covered with precipitated salt.

POST ELECTROLYSIS CHARACTERIZATION: ASSESSMENT OF CHEMICAL STABILITY

To assess the chemical stability of the silver-based electrodes, we operated two different samples at $-200\,mA\,cm^{-2}$ (Figure 4.17) and $-50\,mA\,cm^{-2}$ (Figure 4.4 b) and applied a series of characterization methods (XRD, SEM, and XPS).

We operated a silver-based GDE at $-200\,mA\,cm^{-2}$ in a gas flow-through mode (Figure 4.17). With this flow mode, we attempted to increase the mass transfer of CO_2 and reduce the saturation of the pore network through a higher gas overpressure.

The development of the cathode potential, $E_{Cath.}$, is shown in Figure 4.17 a. The initial $E_{Cath.}$ is more negative compared to the flow-by mode (Figure 4.17 a vs. Figure 4.4 a: $-1.8\,V$ compared to $-1.3\,V$ vs. RHE) because of CO_2 bubble resistance.[65] The $E_{Cath.}$ stabilized at $-1.4\,V$ vs. RHE (Figure 4.17 a). This may be due to an increase of catalytic interface for the HER as the pores are saturated with electrolyte, which reduces the local current density and the ohmic potential losses in the electrolyte.

The flow-through mode, however, is not effective because the electrolyte still floods the GDE and starts forming salts. The increasing saturation of the porous network hinders the flow of CO_2, which raised the gas overpressure from initially 50 mbar to 200 mbar when we stopped the experiment after 84 min (Figure 4.17 b). The gas flow-through can not prevent flooding because electrowetting leads to strongly hydrophilic pores, which apparently would require a much higher gas pressure to drain.

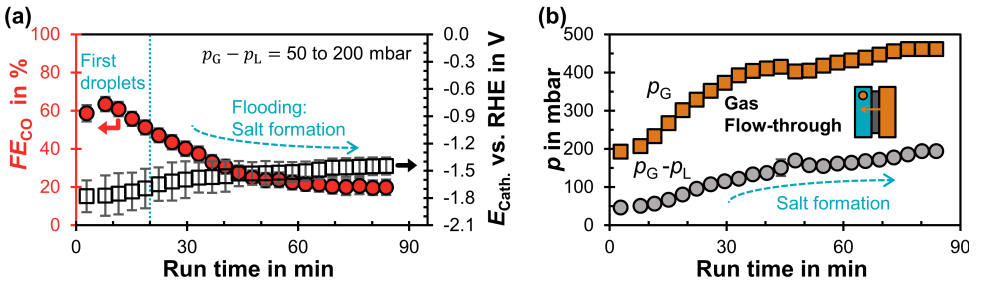

Figure 4.17: Chemical stability test of silver-based GDE at $-200\,mA\,cm^{-2}$ in gas flow-through mode. (a): Faradaic efficiency for CO, FE_{CO}, as a function of run time after starting the potentiostat. The cathode potential, $E_{Cath.}$, against the reversible hydrogen electrode (RHE) is plotted on the right y-axis. The potential was corrected for the ohmic potential drop between the reference electrode and the cathode. Every data point represents a single GC injection. The error bars represent the estimated standard error. (b): Gas compartment pressure, p_G, and pressure difference between gas and liquid compartment, $p_G - p_L$, increased steadily over the course of the experiment.

XRD: No changes to silver bulk composition

The X-ray diffractograms before and after electrolysis consist of a single cubic Ag^0 phase (Figure 4.18 a). The reflections at $2\theta = 44.6°$, 51.9°, 76.6°, 93.2°, and 98.9° were attributed to the (111), (200), (220), (311), and (222) facets of Ag^0, respectively. FWHM (full width at half maximum) analysis of Ag^0 reflections suggest that Ag^0 crystalline domain size was not altered by the electrochemical treatment (Table 4.6).

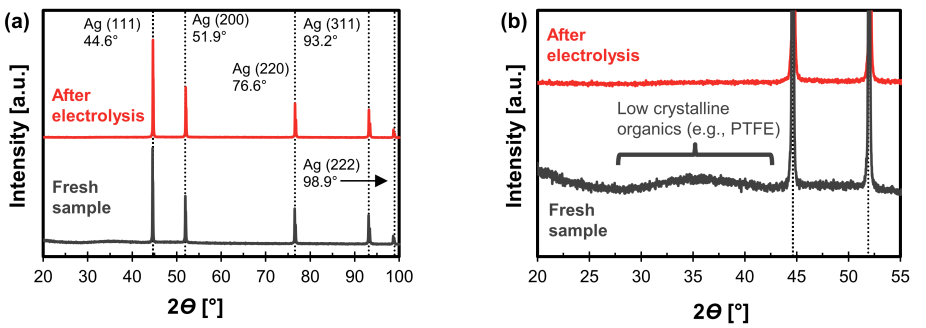

Figure 4.18: X-ray diffractograms for fresh silver-based GDE) and after electrolysis at $-200\,mA\,cm^{-2}$. (a): Ag diffraction pattern. The Powder Diffraction File©(PDF)-2004 database of the International Centre for Diffraction Data was used for peak assignment. Both samples exhibited diffraction patterns of cubic Ag^0 (PDF #87-0720) with standard peak ratios and no variation in crystalline parameters regardless of treatment. (b): Zoom-in on $2\theta = 30° - 55°$. Broad peak caused by low crystalline organics compound(s) (e.g., PTFE) between $2\theta = 30° - 40°$.

A small shoulder between 30° – 40°, visible in fresh GDE, became less prominent in the spent electrode (Figure 4.18 b). This peak can be attributed to low crystalline organics constituting GDEs (e.g. PTFE). No definitive assignment of PTFE peaks could be made due to the low intensity of the these reflections. We hypothesize that the disappearance of the 30° – 40° band might be indicative of PTFE degradation, which was also observed by the complementary analysis techniques (SEM, XPS).

Table 4.6: Silver-based GDE: FWHM (full width at half maximum) analysis for fresh sample and spent sample after electrolysis at $-200\,\mathrm{mA\,cm^{-2}}$.

FWHM	$2\theta = 44.6°$	$2\theta = 51.9°$	$2\theta = 76.6°$
Fresh sample	0.169°	0.195°	0.265°
After electrolysis	0.168°	0.192°	0.252°

SEM: PTFE surface coverage changes at high cathode overpotential
Additional SEM images recorded with the BEC detector show that GDE surface is covered with less PTFE after being operated at $-200\,\mathrm{mA\,cm^{-2}}$ and $E_{\mathrm{Cath.}}$ $-1.8\,\mathrm{V}$ vs. RHE (Figure 4.19). In contrast, the GDE operated at $-50\,\mathrm{mA\,cm^{-2}}$ ($-1.0\,\mathrm{V}$ vs. RHE) looks much more similar to the surface before electrolysis.

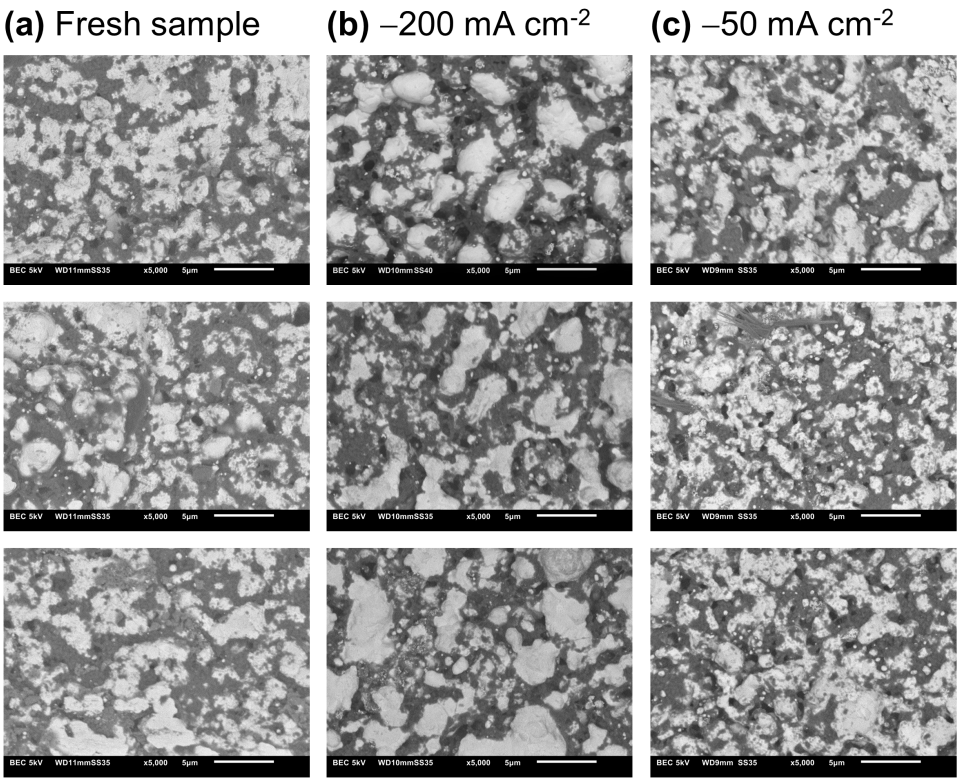

Figure 4.19: Surface coverage with PTFE: SEM shows the elemental contrast with images from the BEC detector (light grey domains: Ag, dark grey domains: PTFE, carbon). The length of the scale bar for a magnification of 5000x is 5 µm. (a): Surface of unused sample. (b): After electrolysis at $-200\,\mathrm{mA\,cm^{-2}}$ for 84 min. (c): After electrolysis at $-50\,\mathrm{mA\,cm^{-2}}$ for 89 min. The images of the electrolysis samples (b) and (c) were taken from the side facing the electrolyte.

XPS: Degradation and removal of PTFE

The surface elemental composition and chemical state of electrodes was evaluated by XPS. Bulk composition and element distribution was derived from the XPS depth profiles.

Elemental composition analysis

The surface chemical composition of GDEs was derived from wide-energy XPS spectra recorded at three separate locations for each sample. The average elemental composition and its standard deviation is summarized in Table 4.7. According to the elemental analysis, the major elements present are C, F, Ag and O, in line with expectations. Used GDE samples had impurities of K and Cu originating from the electrolyte and the copper current collector, respectively. Also, Ca, S, Si and Cl impurities were found in the miniscule amounts. Due to the strong overlap between C 1s / K 2p and Ag 3d / K 2s (Figure 4.21 a), along with a large difference in relative sensitivity factors of those spectral regions, the atomic concentrations of C, Ag and K were adjusted based on the corresponding core-level spectra.

Table 4.7: Elemental composition for silver-based GDEs. (a) Fresh GDE sample. (b) After electrolysis at $-200\,\mathrm{mA\,cm^{-2}}$ for 84 min with at −1.8 V vs. RHE. (c) After electrolysis at $-50\,\mathrm{mA\,cm^{-2}}$ for 89 min at −1.0 V vs. RHE. For the electrolysis samples (b) and (c), the analyzed areas were facing the electrolyte during electrolysis. The average elemental concentration ± the standard error was determined from three analysis locations per sample.

Element	(a) Fresh sample	(b) $-200\,\mathrm{mA\,cm^{-2}}$	(c) $-50\,\mathrm{mA\,cm^{-2}}$
Ag	3.8 ± 0.05 at.%	3.7 ± 0.60 at.%	5.9 ± 0.27 at.%
C	36.3 ± 0.40 at.%	48.7 ± 1.07 at.%	35.4 ± 0.43 at.%
F	57.8 ± 0.48 at.%	40.1 ± 1.08 at.%	51.3 ± 0.27 at.%
Cu	n.a.	0.2 ± 0.05 at.%	0.2 ± 0.02 at.%
O	1.2 ± 0.08 at.%	5.8 ± 0.45 at.%	3.5 ± 0.20 at.%
Ca	0.4 ± 0.03 at.%	0.1 ± 0.004 at.%	n.a.
S	0.3 ± 0.03 at.%	n.a.	n.a.
Si	n.a.	0.8 ± 0.05 at.%	0.9 ± 0.06 at.%
Cl	0.2 ± 0.01 at.%	n.a.	n.a.
K	n.a.	0.7 ± 0.10 at.%	2.6 ± 0.19 at.%

Ag reference foil

Sputter-cleaned Ag foil reference was used to derive the intrinsic asymmetry of Ag^0 peaks in the Ag 3d region (Figure 4.20 a). The foil was cleaned *in situ* by repeated high-energy ion beam sputtering until complete disappearance of O 1s peaks. The Ag oxidation state was confirmed by the modified Auger parameter α = 726.1 eV (Figure 4.20 b). The Ag $3d_{5/2}$ component of the sputter-cleaned foil was adapted as a line shape for Ag $3d_{3/2}$ component with a set of constrains listed in Table 4.8.

Table 4.8: XPS data processing: Ag 3d fitting parameters of Ag^0 reference foil. Indices at parenthesis refer to the maximum allowed deviation (eV) in the constrain.

Ag 3d fitting	Line shape	Position	FWHM	Area
Ag^0 $3d_{5/2}$	Ag^0 ref $3d_{5/2}$	$(368.5)_{0.5}$ eV	$(1.0)_{0.2}$ eV	n.a.
Ag^0 $3d_{3/2}$	Ag^0 ref $3d_{5/2}$	Ag^0 $3d_{5/2}$ + 6 eV	Ag^0 $3d_{5/2}$	$3d_{5/2}$ * 0.68
Ag^0 sh-up $3d_{5/2}$	GL(30)	Ag^0 $3d_{5/2}$ + (3.8)0.2 eV	$(Ag^0\ 3d_{5/2} * 1.2)_{0.2}$	n.a.
Ag^0 sh-up $3d_{3/2}$	GL(30)	Ag^0 sh-up $3d_{5/2}$ + 6 eV	Ag^0 sh-up $3d_{5/2}$	$3d_{5/2}$ * 0.68
Ag_2O $3d_{5/2}$	GL(30)	Ag^0 $3d_{5/2}$ – $(0.8)_{0.2}$ eV	$(1.5)_{0.2}$ eV	n.a.
Ag_2O $3d_{3/2}$	GL(30)	Ag_2O $3d_{5/2}$ + 6 eV	Ag_2O $3d_{5/2}$	$3d_{5/2}$ * 0.68

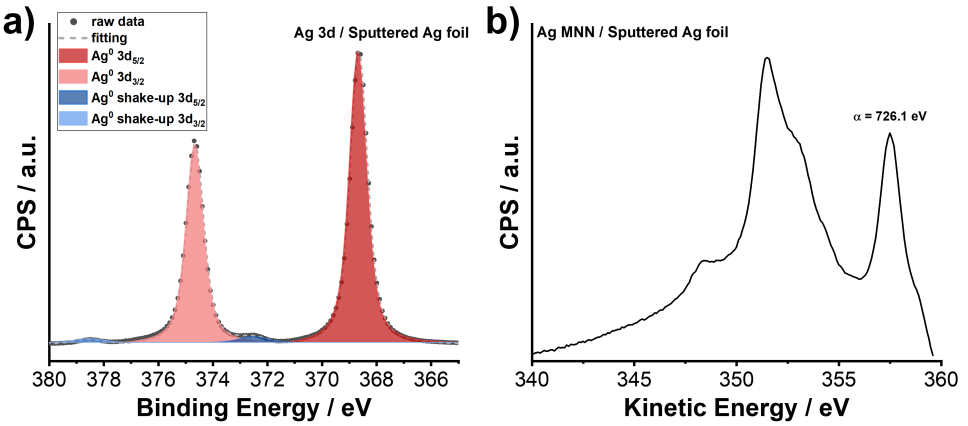

Figure 4.20: (a): Ag 3d and (b): Ag MMN XPS spectra of Ar^+-sputtered Ag reference foil.

Silver-based GDE: Chemical state of silver

Ag 3d spectra of fresh and spent silver-based GDEs suggested that silver is mostly present in its metallic form, yielding asymmetric peaks with the binding energy, BE, of $BE_{5/2} = 368.2 \pm 0.1$ eV (Figure 4.21 a).

This assignment is supported by the values of modified Auger parameters ($\alpha = 725.9 \pm 0.1$ eV), characteristic for Ag^0 (Figure 4.21 b).[66] A presence of native Ag_2O was evident in the fresh GDE sample (Figure 4.21 b), which can be seen as a second component in the surface-sensitive region of Ag MNN ($\alpha_2 = 724.4 \pm 0.1$ eV). However, the fraction of Ag_2O was not affected by the electrolysis significantly, accounting for 2 – 6% of all silver in fresh and spent GDEs. A small component at $BE \approx 377$ eV in spent samples was assigned to the overlapping K 2s spectral region, originating from the residual electrolyte.

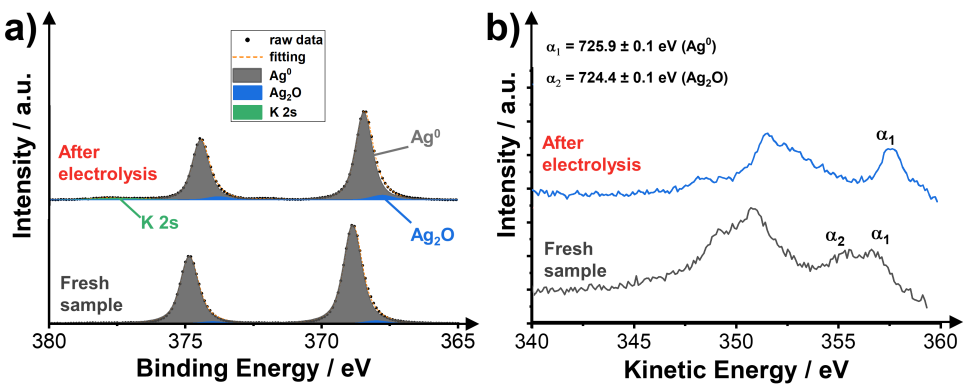

Figure 4.21: (a) Ag 3d and (b) Ag MNN XPS spectra of silver-based GDE before and after electrolysis at $-200\,mA\,cm^{-2}$.

Silver-based GDE: Chemical state of carbon

The C 1s XPS spectra were used to observe the change in carbon bonds distribution. The C 1s spectrum of fresh Ag-GDE is primarily composed of CR (C–C, C–H) and CF_2 peaks with BE of 284.8 eV and 291.8 eV, respectively (Figure 4.22). A spectral region between 286 eV and 290 eV features multiple minor peaks which can be assigned to various forms of oxygenated carbon (COR, C=O, COOR).

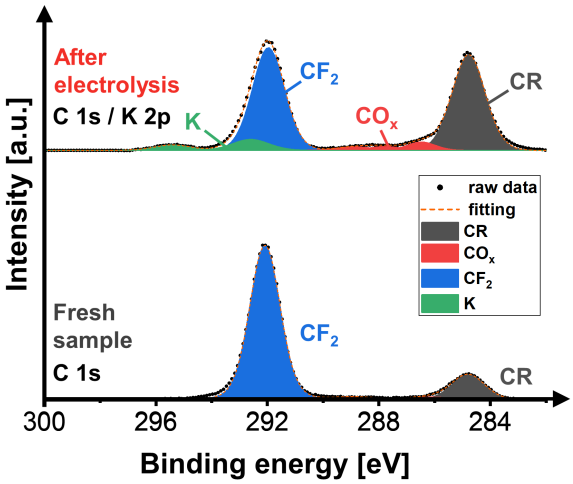

Figure 4.22: Chemical state of carbon before and after electrolysis at $-200\,mA\,cm^{-2}$: XPS spectrum in C 1s region (overlapping with K 2p). Residual amounts of K remain present after rinsing the $KHCO_3$ electrolyte off after electrolysis.

The relative amount of CF_2 bonds was strongly reduced by electrolysis (Table 4.9). The shift to CR and CO_x bonds is especially significant for the sample that was subjected to $j = -200\,mA\,cm^{-2}$ ($-1.8\,V$ vs. RHE). As we know from Table 4.7, the used samples exhibit an increased oxygen concentration relative to the fresh sample (4 – 6 at.% vs. 1 at.%.) As Ag was not oxidized significantly during electrolysis (Figure 4.21), the additional oxygen is present in the form additional CO_x bonds, which probably originate from residual $KHCO_3$ electrolyte salts (Table 4.9).

Table 4.9: Relative fraction of carbon bond types: carbon–fluorine bonds (CF_2), which are present in PTFE, carbon–oxygen bonds (CO_x: COR, CO, or COOR), and saturated C–R bonds like C–C or C–H as a share of all carbon bonds C–X. (a) Fresh GDE sample. (b) After electrolysis at $-200\,mA\,cm^{-2}$ for 84 min ($-1.8\,V$ vs. RHE). (c) After electrolysis at $-50\,mA\,cm^{-2}$ for 89 min ($-1.0\,V$ vs. RHE). For the electrolysis samples (b) and (c), the analyzed areas were facing the electrolyte during electrolysis.

Carbon bond type	(a) Fresh sample	(b) $-200\,mA\,cm^{-2}$	(c) $-50\,mA\,cm^{-2}$
CF_2 / C–X	84 ± 1.6%	45 ± 1.3%	76 ± 0.6%
CO_x / C–X	4 ± 0.4%	7 ± 0.5%	4.0 ± 0.1%
CR / C–X	13 ± 1.2%	48 ± 1.2%	20%

Depth profile analysis

The XPS depth profiles of the silver-based GDE shows a significant change in chemical composition after electrolysis at $-200\,mA\,cm^{-2}$ with an initial cathode potential of $-1.8\,V$ vs. RHE (Figure 4.23 a – c). In contrast, the silver-based GDE operated at $-50\,mA\,cm^{-2}$ ($-1.0\,V$ vs. RHE) shows no significant decrease in F or increase in Ag compared to the fresh sample (Figure 4.23 d – f). We note that the concentration for the $-50\,mA\,cm^{-2}$ experiment (Figure 4.23 d – f) are more homogeneous over the depth profile compared to the fresh sample (Figure 4.23 a – c). The reason for this deviation might be that the profiles were recorded from two different sample batches ($-200\,mA\,cm^{-2}$ experiment: Ag 114-3 and $-50\,mA\,cm^{-2}$ experiment: Ag 178-1).

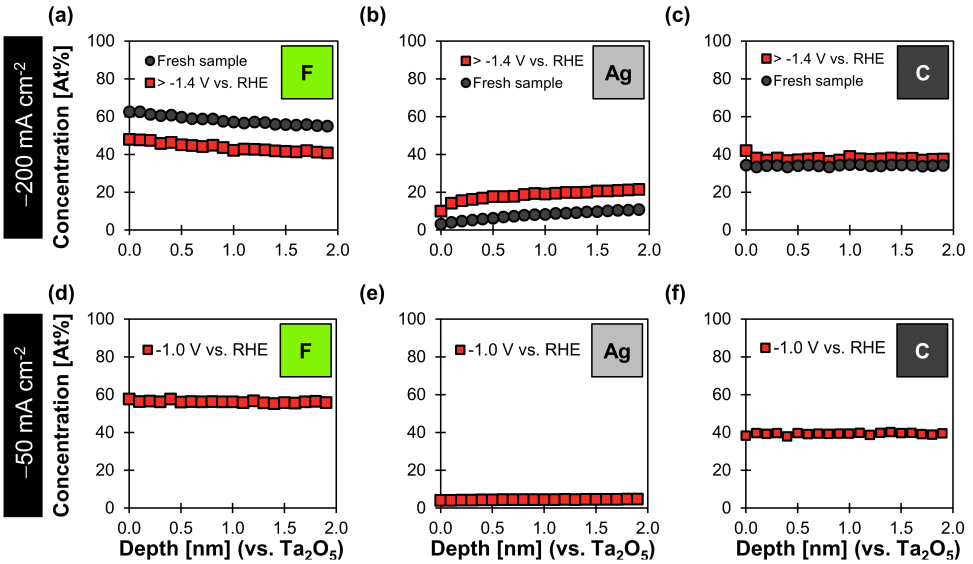

Figure 4.23: XPS depth profiles of silver-based GDEs. The x-axis shows the depth profile calibrated against a Ta_2O_5 standard sputtered with Ar^+ ions. The y-axis shows the relative atomic concentrations of F, Ag, and C (other elements were not measured in this measurement mode). (a), (b), (c): Fresh sample and sample after electrolysis at $-200\,mA\,cm^{-2}$ for 84 min ($-1.8\,V$ vs. RHE). (d), (e), (f): After electrolysis at $-50\,mA\,cm^{-2}$ for 89 min ($-1.0\,V$ vs. RHE).

These findings suggest that PTFE degrades and/or is removed from the GDE surface. The homogeneous loss of F over the profile is in alignment with the reductive elimination mechanism proposed by Shapoval *et al.*.[64] According to this mechanism, F^- is eliminated below a cathodic potential of $-1.3\,V$ vs. RHE and carbonaceous degradation products are left behind (Figure 4.24).

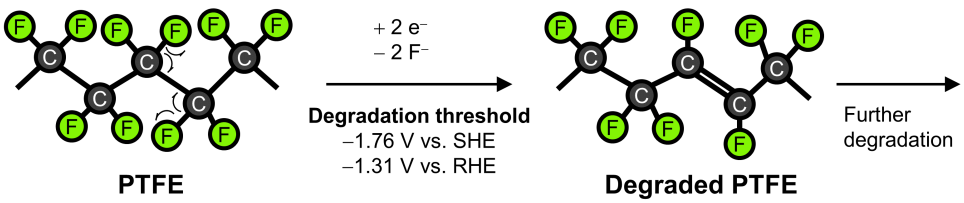

Figure 4.24: Cathodic reduction of PTFE: Shapoval *et al.*.[64] proposed that C–F bonds in sterically stressed sections of the polymer are susceptible to reduction and elimination of the fluorine atom. They reported a degradation threshold of −1.76 V vs. SHE, which corresponds to a cathode potential of −1.31 V vs. RHE in 1 M $KHCO_3$ (pH = 7.56).

4.8. ACKNOWLEDGEMENTS

The authors are grateful for the engineering support provided by Christiaan Schinkel, Stefan ten Hagen, Duco Bosma, and Bart Boshuizen. This research received funding from the Netherlands Organization for Scientific Research (NWO) under project number 733.000.008 in the framework of the Solar to Products programme co-funded by Shell Global Solutions International B.V.. David Franzen, Barbara Ellendorff and Thomas Turek acknowledge financial support by the German Research Foundation (DFG) in the framework of the research unit "Multi-scale analysis of complex three-phase systems: oxygen and CO_2 reduction" (FOR 2397, grant number 276655287).

REFERENCES

[1] P. De Luna, C. Hahn, D. Higgins, S. A. Jaffer, T. F. Jaramillo, and E. H. Sargent, *What would it take for renewably powered electrosynthesis to displace petrochemical processes?* Science **364**, eaav3506 (2019).

[2] M. G. Kibria, J. P. Edwards, C. M. Gabardo, C.-T. Dinh, A. Seifitokaldani, D. Sinton, and E. H. Sargent, *Electrochemical CO_2 reduction into chemical feedstocks: From mechanistic electrocatalysis models to system design,* Advanced Materials **31**, 1807166 (2019).

[3] D. W. Keith, G. Holmes, D. S. Angelo, and K. Heidel, *A process for capturing CO_2 from the atmosphere,* Joule **2**, 1573 (2018).

[4] W. A. Smith, T. Burdyny, D. A. Vermaas, and H. Geerlings, *Pathways to industrial-scale fuel out of thin air from CO_2 electrolysis,* Joule **3**, 1822 (2019).

[5] R. Sharifian, R. M. Wagterveld, I. A. Digdaya, C. Xiang, and D. A. Vermaas, *Electrochemical carbon dioxide capture to close the carbon cycle,* Energy & Environmental Science **14**, 781 (2021).

[6] G. Hammond and M. Newborough, *Glasgow climate pact: a step on the way towards a lower carbon dioxide world,* in *Proceedings of the Institution of Civil Engineers-Civil Engineering*, Vol. 175 (Thomas Telford Ltd) pp. 8–8.

[7] Y. Y. Birdja, E. Pérez-Gallent, M. C. Figueiredo, A. J. Göttle, F. Calle-Vallejo, and M. T. M. Koper, *Advances and challenges in understanding the electrocatalytic conversion of carbon dioxide to fuels,* Nature Energy **4**, 732 (2019).

[8] R. I. Masel, Z. Liu, H. Yang, J. J. Kaczur, D. Carrillo, S. Ren, D. Salvatore, and C. P. Berlinguette, *An industrial perspective on catalysts for low-temperature CO_2 electrolysis,* Nature nanotechnology , 118–128 (2021).

[9] D. Higgins, C. Hahn, C. Xiang, T. F. Jaramillo, and A. Z. Weber, *Gas-diffusion electrodes for carbon dioxide reduction: A new paradigm,* ACS Energy Letters **4**, 317 (2019).

[10] D. M. Weekes, D. A. Salvatore, A. Reyes, A. Huang, and C. P. Berlinguette, *Electrolytic CO_2 reduction in a flow cell,* Accounts of Chemical Research **51**, 910 (2018).

[11] E. W. Lees, B. A. W. Mowbray, F. G. L. Parlane, and C. P. Berlinguette, *Gas diffusion electrodes and membranes for CO_2 reduction electrolysers,* Nature Reviews Materials **7**, 55 (2022).

[12] Y. Chen, A. Vise, W. E. Klein, F. C. Cetinbas, D. J. Myers, W. A. Smith, T. G. Deutsch, and K. C. Neyerlin, *A robust, scalable platform for the electrochemical conversion of CO_2 to formate: Identifying pathways to higher energy efficiencies,* ACS Energy Letters **5**, 1825 (2020).

[13] B. Endrődi, E. Kecsenovity, A. Samu, T. Halmágyi, S. Rojas-Carbonell, L. Wang, Y. Yan, and C. Janáky, *High carbonate ion conductance of a robust PiperION membrane allows industrial current density and conversion in a zero-gap carbon dioxide electrolyzer cell,* Energy & Environmental Science , 4098 (2020).

[14] R. B. Kutz, Q. Chen, H. Yang, S. D. Sajjad, Z. Liu, and I. R. Masel, *Sustainion imidazolium-functionalized polymers for carbon dioxide electrolysis,* Energy Technology **5**, 929 (2017).

[15] F. P. G. De Arquer, C.-T. Dinh, A. Ozden, J. Wicks, C. McCallum, A. R. Kirmani, D.-H. Nam, C. Gabardo, A. Seifitokaldani, and X. Wang, *CO_2 electrolysis to multicarbon products at activities greater than 1 A cm^{-1}*, Science **367**, 661 (2020).

[16] C.-T. Dinh, T. Burdyny, M. G. Kibria, A. Seifitokaldani, C. M. Gabardo, F. P. García de Arquer, A. Kiani, J. P. Edwards, P. De Luna, O. S. Bushuyev, C. Zou, R. Quintero-Bermudez, Y. Pang, D. Sinton, and E. H. Sargent, *CO_2 electroreduction to ethylene via hydroxide-mediated copper catalysis at an abrupt interface,* Science **360**, 783 (2018).

[17] H. Yang, J. J. Kaczur, S. D. Sajjad, and R. I. Masel, *Electrochemical conversion of CO_2 to formic acid utilizing sustainion™ membranes,* Journal of CO_2 Utilization **20**, 208 (2017).

[18] H.-R. M. Jhong, S. Ma, and P. J. Kenis, *Electrochemical conversion of CO_2 to useful chemicals: current status, remaining challenges, and future opportunities,* Current Opinion in Chemical Engineering **2**, 191 (2013).

[19] B. Endrődi, G. Bencsik, F. Darvas, R. Jones, K. Rajeshwar, and C. Janáky, *Continuous-flow electroreduction of carbon dioxide,* Progress in Energy and Combustion Science **62**, 133 (2017).

[20] S. Park, J.-W. Lee, and B. N. Popov, *A review of gas diffusion layer in PEM fuel cells: Materials and designs,* International Journal of Hydrogen Energy **37**, 5850 (2012).

[21] A. El-kharouf, T. J. Mason, D. J. L. Brett, and B. G. Pollet, *Ex-situ characterisation of gas diffusion layers for proton exchange membrane fuel cells,* Journal of Power Sources **218**, 393 (2012).

[22] D. A. Salvatore, D. M. Weekes, J. He, K. E. Dettelbach, Y. C. Li, T. E. Mallouk, and C. P. Berlinguette, *Electrolysis of gaseous CO_2 to CO in a flow cell with a bipolar membrane,* ACS Energy Letters **3**, 149 (2017).

[23] B. De Mot, M. Ramdin, J. Hereijgers, T. J. Vlugt, and T. Breugelmans, *Direct water injection in catholyte-free zero-gap carbon dioxide electrolyzers,* ChemElectroChem **7**, 3839 (2020).

[24] B. Endrődi, E. Kecsenovity, A. Samu, F. Darvas, R. V. Jones, V. Török, A. Danyi, and C. Janáky, *Multilayer electrolyzer stack converts carbon dioxide to gas products at high pressure with high efficiency,* ACS Energy Letters **4**, 1770 (2019).

[25] B. Endrődi, A. Samu, E. Kecsenovity, T. Halmágyi, D. Sebők, and C. Janáky, *Operando cathode activation with alkali metal cations for high current density operation of water-fed zero-gap carbon dioxide electrolysers,* Nature Energy **6**, 439 (2021).

[26] I. V. Zenyuk, D. Y. Parkinson, G. Hwang, and A. Z. Weber, *Probing water distribution in compressed fuel-cell gas-diffusion layers using X-ray computed tomography,* Electrochemistry Communications **53**, 24 (2015).

[27] S. Jovanovic, R. Krause, A. Lüken, J. Ackermann, S. Merz, P. Jakes, R.-A. Eichel, and J. Granwehr, *Post-test raman investigation of silver based gas diffusion electrodes,* Journal of The Electrochemical Society **167**, 086505 (2020).

[28] T. Turek, I. Moussallem, A. Bulan, N. Schmitz, and P. Weuta, *Oxygen-consuming electrode with multilayer catalyst coating and process for the production thereof,* (2016), US Patent 9,243,337 B2.

[29] L. M. Baumgartner, C. I. Koopman, A. Forner-Cuenca, and D. A. Vermaas, *When flooding is not catastrophic – woven gas diffusion electrodes enable stable CO_2 electrolysis,* ACS Applied Energy Materials , 15125 (2022).

[30] L. M. Baumgartner, C. I. Koopman, A. Forner-Cuenca, and D. A. Vermaas, *Narrow pressure stability window of gas diffusion electrodes limits the scale-up of CO_2 electrolyzers,* ACS Sustainable Chemistry & Engineering **10**, 4683 (2022).

[31] D. Kopljar, A. Inan, P. Vindayer, N. Wagner, and E. Klemm, *Electrochemical reduction of CO_2 to formate at high current density using gas diffusion electrodes,* Journal of Applied Electrochemistry **44**, 1107 (2014).

[32] M. E. Leonard, L. E. Clarke, A. Forner-Cuenca, S. M. Brown, and F. R. Brushett, *Investigating electrode flooding in a flowing electrolyte, gas-fed carbon dioxide electrolyzer,* ChemSusChem **13**, 400 (2019).

[33] N. Furuya and H. Aikawa, *Comparative study of oxygen cathodes loaded with Ag and Pt catalysts in chlor-alkali membrane cells,* Electrochimica Acta **45**, 4251 (2000).

[34] T. Haas, R. Krause, R. Weber, M. Demler, and G. Schmid, *Technical photosynthesis involving CO_2 electrolysis and fermentation,* Nature Catalysis **1**, 32 (2018).

[35] P. Jeanty, C. Scherer, E. Magori, K. Wiesner-Fleischer, O. Hinrichsen, and M. Fleischer, *Upscaling and continuous operation of electrochemical CO_2 to CO conversion in aqueous solutions on silver gas diffusion electrodes,* Journal of CO_2 Utilization **24**, 454 (2018).

[36] B. De Mot, J. Hereijgers, M. Duarte, and T. Breugelmans, *Influence of flow and pressure distribution inside a gas diffusion electrode on the performance of a flow-by CO_2 electrolyzer,* Chemical Engineering Journal **378**, 122224 (2019).

[37] K. Yang, R. Kas, W. A. Smith, and T. Burdyny, *Role of the carbon-based gas diffusion layer on flooding in a gas diffusion electrode cell for electrochemical CO_2 reduction,* ACS Energy Letters **6**, 33 (2021).

[38] S. Hernandez-Aldave and E. Andreoli, *Oxygen depolarised cathode as a learning platform for CO_2 gas diffusion electrodes,* Catalysis Science & Technology (2022), 10.1039/D2CY00443G.

[39] I. Moussallem, J. Jörissen, U. Kunz, S. Pinnow, and T. Turek, *Chlor-alkali electrolysis with oxygen depolarized cathodes: history, present status and future prospects,* Journal of Applied Electrochemistry **38**, 1177 (2008).

[40] T. Morimoto, K. Suzuki, T. Matsubara, and N. Yoshida, *Oxygen reduction electrode in brine electrolysis,* Electrochimica Acta **45**, 4257 (2000).

[41] M. Sugiyama, K. Saiki, A. Sakata, H. Aikawa, and N. Furuya, *Accelerated degradation testing of gas diffusion electrodes for the chlor-alkali process,* Journal of applied electrochemistry **33**, 929 (2003).

[42] N. Wagner, M. Schulze, and E. Gülzow, *Long term investigations of silver cathodes for alkaline fuel cells,* Journal of Power Sources **127**, 264 (2004).

[43] I. Moussallem, S. Pinnow, N. Wagner, and T. Turek, *Development of high-performance silver-based gas-diffusion electrodes for chlor-alkali electrolysis with oxygen depolarized cathodes,* Chemical Engineering and Processing: Process Intensification **52**, 125 (2012).

[44] D. Franzen, B. Ellendorff, M. C. Paulisch, A. Hilger, M. Osenberg, I. Manke, and T. Turek, *Influence of binder content in silver-based gas diffusion electrodes on pore system and electrochemical performance,* Journal of Applied Electrochemistry **49**, 705 (2019).

[45] M. C. Paulisch, M. Gebhard, D. Franzen, A. Hilger, M. Osenberg, N. Kardjilov, B. Ellendorff, T. Turek, C. Roth, and I. Manke, *Operando laboratory X-Ray imaging of silver-based gas diffusion electrodes during oxygen reduction reaction in highly alkaline media,* Materials **12**, 2686 (2019).

[46] M. C. Paulisch, M. Gebhard, D. Franzen, A. Hilger, M. Osenberg, S. Marathe, C. Rau, B. Ellendorff, T. Turek, C. Roth, and I. Manke, *Operando synchrotron imaging of electrolyte distribution in silver-based gas diffusion electrodes during oxygen reduction reaction in highly alkaline media,* ACS Applied Energy Materials **4**, 7497 (2021).

[47] F. Bienen, M. C. Paulisch, T. Mager, J. Osiewacz, M. Nazari, M. Osenberg, B. Ellendorff, T. Turek, U. Nieken, and I. Manke, *Investigating the electrowetting of silver-based gas-diffusion electrodes during oxygen reduction reaction with electrochemical and optical methods,* Electrochemical Science Advances , e2100158 (2022).

[48] M. Löffelholz, J. Osiewacz, A. Lüken, K. Perrey, A. Bulan, and T. Turek, *Modeling electrochemical CO_2 reduction at silver gas diffusion electrodes using a TFFA approach,* Chemical Engineering Journal **435**, 134920 (2022).

[49] H. Hoffmann, M. C. Paulisch, M. Gebhard, J. Osiewacz, M. Kutter, A. Hilger, T. Arlt, N. Kardjilov, B. Ellendorff, F. Beckmann, H. Markötter, M. Luik, T. Turek, I. Manke,

and C. Roth, *Development of a modular operando cell for X-ray imaging of strongly absorbing silver-based gas diffusion electrodes,* Journal of The Electrochemical Society **169**, 044508 (2022).

[50] D. Quéré, *Rough ideas on wetting,* Physica A: Statistical Mechanics and its Applications **313**, 32 (2002).

[51] C. A. Schneider, W. S. Rasband, and K. W. Eliceiri, *NIH image to ImageJ: 25 years of image analysis,* Nature Methods **9**, 671 (2012).

[52] Z. Zeng and R. Grigg, *A criterion for non-darcy flow in porous media,* Transport in Porous Media **63**, 57 (2006).

[53] F. T. L. Muniz, M. A. R. Miranda, C. Morilla dos Santos, and J. M. Sasaki, *The scherrer equation and the dynamical theory of X-ray diffraction,* Acta Crystallographica Section A **72**, 385 (2016).

[54] F. Bartell and P. H. Cardwell, *Reproducible contact angles on reproducible metal surfaces. I. contact angles of water against silver and gold,* Journal of the American Chemical Society **64**, 494 (1942).

[55] C. W. Extrand and Y. Kumagai, *An experimental study of contact angle hysteresis,* Journal of Colloid and Interface Science **191**, 378 (1997).

[56] D. L. Wood, C. Rulison, and R. L. Borup, *Surface properties of PEMFC gas diffusion layers,* Journal of The Electrochemical Society **157**, B195 (2010).

[57] N. Parikh, J. Allen, and R. Yassar, *Microstructure of gas diffusion layers for PEM fuel cells,* Fuel Cells **12**, 382 (2012).

[58] M. Lehner, R. Tichler, H. Steinmüller, and M. Koppe, *Power-to-gas: technology and business models* (Springer, 2014).

[59] G. Faita and F. Federico, *Electrolysis cell with gas diffusion electrode,* (2010), US Patent 7,670,472 B2.

[60] N. Chavan, S. Pinnow, G. Polcyn, and T. Turek, *Non-isothermal model for an industrial chlor-alkali cell with oxygen-depolarized cathode,* Journal of Applied Electrochemistry **45**, 899–912 (2015).

[61] M. Li, M. N. Idros, Y. Wu, T. Burdyny, S. Garg, X. S. Zhao, G. Wang, and T. E. Rufford, *The role of electrode wettability in electrochemical reduction of carbon dioxide,* Journal of Materials Chemistry A (2021), 10.1039/D1TA03636J.

[62] E. D. Laird, R. K. Bose, H. Qi, K. K. S. Lau, and C. Y. Li, *Electric field-induced, reversible lotus-to-rose transition in nanohybrid shish kebab paper with hierarchical roughness,* ACS Applied Materials & Interfaces **5**, 12089 (2013).

[63] M. Jouny, W. Luc, and F. Jiao, *General techno-economic analysis of CO_2 electrolysis systems,* Industrial & Engineering Chemistry Research **57**, 2165 (2018).

[64] G. Shapoval, A. Tomilov, A. Pud, and V. Vonsyatskii, *Electrochemical reductive destruction of polytetrafluoroethylene,* Theoretical and Experimental Chemistry **20**, 234 (1984).

[65] M. Duarte, B. De Mot, J. Hereijgers, and T. Breugelmans, *Electrochemical reduction of CO_2: Effect of convective CO_2 supply in gas diffusion electrodes,* ChemElectroChem **6**, 5596 (2019).

[66] C. J. Powell, *Recommended Auger parameters for 42 elemental solids,* Journal of Electron Spectroscopy and Related Phenomena **185**, 1 (2012).

5

DIRECT IMAGING OF LOCAL pH REVEALS BUBBLE-INDUCED MIXING IN A CO_2 ELECTROLYZER

Electrochemical CO_2 reduction poses a promising pathway to produce hydrocarbon chemicals and fuels without relying on fossil fuels. Gas diffusion electrodes allow high selectivity for desired carbon products at high current density by ensuring a sufficient CO_2 mass transfer rate to the catalyst layer. In addition to CO_2 mass transfer, the product selectivity also strongly depends on the local pH at the catalyst surface. In this work, we directly visualize for the first time the 2D pH profile in the catholyte channel of a gas-fed CO_2 electrolyzer equipped with a bipolar membrane. The pH profile is imaged with operando fluorescence lifetime imaging microscopy (FLIM) using a pH-sensitive quinolonium-based dye. We demonstrate that bubble-induced mixing plays an important role for the Faradaic efficiency. Our concentration measurements show that the pH at the catalyst remains lower for -100 mA cm^{-2} than at -10 mA cm^{-2}, implying that bubble-induced advection outweighs the additional OH^- flux at these current densities. We also prove that the pH buffering effect of CO_2 from the gas feed and dissolved CO_2 in the catholyte prevent the GDE from becoming strongly alkaline. Our findings suggest that gas-fed CO_2 electrolyzers with a bipolar membrane and a flowing catholyte are promising designs for scale-up and high current density operation because they are able to avoid extreme pH values in the catalyst layer.

This chapter has been submitted under the title "Direct imaging of local pH reveals bubble-induced mixing in a CO_2 electrolyzer" by Lorenz M. Baumgartner, Aron Kahn, Maxime Hoogland, Jorrit Bleeker, Wolter F. Jager, David A. Vermaas to *ACS Sustainable Chemistry & Engineering* and is currently under revision.

5.1. INTRODUCTION

Electrochemical CO_2 reduction (CO_2R) could be a promising process to make renewable energies more effective in mitigating climate change [1,2] and to ensure energy security. CO_2R could utilize electricity from renewable power sources for the sustainable production of hydrocarbon chemicals and fuels. [3] To this end, CO_2 can be captured from point sources, [4] directly from the air, [5] or the ocean, [6] and then reduced electrochemically. Depending on the cathode catalyst, useful chemical intermediates can be formed (e.g., Ag: CO, [7] Sn: HCOOH, [8] or Cu: C_2H_4 [9]). [10] These could then be further processed into organic chemicals or hydrocarbon fuels using established industrial processes (Fischer-Tropsch or methanol synthesis). [3]

To make electrochemical CO_2 reduction (CO_2R) economically viable, the process has to be operated at a high current density (e.g., $j \geq -200\,\mathrm{mA\,cm^{-2}}$), [11] high Faradaic efficiency (e.g., $FE_{CO} \geq 95\%$), [12] and a low cell potential (e.g., $E_{cell} \leq 3\,V$). [13] The CO_2 mass transfer to the catalyst strongly affects the FE for the desired carbon products (e.g., CO). If the mass transfer of CO_2 cannot keep up with the supply of electrons at sufficiently high j, the excess current is consumed in the hydrogen evolution reaction (HER) leading to a decrease in FE_{CO}. The introduction of gas diffusion electrodes (GDEs) has made it possible to maintain high FE for carbon products at high j by ensuring a sufficient CO_2 mass transfer rate to the catalyst layer (CL). [14]

However, the local pH at the catalyst surface still affects the FE by changing the relative reaction rates of CO_2R and HER. While neutral pH values are not detrimental to CO_2R, [15,16] highly alkaline pH values reduce the reaction rate because of the carbonate equilibrium. The local pH increases due to hydroxide formation in the CO_2R reaction ($CO_2 + H_2O + 2e^- \longrightarrow CO + 2OH^-$). At sufficiently high pH, CO_2 to form bicarbonate ($CO_2 + OH^- \longleftrightarrow HCO_3^-$; $pK_{a,1} = 6.4$) and carbonate ($HCO_3^- + OH^- \longleftrightarrow CO_3^{2-}$; $pK_{a,2} = 10.3$) in homogeneous buffer reactions. [17] Therefore, high local pH in the CL diminishes the FE for CO_2R. [18]

Also a too low pH can have a negative impact on FE_{CO}: Because the exchange current density of proton reduction ($2H^+ + 2e^- \longrightarrow H_2$) is three orders of magnitude higher compared to water reduction ($H_2O + 2e^- \longrightarrow 2OH^-$), [19] the HER is significantly faster in acidic conditions. Therefore, FE_{H_2} can increase at low pH values, especially if the CO_2R is limited by CO_2 mass transfer. [16] At high current densities, however, the locally higher pH near the catalyst surface can alleviate the low selectivity for CO_2R.

In conclusion, we expect high FE for the desired CO_2R products as long as there is sufficient CO_2 mass transfer to the catalyst surface and the local pH is not too acidic or too alkaline. It can be challenging, however, to achieve these ideal conditions in practice because they are affected by many interdependent phenomena (e.g., electrochemical reactions, homogeneous reactions or mass transfer in gas and liquid phase). For this reason, researchers have tried to gain a deeper understanding of the reaction system with numerical simulations in 1D [20,21] or 2D. [18,22,23]

Experimental characterization techniques[24,25] can be used to complement these numerical studies. For example, absorption spectroscopy can determine the pH at plate cathode surfaces[26,27] or inside a BPM.[28] Operando Raman microscopy has allowed to measure the local (bi)carbonate concentrations and pH values depending on the distance from the cathode in a liquid-fed[29] or gas-fed[30] CO_2 electrolysis flow cell. This technique is limited by the relatively low intensity of the Raman effect, which restricts the imaging speed.[31] Fluorescence microscopy, in contrast, can use the strong fluorescence signal of suitable probe molecules to measure spatially-resolved intensity more rapidly.[32] For example, Leenheer *et al.* assessed the activity of water-splitting electrocatalysts by recording 2D images with a pH-sensitive ratiometric dye.[33]

Fluorescence lifetime imaging microscopy (FLIM) is an imaging technique that uses special fluorescence lifetime probe molecules. Because these dye molecules change their fluorescence lifetime depending on their local environment (e.g., pH or concentration of certain species), FLIM can measure the corresponding spatially-resolved local environment of a sample based on the fluorescence lifetime instead of the absolute intensity.[32,34] This makes FLIM especially useful for applications in which inhomogeneous excitation or differences in dye concentration can affect the intensity. While FLIM has been predominantly used to study biological samples,[35,36] it has also enabled the study of ion transport in electrochemical systems, in which the electromigration of charged dye molecules can lead to concentration gradients that would complicate the use of intensity-based imaging. For example, Benneker *et al.* used FLIM to study the mass transfer of NaCl in a microfluidic desalination cell.[37] In another example, de Valença *et al.* investigated the mass transfer of Cu^{2+} ions in an electrochemical cell.[38,39] So far only a limited amount of studies have applied FLIM to CO_2 electrolysis. For example, Kalde *et al.* used FLIM to qualitatively determine electrochemically active areas in a microfluidic model of a GDE.[40]

In this work, we study the electrochemical performance and the local pH profile of a CO_2 electrolyzer with a flowing K_2SO_4 catholyte and a bipolar membrane. We investigate the effect of the process parameters current density, CO_2 saturation, and catholyte flow rate on the Faradaic efficiency for CO. For the first time, we experimentally visualize the 2D pH profile in a CO_2 electrolyzer catholyte channel, which was imaged with operando FLIM using a pH-sensitive quinolinium dye. We demonstrate that bubble-induced mixing plays an important role for the Faradaic efficiency. Our results imply that convective mixing perpendicular to the flow direction and the pH buffering effect of CO_2 prevent the catholyte from becoming strongly alkaline close to the GDE. These findings suggest that CO_2 electrolyzers with a BPM, and a GDE to separate CO_2 gas flow from the flowing catholyte are promising for scale-up and high current density operation because they are able to avoid extreme pH values in the catalyst layer.

5.2. EXPERIMENTAL METHODS

The CO_2 electrolysis with operando fluorescence lifetime imaging microscopy (FLIM) was carried out with the setup shown in Figure 5.1. The 3-compartment electrolysis cell (see SI, Figure 5.11 – 5.13) was equipped with a porous nickel foam as the anode. The cathode GDE was prepared by depositing an Ag catalyst layer (1.0 mg Ag cm^{-2}, 20 wt% Nafion) on a SGL 39BC gas diffusion layer.[41] Its active area had a height of 25 mm and an electrode width of 4 mm (1 cm^2). The adjacent catholyte channel had a matching depth of 4 mm. The gap width between the GDE and the BPM was 2 mm (see SI, Figure 5.12). The BPM separated the anolyte (1 M KOH) and catholyte (0.4 M K_2SO_4, 0.1 mM fluorescent dye) ensuring that no significant bulk pH change occurred. Both electrolytes were recirculated during the experiment (Figure 5.1). The humidified CO_2 feed was supplied to the GDE in flow-by mode. The backpressure of the gas compartment was controlled with a needle valve. A purge gas stream was used to flush the product gases from the catholyte reservoir.

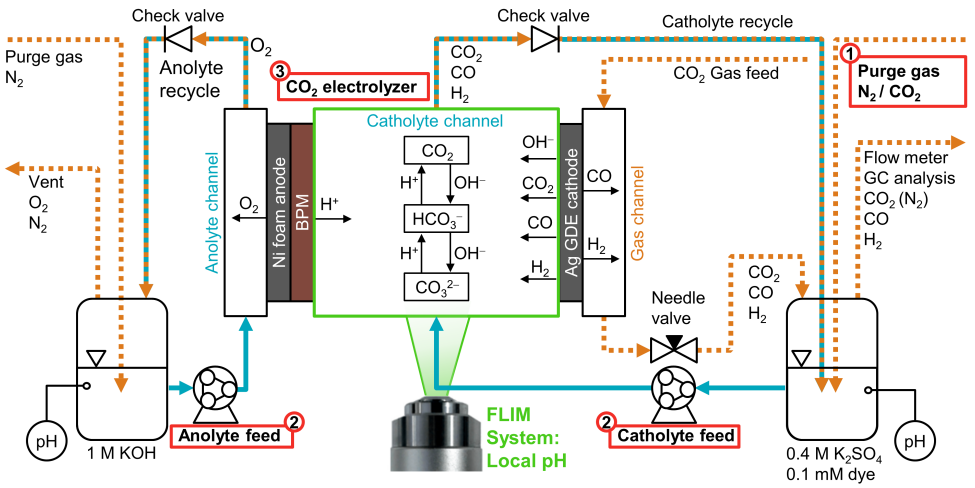

Figure 5.1: Process flow diagram of the CO_2 electrolysis setup with operando FLIM of the local catholyte pH. Process parameters: (1) Catholyte purge gas: N_2 purge or saturation with CO_2; (2) Liquid flow rate: 0.9 or 9.0 mL min^{-1} ($\hat{=} Re = 5$ or $Re = 50$ in catholyte channel); (3) Current density: −10, −50, or −100 mA cm^{-2}. The anolyte and the catholyte channel were separated with a bipolar membrane (BPM). The backpressure of both electrolyte streams was set by check valves. Both electrolytes were recirculated to their respective reservoirs, in which the gaseous products were removed with a purge gas. The bulk pH inside the reservoir was measured with a pH meter. The CO_2 gas feed was humidified to 85% relative humidity (r.h.) at 20 °C and passed into the gas channel of the electrolysis cell at a flow rate of 10 mLn min^{-1}. The gas backpressure was controlled with a manual needle valve. The composition of the cathode product gas was analyzed with gas chromatography (GC). The flow rate was measured with a bubble flow meter. A more detailed process flow diagram is available in the SI (see SI, Figure 5.14).

We investigated the effect of three process parameters (Figure 5.1): The catholyte was continuously purged (1) with N_2 or CO_2 purge gas. The Reynolds number (2) in the catholyte channel, *Re*, was set to 5 or 50 by adjusting the liquid flow rate (see Section 5.5.1

of the SI). After adapting the gas backpressure to achieve a flow-by regime at the GDE, we set a series of current densities (3) in galvanostatic mode (−10, −50, and −100 mA cm^{-2}). For each process parameter set, we waited for 20 min to give the system time to equilibrate. Then we performed three measurements of the gas flow rate and three injections with a gas chromatography (GC) system to determine the Faradaic efficiency of the cathode side.

In parallel, we used the FLIM system to record a series of local pH images at three different heights of the flow cell (see SI, Figure 5.18). The FLIM system (see SI, Figure 5.15) used a diode laser (405 nm, 20 MHz, 300 mW) as the excitation light source. The modulated laser light passed through a spinning disk confocal unit, which uses disks with microlenses and pinholes to restrict the excitation and emission light paths to a single focal plane.[42] We used an inverted microscope with a 5x objective to record images with a width of 2.4 mm and a height of 2.2 mm. We focused the microscope on the center of the catholyte channel, which corresponds to a depth of 2 mm (see SI, Figure 5.18). A diode laser was used to excite the fluorescent quinolinium dye in the catholyte (0.1 mM).[43,44] The fluorescent light emitted by the dye was filtered by the spinning disk unit and recorded with the FLIM camera (512 x 470 pixels). The camera used the frequency-domain technique to record fluorescent lifetime images.[34] The lifetime images are calculated from 6 phase shifts images, which each have an exposure time of 75 ms. This results in a total imaging time of 450 ms per frame. We calibrated the FLIM system with an in-line titration setup (see SI, Figure 5.16). The resulting calibration curve was used to convert fluorescent lifetime images to local pH images (see SI, Figure 5.17).

5.3. RESULTS & DISCUSSION

We carried out a series of galvanostatic CO_2 electrolysis experiments with operando FLIM to image the local pH in the catholyte channel. Supplementary calculations, results, and values of plotted data are included in the **supporting information (SI)**.

5.3.1. OPERANDO FLUORESCENCE LIFETIME IMAGING MICROSCOPY APPLIED TO CO_2 ELECTROLYSIS

For validation , we imaged the local pH of a catholyte channel segment with the dimensions of 2 x 2 mm (Figure 5.2 a),which means one pixel covers about 5 µm x 5 µm. For a current density of 0 mA cm^{-2}, we obtain the 2D pH profile in Figure 5.2 b. We generate the corresponding 1D pH profile by averaging over the y-coordinate of the segment (Figure 5.2 c). The catholyte bulk pH, pH_{min}, of 5.4 ± 1.4 is in good agreement with the feed pH, pH_{feed}, of 5.8, which was obtained from an independent measurement with a pH meter (Figure 5.2 c). The standard deviation of the average pH, $\sigma_{pH}(x)$, may seem relatively large, but the 2D image (Figure 5.2 b) shows that the noise is randomly distributed in y-direction, which makes the profile of $pH_{avg}(x)$ statistically reliable. The FLIM images show an increased average pH, $pH_{avg}(x)$, close to the walls on both sides of the channel (Figure 5.2 a). This is a systematic error, which most likely originates from the fluorescence of the adjacent PET gaskets (see SI, Figure 5.18), which emit a constant fluorescence lifetime corresponding to about pH 6. Because this signal is convoluted with the fluorescence response of the pH-sensitive dye in the catholyte, our images overestimate the pH at the wall when the actual pH is < 6, and probably underestimate the true pH_{max} when an alkaline boundary layer forms during operation.

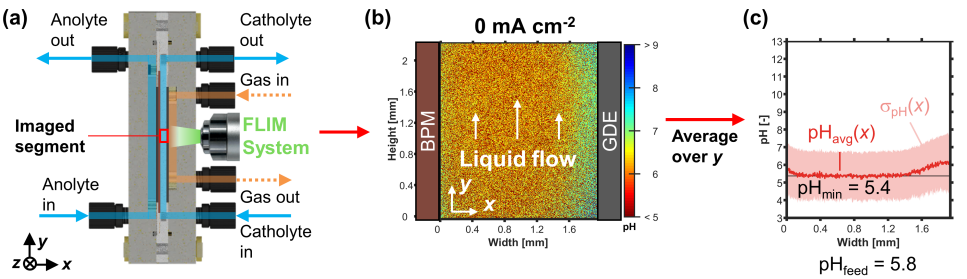

Figure 5.2: Operando FLIM validation. (a) Schematic of the flow cell: Imaging of catholyte flow channel segment in x-y plane. (b) 2D pH profile over channel height (y) and width (x). Left side: The BPM produces H^+ ions during operation. Right side: The GDE is fed CO_2 from the gas channel (not depicted). (c) The 1D pH profile, $pH_{avg}(x)$, was averaged over the height of the channel segment. The shaded red area indicates the standard deviation of the pH value, $\sigma_{pH}(x)$. The minimum value of $pH_{avg}(x)$ is pH_{min}. The maximum value of $pH_{avg}(x)$ is pH_{max}. The pH value of the catholyte feed, pH_{feed}, was measured with a pH meter.

The FLIM results in Figure 5.2 demonstrate that we can map the pH in a 2 mm wide CO_2 electrolyzer flow cell in 2D, accepting noise at the micrometer-scale and an offset near the edges. The quinolinium-based dye is most sensitive for pH changes between pH 6 and pH 9 (see SI, Figure 5.17). This allows to study the local pH near the GDE when a current is applied to the cell.

5.3.2. PERFORMANCE INDICATORS FOR BPM-BASED CO_2 ELECTROLYZERS

Our electrolyzer operates with a similar performance as BPM electrolyzers with flowing catholyte reported in literature (Table 5.1). The E_{cell} of our system is probably higher than that reported by Chen *et al.* (4.5 V vs. 3.5 V) because of the wider catholyte gap, d_{cath}, (2 mm vs. 1.3 mm) and lower operating temperature, T, (20 °C vs. 60 °C).[45] De Mot *et al.* achieved a significantly higher FE_{CO} of 94%.[46] This improvement can not be explained by their higher catalyst loading because the effect of loading on FE_{CO} levels off after about 1.25 mg Ag cm^{-2}.[47] Instead, the higher FE_{CO} can probably be attributed to the difference in catholyte. We used 0.4 M K_2SO_4, a neutral electrolyte without pH buffering capacity. De Mot *et al.*, in contrast, used 0.5 M $KHCO_3$,[46] which suppresses the HER from proton reduction and can buffer the pH in the CL.[48]

Table 5.1: Electrochemical performance of CO_2 electrolyzers with BPM and flowing catholyte. The nickel anode was pressed against the BPM in zero-gap configuration and supplied with KOH anolyte. The current density is j. The Faradaic efficiency is FE. The bulk pH of the catholyte feed is pH_{feed}. The thickness of the catholyte gap between BPM and cathode GDE is d_{cath}. The electrolyzer temperature is T. The cell potential is E_{cell}. This work: The FE_{CO} of 70% was measured for a Reynolds number, Re, of 5, which corresponds to a catholyte flow rate of 0.9 mL min^{-1}. The catholyte was purged with N_2 to remove dissolved CO_2.

Parameter	This work	Chen *et al.*[45]	De Mot *et al.*[46]
GDE catalyst	1.0 mg Ag cm^{-2}	0.5 mg SnO_2 cm^{-2}	2.5 mg Ag cm^{-2}
j	−100 mA cm^{-2}	−100 mA cm^{-2}	−100 mA cm^{-2}
FE	CO: 70%	HCOOH: 73%	CO: 94%
Catholyte	0.4 M K_2SO_4	0.4 M K_2SO_4	0.5 M $KHCO_3$
pH_{feed}	5.5	n.a.	7.6
d_{cath}	2.0 mm	1.3 mm	1.0 mm
T	20 °C	60 °C	60 °C
E_{cell}	4.5 V	3.5 V	4.6 V

It is interesting that our electrolyzer exhibits a very poor FE_{CO} at −10 mA cm^{-2} (Figure 5.3) because CO_2 mass transfer limitation does yet not occur at such a low j.[49] Further, we have previously demonstrated that this GDE model can sustain a FE_{CO} of 89% to 74% for j ranging from −10 to −200 mA cm^{-2} with a 1 M $KHCO_3$ catholyte.[50] Therefore, the poor FE_{CO} at −10 mA cm^{-2} is probably caused by differences in the local pH in the CL when using K_2SO_4 catholyte.

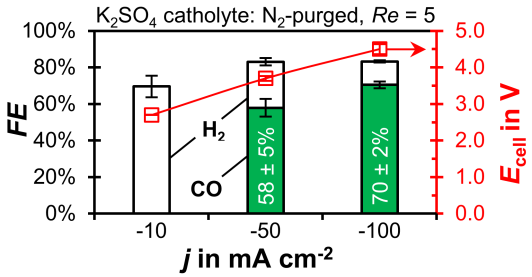

Figure 5.3: CO_2 reduction performance for gas-fed CO_2 electrolyzers with N_2-purged catholyte at $Re = 5$. The FE for CO and H_2 is plotted as a function of current density, j, on the left y-axis. The error bars represent the estimated standard errors of three GC injections. The cell potential, E_{cell}, is plotted on the right y-axis.

We expect the K_2SO_4 catholyte in this experiment to offer minimal pH buffering (Figure 5.3), especially when the catholyte is purged with N_2, removing dissolved CO_2 and preventing homogeneous buffering reactions in the bulk of the liquid. Therefore, the catholyte can undergo more extreme pH changes, which could lead to poor conditions for the CO_2R in the CL. For example, CO_2 from the gas phase might neutralize the OH^- produced at the catalyst surface by forming HCO_3^- and CO_3^{2-}. Then the H^+ produced at the BPM could net acidify the catholyte.[45] On the other hand, the OH^- formation inside the CL might instead lead to a locally high pH if the removal of ionic product species (OH^-, HCO_3^-, and CO_3^{2-}) by the catholyte is too slow.[51] To clarify the effect of low current density on the local pH in the CL, we analyze the catholyte pH profiles through FLIM when different current densities are applied (Figure 5.4).

5.3.3. BUBBLE-INDUCED MIXING LIMITS pH INCREASE AND ENHANCES MASS TRANSFER

At $-10\,\mathrm{mA\,cm^{-2}}$, the FLIM images show that the flowing catholyte prevents the acidification of the GDE (Figure 5.4 a). Instead, we see the development of an alkaline boundary layer at the GDE, which originates from the OH^- released by the electrochemical reaction in the CL.[52] Among all the current densities, $-10\,\mathrm{mA\,cm^{-2}}$ exhibits the highest local pH close to the CL (Figure 5.4 a: $pH_{max} = 7.4$).

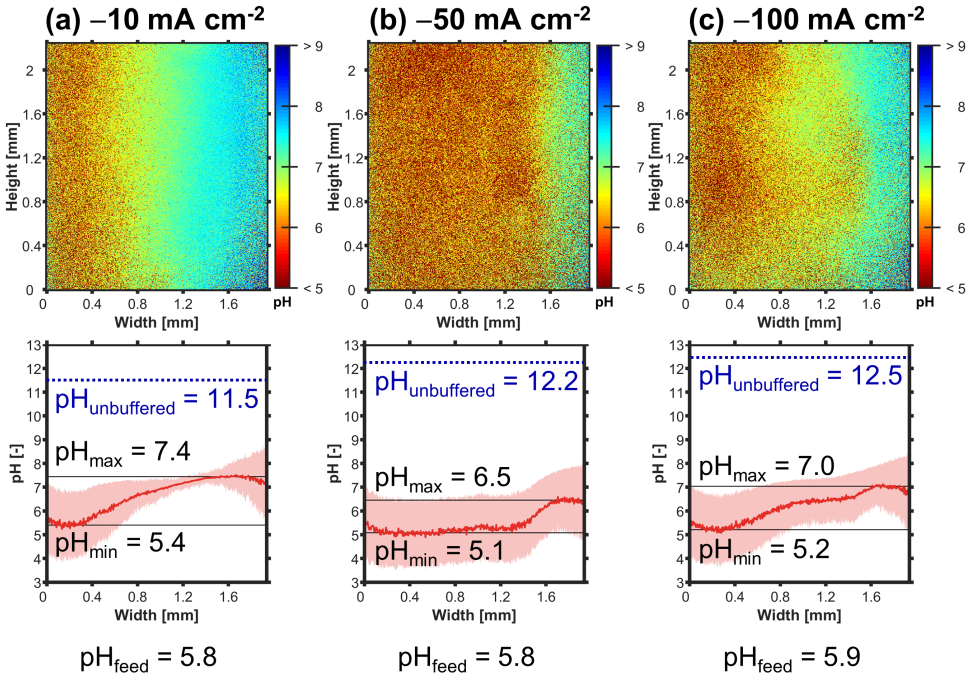

Figure 5.4: FLIM: Catholyte pH profiles at middle of channel height ($y = 12.5\,\mathrm{mm}$) with N_2-purged catholyte at $Re = 5$. Left side of each panel: The BPM produces H^+ ions during operation. Right side: The GDE forms OH^- and is fed CO_2 from the gas channel (not depicted). The subfigures (a) – (c) show the effect of increasing j. Upper panels: 2D pH profile over channel height and width. Bottom panels: The pH profile, pH_{avg}, was averaged over the height of the channel segment shown in the upper panel. The shaded red area indicates the standard deviation of the pH value. The minimum value of pH_{avg} is pH_{min}. The maximum value of pH_{avg} is pH_{max}. The pH value of the catholyte feed, pH_{feed}, was measured with a pH meter. The blue, dotted line indicates the value of the unbuffered pH limit, $pH_{unbuffered}$, which we would expect if no neutralization with H^+ occurred, no homogeneous buffering reactions took place, and OH^- was evenly mixed across the channel's width (see SI, Section 5.5.3).

At $-50\,\mathrm{mA\,cm^{-2}}$, we see a significantly thinner boundary layer and a lower pH_{max} despite the 5x increase in OH^- formation rate (Figure 5.4 b). Further, we observe the formation of H_2 and/or CO bubbles at the cathode surface (see SI, Figure 5.20). These bubbles probably do not form in significant quantities at $-10\,\mathrm{mA\,cm^{-2}}$ because H_2 and CO molecules are removed quickly enough by diffusing into the gas channel and by dissolv-

ing into the liquid phase. At higher current densities, the concentrations of dissolved product gases exceed the nucleation threshold[53] and bubbles form at the surface of the GDE. We hypothesize that the growth, break-off, and the wake flow of these bubbles leads to bubble-induced mixing between the boundary layer and the bulk of the catholyte.[54,55] This additional mass transfer mechanism enhances the removal of product ions from the CL, which decreases pH_{max} to 6.5 (Figure 5.4 b).

We hypothesize that pH_{max} has to be sufficiently close to the pK_a of the bicarbonate reaction for high FE_{CO}. This condition is necessary to ensure that CO_2 can be available as a dissolved gas. At $-10\,mA\,cm^{-2}$, for example, pH_{max} reaches a value of 7.4, which is too high compared to $pK_{a,1} = 6.4$. The true pH directly next to the GDE is probably higher than 7.4 because the fluorescence of the PET gasket makes the value appear closer to pH 6. As a results of the high local pH, this experimented yields a poor FE_{CO} of 0%. At $-50\,mA\,cm^{-2}$, the pH_{max} of 6.5 is more favorable and FE_{CO} rises from 0% to 58% (Figure 5.3).

5

At $-100\,mA\,cm^{-2}$, the thickness of the pH boundary layer and pH_{max} increase again (Figure 5.4 c). We also observed increased bubble flow in the catholyte, which leads to the inhomogeneity in 2D pH profile. The OH^- formation rate in the CL is directly proportional to j. In contrast, bubble-induced mass transfer is only proportional to $j^{0.5}$. The rate of this process is determined by the Sherwood number for bubble-induced mass transfer, Sh_B, which depends on the square root of the Reynolds number for gas evolution, Re_B, and thus also on $j^{0.5}$ ($Sh_B \propto Re_B^{0.5} \propto j^{0.5}$).[54,55] Therefore, we can expect the formation of OH^- in the CL to outpace the removal through bubble-induced mixing at sufficiently high j. For this reason, pH_{max} in the catholyte is higher at $-100\,mA\,cm^{-2}$ than for the $-50\,mA\,cm^{-2}$ case (Figure 5.4 b vs. c: 6.5 vs. 7.0). It is interesting that the corresponding FE_{CO} increases from 58% to 70% (Figure 5.3). Perhaps the higher pH in the CL suppresses the HER by slowing down the proton reduction. At the same time, the local pH might not yet be so high that dissolved CO_2 is fully converted to HCO_3^- ($pK_{a,1} = 6.4$).

For all current densities, the pH_{max} in the catholyte remains far below $pH_{unbuffered}$ (Figure 5.4). This is the pH limit we would expect if (1) the released OH^- was evenly mixed across the channel's width, (2) no neutralization with H^+ occurred, and (3) no homogeneous buffering reactions with CO_2 took place (see Section 5.5.3 of SI). In reality, the CO_2 diffusing to the CL from the gas channel must result in a significant buffering of the pH by forming HCO_3^- and CO_3^{2-} species. This is clearly visible at $j = -10\,mA\,cm^{-2}$ because there is little bubble-induced mixing to facilitate the neutralization with H^+ (Figure 5.4 b). At $j \geq -50\,mA\,cm^{-2}$, the H^+ released at the BPM leads to a significant acidification of the catholyte, which is visible by the drop of pH_{min} (Figure 5.4 a vs. c: 5.4 vs. 5.1). Further, the mixing and neutralization of H^+ and OH^- flattens the pH profile (Figure 4 b and c). The release of H^+ is likely to cause an even stronger (local) acidification than $pH_{min} = 5.1$, but this can not resolved with our FLIM dye, which has a plateau in the calibration curve for pH ≤ 5 (Figure 5.17). We can follow the development of the boundary layers at $-100\,mA\,cm^{-2}$ by looking at the different positions in the cell (Figure 5.5).

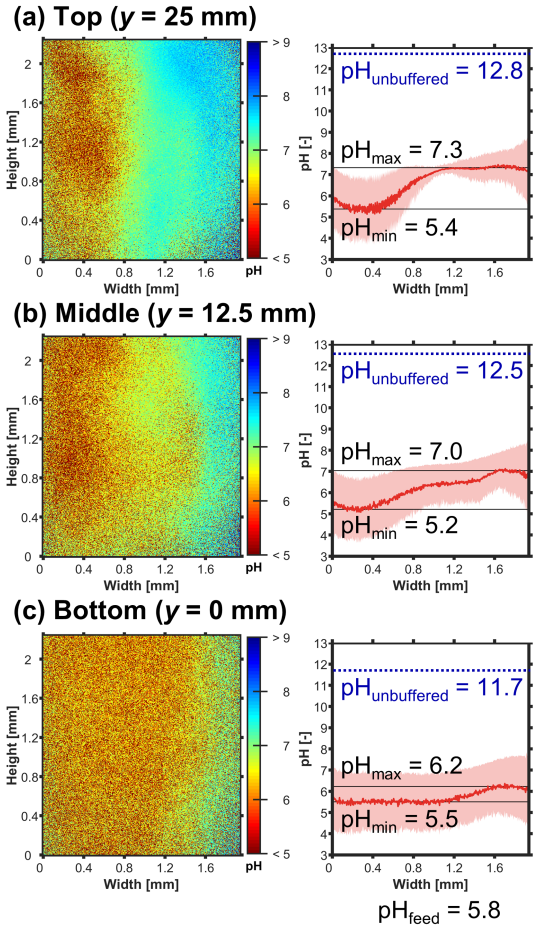

Figure 5.5: FLIM: Catholyte pH profile over the height of the electrolyzer at $j = -100\,\mathrm{mA\,cm^{-2}}$ with N_2-purged catholyte at $Re = 5$. The subfigures (a) – (c) show the pH profiles at different y-positions. Left panels: 2D pH profile over channel height and width . Right panels: The pH profile, pH_{avg}, was averaged over the height of the channel segment shown in the left panel. The shaded red area indicates the standard deviation of the pH value. The minimum value of pH_{avg} is pH_{min}. The maximum value of pH_{avg} is pH_{max}. The pH value of the catholyte feed, pH_{feed}, was measured with a pH meter. The blue, dotted line indicates the value of the unbuffered pH limit, $pH_{unbuffered}$, which we would expect if no neutralization with H^+ occurred, no homogeneous buffering reactions took place, and OH^- was evenly mixed across the channel's width (see SI, Section 5.5.3).

As the catholyte flows upward and accumulates OH^-, pH_{max} increases along the height of the reactor (Figure 5.5 a vs. c: 6.2 vs. 7.3). Because the increasing boundary thickness slows down the removal of OH^-, we can expect the local pH in the upper parts of the CL to become less favorable for CO_2R. To illustrate, the value of $pH_{max}(y = 25\,\mathrm{mm})$ at $-100\,\mathrm{mA\,cm^{-2}}$ is similar to $pH_{max}(y = 12.5\,\mathrm{mm})$ at $-10\,\mathrm{mA\,cm^{-2}}$ (Figure 5.5 a vs. Figure 5.4 b: 7.3 vs. 7.4), which had a FE_{CO} of 0%. This implies that scaled-up electrodes

would have a poor local FE_{CO} because the top part of the electrode would mostly be producing H_2.[18,23] However, the observed pH_{max} is still significantly lower than the expected $pH_{unbuffered}$ along the height of the channel (Figure 5.6). This raises the question to what extent the supply of CO_2 from the GDE is able to buffer the increase of pH_{max}. To deconvolute the effect of current density, forced convection and CO_2 saturation, we studied the cases of saturating the catholyte feed with CO_2 and increasing the flow rate.

5.3.4. CO_2 SATURATION LIMITS PH INCREASE AND ENHANCES FE_{CO}

Saturating the catholyte feed with CO_2 improves the FE_{CO} at all investigated current densities (Figure 5.6). For example, we see an increase from 70% to 77% at $-100\,mA\,cm^{-2}$. This improvement is probably not primarily caused by the higher convective mass transfer of CO_2 from the saturated electrolyte bulk, which corresponds to only an additional partial current density for CO, j_{CO}, of $-2\,mA\,cm^{-2}$ (see Section 5.5.4 of SI). For example, if the CO_2 mass transfer were limiting at $-100\,mA\,cm^{-2}$, the additional convective CO_2 flux could only explain an increase in FE_{CO} from 70% to 72%. This suggests that there are other important mechanisms improving FE_{CO}, such as a difference in local pH changing the relative reaction rates in the CL.

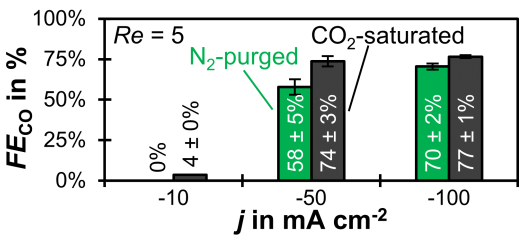

Figure 5.6: Effect of CO_2 saturation: FE_{CO} as a function of j for CO_2-saturated and N_2-purged catholyte at $Re = 5$. The error bars represent the estimated standard errors of three GC injections.

The saturation with CO_2 reduces pH_{max} at all current densities (Figure 5.7). For example at $-100\,mA\,cm^{-2}$, pH_{max} drops from 7.0 to 5.9 (Figure 5.7 b vs. d). This happens through multiple mechanisms. First, the dissolved CO_2 acidifies the electrolyte by forming carbonic acid, which dissociates further into H^+ and HCO_3^-. This is illustrated by the decrease in pH_{feed} from 5.8 to 5.3 (Figure 5.7 a vs. c). Second, the dissolved CO_2 acts as a pH buffer by forming (bi)carbonate ions. This is significant because, e.g., the CO_2 in catholyte bulk could absorb 96% of the OH^- released at $-100\,mA\,cm^{-2}$ (see Section 5.5.5 of SI). Third, the CO_2 saturated catholyte releases CO_2 bubbles at the BPM,[28,56] which increases the bubble-induced mixing. These bubbles lead to the inhomogeneities seen in the 2D pH profiles (Figure 5.7 c vs. d). The bubble-induced mixing limits the increase of pH_{max} by enhancing the removal of product ions and also boosts the CO_2 flux from the catholyte bulk to the CL. In summary, saturating the catholyte with CO_2 improves FE_{CO} by making the local environment in the CL more favorable for CO_2R.

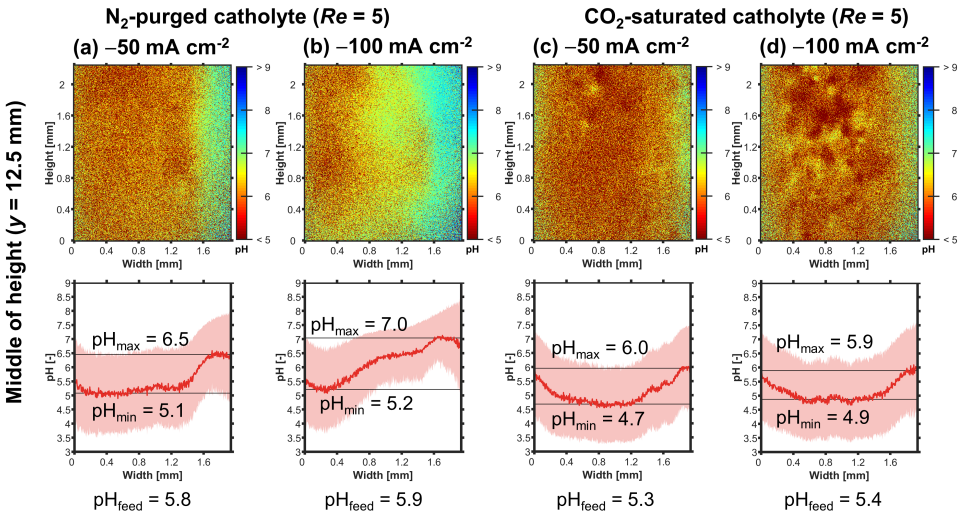

Figure 5.7: FLIM: Effect of CO_2 saturation on catholyte pH profiles at middle of channel height ($y = 12.5\,mm$) at $Re = 5$. (a) and (b): Profiles for N_2-purged catholyte with increasing j. (c) and (d): Profiles for CO_2-saturated catholyte. Upper panels: 2D pH color profile over channel height and width . Bottom panels: The pH profile, pH_{avg}, was averaged over the height of the channel segment shown in the upper panel. The shaded red area indicates the standard deviation of the pH value. The minimum value of pH_{avg} is pH_{min}. The maximum value of pH_{avg} is pH_{max}. The pH value of the catholyte feed, pH_{feed}, was measured with a pH meter.

5

5.3.5. CATHOLYTE REYNOLDS NUMBER INTERFERES WITH BUBBLE-INDUCED MIXING

The effect of additionally increasing the catholyte Reynolds number, Re, on FE_{CO} is less straightforward. At $-100\,mA\,cm^{-2}$, FE_{CO} improves from 77% to 85% when Re is increased from 5 to 50 (Figure 5.8). This might be due to additional convective CO_2 flux from the bulk of the catholyte. This flux is enhanced by a factor of 3.2 when Re is increased by a factor of 10 ($Sh \propto Re^{0.5}$). This increased CO_2 flux can sustain an additional j_{CO} of $-4\,mA\,cm^{-2}$ (see Section 5.5.4 of SI), which would correspond to an increase in FE_{CO} from 77% to 81% FE_{CO}. There might also be important other mechanisms, such as the change in local pH, possibly explaining the observed increase to 85% FE_{CO}.

No significant improvement of FE_{CO} occurs at $-50\,mA\,cm^{-2}$ for the CO_2-saturated case (Figure 5.8). It is plausible that the effect of Re also depends on j because both process parameter can influence the local pH. We can further investigate the mass transfer phenomena in the catholyte gap with snapshots of the local pH profiles (Figure 5.9).

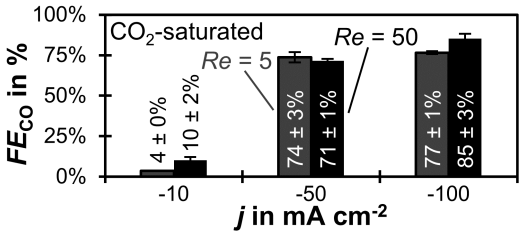

Figure 5.8: Effect of Reynolds number in catholyte channel, *Re*. FE_{CO} as a function of j and *Re* for CO_2-saturated catholyte. The error bars represent the estimated standard errors of three GC injections.

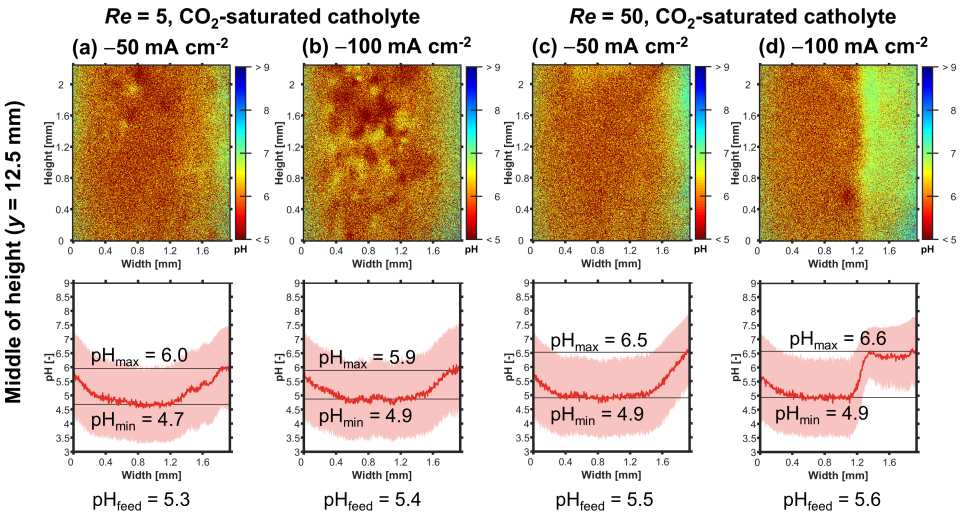

Figure 5.9: FLIM: Effect of Reynolds number, *Re*, on pH profiles at middle of channel height ($y = 12.5$ mm) with CO_2-saturated catholyte. (a) and (b): Profiles for $Re = 5$ with increasing j. (c) and (d): Profiles for $Re = 50$. Upper panels: 2D pH profile over channel height and width. Bottom panels: The pH profile, pH_{avg}, was averaged over the height of the channel segment shown in the upper panel. The shaded red area indicates the standard deviation of the pH value. The minimum value of pH_{avg} is pH_{min}. The maximum value of pH_{avg}) is pH_{max}. The pH value of the catholyte feed, pH_{feed}, was measured with a pH meter.

To our surprise, increasing *Re* from 5 to 50 results in a higher local pH at the GDE. At $-100\,mA\,cm^{-2}$, for example, pH_{max} rises from 5.9 to 6.6 (Figure 5.9 b vs. d). This is counter-intuitive because we would expect the increased forced convection to the accelerate the removal of OH^-. We hypothesize that the higher catholyte *Re* reduces the contribution of bubble-induced mass transfer . The 10x higher liquid flow rate exerts stronger drag forces on bubbles, which hinders their lateral motion. Therefore, rising bubbles are confined closer to the surface of the electrodes and less bubble mixing perpendicular to the catholyte flow direction occurs.[57] This claim is supported by our 2D pH profiles showing less disturbances through bubbles and a more laminar flow profile when comparing $Re = 50$ to $Re = 5$ (Figure 5.9 d vs. b). This finding reveals that bubble mixing contributes significantly to the mass transfer in the catholyte channel.

At $-50\,mA\,cm^{-2}$, increasing *Re* from 5 to 50 must lead to a reduction in bubble-induced CO_2 mass transfer from the catholyte, which is not sufficiently compensated by the additional mass transfer of CO_2 through forced convection. Therefore, the CO_2 mass transfer stagnates and FE_{CO} does not change significantly (Figure 5.8: $74 \pm 3\%$ to $71 \pm 1\%$). We hypothesize that the CO_2 mass transfer is more important than the local pH for both cases because their pH_{max} is close to the pK_a of the bicarbonate reaction (Figure 5.9 a or c: $pH_{max} = 6.0$ or 6.5 vs. $pK_{a,1} = 6.4$).

If j is increased from $-50\,mA\,cm^{-2}$ to $-100\,mA\,cm^{-2}$ at $Re = 50$, the contribution of bubble mixing rises again because of the higher gas evolution rate. This increased mixing prevents a significant change to pH_{max} despite the higher OH^- formation rate (Figure 5.9 c vs d: pH_{max}: 6.5 vs. 6.6). Further, the additional bubble mixing also enhances the CO_2 mass transfer from the bulk, which then boosts FE_{CO} from 71% to 85% (Figure 5.8).

The importance of the CO_2 mass transfer from the catholyte bulk is further highlighted by comparing the effect of *Re* between the CO_2-saturated and the N_2-purged cases (Figure 5.8 vs. see SI, Figure 5.22). If j is increased from $-50\,mA\,cm^{-2}$ to $-100\,mA\,cm^{-2}$ at $Re = 50$ for the N_2 case, no significant change of FE_{CO} occurs (see SI, Figure 5.22: $70 \pm 2\%$ to $73 \pm 1\%$).

5.3.6. INTERMEDIATE pH AND HIGH CURRENT DENSITY LEAD TO HIGH FE

The scatter plot in Figure 5.10 shows FE_{CO} as a function of pH_{max} and the process parameters. We hypothesize that these three factors are critical to ensure a high FE_{CO}:

- Maximum pH in the electrolyte close to pK_a of the bicarbonate reaction ($pK_{a,1} = 6.4$): e.g., $pH_{max} \leq 7.0$
- Removal of ions from inside the porous CL to the catholyte: OH^-, HCO_3^-, and CO_3^{2-}
- Dissolved CO_2 is available in the CL

The CO_2 feed in the gas channel, present in all our cases, already limits the pH_{max}. Additionally, mixing induced from gas bubbles contributes to both the first (local pH in electrolyte) and the second (local pH in CL) factor. The process parameter with the strongest effect on FE_{CO} is j because it leads to bubble-induced mixing at $-50\,mA\,cm^{-2}$ or higher. This important mechanism keeps pH_{max} close enough to $pK_{a,1}$. It further removes product ions from the CL and ensures that CO_2 is available in the CL. For this reason, all experiments with $j \geq -50\,mA\,cm^{-2}$ have a $FE_{CO} \geq 58\%$ (Figure 5.10).

Saturating the catholyte with CO_2 also has a positive effect on FE_{CO}, which is probably due to a combination of additional pH buffering, bubble mixing, and CO_2 mass transfer. For these reasons, we find the highest values for FE_{CO} for experiments with CO_2-saturated feed and $j = -100\,mA\,cm^{-2}$ (Figure 5.10: #9 and #6).

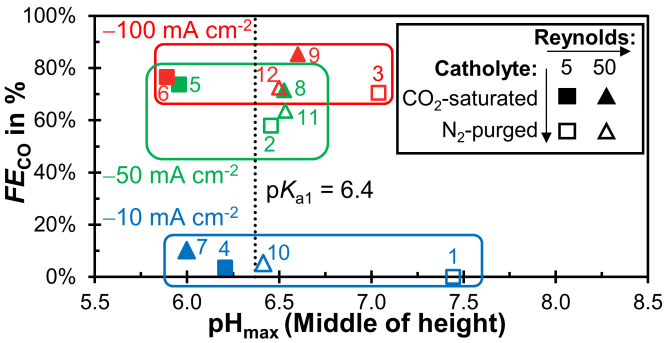

Figure 5.10: Faradaic efficiency for CO, FE_{CO}, as a function of the maximum pH at the middle height of the catholyte channel, pH_{max}. The current density, j, is represented by the color of the data points (blue: $-10\,mA\,cm^{-2}$, green: $-50\,mA\,cm^{-2}$, red: $-100\,mA\,cm^{-2}$). The Reynolds number of the catholyte, *Re*, is indicated by the marker shape (square: $Re = 5$, triangle: $Re = 50$). Experiments with CO_2-saturated catholyte have filled markers. The dotted line represents the pK_a of the bicarbonate reaction ($CO_2 + OH^- \longleftrightarrow HCO_3^-$; p$K_{a,1}$ = 6.4).[17] The number next to each marker indicates the ID number (#) of each parameter set.

The effect of *Re* is less clear because the higher liquid flow rate increases the mass transfer through forced convection, but suppresses bubble-induced mixing. However, since a high *Re* seems to be beneficial for FE_{CO} at $j = -100\,mA\,cm^{-2}$ with a CO_2-saturated catholyte (Figure 5.10: #9), this is still a relevant parameter for process optimization. It might be interesting, for example, to have a more quantitative study on how *Re* influences the dynamics of bubble growth, release, and mixing.

It is remarkable that we obtain a poor FE_{CO} for experiments with $j = -10\,mA\,cm^{-2}$ although their pH_{max} ranges from 6.0 to 7.4 (Figure 5.10: #1, #4, #7, and #10). This phenomenon might be explained through significantly higher pH values inside the porous CL, which are not accessible through FLIM. It is possible that bubble-induced mixing is necessary to exchange the catholyte inside the porous CL with the catholyte from the channel. Because this mass transfer mechanism is missing at $j = -10\,mA\,cm^{-2}$, the product ions (OH^-, HCO_3^-, and CO_3^{2-}) can not be removed sufficiently fast leading to an unfavorably high pH in the CL. This hypothesis could be validated with numerical studies in the in future.

Close to the GDE of our gas-fed electrolyzer, the catholyte pH remains below 7.0 for all experiments with high j and high FE_{CO} (Figure 5.10: e.g., #9 and #6). In contrast, close to the plate electrode of a liquid-fed electrolyzer, the pH is estimated to be above 10 at only $-15\,mA\,cm^{-2}$.[52] This raises the question how the pH close to the GDE develops for our system at $j \geq -200\,mA\,cm^{-2}$. At these conditions, the strong bubble formation leads to a turbulent two-phase flow. This complicates recording the local pH with our FLIM system due to the limited imaging speed (450 ms per image). However, we can speculate that bubble-induced mixing and neutralization with the H^+ from the BPM can maintain a moderate local pH at the GDE for much larger current densities. This might explain why the gas-fed BPM electrolyzer of De Mot *et al.* can operate at $-300\,mA\,cm^{-2}$ while

maintaining a high $FE_{CO} > 70\%$.[46]

5.4. CONCLUSION

We have studied how process parameters (current density, CO_2 saturation of the electrolyte, and catholyte flow rate) affect the Faradaic efficiency of a gas-fed CO_2 electrolyzer with flowing K_2SO_4 catholyte and bipolar membrane. We complemented these measurements with operando fluorescence lifetime imaging microscopy (FLIM) to image the growth of an alkaline boundary layer along the cathode GDE. Three key factors limit the pH increase at the GDE to ≤ 7.0 and enable high FE_{CO} of 77% – 85%: (1) CO_2 from the gas phase acts as pH buffer, (2) Bubble-induced mixing enhances the mass transfer in the catholyte channel and the ion exchange between the catalyst layer and catholyte, and (3) the CO_2-saturated catholyte acts as pH buffer and leads to additional bubble-induced mixing by releasing CO_2 at the BPM.

We find the mass transfer contribution of bubble-induced mixing to be more significant than the contribution of forced convection through the flowing catholyte. The bubble-induced mixing is only effective after exceeding a threshold in current density, which makes the maximum pH at $-10\,mA\,cm^{-2}$ higher than at -50 or $-100\,mA\,cm^{-2}$. High mass transfer rates across the channel are essential to enable a neutralization of OH^- from the cathode with H^+ from the BPM. This neutralization within the channel might be able to limit the pH increase at the cathode and thereby allow a high FE_{CO}. Therefore, gas-fed CO_2 electrolyzers with BPM are promising systems for scale-up and operation at high current densities.

5.5. SUPPORTING INFORMATION

This section includes more detailed experimental descriptions, supplementary calculations, and additional results. The digital version of the Supporting Information (SI) includes an Excel file with the values for plotted data and all recorded experimental parameters for the CO_2 electrolysis experiments.

5.5.1. ENGINEERING OF THE CO_2 ELECTROLYSIS SETUP

We used a 3-compartment flow cell to carry out the CO_2 electrolysis experiments (Figure 5.11). All tubing connections had an outer diameter of 1/8 inch. The cell components were pressed together with four M4 bolts tightened with a torque of 2 Nm. The anode flow plate was made of stainless steel and served as a current collector Figure 5.11. The anolyte flow channel had a width of 3 mm and a depth of 4 mm. The flow plate was sealed against the anode spacer with a butyl rubber O-ring. The 1 mm thick anode spacer aligned the nickel foam anode (Ni-4753.01, Recemat BV, Netherlands). The anode was 1 mm thick, had an estimated average pore diameter of 0.4 mm, and a porosity of 95.2%. The anode was pressed against the BPM (Fumasep FBM, Fumatech GmbH, Germany). The membrane spacer was made of PET with a thickness of 140 µm. The active area of the BPM and GDE was controlled by PET gaskets with a rectangular hole (25 mm height x 4 mm depth = 1 cm^2).

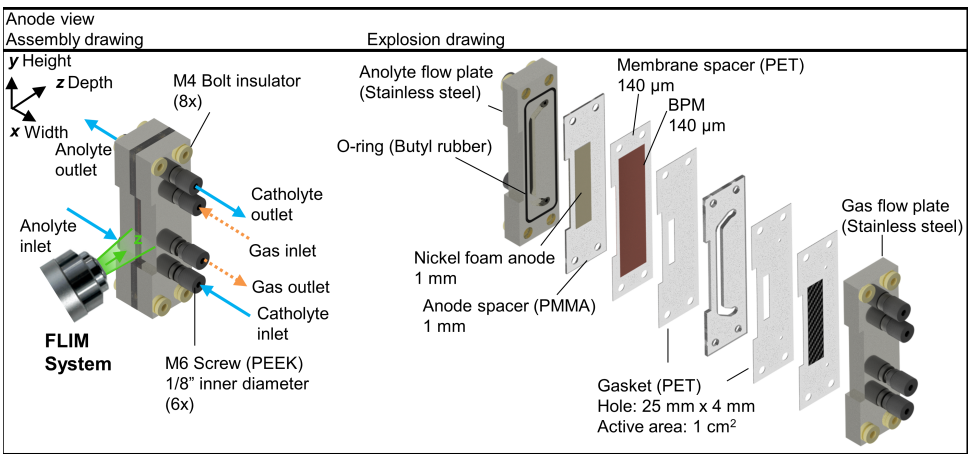

Figure 5.11: Anode view of the 3-compartment electrolysis flow cell.

The catholyte flow channel had a width of 2 mm and a depth of 4 mm (Figure 5.12). The channel was cut from a PMMA sheet with a diamond milling bit to create a highly transparent surface. The GDE was manufactured by spray-coating an Ag catalyst layer on a commercial Sigracet 39BC (SGL Carbon, Germany). We described the deposition method in more detail in a previous publication.[41] The Nafion content in the catalyst layer (CL) was 20 wt%. The Ag loading was 0.94 mg Ag cm^2. The GDE was aligned by two PET spacers with a thickness of 140 µm each. Assuming a GDE thickness of 325 µm, these spacers yielded a GDE compression of 14%. The gas flow plate was pressed against the GDE as a current collector. The gas flow channel had a width of 3 mm and a depth of 4 mm. The flow plate was sealed against the GDE spacer with butyl rubber O-rings.

The liquid outlets were located at the top to facilitate the removal of gas bubbles from the liquid channel (Figure 5.13). The gas outlet was located at the bottom of the cell to allow the drainage of any electrolyte that broke through the GDE into the gas channel during the start-up phase. The FLIM system recorded images of the catholyte channel in the x-y plane.

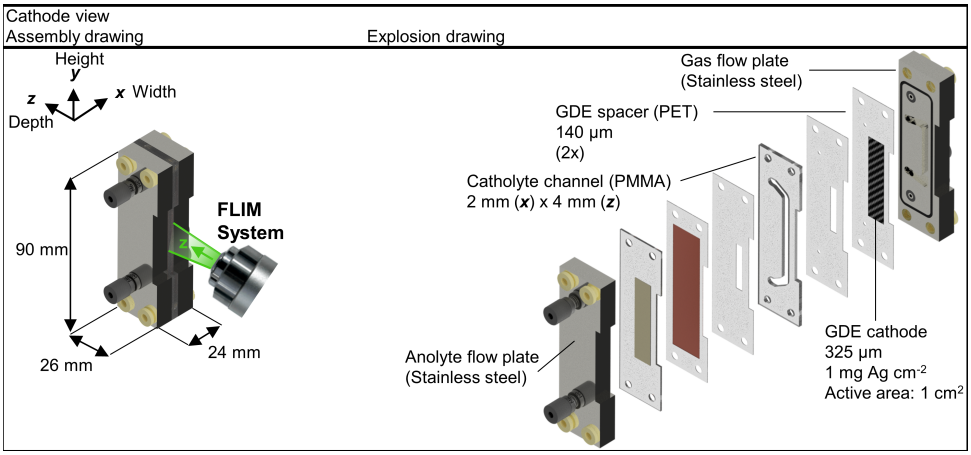

Figure 5.12: Cathode view of the 3-compartment electrolysis flow cell.

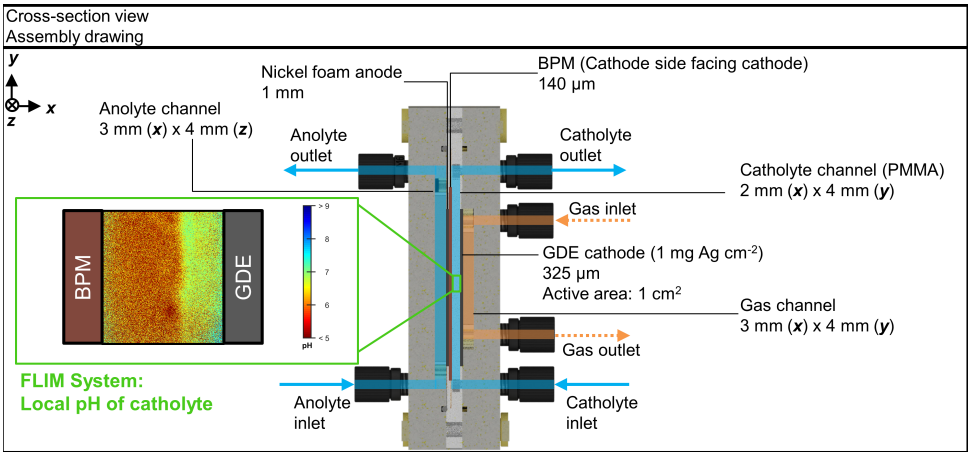

Figure 5.13: Cross-section view of the 3-compartment electrolysis flow cell.

The flow cell was installed in the CO_2 electrolysis setup (Figure 5.14). All fluid lines were made of PE. They had an outer diameter of 1/8 inch and inner diameter of 1/16 inch.

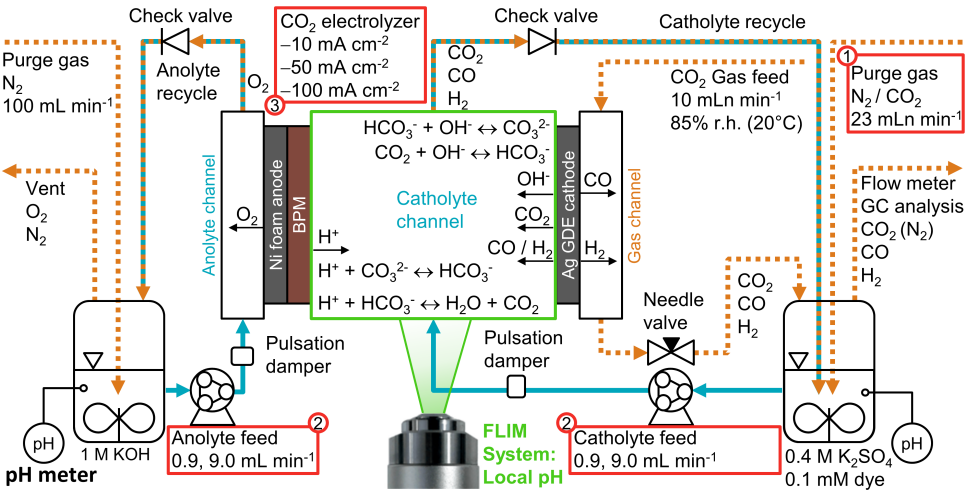

Figure 5.14: Process flow diagram of the CO_2 electrolysis setup with operando FLIM of the local catholyte pH. Process parameters: (1) Catholyte purge gas: N_2 purge or saturation with CO_2; (2) Liquid flow rate: 0.9 or 9.0 mL min^{-1} ($\hat{=} Re = 5$ or $Re = 50$ in catholyte channel); (3) Current density: −10, −50, or −100 mA cm^{-2}. Peristaltic pumps supplied the anolyte and catholyte to the CO_2 electrolyzer. Pulsation dampers were used to reduce the pressure fluctuations caused by the pumps. The anolyte and the catholyte channel were separated with a bipolar membrane (BPM). The backpressure of both electrolyte streams was set by check valves with a cracking pressure of 69 mbar. Both electrolytes were recirculated to their respective reservoirs, in which the gaseous products were removed with a purge gas. Magnetic stirrers were used to accelerate the mixing of the electrolyte. The bulk pH inside the reservoirs was measured with a pH meter. The CO_2 gas feed was humidified to 85% relative humidity (r.h.) at 20 °C inside a bubble column and passed into the gas channel of the electrolysis cell. The gas backpressure was controlled with a manual needle valve. The composition of the cathode product gas was analyzed with gas chromatography (GC). The flow rate was measured with a bubble flow meter.

Gas feed

The CO_2 gas feed was supplied from a gas cylinder (Figure 5.14). The feed flow rate of 10 mLn min^{-1} (Normal conditions: 0 °C , 1 atm) was controlled with a mass flow controller (F-201CV-020-RAD-3A-V, Bronkhorst BV, Netherlands). This flow rate corresponds to a maximum CO_2 conversion of 7% at −100 mA cm^{-2} (assuming FE_{CO} = 100%). The gas was humidified to 85% relative humidity (r.h.) at 20 °C inside a bubble column. [41] and passed through the gas channel. We used a manual needle valve (SS-SS2, Swagelok, Netherlands) to control the gas backpressure. This allowed us to set a flow-by flow regime at the GDE. [50,58]

Electrolytes

Both electrolytes were pumped with a peristaltic pump (Masterflex L/S, Cole Parmer). In-line pulsation dampers (PFD 1.06 KPZ, KNF, Switzerland) were used to dampen the flow rate fluctuations of the pump (Figure 5.14). After being pumped through the cell, the electrolytes passed through a check valve (SS-CHS2-1, Swagelok, Netherlands). The check valves had a nominal cracking pressure of 69 mbar, which set the backpressure of the electrolytes. Both electrolytes were recirculated into their storage bottles and mixed with a magnetic stirrer. The anolyte (1 M KOH) was purged with N_2 to vent the O_2 product gas and any CO_2 that might have crossed over (Figure 5.14). The purge flow rate was set to 100 mL min^{-1} with a rotameter (Reference conditions: 20 °C, 1 atm).

Process parameter 1: Catholyte Purge gas
The catholyte (0.4 M K_2SO_4, 0.1 mM fluorescent dye) was purged with N_2 (23 mLn min^{-1}) or CO_2 (15 mLn min^{-1}) to flush the product gases. The gas flow rate was controlled with a mass flow controller (calibrated for normal conditions: 0 °C, 1 atm). In the case of the N_2 purge, the catholyte had a low CO_2 saturation because the N_2 stripped dissolved CO_2 from the electrolyte. In the case of the CO_2 purge, the catholyte had a high CO_2 saturation because CO_2 bubbles were brought into close contact with the liquid.

Process parameter 2: Reynolds number / Catholyte flow rate
We set the hydraulic Reynolds number in the catholyte channel, Re, to 5 or 50 by adjusting the liquid flow rate of the peristaltic pump, F_L, to 0.9 mL min^{-1} or 9.0 mL min^{-1}. We note that this Reynolds number differs from the gas bubble Reynolds number Re_B from the main paper and the Reynolds number along a plate electrode, Re_H, used in Section 5.5.4. The hydraulic Reynolds number in the catholyte channel, Re, is calculated with (5.1). The hydraulic diameter of the channel is d_H in mm. The superficial liquid velocity is u in m s^{-1}. We approximate the kinematic viscosity of the catholyte, ν, with the corresponding value of water at 20 °C ($\nu = 1 \times 10^{-6}\,m^2\,s^{-1}$).[59]

$$Re = \frac{d_H \cdot u}{\nu} \tag{5.1}$$

The value of d_H is a function of the channel width, W, in mm and depth, D, in mm (5.2).

$$d_H = 2 \cdot \frac{W \cdot D}{W + D} = 2 \cdot \frac{8\,mm}{2\,mm + 4\,mm} = 2.67\,mm \tag{5.2}$$

$$u = \frac{F_L}{W \cdot D} \tag{5.3}$$

Process parameter 3: Current density
After setting the purge gas flow rate and the liquid flow rate, we used a potentiostat (XP20, Ivium technologies, Netherlands) to set three galvanostatic current density steps (−10, −50, and −100 mA cm^{-2}).

Steady state measurements
The system was given 20 min to equilibrate after setting each process parameter set. Then we recorded the cell potential with the potentiostat. The bulk pH of the catholyte and anolyte were determined with a pH meter (913 pH Meter, Metrohm AG, Switzerland). The gas flow rate was measured three times with a bubble flow meter to calculate an average gas flow rate for the product mixture, $\dot{V}_{mix}$. We used a syringe pump to take three gas samples from the product gas stream. These were analyzed with a gas chromatography (GC) system (CompactGC 4.0, Interscience BV, Nederland) to determine the volumetric concentration, C_i, of the following gas species (CO_2, CO, H_2, N_2, O_2, CH_4, and C_2H_4). No CH_4 or C_2H_4 was detected during our experiments.

The Faradaic efficiency of gas species FE_i (H_2, CO) was calculated from the current density, j, in mA cm^{-2}, the electrode area, $A = 1\,cm^2$, Faraday's constant, $F = 96485\,A\,s\,mol^{-1}$, the stoichiometric number of electrons exchanged, z_i ($z_i = 2$ for H_2 and CO), and the molar flux of the species, $\dot{N}_i$, in mol s^{-1} (5.4).

$$FE_i = \frac{z_i \cdot F \cdot \dot{N}_i}{j \cdot A} \tag{5.4}$$

The molar flux of the species, $\dot{N}_i$, was estimated with the ideal gas law (5.5), in which the gas pressure is $p = 1$ bar, the gas temperature is 293.15 °C, and the ideal gas constant is $R = 8.3145\,J\,K^{-1}\,mol^{-1}$.

$$\dot{N}_i = \frac{p \cdot \dot{V}_{mix} \cdot C_i}{R \cdot T} \tag{5.5}$$

5.5.2. FLUORESCENCE IMAGING MICROSCOPY (FLIM)

The FLIM system measured the phase-shift fluorescence lifetime, τ_ϕ, in the sample region of the flow cell (Figure 5.15) using the frequency-domain technique.[32,34] The diode laser (405 nm) serves as a light source with a modulation frequency of 20 MHz. The laser light passes through a filter and enters the spinning disk confocal unit (Crest V2, CrestOptics, Italy). The microlense disk focuses the incident light onto the Nipkow pinhole disk (70 µm diameter pinholes), which restricts the light path to the focal plane while scanning the sample region.[42] The focused laser light passes through the objective (5x magnification) of the microscope (Zeiss Axiovert 200M, Carl Zeiss AG, Germany) to excite fluorescent dye molecules in the focal plane of the channel. The focal plane was in a depth of 2 mm and had a focal depth of about 520 µm. These probe molecules emit fluorescent light in a lower wavelength spectrum and, depending on their local pH, the phase of the signal is shifted relative to the phase of the excitation light source. The emitted fluorescent light passes back through the spinning disk unit and is reflected by a dichroic mirror. After passing through the emission filter, the emitted light reaches the FLIM camera (Toggel, Lambert Instruments, Netherlands). The FLIM camera has a resolution of 512 x 470 pixels, which yields a spatial resolution of 4.76 µm per pixel. We recorded all images with a camera gain of 2 and an exposure time of 75 ms. Each FLIM image is calculated from 6 images with different phase shifts. This yields a total imaging time of 450 ms per FLIM image.

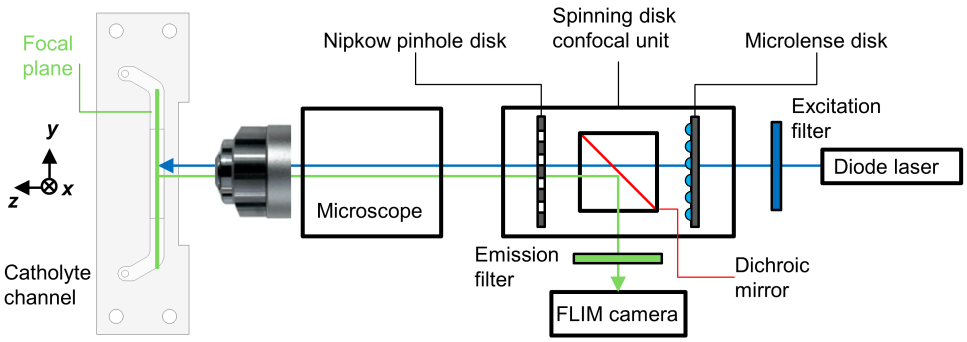

Figure 5.15: Schematic of FLIM system: Microscope: 5x objective, Modulated diode laser: 405 nm, 20 MHz, 300 mW. FLIM camera: 75 ms exposure time, 6 phase shift images, 2x camera gain.

We calibrated the FLIM system with an in-line titration setup (Figure 5.16). The dye and K_2SO_4 concentration were the same as for the CO_2 electrolysis experiments. We used a low phosphate buffer concentration of 0.0001 M to minimize the influence of phosphate ions on τ_ϕ.[44] The electrolyte was continuously purged with N_2 to prevent ambient CO_2 from dissolving in the electrolyte and influencing the pH. We recirculated the electrolyte through the flow cell (Figure 5.13) to record fluorescence lifetime images for a range of pH values. The pH of the electrolyte was adjusted by incrementally adding base solution to the electrolyte with a syringe pump. The base solution had the same dye and K_2SO_4 concentration to keep the corresponding concentrations in the bulk of the electrolyte constant. After a stabilization period of 2 min, we measured the pH with a pH meter and recorded the FLIM image. The average τ_ϕ in the center of the channel was calculated with the image processing software LIFA (Lambert Instruments, Netherlands) (Figure 5.16).

We used a quinolinium dye[43,44] to obtain the calibration curve for the pH and τ_ϕ (Figure 5.17). The curve has a τ_ϕ-plateau in the acidic region, which makes it impossible to distinguish the pH between 3.0 and 5.5. The dye is most sensitive to changes in τ_ϕ for the pH region between 6.3 and 9. We kept the optical FLIM parameters of the calibration and the CO_2 electrolysis experiments constant to minimize systematic errors.

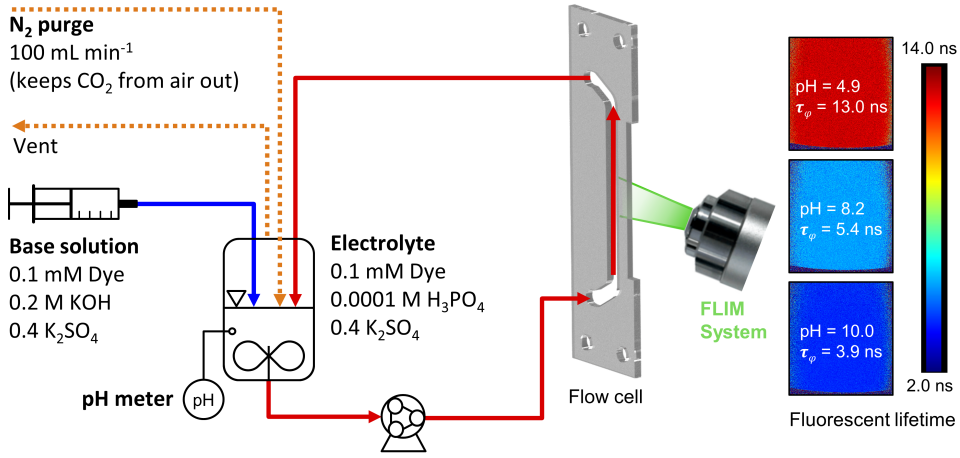

Figure 5.16: FLIM calibration produce: In-line titration coupled with the FLIM system.

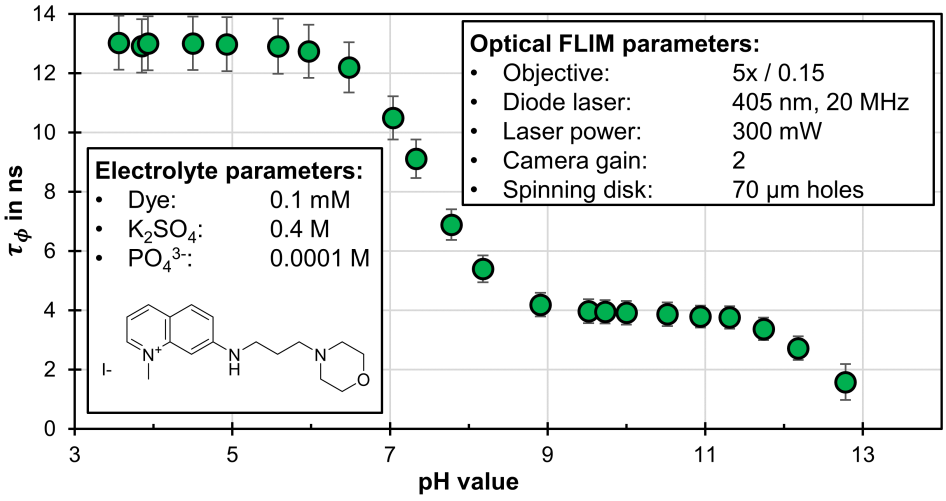

Figure 5.17: Calibration curve to calculate pH from the phase-shift fluorescent lifetime, τ_ϕ.

The geometry of the catholyte flow channel and the alignment with the microscope of the FLIM system are shown in Figure 5.18. The straight channel segment with a length of 7.5 mm was left without active area (Figure 5.18 a) to ensure a fully developed hydrodynamic flow profile. The microscope was focused on the outer channel wall (z_0-plane) as a reference point (Figure 5.18 b). Then the control software of the microscope was used to move the focal plane to the center of the channel depth in z-direction (z_2-plane) to carry out the imaging.

To process the FLIM images, we determined the wall coordinates of the channel with intensity images (Figure 5.18 c). The sides of the fluorescence lifetime images were cropped with these coordinates. The PET gaskets forming the wall of the channel show a lower fluorescence lifetime than the bulk of the electrolyte, which most likely originates from the fluorescence of the gasket material. [60] We assume that the gaskets exhibit a constant fluorescence lifetime, τ_ϕ, of about 11.5 ns. According to the calibration curve (Figure 5.17), this phenomenon leads to a systematic error, which lets the edges of the image appear to be close to pH 6. Therefore, the local pH near the walls in our images is overestimated at low pH (< 6) and underestimated at high pH (> 6).

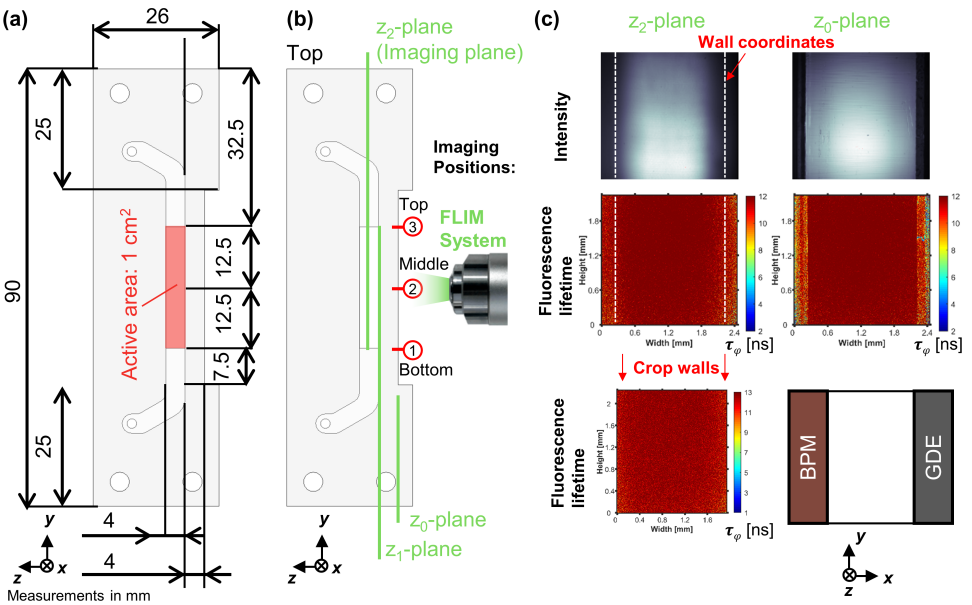

Figure 5.18: Flow channel geometry and FLIM procedure. (a) Geometry of flow cell. (b) Location of the three imaging positions (1): Bottom, (2): Middle, (3): Top. The outer channel wall (z_0) was used as a focusing reference. The imaging plane (z_2) was located in the middle of the channel depth (2 mm). (c) FLIM data processing: Intensity and phase-shift fluorescence lifetime, τ_ϕ, images of the 0.4 M K_2SO_4 catholyte with 0.1 mM fluorescent quinolinium dye.

During CO_2 electrolysis, we recorded 5 to 10 images at each channel height (Figure 5.18 b) for each process parameter set. Of these images, we selected examples with small amounts of bubble coverage and a clear view of the catholyte channel. These were then further processed with Matlab (Version R2019a). After cropping the walls, the fluorescent lifetime images were converted to 2D pH profiles (Figure 5.19) with the calibration curve. Typically, the local pH value close to the GDE (right side of image) rises because the electrochemical reactions release OH^- ions. We calculated 1D pH profiles by averaging the pH value over the y-axis of the 2D segment. For these 1D profiles, $pH_{avg}(x)$ is the y-averaged value over the channel width. The corresponding standard error is $\sigma_{pH}(x)$. The minimum pH of the profile is indicated by pH_{min}; the maximum is indicated by pH_{max}.

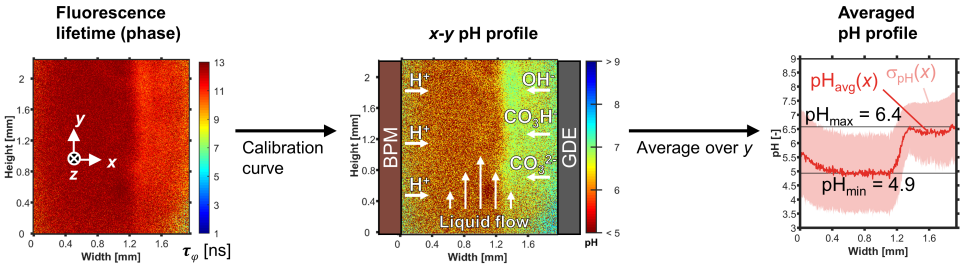

Figure 5.19: FLIM image processing. The pH profile, $pH_{avg}(x)$, was averaged over the height of the channel segment shown in the upper panel. The shaded red area indicates the standard deviation of the pH value, $\sigma_{pH}(x)$. The minimum value of $pH_{avg}(x)$ is pH_{min}. The maximum value of $pH_{avg}(x)$ is pH_{max}.

The intensity and corresponding fluorescent lifetime images show examples for different effects of gas bubble evolution (Figure 5.20). Typically, gas bubbles form at the surface of the GDE or the BPM (Figure 5.20 a). They grow until they reach a certain diameter and are released into the flow. This leaves the electrode surface uncovered for a while until the growth cycle starts again. Gas bubbles reduce the intensity of the fluorescence signal even if they are outside of the focal plane. The fluorescent lifetime, τ_ϕ, of the focal plane can still be measured as long as there is a sufficient signal-to-noise ratio.

This means that τ_ϕ is still available in proximity to growing, stagnant bubbles only casting partial shadows (Figure 5.20 a). However, the intensity close to the GDE often decreases because of intense shadows. In addition to bubbles forming at the surface, these shadows are caused by a lower fluorescence emission of the dye at high pH.[44] As a result, intense shadows cause a noisy signal close to the GDE (Figure 5.20 a). Another phenomenon of the gas bubble evolution are small, moving bubbles (Figure 5.20 b), which follow the flow of the catholyte. These bubbles typically just reduce the intensity slightly, so that τ_ϕ experiences only little noise. Occasionally smaller bubbles coalesce and form large, moving bubbles (Figure 5.20 c) taking up most of the channel cross-section. These bubbles cast intense shadows leading to a poor signal-to-noise ratio.

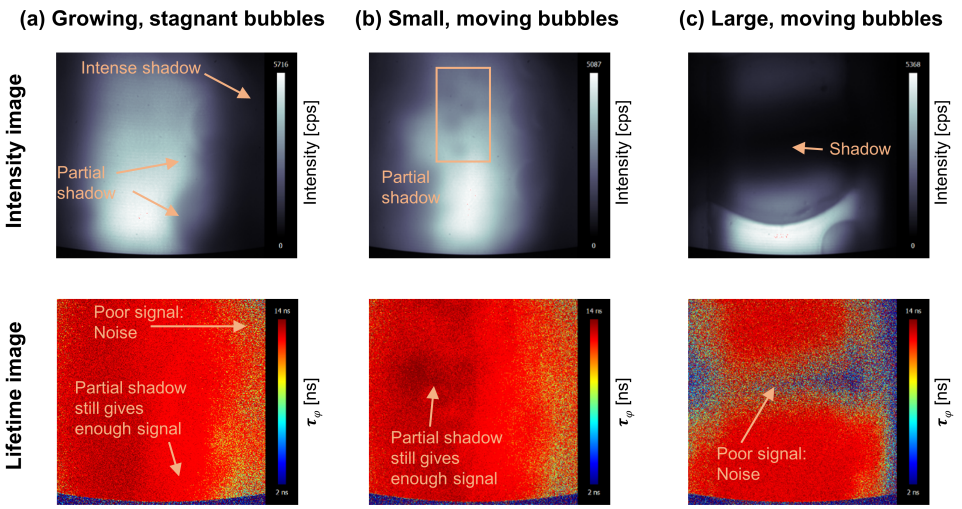

Figure 5.20: FLIM imaging of catholyte channel with bubble formation. Top: Intensity images. Bottom: corresponding fluorescence lifetime images. The channel walls were not cropped for these example images. (a) Growing bubbles at the GDE surface (b) Small, moving bubbles in the bulk of the catholyte flow (c) Large, moving bubble filling out the cross-section of the channel.

5.5.3. CALCULATION OF UNBUFFERED pH LIMIT

We calculate the unbuffered pH limit, $pH_{unbuffered}$, by making the following assumptions:

- OH^- is perfectly mixed across the channel width (x-direction)
- No neutralization with H^+ occurs
- No homogenous buffering reactions with CO_2 take place

To set up the mass balance, we further assume that the catholyte flows through the channel segment at a volumetric flow rate, F_L, (Figure 5.21). At the inlet ($y = 0$), the initial concentration of C_{OH^-} is determined by pH_{feed} using (5.6).

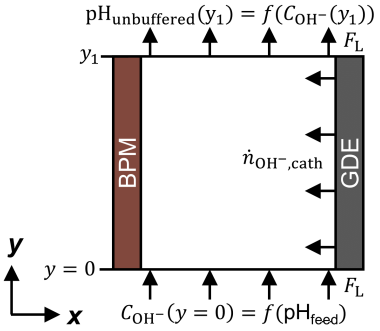

Figure 5.21: Mass balance to calculate the unbuffered pH limit, $pH_{unbuffered}$, over a channel segment with the height y_1. The molar flux of OH^- produced in the reaction is $\dot{n}_{OH^-,cath}$.

$$C_{OH^-} = 10^{-pOH} = 10^{-(14-pH)} \tag{5.6}$$

We consider the pH increase over the height of a channel segment with the height y_1 (Figure 5.21). For example, to calculate $pH_{unbuffered}$ at the middle of the channel height, we set y_1 to 1.25 cm. The electrochemical reaction releases a uniform flux of OH^-, $\dot{n}_{OH^-,cath}$, in $mol\,cm^{-2}\,s^{-1}$, which depends on j according to (5.7).

$$\dot{n}_{OH^-,cath} = \frac{j}{F} \tag{5.7}$$

Over the considered electrode height of y_1 and depth of $D = 0.4$ cm (z-direction), the cumulative flux $\dot{N}_{OH^-,cath}(y_1)$ is released according to (5.8).

$$\dot{N}_{OH^-,cath}(y_1) = \dot{n}_{OH^-,cath} \cdot D \cdot y_1 \tag{5.8}$$

The released OH^- mixes with the catholyte stream and increases the concentration of OH^- according to (5.9).

$$C_{OH^-}(y_1) = C_{OH^-}(y_0) + \frac{\dot{N}_{OH^-,cath}(y_1)}{F_L} \tag{5.9}$$

The value of $pH_{unbuffered}$ is then calculated with (5.10).

$$pH_{unbuffered}(y_1) = 14 - \left(-\log_{(}10) C_{OH^-}(y_1)\right) \tag{5.10}$$

5.5.4. CALCULATION OF CONVECTIVE CO_2 MASS TRANSFER

We calculate the limiting partial current density for CO, $j_{CO,lim}$ with (5.11). This quantity corresponds to the convective mass transfer of CO_2 from the bulk of the flowing catholyte to the electrode surface, $\dot{N}_{CO_2,conv}$. The number of electrons transferred in the reaction is $z_{CO} = 2$.

$$j_{CO,lim} = \frac{z_{CO} \cdot F \cdot \dot{N}_{CO_2,conv}}{A} \tag{5.11}$$

We calculate $\dot{N}_{CO_2,conv}$ in $mol\,s^{-1}$ with (5.12), in which k_{conv} is the convective mass transfer coefficient in $cm\,s^{-1}$. The mass transfer is driven by the CO_2 concentration gradient, ΔC_{CO_2}, which takes a maximum value of $C_{CO_2,bulk}$ if the CO_2 concentration at the electrode surface drops to zero. The bulk concentration of CO_2 at 25 °C is approximated with $C_{CO_2,bulk} = 34\,mmol\,L^{-1}$.[52]

$$\dot{N}_{CO_2,conv} = A \cdot k_{conv} \cdot \Delta C_{ceCO2} \approx A \cdot k_{conv} \cdot C_{CO_2,bulk} \tag{5.12}$$

The value of k_{conv} is determined by the correlation (5.13) of the Sherwood number, Sh, with the Reynolds number over the height of the electrode, Re_H, and the Schmidt number, Sc.[55] The height of the electrode, H, is 2.5 cm. The diffusion coefficient for CO_2 in water at 25 °C is $D_{CO_2} = 1.9 \times 10^{-5}\,cm^2\,s^{-1}$.[52]

$$k_{conv} = \frac{D_{CO_2} \cdot Sh}{H} = 0.664 \cdot \frac{D_{CO_2}}{H} \cdot Re_H^{0.5} \cdot Sc^{0.333} \tag{5.13}$$

We calculate the Reynolds number over the height of the electrode, Re_H, with (5.14). We note that this Reynolds number is different than the hydraulic Reynolds number, Re, defined by (5.1). The superficial liquid velocity, u, is given by (5.3). We approximate the kinematic viscosity of the catholyte, ν, with the corresponding value of water at 20 °C ($\nu = 1 \times 10^{-6}\,m^2\,s^{-1}$).[59] The value of Sc is given by (5.15).

$$Re_H = \frac{H \cdot u}{\nu} \tag{5.14}$$

$$Sc = \frac{\nu}{D_{CO_2}} = 532 \tag{5.15}$$

The resulting values for k_{conv} and $j_{CO,lim}$ are listed for hydraulic Reynolds numbers of $Re = 5$ and $Re = 50$ in Table 5.2.

Table 5.2: CO_2 mass transfer through forced convection. The hydraulic Reynolds number is Re. The volumetric catholyte flow rate is F_L. The superficial liquid velocity is u. The Reynolds number along the height of the electrode is Re_H. The convective mass transfer coefficient is k_{conv}. The corresponding limiting current density for CO is $j_{CO,lim}$.

Re	F_L	u	Re_H	k_{conv}	$j_{CO,lim}$
-	$mL\,min^{-1}$	$cm\,s^{-1}$	-	$cm\,s^{-1}$	$mA\,cm^{-2}$
5	0.9	0.19	46	2.8×10^{-4}	1.8
50	9.0	1.88	464	8.8×10^{-4}	5.8

The effect of increasing the Reynolds number on the FE_{CO} is shown in Figure 5.22.

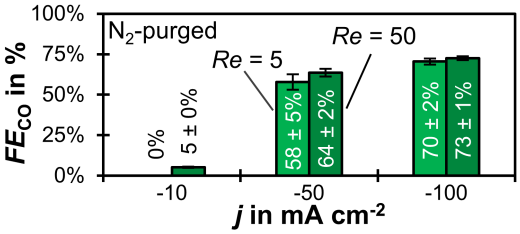

Figure 5.22: Effect of Reynolds number in catholyte channel, *Re*. FE_{CO} as a function of j and *Re* for N_2-purged catholyte. The error bars represent the estimated standard errors of three GC injections.

5.5.5. CALCULATION OF CO_2 BUFFERING CAPACITY

We estimate the nominal pH buffer capacity of the dissolved CO_2, $\dot{N}_{CO_2,buff}$, in $mol\,s^{-1}$ with (5.16). This value corresponds to the molar flux of OH^- that the dissolved CO_2 could absorb through the formation of CO_3^{2-}. For simplification, we neglect equilibrium reactions and assume that every dissolved molecule of CO_2 absorbs 2 molecules of OH^-.

$$\dot{N}_{CO_2,buff} = F_L \cdot 2 \cdot C_{CO_2,bulk} \tag{5.16}$$

We compare this buffering capacity with the total molar flux of OH^- formed in electrochemical reactions (Table 5.3). We neglect the consumption of CO_2 through the CO_2R reaction. This gives us an approximate ratio of $\dot{N}_{CO_2,buff}$ to $\dot{N}_{OH^-,cath}$ (Table 5.3).

$$\dot{N}_{OH^-,cath} = \frac{j \cdot A}{F} \tag{5.17}$$

Table 5.3: Nominal buffering capacity of dissolved CO_2. The hydraulic Reynolds number is *Re*. The volumetric catholyte flow rate is F_L. The current density is j. The nominal pH buffer capacity of the dissolved CO_2 is $\dot{N}_{CO_2,buff}$. The total molar flux of OH^- formed in electrochemical reactions is $\dot{N}_{OH^-,cath}$.

Re	F_L	j	$\dot{N}_{CO_2,buff}$	$\dot{N}_{OH^-,cath}$	$\frac{\dot{N}_{CO_2,buff}}{\dot{N}_{OH^-,cath}}$
-	$mL\,min^{-1}$	$mA\,cm^{-2}$	$mol\,s^{-1}$	$mol\,s^{-1}$	-
5	0.9	50	9.9×10^{-7}	5.2×10^{-7}	191%
5	0.9	100	9.9×10^{-7}	1.0×10^{-6}	96%
50	9.0	50	9.9×10^{-6}	5.2×10^{-7}	1910%
50	9.0	100	9.9×10^{-6}	1.0×10^{-6}	955%

5.5.6. COMPLETE SET OF pH PROFILES

The following section shows the 2D and 1D pH profiles for each parameter set (Figure 5.23 – Figure 5.30.

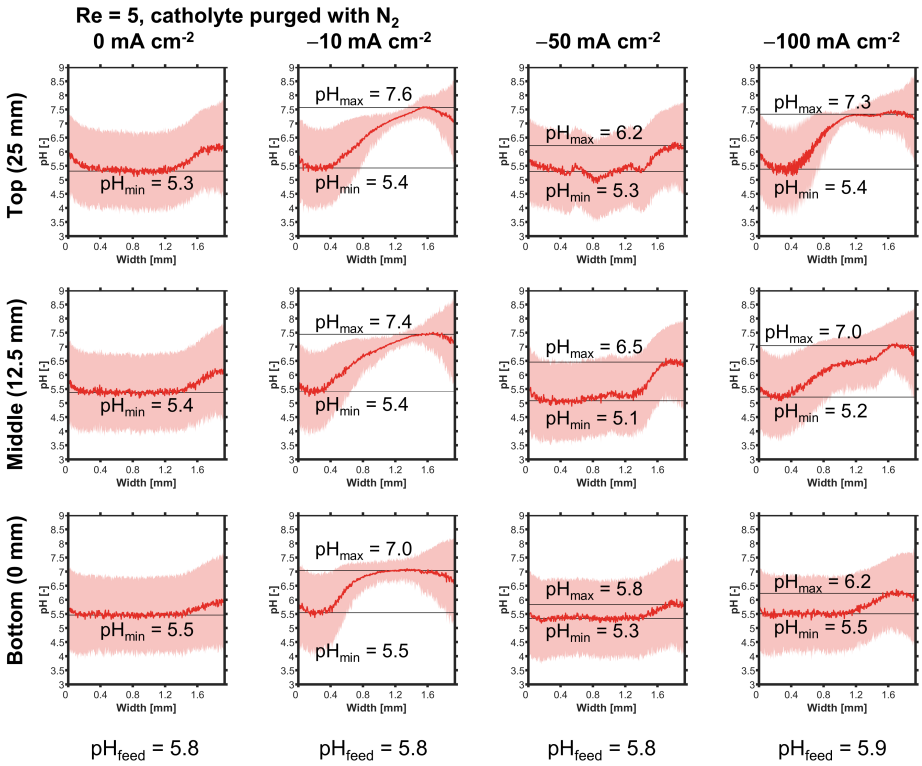

Figure 5.23: 1D pH profiles for $Re = 5$ and N_2-purged catholyte. The pH profile, pH_{avg}, was averaged over the height of the channel segment shown in the upper panel. The shaded red area indicates the standard deviation of the pH value. The minimum value of pH_{avg} is pH_{min}. The maximum value of pH_{avg} is pH_{max}. The pH value of the catholyte feed, pH_{feed}, was measured with a pH meter.

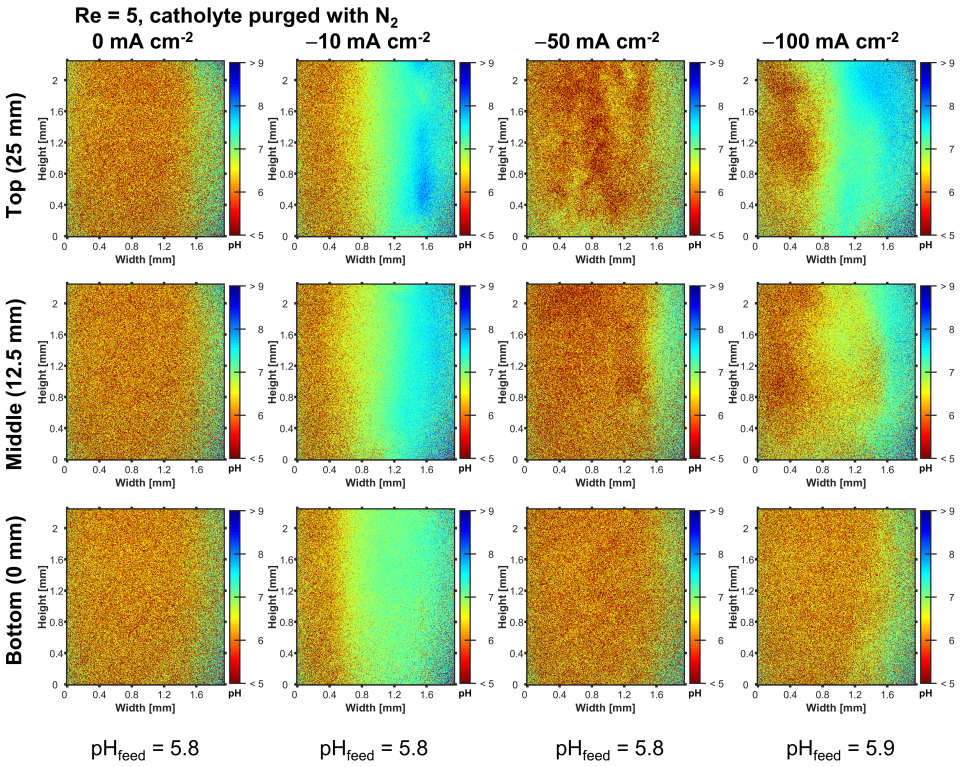

Figure 5.24: 2D pH profiles for $Re = 5$ and N_2-purged catholyte. The pH value of the catholyte feed, pH_{feed}, was measured with a pH meter.

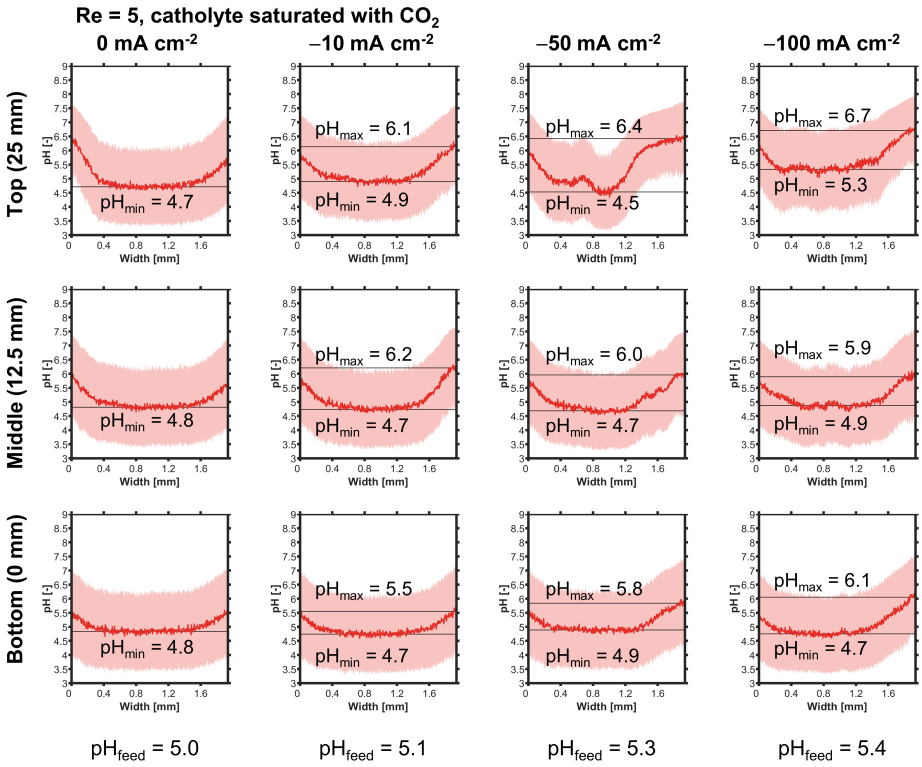

Figure 5.25: 1D pH profiles for $Re = 5$ and CO_2-saturated catholyte. The pH profile, pH_{avg}, was averaged over the height of the channel segment shown in the upper panel. The shaded red area indicates the standard deviation of the pH value. The minimum value of pH_{avg} is pH_{min}. The maximum value of pH_{avg} is pH_{max}. The pH value of the catholyte feed, pH_{feed}, was measured with a pH meter.

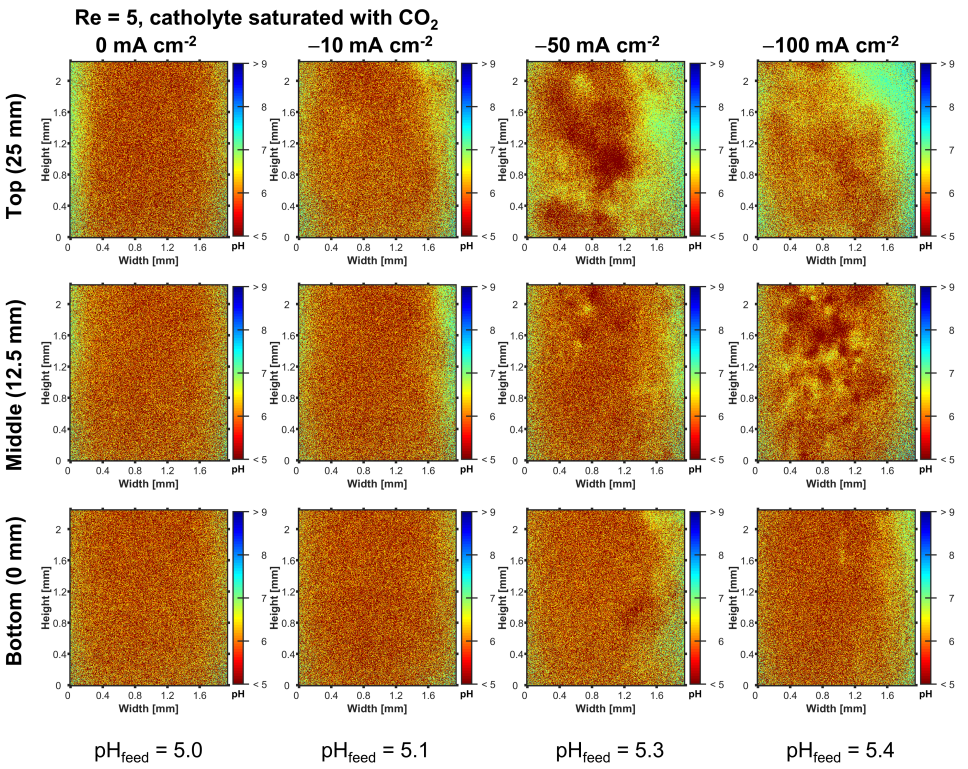

Figure 5.26: 2D pH profiles for $Re = 5$ and CO_2-saturated catholyte. The pH value of the catholyte feed, pH_{feed}, was measured with a pH meter.

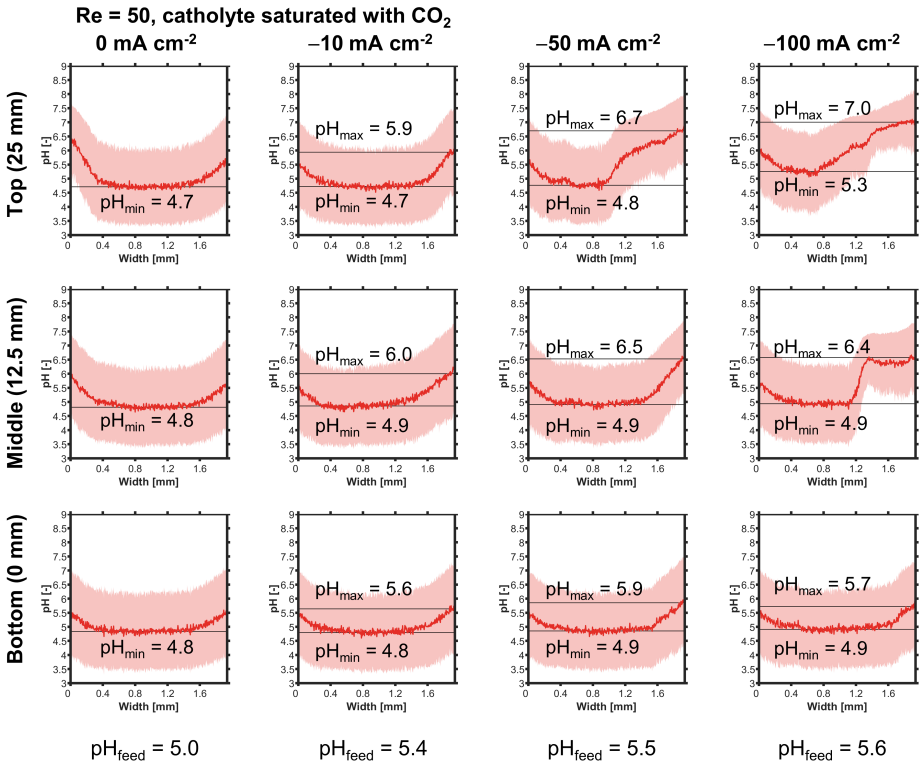

Figure 5.27: 1D pH profiles for $Re = 50$ and CO_2-saturated catholyte. The pH profile, pH_{avg}, was averaged over the height of the channel segment shown in the upper panel. The shaded red area indicates the standard deviation of the pH value. The minimum value of pH_{avg} is pH_{min}. The maximum value of pH_{avg} is pH_{max}. The pH value of the catholyte feed, pH_{feed}, was measured with a pH meter.

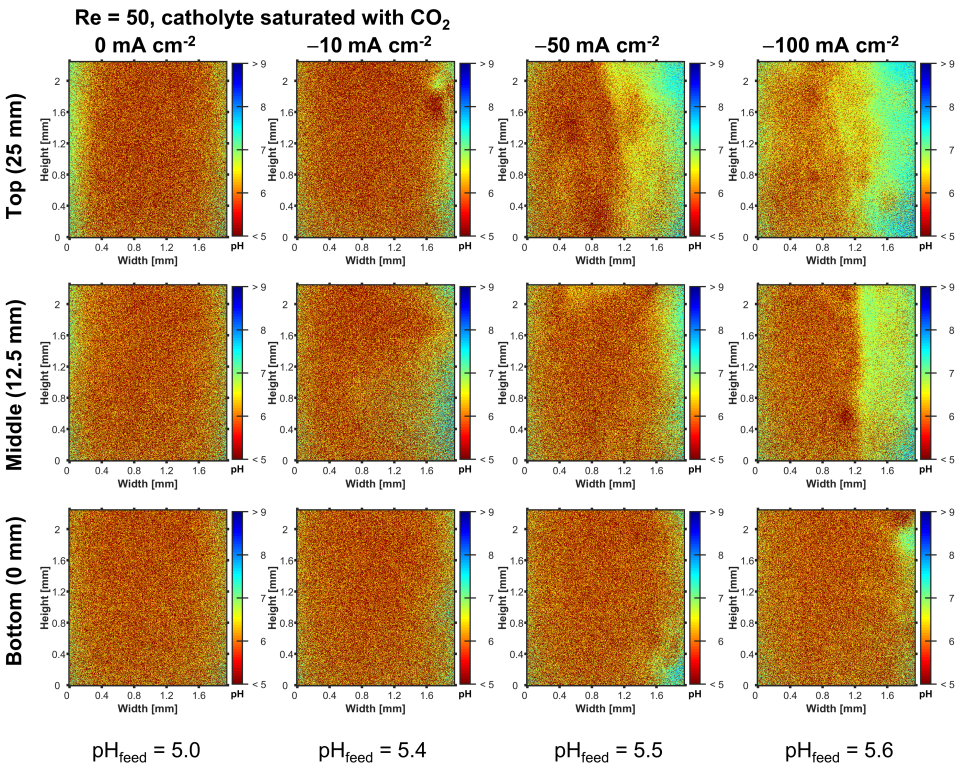

Figure 5.28: 2D pH profiles for $Re = 50$ and CO_2-saturated catholyte. The pH value of the catholyte feed, pH_{feed}, was measured with a pH meter.

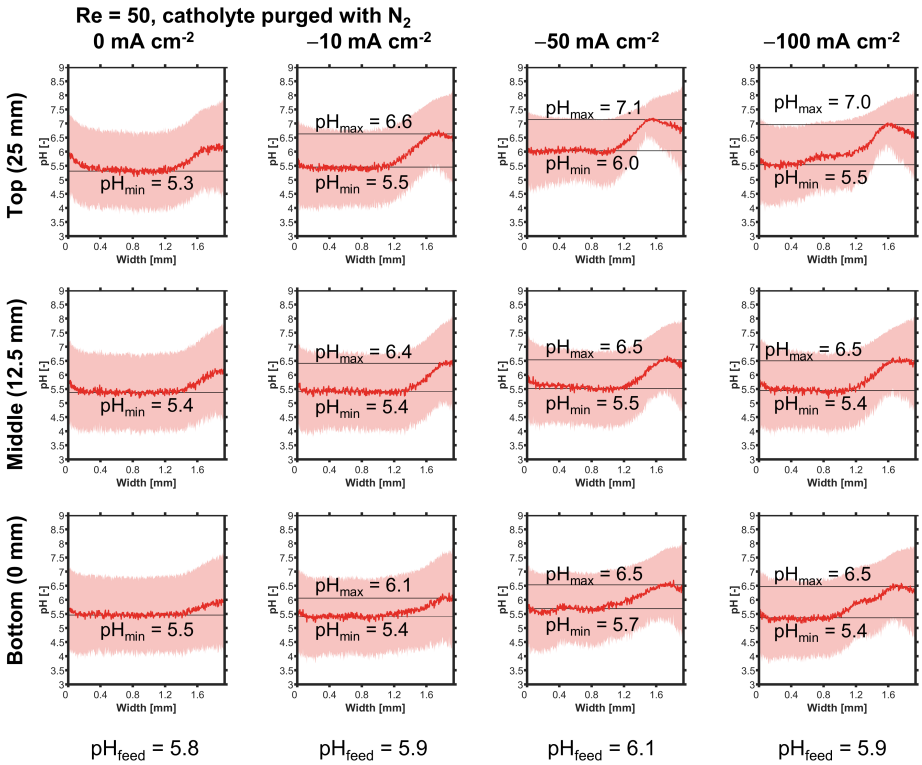

Figure 5.29: 1D pH profiles for $Re = 50$ and N_2-purged catholyte. The pH profile, pH_{avg}, was averaged over the height of the channel segment shown in the upper panel. The shaded red area indicates the standard deviation of the pH value. The minimum value of pH_{avg} is pH_{min}. The maximum value of pH_{avg} is pH_{max}. The pH value of the catholyte feed, pH_{feed}, was measured with a pH meter.

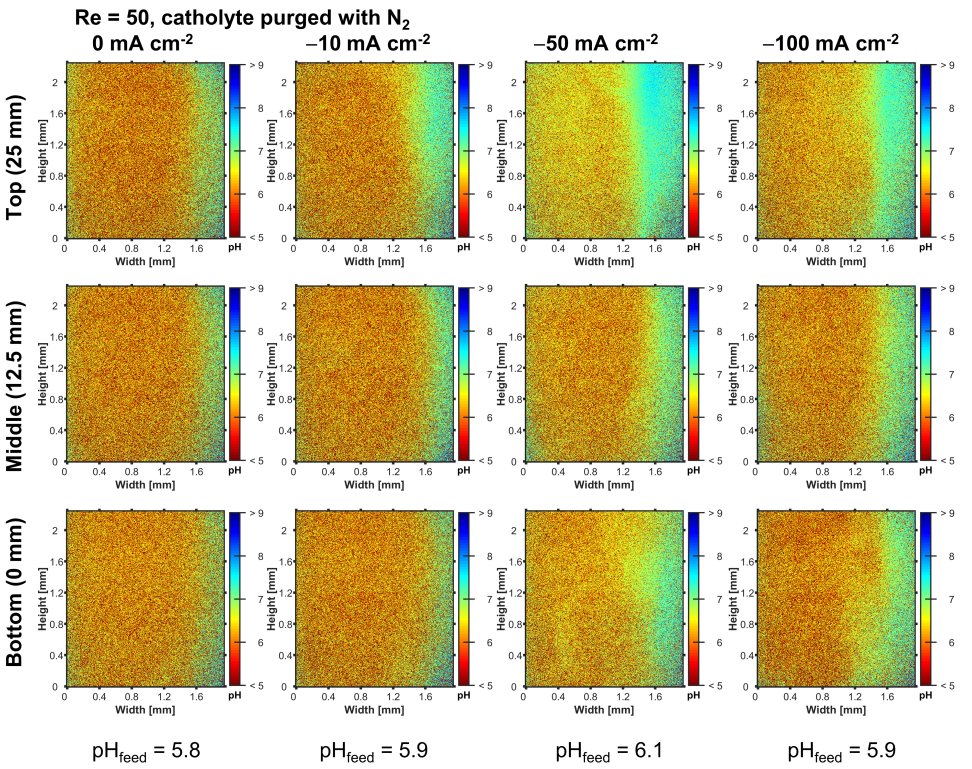

Figure 5.30: 2D pH profiles for $Re = 50$ and N_2-purged catholyte. The pH value of the catholyte feed, pH_{feed}, was measured with a pH meter.

5.6. ACKNOWLEDGEMENTS

The authors thank Christiaan Schinkel, Stefan ten Hagen, and Duco Bosma for their engineering support. This project has received funding from the European Research Council (ERC) under the European Union's Horizon 2020 research and innovation programme (grant agreement No 852115).

REFERENCES

[1] J. Blau, *The Paris Agreement: climate change, solidarity, and human rights* (Springer, 2017).

[2] G. Hammond and M. Newborough, *Glasgow climate pact: a step on the way towards a lower carbon dioxide world,* in *Proceedings of the Institution of Civil Engineers-Civil Engineering*, Vol. 175 (Thomas Telford Ltd) pp. 8–8.

[3] P. De Luna, C. Hahn, D. Higgins, S. A. Jaffer, T. F. Jaramillo, and E. H. Sargent, *What would it take for renewably powered electrosynthesis to displace petrochemical processes?* Science **364**, eaav3506 (2019).

[4] S. Roussanaly, N. Berghout, T. Fout, M. Garcia, S. Gardarsdottir, S. M. Nazir, A. Ramirez, and E. S. Rubin, *Towards improved cost evaluation of carbon capture and storage from industry,* International Journal of Greenhouse Gas Control **106**, 103263 (2021).

[5] D. W. Keith, G. Holmes, D. S. Angelo, and K. Heidel, *A process for capturing CO_2 from the atmosphere,* Joule **2**, 1573 (2018).

[6] R. Sharifian, R. M. Wagterveld, I. A. Digdaya, C. Xiang, and D. A. Vermaas, *Electrochemical carbon dioxide capture to close the carbon cycle,* Energy & Environmental Science **14**, 781 (2021).

[7] H. M. Jhong, F. R. Brushett, and P. J. Kenis, *The effects of catalyst layer deposition methodology on electrode performance,* Advanced Energy Materials **3**, 589 (2013).

[8] H. Yang, J. J. Kaczur, S. D. Sajjad, and R. I. Masel, *Electrochemical conversion of CO_2 to formic acid utilizing sustainion™ membranes,* Journal of CO_2 Utilization **20**, 208 (2017).

[9] C. M. Gabardo, C. P. O'Brien, J. P. Edwards, C. McCallum, Y. Xu, C.-T. Dinh, J. Li, E. H. Sargent, and D. Sinton, *Continuous carbon dioxide electroreduction to concentrated multi-carbon products using a membrane electrode assembly,* Joule (2019), https://doi.org/10.1016/j.joule.2019.07.021.

[10] D. M. Weekes, D. A. Salvatore, A. Reyes, A. Huang, and C. P. Berlinguette, *Electrolytic CO_2 reduction in a flow cell,* Accounts of Chemical Research **51**, 910 (2018).

[11] S. Verma, B. Kim, H. M. Jhong, S. Ma, and P. J. Kenis, *A gross-margin model for defining technoeconomic benchmarks in the electroreduction of CO_2,* ChemSusChem **9**, 1972 (2016).

[12] R. I. Masel, Z. Liu, H. Yang, J. J. Kaczur, D. Carrillo, S. Ren, D. Salvatore, and C. P. Berlinguette, *An industrial perspective on catalysts for low-temperature CO_2 electrolysis,* Nature nanotechnology , 118–128 (2021).

[13] D. Salvatore and C. P. Berlinguette, *Voltage matters when reducing CO_2 in an electrochemical flow cell,* ACS Energy Letters **5**, 215 (2020).

[14] D. Higgins, C. Hahn, C. Xiang, T. F. Jaramillo, and A. Z. Weber, *Gas-diffusion electrodes for carbon dioxide reduction: A new paradigm,* ACS Energy Letters **4**, 317 (2019).

[15] Y. Y. Birdja, E. Pérez-Gallent, M. C. Figueiredo, A. J. Göttle, F. Calle-Vallejo, and M. T. M. Koper, *Advances and challenges in understanding the electrocatalytic conversion of carbon dioxide to fuels,* Nature Energy **4**, 732 (2019).

[16] M. C. O. Monteiro, M. F. Philips, K. J. P. Schouten, and M. T. M. Koper, *Efficiency and selectivity of CO_2 reduction to CO on gold gas diffusion electrodes in acidic media,* Nature Communications **12**, 4943 (2021).

[17] X.-x. Wang, H. Fu, D.-m. Du, Z.-y. Zhou, A.-g. Zhang, C.-f. Su, and K.-s. Ma, *The comparison of pKa determination between carbonic acid and formic acid and its application to prediction of the hydration numbers,* Chemical Physics Letters **460**, 339 (2008).

[18] R. Kas, A. G. Star, K. Yang, T. Van Cleve, K. C. Neyerlin, and W. A. Smith, *Along the channel gradients impact on the spatioactivity of gas diffusion electrodes at high conversions during CO_2 electroreduction,* ACS Sustainable Chemistry & Engineering **9**, 1286 (2021).

[19] R. Kas, K. Yang, G. P. Yewale, A. Crow, T. Burdyny, and W. A. Smith, *Modeling the local environment within porous electrode during electrochemical reduction of bicarbonate,* Industrial & Engineering Chemistry Research (2022), 10.1021/acs.iecr.2c00352.

[20] L.-C. Weng, A. T. Bell, and A. Z. Weber, *Modeling gas-diffusion electrodes for CO_2 reduction,* Physical Chemistry Chemical Physics **20**, 16973 (2018).

[21] L.-C. Weng, A. T. Bell, and A. Z. Weber, *Towards membrane-electrode assembly systems for CO_2 reduction: a modeling study,* Energy & Environmental Science **12**, 1950 (2019).

[22] Z. Yang, D. Li, L. Xing, H. Xiang, J. Xuan, S. Cheng, E. H. Yu, and A. Yang, *Modeling and upscaling analysis of gas diffusion electrode-based electrochemical carbon dioxide reduction systems,* ACS Sustainable Chemistry & Engineering **9**, 351 (2020).

[23] J. W. Blake, V. Konderla, L. M. Baumgartner, D. A. Vermaas, J. T. Padding, and J. W. Haverkort, *Inhomogeneities in the catholyte channel limit the upscaling of CO_2 flow electrolysers,* ACS Sustainable Chemistry & Engineering (2023), 10.1021/acssuschemeng.2c06129.

[24] M. C. O. Monteiro and M. T. M. Koper, *Measuring local ph in electrochemistry,* Current Opinion in Electrochemistry **25**, 100649 (2021).

[25] D. Hursán and C. Janáky, *Operando characterization of continuous flow CO_2 electrolyzers: current status and future prospects,* Chemical Communications (2023), 10.1039/D2CC06065E.

[26] M. Dunwell, X. Yang, B. P. Setzler, J. Anibal, Y. Yan, and B. Xu, *Examination of near-electrode concentration gradients and kinetic impacts on the electrochemical reduction of CO_2 using surface-enhanced infrared spectroscopy,* ACS Catalysis **8**, 3999 (2018).

[27] K. Yang, R. Kas, and W. A. Smith, *In situ infrared spectroscopy reveals persistent alkalinity near electrode surfaces during CO_2 electroreduction,* Journal of the American Chemical Society (2019), 10.1021/jacs.9b07000.

[28] Z. Yan, J. L. Hitt, Z. Zeng, M. A. Hickner, and T. E. Mallouk, *Improving the efficiency of CO_2 electrolysis by using a bipolar membrane with a weak-acid cation exchange layer,* Nature Chemistry **13**, 33 (2021).

[29] Z. Zhang, L. Melo, R. P. Jansonius, F. Habibzadeh, E. R. Grant, and C. P. Berlinguette, *pH matters when reducing CO_2 in an electrochemical flow cell,* ACS Energy Letters , 3101 (2020).

[30] X. Lu, C. Zhu, Z. Wu, J. Xuan, J. S. Francisco, and H. Wang, *In-situ observation of the pH gradient near the gas diffusion electrode of CO_2 reduction in alkaline electrolyte,* Journal of the American Chemical Society (2020), 10.1021/jacs.0c06779.

[31] E. J. Heller, R. Sundberg, and D. Tannor, *Simple aspects of raman scattering,* The Journal of Physical Chemistry **86**, 1822 (1982).

[32] J. R. Lakowicz, *Principles of fluorescence spectroscopy* (Springer Science & Business Media, 2013).

[33] A. J. Leenheer and H. A. Atwater, *Imaging water-splitting electrocatalysts with ph-sensing confocal fluorescence microscopy,* Journal of The Electrochemical Society **159**, H752 (2012).

[34] E. B. van Munster and T. W. J. Gadella, *Fluorescence lifetime imaging microscopy (flim),* in *Microscopy Techniques*, edited by J. Rietdorf (Springer Berlin Heidelberg, Berlin, Heidelberg, 2005) pp. 143–175.

[35] H.-J. Lin, P. Herman, and J. R. Lakowicz, *Fluorescence lifetime-resolved pH imaging of living cells,* Cytometry Part A **52A**, 77 (2003).

[36] C. Hille, M. Berg, L. Bressel, D. Munzke, P. Primus, H.-G. Löhmannsröben, and C. Dosche, *Time-domain fluorescence lifetime imaging for intracellular pH sensing in living tissues,* Analytical and bioanalytical chemistry **391**, 1871 (2008).

[37] A. M. Benneker, B. Gumuscu, E. G. H. Derckx, R. G. H. Lammertink, J. C. T. Eijkel, and J. A. Wood, *Enhanced ion transport using geometrically structured charge selective interfaces,* Lab on a Chip **18**, 1652 (2018).

[38] J. C. de Valença, A. Kurniawan, R. M. Wagterveld, J. A. Wood, and R. G. H. Lammertink, *Influence of Rayleigh-Bénard convection on electrokinetic instability in overlimiting current conditions,* Physical Review Fluids **2**, 033701 (2017).

[39] J. de Valença, M. Jõgi, R. M. Wagterveld, E. Karatay, J. A. Wood, and R. G. H. Lammertink, *Confined electroconvective vortices at structured ion exchange membranes,* Langmuir **34**, 2455 (2018).

[40] A. M. Kalde, M. Grosseheide, S. Brosch, S. V. Pape, R. G. Keller, J. Linkhorst, and M. Wessling, *Micromodel of a gas diffusion electrode tracks in-operando pore-scale wetting phenomena,* Small **18**, 2204012 (2022).

[41] L. M. Baumgartner, C. I. Koopman, A. Forner-Cuenca, and D. A. Vermaas, *Narrow pressure stability window of gas diffusion electrodes limits the scale-up of CO_2 electrolyzers,* ACS Sustainable Chemistry & Engineering **10**, 4683 (2022).

[42] T. Tanaami, S. Otsuki, N. Tomosada, Y. Kosugi, M. Shimizu, and H. Ishida, *High-speed 1-frame/ms scanning confocal microscope with a microlens and nipkow disks,* Applied optics **41**, 4704 (2002).

[43] W. F. Jager, T. S. Hammink, O. van den Berg, and F. C. Grozema, *Highly sensitive water-soluble fluorescent pH sensors based on the 7-amino-1-methylquinolinium chromophore,* The Journal of Organic Chemistry **75**, 2169 (2010).

[44] J. Bleeker, A. P. Kahn, L. M. Baumgartner, F. C. Grozema, D. A. Vermaas, and W. F. Jager, *Quinolinium-based fluorescent probes for dynamic pH monitoring in aqueous media at high pH using fluorescence lifetime imaging (flim),* ACS sensors (2023).

[45] Y. Chen, A. Vise, W. E. Klein, F. C. Cetinbas, D. J. Myers, W. A. Smith, T. G. Deutsch, and K. C. Neyerlin, *A robust, scalable platform for the electrochemical conversion of CO_2 to formate: Identifying pathways to higher energy efficiencies,* ACS Energy Letters **5**, 1825 (2020).

[46] B. De Mot, J. Hereijgers, N. Daems, and T. Breugelmans, *Insight in the behavior of bipolar membrane equipped carbon dioxide electrolyzers at low electrolyte flowrates,* Chemical Engineering Journal , 131170 (2021).

[47] M. Duarte, B. De Mot, J. Hereijgers, and T. Breugelmans, *Electrochemical reduction of CO_2: Effect of convective CO_2 supply in gas diffusion electrodes,* ChemElectroChem **6**, 5596 (2019).

[48] S. Verma, X. Lu, S. Ma, R. I. Masel, and P. J. Kenis, *The effect of electrolyte composition on the electroreduction of CO_2 to CO on Ag based gas diffusion electrodes,* Physical Chemistry Chemical Physics **18**, 7075 (2016).

[49] T. Burdyny and W. A. Smith, *CO_2 reduction on gas-diffusion electrodes and why catalytic performance must be assessed at commercially-relevant conditions,* Energy & Environmental Science (2019), 10.1039/C8EE03134G.

[50] L. M. Baumgartner, C. I. Koopman, A. Forner-Cuenca, and D. A. Vermaas, *When flooding is not catastrophic – woven gas diffusion electrodes enable stable CO_2 electrolysis,* ACS Applied Energy Materials , 15125 (2022).

[51] J. W. Blake, J. T. Padding, and J. W. Haverkort, *Analytical modelling of CO_2 reduction in gas-diffusion electrode catalyst layers,* Electrochimica Acta **393**, 138987 (2021).

[52] N. Gupta, M. Gattrell, and B. MacDougall, *Calculation for the cathode surface concentrations in the electrochemical reduction of CO_2 in $KHCO_3$ solutions,* Journal of applied electrochemistry **36**, 161 (2006).

[53] S. F. Jones, G. M. Evans, and K. P. Galvin, *Bubble nucleation from gas cavities — a review,* Advances in Colloid and Interface Science **80**, 27 (1999).

[54] H. Vogt and K. Stephan, *Local microprocesses at gas-evolving electrodes and their influence on mass transfer,* Electrochimica Acta **155**, 348 (2015).

[55] T. Burdyny, P. J. Graham, Y. Pang, C.-T. Dinh, M. Liu, E. H. Sargent, and D. Sinton, *Nanomorphology-enhanced gas-evolution intensifies CO_2 reduction electrochemistry,* ACS Sustainable Chemistry & Engineering **5**, 4031 (2017).

[56] M. Ma, S. Kim, I. Chorkendorff, and B. Seger, *Role of ion-selective membranes in the carbon balance for CO_2 electroreduction via gas diffusion electrode reactor designs,* Chemical Science **11**, 8854 (2020).

[57] J. W. Lee, D. K. Sohn, and H. S. Ko, *Study on bubble visualization of gas-evolving electrolysis in forced convective electrolyte,* Experiments in Fluids **60**, 1 (2019).

[58] B. De Mot, J. Hereijgers, M. Duarte, and T. Breugelmans, *Influence of flow and pressure distribution inside a gas diffusion electrode on the performance of a flow-by CO_2 electrolyzer,* Chemical Engineering Journal **378**, 122224 (2019).

[59] J. H. Lienhard, *A heat transfer textbook* (Dover Publications, 2019).

[60] I. Ouchi, R. Miyamura, M. Sakaguchi, S. Hosaka, and M. Kitagawa, *Excitation and emission spectra of polyethylene terephthalate and polyethylene 2, 6-naphthalate films,* Polymers for Advanced Technologies **10**, 195 (1999).

6

CONCLUSION

We assess the feasibility of sustainable production of fuels and chemicals through CO_2 electrolysis by comparing the requirements for industrial-scale CO_2 electrolysis with recent developments in the field and key findings of this thesis.

6.1. WHAT WOULD CO_2 ELECTROLYSIS REQUIRE AT AN INDUSTRIAL SCALE?

The global economy requires hydrocarbon fuels and chemicals at a scale of hundreds of millions of tons per year. For example, the International Civil Aviation Organization estimates that the global consumption of aviation fuel amounted to 200 Mt in 2016.[1] Two of the most important organic bulk chemicals[2] are ethylene (C_2H_4: 160 Mt in 2016)[3] and methanol (H_3COH: 85 Mt in 2016).[4] To illustrate the requirements of replacing conventional fossil fuel-based production with CO_2 electrolysis-based production, we make a case study based on the global H_3COH production (Figure 6.1).

The global demand for H_3COH could be covered by 26 industrial plants with an individual output capacity of 3.3 Mt year^{-1} (Figure 6.1). According to a theoretical plant design by Smith *et al.*[5], direct air capture would provide the CO_2 feedstock, which would be reduced to CO by CO_2 electrolysis. Alkaline water electrolysis would produce H_2 to convert CO to H_3COH in the final methanol synthesis step.

When operating at a current density of 400 mA cm^{-2}, the CO_2 electrolysis process for one of these methanol plants would require a total cell area of 175 000 m^2 (Figure 6.1).[5] This cell area would be split up into a number of CO_2 electrolyzer stacks.

We can use a stack with a cell area of 4 m^2 as an example, for which techno-economic calculations exist in literature.[6] For the numbers of this study, each methanol plant would require 43 750 CO_2 electrolyzers stacks (Figure 6.1).

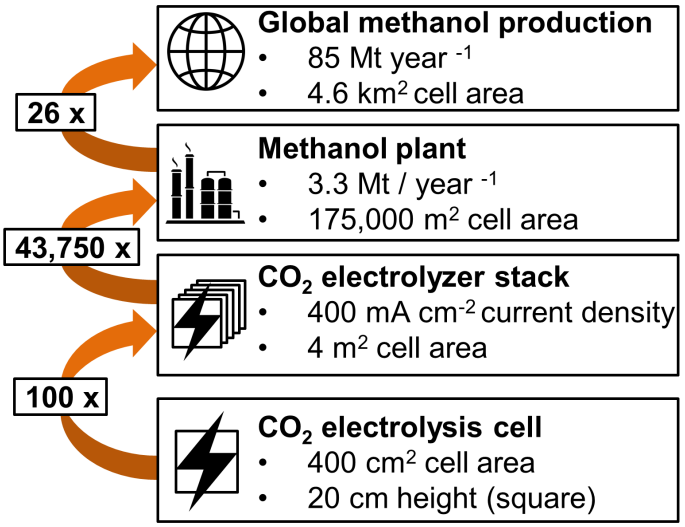

Figure 6.1: CO_2 electrolysis requirements to cover global methanol production (H_3COH: 85 Mt in 2016)[4]. Methanol plant assumptions:[5] 10,000 t H_3COH day^{-1}, −400 mA cm^{-2} CO_2 electrolyzer current density, 100% Faradaic efficiency for CO, 90% uptime. CO_2 electrolyzer stack assumptions based on techno-economic analysis by Verma *et al.*.[6]

6

Each CO_2 electrolyzer stack would consist of 100 electrolysis cells with an individual cell area of 400 cm^2 (Figure 6.1).[6] We note that the cell area of this example is relatively small, which leads to the large number of 43 750 CO_2 electrolyzers stacks. In practice, a larger cell area is highly desirable because this reduces the capital costs (e.g., for electrical connections or plumbing connections). For comparison, commercial alkaline water electrolysis stacks typically consist of 30 to 200 cells with an individual area of 10 000 to 30 000 cm^2.[7]

Verma *et al.* estimate a capital expenditure of 2500 USD per 4 m^2-CO_2 electrolyzer stack by calculating the costs of the individual cell components (e.g., bipolar plates, gaskets, or flow channels) for this geometry. To recover these capital costs, the cell lifetime would have to be at least 1800 h.[6] For an economically viable process, however, a lifetime of several years would be highly desirable (e.g., ≥ 2 years = ≥ 17 500 h).[8]

The combined cell area of all 26 methanol plants amounts to 4.6 km^2, which would require a substantial amount of catalyst metals (Table 6.1). We can estimate the required amounts based on common catalyst loadings and compare them to the global production rates, which can serve as a rough indicator for feasibility. The cathode gas diffusion electrodes (GDEs) would require 46 t of silver, which is relatively low compared to the global mining rate of 23 kt $year^{-1}$.

Iridium is the standard anode catalyst for CO_2 electrolysis because it is stable in neutral or acidic pH conditions, which are inevitable in commonly used CO_2 electrolyzers with

Table 6.1: Electrode metals required to produce 85 Mt year^{-1} H_3COH with CO_2 electrolysis. The geometric cell area of all CO_2 electrolyzers is 26 x 175 000 m^2 = 4.6 km^2. The GDE cathode uses dispersed Ag loaded onto a GDE.[13] Ir-based anode are made of IrO_2-coated porous titanium structures.[14] We assumed an optimistic loading of 0.5 mg Ir cm^{-2}.[10] Alternatively, Ni-based anodes are made of porous nickel foams. We used the material specifications of the foam used in Chapter 5.

Metal	Ag	Ir	Ni
Component	Cathode	Anode	Anode
Loading	1.0 mg cm^{-2}	0.5 mg cm^{-2}	43 mg cm^{-2}
Required mass	46 t	23 t	1957 t
Global production	23 kt year^{-1} (2014)[15]	7 t year^{-1} (2020)[10]	2 Mt year^{-1} (2016)[16]

anion exchange membrane.[9] Unfortunately, iridium is only mined at a rate of 7 t year^{-1} globally because it is one of the rarest elements in the earth's crust.[10] This scarcity would likely hinder its employment as an anode catalyst for large scale-CO_2 electrolysis. Further, iridium would also be required for other applications like PEM water electrolysis. Minke *et al.* estimate current iridium-mining rates would limit the global PEM electrolysis capacity to 60 GW by 2050.[10] For illustration, this capacity would correspond to an annual production of about 12 Mt H_2, which is relatively modest in comparison with the 85 Mt of H_2 produced from fossil fuels in 2016.[11] These numbers suggest there would not be enough Ir available to carry out CO_2 electrolysis at the scale necessary for 85 Mt methanol year^{-1}.

Nickel could be used as an alternative anode catalyst, which is mined at a much larger scale relative to the required amount for CO_2 electrolysis (Table 6.1: 2 Mt year^{-1} vs. 1957 t). It might be necessary to optimize the loading, however, because nickel is also required in large quantities for lithium ion batteries, alkaline electrolyzers, and stainless steel. Nickel requires a special electrolyzer design with an alkaline electrolyte because it oxidizes to Ni^{2+} below pH 9 at 25 °C.[12]

We would like to highlight that the amounts of metal catalysts listed in Table 6.1 would only cover the annual production of methanol (H_3COH: 85 Mt). However, to also cover the production of aviation fuels (C_9H_x to $C_{16}H_x$: 200 Mt)[1] and ethylene (C_2H_4: 160 Mt),[3] these metal amounts would have to be increased by a factor of 35. We estimate this factor based on the relative molecular carbon contents and relative fuel/ethylene production rates.

To keep the material requirements and the capital expenditure of CO_2 electrolyzers low, they have to operate at high current density with a long lifetime. The capital costs can further be reduced by scaling up the cell area and thereby reducing the number of required stacks. Due to iridium's scarcity, CO_2 electrolyzers have to be designed so they can operate with Ni-based instead of Ir-based anodes.

Another important aspect is the enormous energy consumption of the overall process (CO_2 capture, CO_2 electrolysis, and water electrolysis). For illustration, Smith et al. cal-

culate that one methanol plant with an annual capacity of 3.3 Mt year^{-1} would require solar panels with an area of 243 km^2 —about four times the area of Manhattan (New York). Therefore, CO_2 electrolyzers also have to operate at a low cell potential and a high Faradaic efficiency to maximize the energy efficiency.

Together with other techno-economic studies we can conclude that the following requirements have to be met for industrial-scale CO_2 electrolysis:[8,17]

- Faradaic efficiency for CO, FE_{CO}: ≥ 95%
- Current density, j: −400 mA cm^{-2}
- Cell potential, E_{cell}: ≤ 3 V (≙ Energy Efficiency: ≥ 46%)[18]
- CO_2 electrolyzer design with Ni-based anodes (Ir-free)
- Cell electrode area ≥ 400 cm^2 (≙ height ≥ 20 cm for square cell)
- Cell lifetime of several years (e.g., ≥ 2 years = ≥ 17 500 h)

6.2. WHAT CAN CO_2 ELECTROLYSIS CURRENTLY ACHIEVE?

During the course of this PhD project, a number of other research groups have made important contributions to the field of CO_2 electrolysis, which we will briefly present here. Further, we will provide the answers to the research questions (RQ) posed in the introduction of this thesis and discuss how they contribute to the key issues of electrolyzer design, scale-up, and stability.

6.2.1. CO_2 ELECTROLYZERS WITH BIPOLAR MEMBRANE AND FLOWING CATHOLYTE REPLACE IRIDIUM BY ENABLING NICKEL ANODES

To date, the best-performing CO_2 electrolyzers all employ an iridium-based anode. These anodes have been already commercialized for the mature PEM water electrolysis technology and enable the stable operation of CO_2 electrolyzers at the lab-scale.[9] Many CO_2 electrolyzers with iridium-based anode feature a membrane electrode assembly (MEA), in which an anion exchange membrane (AEM) is pressed directly against the cathode. Reactors with such an AEM-MEA configuration can already meet the previously listed electrochemical requirements. For example, Endrődi *et al.* achieved a FE_{CO} = 86% at a current density of −450 mA cm^{-2} with a low E_{cell} of 2.8 V (Table 6.2).[19]

Motivated by the dilemma of iridium's scarcity, the field has developed CO_2 electrolyzers with bipolar membrane (BPM) as an alternative to the AEM-MEA systems. The integration of a BPM allows to select different electrolytes for the anode (e.g., KOH) and the cathode (e.g., $KHCO_3$ or K_2SO_4). This feature has enabled the employment of nickel-based anodes, which require an alkaline anolyte to be stable (e.g., KOH).[25]

The comparison with a state-of-the-art AEM-MEA electrolyzer[19] shows that recent BPM electrolyzers[21,24] still require improvements to their the electrochemical performance

Table 6.2: Electrochemical performance of gas-fed CO_2 electrolyzers. Electrolyzers with anion exchange membrane (AEM) and membrane electrode assembly (MEA) are catholyte-free and require Ir-based anodes. Electrolyzers with bipolar membrane (BPM) can use an alkaline anolyte and Ni-based anodes. The catholyte can be flowing (f.) or stationary (s.). Yang *et al.* infused their BPM-MEA with KOH.[20] All listed electrolyzers were equipped with gas diffusion electrodes (GDEs). The current density is j. The Faradaic efficiency for the listed product is FE_i. The cell potential is E_{cell}.

Electrolyzer	Anode	Cathode	j	Product i	FE_i	E_{cell}
AEM-MEA[19]	Ir-based	Ag-GDE	$-450\,\text{mA}\,\text{cm}^{-2}$	CO	86%	2.8 V
BPM + f. catholyte[21]	Ni foam	SnO_2-GDE	$-450\,\text{mA}\,\text{cm}^{-2}$	HCOOH	85%	5.5 V
BPM-MEA[22]	Ni foam	Ag-GDE	$-300\,\text{mA}\,\text{cm}^{-2}$	CO	30%	4.7 V
BPM-MEA + KOH[20]	Ni foam	Ag-GDE	$-200\,\text{mA}\,\text{cm}^{-2}$	CO	45%	4.8 V
BPM + s. catholyte[23]	Ir-based	Cu-GDE	$-300\,\text{mA}\,\text{cm}^{-2}$	C_2H_4	17%	3.9 V
BPM + f. catholyte[24]	Ni foam	Ag-GDE	$-300\,\text{mA}\,\text{cm}^{-2}$	CO	70%	8.4 V
BPM + f. catholyte[24]	Ni foam	Ag-GDE	$-350\,\text{mA}\,\text{cm}^{-2}$	CO	24%	10 V

(Table 6.2). E_{cell}, for example, is much lower for the MEA-type electrolyzer of Endrődi *et al.*[19] compared to the BPM-type electrolyzer by Chen *et al.*[21] (Table 6.2: 2.8 V vs. 5.5 V). However, other examples listed in Table 6.2 suggest that E_{cell} can be further optimized.[20,22,23] For example, ohmic losses can be lowered by reducing the thickness of the membrane[26] or the catholyte gap.[23]

Maintaining a high FE at higher current densities can also be challenging for BPM systems. In the example of De Mot *et al.*,[24] FE_{CO} drops from 70% to 24% when the current density is changed from $-300\,\text{mA}\,\text{cm}^{-2}$ to $-350\,\text{mA}\,\text{cm}^{-2}$ (Table 6.2). It is difficult to understand which mechanism is responsible for this performance decay because this electrolyzer type features a number of complex phenomena (e.g., electrochemical reactions, homogeneous reactions, convection, diffusion, and migration). Therefore, numerical and/or experimental studies improving the understanding of the local reaction environment might be able to guide the optimization of this reactor type.

The local reaction environment in a BPM-electrolyzer was studied in this thesis (**RQ7** and **RQ8**). We experimentally visualize the 2D pH profile in a CO_2 electrolyzer catholyte channel, which was imaged with operando FLIM using a pH-sensitive quinolinium dye (Chapter 5). At a low current density of $-10\,\text{mA}\,\text{cm}^{-2}$, we observe the development of an alkaline boundary layer at the cathode GDE (pH $\geq$ 7.4) resulting in a poor FE_{CO}. At current densities of $-50\,\text{mA}\,\text{cm}^{-2}$ or higher, bubble-induced mixing occurs. This phenomenon removes product ions and leads to an intermediate pH in the catholyte channel (**RQ8**: Chapter 5). By limiting the pH increase, bubble-induced mixing further ensures that CO_2 is available in the catalyst layer of the GDE, which improves the FE_{CO} (**RQ7**: Chapter 5). Further, saturating the catholyte with CO_2 also improved FE_{CO}, probably through a combination of lowering the bulk pH value, providing pH buffering capacity, and additional bubble-induced mixing (**RQ7** and **RQ8**: Chapter 5). Interestingly, increasing the catholyte flow rate did not always lead to a higher overall mass transfer in the catholyte channel (**RQ7** and **RQ8**: Chapter 5). This is because the higher drag forces of the liquid reduce the contribution of bubble mixing.

Future efforts to operate CO_2 electrolyzers with BPM at high current density have to ensure a sufficiently high mass transfer in the catholyte channel. This will maintain a favorable reaction environment at the cathode GDE (intermediate local pH, high CO_2 concentration) and enable a high Faradaic efficiency. For scale-up, it might be beneficial to optimize the channel geometry (e.g., modifying the aspect ratio to exploit bubble mixing). Further, possible interactions between process parameters (e.g. between the current density-dependent bubble formation and the catholyte flow rate) have to be considered to optimize the mass transfer in the catholyte channel.

6.2.2. CURRENT CO_2 ELECTROLYZER SCALE

Most studies in the field have been carried out in cells with a geometric electrode area of $\leq 5\,cm^2$.[27,28] To the best of our knowledge, the largest reported CO_2 electrolyzer had an electrode area of 250 cm^2 in MEA configuration (Figure 6.2).[29] This value is smaller than the 400 cm^2 cell area in the techno-economic analysis by Verma *et al.*,[6] which suggest that the capital costs would be significantly higher. Nonetheless, it is promising for future industrial application that the stackability of CO_2 electrolysis cells has already been explored successfully.[14,30]

The largest cell area reported for CO_2 electrolysis is several orders of magnitude smaller (Figure 6.2) in comparison with mature electrolysis technologies (e.g., alkaline water electrolysis[7] or chlor-alkali electrolysis).[31,32] Therefore, we can assume that the ratio of electrolysis capacity and capital costs will be less favorable for CO_2 electrolysis. We also note that the scale-up of e.g., water electrolyzers is a lot simpler than the scale-up of CO_2 electrolyzers because less side reactions can occur at the electrodes.

For CO_2 electrolyzers with flowing catholyte, the largest reported cell area is even smaller (Figure 6.2: 100 cm^2).[33] The scale-up of CO_2 electrolyzers with flowing catholyte is particularly challenging because the porous GDE is in direct contact with the electrolyte. This means that for sufficiently tall cells, the hydrostatic pressure of the electrolyte can flood the GDE and thereby impede the mass transfer of CO_2.

Most CO_2 electrolyzers use gas diffusion electrode (GDE) based on commercial carbon-based gas diffusion layers (GDLs). Because these materials have been developed for hydrogen fuel cells and PEM electrolysis,[34] they often feature cracks in their microporous layer (MPL).[35] The presence of cracks is not optimal for the application of these materials in CO_2 electrolysis because they prevent the separation of gas and liquid phase over a wide differential pressure range.[36]

This thesis shows that cracks in the MPL result in a narrow stable pressure window. We demonstrate that increasing the thickness of carbon paper-based GDEs improves the flooding resistance (**RQ1**: Chapter 2). In the best case, this would allow a cell height of 81 cm for CO_2 electrolyzers with flowing catholyte. However, this is not a viable strategy to prevent flooding because the increased thickness also significantly hampers the mass transfer of CO_2 resulting in poor Faradaic efficiency (**RQ2**: Chapter 2). In addition,

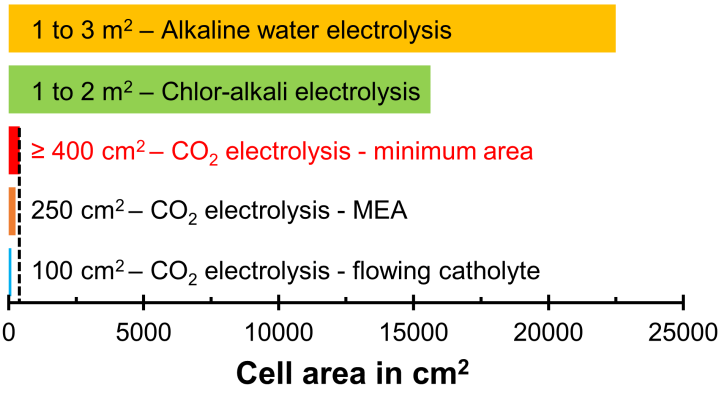

Figure 6.2: Comparison of of CO_2 electrolyzer cell size. Alkaline water electrolysis:[7] Cell area corresponds to a cell height of 1000 to 2000 cm (circular geometry). Chlor-alkali electrolysis with oxygen depolarized cathode (ODC): Cell area corresponds to a cell height of 1000 to 1500 cm (square geometry).[31,32] CO_2 electrolysis - minimum required cell area to reach the break-even-point in the techno-economic analysis of Verma *et al.*.[6] Cell area corresponds to a cell height of 20 cm (square geometry). CO_2 electrolysis - MEA: based on the work of Kaczur et al..[29] CO_2 electrolysis - flowing catholyte: based on the work of Jeanty *et al.*.[33]

the Faradaic efficiency of thick carbon paper is further diminished through electrolyte flooding (**RQ3**: Chapter 3).

Chapter 3 demonstrates that the flooding resistance is decreased when operating at industrially relevant current density. Due to the electrical potential applied at these conditions, the GDE experiences electrowetting, which reduces the hydrophobicity of its surface. For example, we found that a GDE based on a SGL 39BC substrate could operate at $-200\,mA\,cm^{-2}$ with $FE_{CO} = 74\%$ while allowing a maximum cell height of 22 cm without flooding (Chapter 3). This is relatively modest in comparison with the cell height of mature electrolysis technologies (Figure 6.2: 100 – 200 cm).[7]

This thesis identifies two viable strategies for the scale-up of CO_2 electrolyzers with flowing catholyte. First, we show that carbon cloth-based GDEs already permit cell heights $> 100\,cm$ because their bimodal pore structure can tolerate electrolyte flooding to a certain extent while maintaining an average FE_{CO} of 70% at $-200\,mA\,cm^{-2}$ (**RQ3**: Chapter 3). We recommend to test this material at a higher current density and integrate it into a reactor design that can drain the electrolyte from the gas channel.

Second, developing a GDL material with a crack-free MPL could improve the flooding resistance by an order of magnitude (**RQ1**: Chapter 2). Unfortunately, the investigated commercial material with a crack-free MPL (Freudenberg H23C6) is not chemically stable under electrolysis conditions (Chapter 3). Therefore, the field would greatly benefit from further studying the degradation mechanism in more detail.[37] In this context, the sealing of GDL cracks with hydrophobic particles,[38] is another interesting development. If implemented on a large scale by GDL manufacturers, this approach could have a major

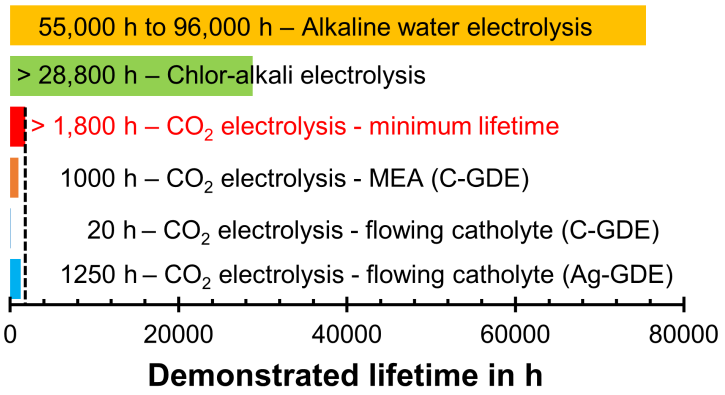

Figure 6.3: Comparison of demonstrated CO_2 electrolysis cell operation time. Alkaline water electrolysis:[40] cell stacks are usually replaced after 6 to 11 years. Chlor-alkali electrolysis with oxygen consuming cathode:[41] operation for more than 3 years. Lifetime could be extended with higher catalyst loading. CO_2 electrolysis - minimum lifetime estimated by the techno-economic analysis by Verma *et al.* to recover the capital expenditure of the electrolysis stack.[6] CO_2 electrolysis with MEA (C-GDE):[42] Ag-catalyst on carbon-based GDE, $-200\,mA\,cm^{-2}$, no failure reported. CO_2 electrolysis with flowing catholyte (Ag-GDE):[43] Commercial silver-based GDE (ODC) from Covestro, $-300\,mA\,cm^{-2}$, no failure reported. CO_2 electrolysis with flowing catholyte (C-GDE):[13] Ag-catalyst on carbon paper-based GDE, $-190\,mA\,cm^{-2}$, Gas diffusion layer failure: hydrophobicity loss due to (electro-)chemical degradation.

impact on the scalability of carbon-based GDEs.

6.2.3. CURRENT CO_2 ELECTROLYZER LIFETIME

The majority of studies in the field report CO_2 electrolysis measurements lasting less than 100 h.[9] Many of these studies focus on cathode catalyst synthesis and only carry out short performance tests. However, the duration is also often limited by the durability of the commonly used carbon-based cathode GDEs. Failure mechanisms include the poisoning or erosion of the catalyst, the formation of carbonate salt, and loss of hydrophobicity.[39]

To the best of our knowledge, the longest experiment with a carbon-based GDE was carried out in an MEA electrolzer for 1000 h and ended without failure.[42] More commonly, however, MEA electrolyzers can only be operated for a much shorter time because carbonate salts form and block the gas channel. It was recently discovered that this problem can be mitigated through periodic rinsing of the gas channel.[14,44,45] Therefore, it is realistic that MEA electrolyzers could already achieve the minimum lifetime of 1800 h estimated in the example of Verma *et al.* (Figure 6.3).[6] By reaching this minimum lifetime, the electrolyzer stack in this case study would have been able to recover its capital costs. Naturally, it would be desirable to have a much longer lifetime to make the process more economical.

Demonstrating a long lifetime for CO_2 electrolyzers with flowing catholyte is particularly

interesting to the field because these allow the employment of Ni-based anodes. Unfortunately, the lifetime of carbon-based GDEs is especially low in these systems because the GDL substrate is prone to (electro)-chemical degradation (Figure 6.3: e.g., 20 h).[13] The degradation of carbon-based materials leads to the loss of hydrophobicity, which results in GDE flooding and a poor Faradaic efficiency.

Silver-based GDEs might offer a promising alternative. For example, Haas *et al.* successfully operated a CO_2 electrolyzer with flowing catholyte for 1250 h by employing a commercial silver-based GDE from Covestro (Figure 6.3).[43] This GDE was originally developed for industrial chlor-alkali electrolysis with oxygen depolarized cathodes (ODC).[46]

Overall, the field has to demonstrate significantly longer cell durability for CO_2 electrolysis to be economically viable. In comparison, the cell lifetime of mature industrial electrolysis technologies, such as alkaline[40] or chlor-alkali electrolysis,[41] has been orders of magnitude higher (Figure 6.3).

Chapter 2 of this thesis tests how the operational lifetime of CO_2 electrolyzers with flowing catholyte is limited by the substrate of the carbon-based GDE (carbon paper, carbon cloth, or nonwoven). For example, we find a Ag-GDE based on an SGL 39BC carbon paper looses it hydrophobicity after only 20 h of operation at $-190\,mA\,cm^{-2}$. This degradation leads to flooding, which in turn drops the FE_{CO} from an initial value of 70% to 10% (**RQ4**: Chapter 2). Nonwoven GDLs from Freudenberg exhibited an especially poor (electro-)chemical stability, which lets them loose their hydrophobicity within 30 min when a current density of $-200\,mA\,cm^{-2}$ is applied. We hypothesize that the carbon fibers are of this GDL are graphitized to a lower degree during manufacturing to make them more flexible, but this also reduces their chemical stability (Chapter 2).

This thesis shows that a carbon cloth-based GDE can perform CO_2 electrolysis for 120 h without reduction in Faradaic efficiency (**RQ4**: Chapter 3). This promising result raises the question for how long this material can be stably operated. Further, it motivates more systematic degradation studies, which should investigate the (electro-)chemical stability of carbon fiber substrates with different surface chemistry and carbonization degrees.

Chapter 4 of this thesis explores carbon-free, silver-based GDEs as an alternative. The silver-based GDEs made in our lab experience strong electrowetting, which lead to flooding and a poor Faradaic efficiency. In addition, we observed the electrochemical degradation of PTFE (**RQ5** and **RQ6**: Chapter 4), which might limit their long-term stability.

Haas *et al.*, in contrast, performed stable CO_2 electrolysis for 1250 h with the silver-based GDE from Covestro.[43] Therefore, this product is highly promising for the development of gas-fed CO_2 electrolyzers with a flowing catholyte. In addition, this demonstration also included the downstream processing of the product gases, which were converted to butanol and hexanol with a fermentation unit.[43] Unfortunately, the exact structure of this commercial GDE is proprietary, which limits the understanding the field can gain

for further GDE development.

In conclusion, CO_2 electrolysis is currently not viable at an industrial scale. Iridium is not available in sufficient quantities to serve as an anode catalyst at large scale. The CO_2 electrolysis field, therefore, has to further develop reactor designs with BPM, which allow the substitution of Ir-based anodes through Ni-based anodes. Further, the cell area and the lifetime of the cathode GDEs have to be increased substantially. In the next step, the engineering of cell stacks has to be further advanced, which includes the design of gaskets, flow fields, and bipolar plates. At this stage, the heat management of stack will also require more attention. Luckily, this development process can be accelerated by utilizing components and know-how from adjacent fields (e.g., PEM electrolysis, hydrogen fuel cells). Finally, the CO_2 electrolyzers have to be integrated with other unit operations (e.g, CO_2 capture, product gas separation, methanol synthesis) to showcase a fully functional process in a pilot plant.

6.3. HOW CAN WE PRODUCE HYDROCARBON FUELS AND CHEMICALS SUSTAINABLY?

In context of the energy transition, electrochemical CO_2 conversion to hydrocarbon fuels and chemicals will likely play a minor role over the next decade. Given the limitations of current CO_2 electrolyzer designs, it will take years to build mature pilot plants and even longer for a large scale employment of the technology. However, mitigating the effects of climate change will require more immediate action.

Fortunately, the thermocatalytic reduction of CO_2 allows a faster and less risky route to sustainable hydrocarbon fuel and chemical production.[47,48] In fact, multiple industry consortia have already announced projects for the production of sustainable fuels.

For example, Highly Innovative Fuels, a subsidiary of the Porsche AG, opened its Haru Oni synthetic gasoline plant in 2022, located in Punta Arenas, one of the windiest regions in Chile.[49] In its demonstration phase (2023), the plant will be equipped with a 3.4 MW wind turbine from Siemens Gamesa. The turbine will power a direct air capture unit from Global Thermostats to capture CO_2 and a 1.2 MW PEM electrolyzer from Siemens Energy to provide H_2 through water electrolysis. Methanol will be produced from CO_2 and H_2 in a methanol synthesis reactor from MAN. Its methanol production capacity is 594 t $year^{-1}$. The plant will be equipped with a Methanol To Gasoline (MTG) unit from ExxonMobil to produce synthetic gasoline at a rate of 96 t $year^{-1}$. In its final phase (2027), the Haru Oni plant is to be powered by a 2.5 GW wind farm. The methanol production capacity is projected to reach 1 Mt $year^{-1}$, which is used for the production of gasoline at a rate of 162 kt $year^{-1}$.

In another example, Norsk e-fuel announced a sustainable aviation fuel plant, which is to start its demonstration phase by 2024 in Norway.[50] A direct air capture unit from Climeworks will provide CO_2 for the production of synthesis gas in a reverse water-gas

shift reactor. The necessary H_2 will be provided by an alkaline electrolyzer from Sunfire. A Fischer-Tropsch reactor will convert the synthesis gas to a mixture of hydrocarbons, which are refined to sustainable aviation fuel in a final step. The fuel production capacity is supposed to reach 20 kt year^{-1} by 2026 and 82 kt year^{-1} by 2029.

Admittedly, the production scale of these two examples is still pretty small compared to 200 Mt of aviation fuel consumed globally (2016).[1] However, once the thermocatalytic CO_2 conversion technology has been demonstrated, securing funding and constructing additional plants can occur more rapidly. This approach is also appealing because thermocatalytic reduction plants could be retrofitted in the future if CO_2 electrolyzers reach a competitive development stage.

REFERENCES

[1] UN-ICAO, *Trends and scenario on alternative fuels – working paper,* (2017), https://www.icao.int/Meetings/CAAF2/Documents/CAAF.2.WP.006.4.en.pdf (last accessed on 24.02.2023).

[2] H. Danner and R. Braun, *Biotechnology for the production of commodity chemicals from biomass,* Chemical Society Reviews **28**, 395 (1999).

[3] S. Lewandowski, *Ethylene-global - Asia chemical conference,* (2016), http://cdn.ihs.com/www/pdf/Steve-Lewandowski-Big-Changes-Ahead-for-Ethylene-Implications-for-Asia.pdf (last accessed on 24.02.2023).

[4] D. Sheldon, *Methanol production-a technical history,* Johnson Matthey Technology Review **61**, 172 (2017).

[5] W. A. Smith, T. Burdyny, D. A. Vermaas, and H. Geerlings, *Pathways to industrial-scale fuel out of thin air from CO_2 electrolysis,* Joule **3**, 1822 (2019).

[6] S. Verma, B. Kim, H. M. Jhong, S. Ma, and P. J. Kenis, *A gross-margin model for defining technoeconomic benchmarks in the electroreduction of CO_2,* ChemSusChem **9**, 1972 (2016).

[7] M. Lehner, R. Tichler, H. Steinmüller, and M. Koppe, *Power-to-gas: technology and business models* (Springer, 2014).

[8] R. I. Masel, Z. Liu, H. Yang, J. J. Kaczur, D. Carrillo, S. Ren, D. Salvatore, and C. P. Berlinguette, *An industrial perspective on catalysts for low-temperature CO_2 electrolysis,* Nature nanotechnology , 118–128 (2021).

[9] A. Vass, A. Kormanyos, Z. Kószó, B. Endrődi, and C. Janaky, *Anode catalysts in CO_2 electrolysis: Challenges and untapped opportunities,* ACS Catalysis **12**, 1037 (2022).

[10] C. Minke, M. Suermann, B. Bensmann, and R. Hanke-Rauschenbach, *Is iridium demand a potential bottleneck in the realization of large-scale PEM water electrolysis?* international journal of hydrogen energy **46**, 23581 (2021).

[11] F. Dawood, M. Anda, and G. Shafiullah, *Hydrogen production for energy: An overview,* International Journal of Hydrogen Energy **45**, 3847 (2020).

[12] B. Beverskog and I. Puigdomenech, *Revised pourbaix diagrams for nickel at 25–300 °c,* Corrosion Science **39**, 969 (1997).

[13] L. M. Baumgartner, C. I. Koopman, A. Forner-Cuenca, and D. A. Vermaas, *Narrow pressure stability window of gas diffusion electrodes limits the scale-up of CO_2 electrolyzers,* ACS Sustainable Chemistry & Engineering **10**, 4683 (2022).

[14] B. Endrődi, E. Kecsenovity, A. Samu, F. Darvas, R. V. Jones, V. Török, A. Danyi, and C. Janáky, *Multilayer electrolyzer stack converts carbon dioxide to gas products at high pressure with high efficiency,* ACS Energy Letters **4**, 1770 (2019).

[15] H. Sverdrup, D. Koca, and K. V. Ragnarsdottir, *Investigating the sustainability of the global silver supply, reserves, stocks in society and market price using different approaches,* Resources, Conservation and Recycling **83**, 121 (2014).

[16] M. J. Eckelman, B. K. Reck, and T. Graedel, *Exploring the global journey of nickel with Markov chain models,* Journal of Industrial Ecology **16**, 334 (2012).

[17] M. G. Kibria, J. P. Edwards, C. M. Gabardo, C.-T. Dinh, A. Seifitokaldani, D. Sinton, and E. H. Sargent, *Electrochemical CO_2 reduction into chemical feedstocks: From mechanistic electrocatalysis models to system design,* Advanced Materials **31**, 1807166 (2019).

[18] D. Salvatore and C. P. Berlinguette, *Voltage matters when reducing CO_2 in an electrochemical flow cell,* ACS Energy Letters **5**, 215 (2020).

[19] B. Endrődi, E. Kecsenovity, A. Samu, T. Halmágyi, S. Rojas-Carbonell, L. Wang, Y. Yan, and C. Janáky, *High carbonate ion conductance of a robust PiperION membrane allows industrial current density and conversion in a zero-gap carbon dioxide electrolyzer cell,* Energy & Environmental Science , 4098 (2020).

[20] K. Yang, M. Li, S. Subramanian, M. A. Blommaert, W. A. Smith, and T. Burdyny, *Cation-driven increases of CO_2 utilization in a bipolar membrane electrode assembly for CO_2 electrolysis,* ACS Energy Letters **6**, 4291 (2021).

[21] Y. Chen, A. Vise, W. E. Klein, F. C. Cetinbas, D. J. Myers, W. A. Smith, T. G. Deutsch, and K. C. Neyerlin, *A robust, scalable platform for the electrochemical conversion of CO_2 to formate: Identifying pathways to higher energy efficiencies,* ACS Energy Letters **5**, 1825 (2020).

[22] M. A. Blommaert, S. Subramanian, K. Yang, W. A. Smith, and D. A. Vermaas, *High indirect energy consumption in aem-based CO_2 electrolyzers demonstrates the potential of bipolar membranes,* ACS Applied Materials & Interfaces **14**, 557 (2022).

[23] K. Xie, R. K. Miao, A. Ozden, S. Liu, Z. Chen, C.-T. Dinh, J. E. Huang, Q. Xu, C. M. Gabardo, and G. Lee, *Bipolar membrane electrolyzers enable high single-pass CO_2 electroreduction to multicarbon products,* Nature communications **13**, 3609 (2022).

[24] B. De Mot, J. Hereijgers, N. Daems, and T. Breugelmans, *Insight in the behavior of bipolar membrane equipped carbon dioxide electrolyzers at low electrolyte flowrates,* Chemical Engineering Journal , 131170 (2021).

[25] D. A. Vermaas and W. A. Smith, *Synergistic electrochemical CO_2 reduction and water oxidation with a bipolar membrane,* ACS Energy Letters **1**, 1143 (2016).

[26] M. A. Blommaert, D. Aili, R. A. Tufa, Q. Li, W. A. Smith, and D. A. Vermaas, *Insights and challenges for applying bipolar membranes in advanced electrochemical energy systems,* ACS Energy Letters , 2539 (2021).

[27] J. J. Kaczur, H. Yang, Z. Liu, S. D. Sajjad, and R. I. Masel, *A review of the use of immobilized ionic liquids in the electrochemical conversion of CO_2,* C **6**, 33 (2020).

[28] A. A. Samu, A. Kormányos, E. Kecsenovity, N. Szilágyi, B. Endrődi, and C. Janáky, *Intermittent operation of CO_2 electrolyzers at industrially relevant current densities,* ACS Energy Letters **7**, 1859 (2022).

[29] J. J. Kaczur, H. Yang, Z. Liu, S. D. Sajjad, and R. I. Masel, *Carbon dioxide and water electrolysis using new alkaline stable anion membranes,* Frontiers in chemistry **6**, 263 (2018).

[30] M. Quentmeier, B. Schmid, H. Tempel, H. Kungl, and R.-A. Eichel, *Toward a stackable CO_2-to-CO electrolyzer cell design —impact of media flow optimization,* ACS Sustainable Chemistry & Engineering **11**, 679 (2023).

[31] G. Faita and F. Federico, *Electrolysis cell with gas diffusion electrode,* (2010), US Patent 7,670,472 B2.

[32] N. Chavan, S. Pinnow, G. Polcyn, and T. Turek, *Non-isothermal model for an industrial chlor-alkali cell with oxygen-depolarized cathode,* Journal of Applied Electrochemistry **45**, 899–912 (2015).

[33] P. Jeanty, C. Scherer, E. Magori, K. Wiesner-Fleischer, O. Hinrichsen, and M. Fleischer, *Upscaling and continuous operation of electrochemical CO_2 to CO conversion in aqueous solutions on silver gas diffusion electrodes,* Journal of CO_2 Utilization **24**, 454 (2018).

[34] G. Athanasaki, A. Jayakumar, and A. Kannan, *Gas diffusion layers for pem fuel cells: Materials, properties and manufacturing–a review,* International Journal of Hydrogen Energy (2022).

[35] C. Simon, D. Kartouzian, D. Müller, F. Wilhelm, and H. A. Gasteiger, *Impact of microporous layer pore properties on liquid water transport in PEM fuel cells: Carbon black type and perforation,* Journal of The Electrochemical Society **164**, F1697 (2017).

[36] B. De Mot, J. Hereijgers, M. Duarte, and T. Breugelmans, *Influence of flow and pressure distribution inside a gas diffusion electrode on the performance of a flow-by CO_2 electrolyzer,* Chemical Engineering Journal **378**, 122224 (2019).

[37] K. Yang, R. Kas, W. A. Smith, and T. Burdyny, *Role of the carbon-based gas diffusion layer on flooding in a gas diffusion electrode cell for electrochemical CO_2 reduction,* ACS Energy Letters **6**, 33 (2021).

[38] Y. Wu, L. Charlesworth, I. Maglaya, M. N. Idros, M. Li, T. Burdyny, G. Wang, and T. E. Rufford, *Mitigating electrolyte flooding for electrochemical CO_2 reduction via infiltration of hydrophobic particles in a gas diffusion layer,* ACS Energy Letters , 2884 (2022).

[39] U. O. Nwabara, E. R. Cofell, S. Verma, E. Negro, and P. J. A. Kenis, *Durable cathodes and electrolyzers for the efficient aqueous electrochemical reduction of CO_2,* ChemSusChem **13**, 855 (2020).

[40] A. Buttler and H. Spliethoff, *Current status of water electrolysis for energy storage, grid balancing and sector coupling via power-to-gas and power-to-liquids: A review,* Renewable and Sustainable Energy Reviews **82**, 2440 (2018).

[41] N. Furuya and H. Aikawa, *Comparative study of oxygen cathodes loaded with Ag and Pt catalysts in chlor-alkali membrane cells,* Electrochimica Acta **45**, 4251 (2000).

[42] R. B. Kutz, Q. Chen, H. Yang, S. D. Sajjad, Z. Liu, and I. R. Masel, *Sustainion imidazolium-functionalized polymers for carbon dioxide electrolysis,* Energy Technology **5**, 929 (2017).

[43] T. Haas, R. Krause, R. Weber, M. Demler, and G. Schmid, *Technical photosynthesis involving CO_2 electrolysis and fermentation,* Nature Catalysis **1**, 32 (2018).

[44] B. De Mot, M. Ramdin, J. Hereijgers, T. J. Vlugt, and T. Breugelmans, *Direct water injection in catholyte-free zero-gap carbon dioxide electrolyzers,* ChemElectroChem **7**, 3839 (2020).

[45] B. Endrődi, A. Samu, E. Kecsenovity, T. Halmágyi, D. Sebők, and C. Janáky, *Operando cathode activation with alkali metal cations for high current density operation of water-fed zero-gap carbon dioxide electrolysers,* Nature Energy **6**, 439 (2021).

[46] I. Moussallem, J. Jörissen, U. Kunz, S. Pinnow, and T. Turek, *Chlor-alkali electrolysis with oxygen depolarized cathodes: history, present status and future prospects,* Journal of Applied Electrochemistry **38**, 1177 (2008).

[47] H. Guzmán, F. Salomone, E. Batuecas, T. Tommasi, N. Russo, S. Bensaid, and S. Hernández, *How to make sustainable CO_2 conversion to methanol: Thermocatalytic versus electrocatalytic technology,* Chemical Engineering Journal , 127973 (2020).

[48] A. Zachopoulos and E. Heracleous, *Overcoming the equilibrium barriers of CO_2 hydrogenation to methanol via water sorption: A thermodynamic analysis,* Journal of CO_2 Utilization **21**, 360 (2017).

[49] *Haru Oni demonstration plant,* (2022), https://www.hifglobal.com/haru-oni (last accessed on 24.02.2023).

[50] *Norsk e-Fuel press release,* (2022), https://www.norsk-e-fuel.com/ (last accessed on 24.02.2023).

7

SUMMARY

Many countries in the world are replacing fossil fuels with renewable power sources to reduce their greenhouse gas emissions and increase their energy security. For this reason, there is a high urgency to develop sustainable production processes for hydrocarbon fuels and organic chemicals by utilizing intermittent wind and solar power. One possible pathway involves capturing CO_2 directly from the air and converting it to chemical building blocks, such as C_2H_4, CO, or HCOOH, using electrochemical CO_2 reduction (CO_2R). These intermediates could then be further converted to the desired fuels and chemicals using established processes such as Fischer-Tropsch or methanol synthesis.

Before CO_2R can be implemented at an industrial scale, a number of technical requirements have to be met (e.g., current density of 200 to 500 $mA\,cm^{-2}$, cell voltage < 3 V, Faradaic efficiency for CO, $FE_{CO} \geq 95$, and a cell lifetime 2 > years). A fundamental challenge of CO_2R is that the competing hydrogen evolution reaction (HER) often takes place under similar reaction conditions. This can reduce the *FE* for the desired CO_2 reduction products. Another challenge is to develop a scalable reactor design, which implies avoiding scarce anode catalysts like iridium and understanding the water management at the electrodes.

While avoiding scarce materials can be achieved by selecting suitable electrocatalysts and controlling the electrolyte pH, the most promising approach to reach high current density, high *FE*, and low cell voltage utilizes porous gas diffusion electrodes (GDEs). However, the design of GDEs requires trade-offs between important properties like electrical conductivity, gas diffusivity, or hydrophobicity. The complexity of GDEs makes the scale-up of CO_2 electrolyzers difficult. For example, GDEs face the problem of electrolyte flooding the pores of the material, which suppresses the diffusion of CO_2 to the catalyst. This phenomenon can occur for a number of reasons, for example due to hydraulic pressure differences in the reactor or due to chemical degradation of the GDE. This thesis aims to address these challenges by experimentally studying the mass transfer and flooding phenomena in gas-fed CO_2 electrolyzers with flowing catholyte.

Chapter 2 investigates the effect of GDE structure on the resistance against electrolyte flooding and breakthrough due to pressure differences between the gas and the liquid phase. It further examines how the structure impacts FE_{CO} at industrially relevant current density (200 mA cm^{-2}). To prepare the GDE samples, we deposited an Ag catalyst layer on a selection of commercial gas diffusion layer (GDL) materials with different carbon fiber substrate (CFS) structures (paper, nonwoven, and cloth) and thicknesses (250 – 450 µm). Additionally, we investigate how cracks in the microporous layer (MPL) affect the flooding resistance and the mass transfer properties. The results suggest that GDEs based on carbon cloth and/or thin paper substrates exhibit high FE_{CO} at the cost of a low flooding resistance against liquid–gas overpressure (< 50 mbar). Because of hydrostatic pressure differences between gas and liquid compartments, this poor flooding resistance would limit the maximum cell height to less than 51 cm if the electrolyzer should be operated in flow-by mode. The trade-off between flooding resistance and mass transfer capability has to be overcome before CO_2 electrolyzers can be constructed at an industrial scale. The GDE with a crack-free MPL (Freudenberg H23C6) exhibits an impressive flooding resistance of 390 mbar, but it is not chemically stable under electrolysis conditions. Our study implies that the layers of the ideal GDE have to be optimized for different objectives: The CFS should be thin and/or highly porous to minimize the diffusional pathway. The MPL should be crack-free to protect the GDE from electrolyte flooding.

Chapter 3 examines how the GDE structure affects the flooding behavior and the FE_{CO} at different operating conditions (cathode potential, differential pressure). We controlled the differential pressure across the GDE to show the impact of electrowetting *operando* at 200 mA cm^{-2}. We find that the scale-up of electrolyzers operating in a flow-by regime is not viable with currently available commercial GDL materials. The relatively low capillary pressure and electrowetting make it difficult to keep the gas and liquid phase separated beyond 200 mA cm^{-2}. A thick carbon paper with a small average CFS pore size (Toray TGP-H-120) achieved the widest flow-by pressure window of 47 mbar, which corresponds to a relatively modest electrode height of 48 cm. The high thickness, however, also leads to a poor diffusivity limiting the FE_{CO} to less than 46%. Instead, we propose the scale-up of an electrolyzer with a carbon cloth GDE, which can tolerate GDE flooding and electrolyte breakthrough. We find that a carbon cloth (ELAT LT1400W) allowed the highest FE_{CO} of 84% at 200 mA cm^{-2}. The bimodal pore size distribution allows this GDE to maintain a high effective diffusivity at higher liquid overpressures (e.g., > 100 mbar). We hypothesize that high liquid overpressure leads to electrolyte breakthrough through the large pores between the fiber bundles. This preferential drainage keeps the small pores within the fiber bundles gas-filled ensuring fast mass transport to the catalyst. This promising electrolyzer design would therefore enable a cell height of at least 100 cm and operate at an estimated average FE_{CO} of 69% at 200 mA cm^{-2}. We demonstrate that this materials permits stable CO production for at least 125 h.

The limits of carbon-based GDEs stimulated the investigation of alternative, carbon-free GDE structures. Chapter 4 explores the adaption of a silver-based GDE from a Chlor-alkali electrolysis process as a cathode for CO_2 electrolysis. We determine the impact of

electrowetting on FE_{CO} at industrially relevant current density. In addition, we assessed the chemical stability of the GDE with XPS and XRD characterization. The characterization of used GDEs reveals a potential-dependent degradation, which can be explained through chemical PTFE degradation and/or physical erosion of PTFE through the restructuring of the silver surface. Our results further suggest that electrowetting-induced flooding lets FE_{CO} drop below 40% after only 30 min of electrolysis. We conclude that the effect of electrowetting has to be managed more carefully before the investigated silver-based GDEs can compete with carbon-based GDEs as cathodes for CO_2 electrolysis. Further, not only the conductive phase (such as carbon or silver), but also the binder (such as PTFE), should be carefully selected for stable CO_2 reduction.

Chapter 5 visualizes the 2D pH profile in the catholyte channel of a CO_2 electrolyzer with a bipolar membrane (BPM). This electrolyzer type allows an anode based on relatively abundant nickel instead of scarce iridium. We investigate the effect of the process parameters current density, CO_2 saturation, and catholyte flow rate on the FE_{CO}. The pH profile is imaged with *operando* fluorescence lifetime imaging microscopy (FLIM) using a pH-sensitive quinolonium-based dye. The results show that the pH buffering effect of CO_2 from the gas feed and dissolved CO_2 in the catholyte prevent the GDE from becoming strongly alkaline. We find the mass transfer contribution of bubble-induced mixing to be more significant than the contribution of forced convection through the flowing catholyte. The bubble-induced mixing is only effective after exceeding a threshold in current density, which makes the maximum pH at $10\,mA\,cm^{-2}$ higher than at 50 or $100\,mA\,cm^{-2}$. These bubbles can lead to convective mixing perpendicular to the flow direction, which facilitates the neutralization of OH^- from the cathode with H^+ from the BPM. By keeping the bulk pH relatively constant, bubble-induced mixing might be able to limit the pH increase at the cathode and thereby allow a high FE_{CO}. Therefore, gas-fed CO_2 electrolyzers with BPM are promising systems for scale-up and operation at high current densities.

In conclusion, CO_2 electrolysis is currently not viable at an industrial scale until the cell area and the lifetime of the cathode GDEs have been increased substantially. This requires further research and development of suitable electrode materials. Further, CO_2 electrolysis field has to further develop reactor designs with BPM, which allow the substitution of scarce Ir-based anodes with Ni-based anodes. After solving this problem, CO_2 electrolyzers have to be integrated with other unit operations (e.g, CO_2 capture, product gas separation, methanol synthesis) to showcase a fully functional process in a pilot plant.

8

SAMENVATTING

Overal in de wereld vervangen landen fossiele brandstoffen met hernieuwbare energiebronnen om uitstoot te verminderen en hun energiezekerheid te vergroten. Daarom is er een grote urgentie om duurzame productieprocessen te ontwikkelen voor koolwaterstof gebaseerde brandstoffen en chemicaliën door gebruik te maken van intermitterende wind- en zonne-energie. Eén mogelijkheid is om CO_2 direct uit de lucht op te vangen en om te zetten in chemische bouwstenen, zoals C_2H_4, CO of HCOOH, met behulp van elektrochemische CO_2-reductie (CO_2R). Deze tussenproducten kunnen dan verder worden omgezet in de gewenste brandstoffen en chemicaliën met behulp van bestaande processen zoals Fischer-Tropsch of methanolsynthese.

Voordat CO_2 op industriële schaal kan worden geïmplementeerd, moet aan een aantal technische eisen worden voldaan (bijv. current densities van 200 to 500 $mA\,cm^{-2}$, celvoltage < 3 V, Faradaic efficiëntie voor CO, $FE_{CO} \geq 95$, en een cellevensduur van 2 > jaar. Een fundamentele uitdaging van CO_2R is dat de concurrerende waterstofevolutiereactie (HER) vaak plaatsvindt onder vergelijkbare reactieomstandigheden. Dit kan de FE voor de gewenste CO_2-reductieproducten verlagen. Een andere uitdaging is het ontwikkelen van een schaalbaar reactorontwerp, wat inhoudt dat schaarse anodekatalysatoren zoals iridium moeten worden vermeden en dat de waterhuishouding bij de elektrodes goed moet worden begrepen.

Alhoewel het vermijden van schaarse materialen kan worden bereikt door het selecteren van geschikte elektrokatalysatoren en het regelen van de pH van de elektrolyt, is de meest veelbelovende benadering om een hoge current density, hoge FE en lage celspanning te bereiken, gebruik van poreuze gasdiffusie-elektroden (GDE's). Het ontwerp van GDE's vereist echter een afweging tussen belangrijke eigenschappen zoals elektrische geleidbaarheid, diffusie van gas of hydrofobiciteit. De complexiteit van GDE's maakt het opschalen van CO_2-elektrolyzers moeilijk. GDE's hebben bijvoorbeeld het probleem dat de elektrolyt de poriën van het materiaal "flood", waardoor de diffusie van CO_2 naar de katalysator wordt onderdrukt. Dit fenomeen kan om verschillende redenen optreden,

bijvoorbeeld door hydraulische drukverschillen in de reactor of door chemische degradatie van de GDE. Dit proefschrift heeft als doel deze uitdagingen te tackelen door experimenteel de massaoverdracht en overstromingsverschijnselen te bestuderen in "gas-fed" CO_2 elektrolyzers met een stromende katoliet.

Hoofdstuk 2 onderzoekt het effect van de structuur van de GDE op de weerstand tegen elektrolyt flooding en "break-through" als gevolg van drukverschillen tussen de gas- en de vloeistoffase. Verder wordt onderzocht hoe de structuur de FE_{CO} beïnvloedt bij industrieel relevante current densities (200 mA cm^{-2}). Om de GDEs voor te bereiden, plaatsten we een Ag-katalysatorlaag op een selectie van commerciële gasdiffusielagen (GDL) met verschillende koolstofvezelsubstraten (CFS) (papier, vlies en doek) en diktes (250 – 450 µm). Daarnaast onderzoeken we hoe scheuren in de microporeuze laag (MPL) de weerstand tegen flooding en de massatransporteigenschappen beïnvloeden. De resultaten suggereren dat GDE's gebaseerd op carbon cloth en/of dunne papieren substraten een hoge FE_{CO} hebben ten koste van een lage floodingweerstand tegen vloeistof-gas overdruk (< 50 mbar). Vanwege hydrostatische drukverschillen tussen gas- en vloeistofcompartimenten zou deze lage overstromingsweerstand de maximale celhoogte beperken tot minder dan 51 cm als de elektrolyzer in een flow-by modus zou werken. Er moet een compromis worden gemaakt tussen floodingweerstand en massatransport voordat CO_2-elektrolyzers op industriële schaal kunnen worden gebouwd. De GDE met een scheurvrije MPL (Freudenberg H23C6) vertoont een indrukwekkende overstromingsweerstand van 390 mbar, maar is chemisch niet stabiel onder elektrolysecondities. Onze studie wijst aan dat de lagen van de ideale GDE geoptimaliseerd moeten worden voor verschillende doelstellingen: De CFS moet dun en/of zeer poreus zijn om de diffusieroute te minimaliseren. De MPL moet scheurvrij zijn om de GDE te beschermen tegen overstroming door elektrolyten.

Hoofdstuk 3 onderzoekt hoe de GDE-structuur het overstromingsgedrag en de FE_{CO} beïnvloedt bij verschillende operationele omstandigheden (kathodepotentiaal, drukverschil). We controleerden het drukverschil over de GDE om de invloed van electrowetting operando bij 200 mA cm^{-2} te laten zien. We ontdekten dat het opschalen van elektrolyzers die werken in een flow-by regime niet haalbaar is met de huidige commerciële GDL-materialen. De relatief lage capillaire druk en electrowetting maken het moeilijk om de gas- en vloeistoffase gescheiden te houden boven 200 mA cm^{-2}. Een dik carbonpapier met een kleine gemiddelde CFS poriegrootte (Toray TGP-H-120) bereikte het breedste flow-by drukbereik van 47 mbar, wat overeenkomt met een relatief bescheiden elektrodehoogte van 48 cm. De grote dikte leidt echter ook tot een slechte diffusiviteit waardoor de FE_{CO} wordt beperkt tot minder dan 46%. In plaats daarvan stellen we voor om een elektrolytische cel op te schalen met een carbon cloth GDE, waar het vollopen van de GDE en elektrolytdoorbraak geen grote gevolgen heeft. We ontdekten dat een carbon cloth (ELAT LT1400W) de hoogste FE_{CO} van 84% bij 200 mA cm^{-2} behaalde. De bimodale poriegrootteverdeling zorgt ervoor dat deze GDE een hoge effectieve diffusie behoudt bij hogere vloeistofoverdrukken (bijv. > 100 mbar). We veronderstellen dat een hoge vloeistofoverdruk leidt tot doorbraak van elektrolyten door de grote poriën tussen de vezelbundels. Deze preferentiële drainage houdt de kleine poriën binnen de vezel-

bundels gevuld met gas, waardoor een snel massatransport naar de katalysator wordt gegarandeerd. Dit veelbelovende elektrolyzerontwerp zou daarom een celhoogte van minstens 100 cm mogelijk maken en werken met een geschatte gemiddelde FE_{CO} van 69% bij 200 mA cm^{-2}. We tonen aan dat deze materialen stabiele CO-productie mogelijk maken gedurende minstens 125 uur.

De beperkingen van op koolstof gebaseerde GDE's stimuleerden het onderzoek naar alternatieve, koolstofvrije GDE-structuren. Hoofdstuk 4 onderzoekt de modificatie van een op zilver gebaseerde GDE uit een Chlooralkali-elektrolyseproces als kathode voor CO_2-elektrolyse. We bepalen de invloed van electrowetting op FE_{CO} bij industrieel relevante current densities. Daarnaast beoordeelden we de chemische stabiliteit van deze GDEs met XPS- en XRD-karakterisatie. De karakterisatie van gebruikte GDE's laat een potentiaalafhankelijke degradatie zien, die verklaard kan worden door chemische PTFE-degradatie en/of fysieke erosie van PTFE door herstructurering van het zilveroppervlak. Onze resultaten suggereren verder dat door elektrowetting geïnduceerde flooding de FE_{CO} laat dalen tot onder 40% na slechts 30 minuten elektrolyse. We concluderen dat het effect van electrowetting zorgvuldiger moet worden gemanaged voordat de onderzochte zilver-gebaseerde GDE's kunnen concurreren met koolstof-gebaseerde GDE's als kathoden voor CO_2 elektrolyse. Verder moet niet alleen de geleidende fase (zoals koolstof of zilver), maar ook het bindmiddel (zoals PTFE) zorgvuldig worden geselecteerd voor stabiele CO_2-reductie.

Hoofdstuk 5 laat het 2D pH-profiel in het katholietkanaal van een CO_2-elektrolyt met een bipolair membraan (BPM) zien. Dit type elektrolyse maakt een nikkel anode mogelijk in plaats van het schaarse iridium. We onderzoeken het effect van de procesparameters current density, CO_2-verzadiging en katholytdebiet op de FE_{CO}. Het pH-profiel wordt in beeld gebracht met operando fluorescentie lifetime imaging microscopie (FLIM) met behulp van een pH-gevoelige kleurstof op basis van quinolonium. De resultaten laten zien dat het pH-bufferende effect van CO_2 uit de gastoevoer en opgelost CO_2 in de katholiet voorkomt dat de GDE sterk alkalisch wordt. We vinden dat de bijdrage aan het massatransport van door bellen geïnduceerde menging significanter is dan de bijdrage van geforceerde convectie door de gepompt katholyt. De door bellen geïnduceerde menging is alleen effectief na het overschrijden van een drempelwaarde in current density, waardoor de maximale pH bij 10 mA cm^{-2} hoger is dan bij 50 of 100 mA cm^{-2}. Deze belletjes kunnen leiden tot convectie door de stromende katholyt. Deze bellen kunnen leiden tot convectieve menging loodrecht op de stroomrichting, wat de neutralisatie van OH^- uit de kathode met H^+ uit de BPM vergemakkelijkt. Door de pH in de bulk relatief constant te houden, kan menging door bellen de pH-stijging aan de kathode beperken en zo een hoge FE_{CO} mogelijk maken. Daarom zijn gasfed CO_2-elektrolyzers met BPM veelbelovende systemen voor opschaling en gebruik bij hoge stroomdichtheden.

Concluderend kan worden gesteld dat CO_2-elektrolyse momenteel niet vatbaar is op industriële schaal totdat het celoppervlak en de levensduur van de kathode GDE's aanzienlijk kan worden vergroot. Dit vereist verder onderzoek en ontwikkeling van geschikte elektrodematerialen. Verder moet het veld van CO_2 elektrolyse reactorontwerpen met

BPM verder ontwikkelen, die de vervanging van de schaarse op Ir-gebaseerde anoden door op Ni-gebaseerde anoden mogelijk maken. Nadat dit probleem is opgelost, moeten CO_2-elektrolyzers worden geïntegreerd met andere unitoperaties (bijv. CO_2-afvang, scheiding van productgassen, methanolsynthese) om een volledig functioneel proces in een proeffabriek te demonstreren.

ACKNOWLEDGEMENTS

Over the last four years, many people have supported me and contributed to my PhD journey. I would not have been able to complete my thesis without you!

To start, I would like to thank my PhD defense committee for their interest and valuable time (**Dr. Antoni-Forner Cuenca**, **Prof. Tom Breugelmans**, **Prof. Wiebrien de Jong**, **Prof. Johan Padding**, and **Dr. Valeria Garbin**).

Prof. Chris Kleijn, I am very grateful to have you as my promotor. Your honesty, experience, and judgment were invaluable for the success of my PhD project. Despite your many other obligations, you were always available in critical moments!

Dr. David Vermaas, thank you for being a wonderful supervisor and promotor. Five years ago, I accepted the offer to join your group and I have not regretted it for a second! Your creative ideas, unconditional optimism, and great humor have been a wonderful source of motivation. I think they complement my typically more skeptical / realist approach to research in a very productive way. Your trust and patience have given me the freedom to learn many new skills as a researcher and grow as a person.

Prof. Chris Kleijn, **Dr. Luis Portela**, **Prof. Sasa Kenjeres**, **Dr. David Vermaas**, **Dr. Valeria Garbin**, and **Dr. Bijoy Bera**, your wide range of scientific expertise and commitment attracts many skilled and interesting students to the Transport Phenomena Section. Thank you for providing the most fun and professional environment I have worked in so far. **Sandra Paffen**, you always helped me solve administrational problems very quickly. This was a great relief and allowed me to focus on teaching and research!

My special appreciation goes to all the technicians supporting my research. The procurement, engineering, and experimental work went extremely smoothly thanks to your tremendous know-how and helpfulness. **Evert Wagner**, thank you for your patience and dedication. You have played a vital role in ensuring lab safety and keeping the group's IT and lab infrastructure running smoothly. I hope my many requests through the last years were not too annoying for you ("I can't magically conjure up tables"). **Christiaan Schinkel**, you are one of the friendliest and most helpful people I know. Your can-do attitude and amazing technical skills make it an absolute pleasure working with you! **Stefan ten Hagen**, you designed and made many important components for my experimental setups. I really appreciate that you always found the time to help me out when I had an urgent problem. This was critical to solving important problems quickly. Without your quick help, my projects would have been delayed for many weeks! **Duco Bosma**, I am amazed at the width and depth of your technical expertise! Thank you for the SEM instructions and solving some really tough problems that had me almost throw in the

towel: e.g., fixing the ball bearings of the airbrush coater and solving the mystery of the leaking electrolyzer gaskets. **Joost Middelkoop**, thanks to your clever alarm box, we did not have a single instance of liquid electrolyte getting into the GC! **Andries Oort** and **Kevin Kamman** at the workshop were very helpful manufacturing flow cell parts and gaskets. I would also like to thank **Bart Boshuizen** for his Labview support, **Liliana Baron** for GC support, and **Baukje Kerpstra** for analyzing ICP-MS samples.

I had the pleasure to work with many great colleagues during my PhD program. **Dr. Annekatrien Daalmans**, thank you for helping me with my Dutch taxes and helping me get started! **Dr. Marijn Blommaert**, you are a great role model on getting the PhD project done. Thank you so much for giving me your thesis template. You must have saved me at least two or three weeks of sad troubleshooting! **Dr. Rose Sharifian**, thank you for chatting about time management strategies with me. I really enjoyed going to the South Hampton Electrochemistry summer school together. It is very inspiring that you founded a company based on your PhD work! **Matheus Garcia**, thank you for making the graduate school's PhD start-up module fun. Your fluid mechanics knowledge has been very useful for me. It is always nice chatting with you! **Xiaolin Wu**, I always liked seeing your challenging experimental research and chatting about cats during lunch breaks. **Dr. Artem Blishchik**, thank you for being my roommate at the Eindhoven conferences (especially at the weird industrial-style hotel). I really enjoyed game nights with you. It was always interesting to hear your perspective on things! **Romana Perinajová**, thank you for showing me the ropes at the beginning of my PhD. Also, thank you for lending me a ladder and a staple gun so I could do some home improvement! You were a great office mate – I am a bit sad that you basically disappeared from campus with the start of the pandemic. **Dr. Elin Vesper**, you also helped me a lot to get started in the beginning. It was very nice to have a fellow German to chat with – thank you for the encouragement to try making Knödel again after a failed attempt, they turned out very delicious the second time! **Kostadin Petrov**, it was very nice to have some group-internal collaborations on CO_2 electrolysis research with you! You bring a lot of good humor to the group – I especially enjoyed going to the ECCM graduate school together. Thank you for taking over my spot in the TP board and the airbrush coater as I was approaching my final year. I admire your artistic talent! Thank you very much for showing me Adobe Firefly and making pottery with me at the Veldhoven conference! **Nathalie Ligthart**, you always contribute to a joyful working experience – you took the use of silicone glue to the next level! Thank you for posting my research on social media and helping to maintain order in the labs. **Dr. Andrey Goryachev**, thank you for productive scientific discussions and teaching me a lot about XRD and XPS characterization during our joint research project. **Dr. Brice Saint-Michel**, thank you for demonstrating the static contact angle measurements and bringing a lot of humor to the group. **Dr. Matthäa Holland-Cunz**, it was fantastic to meet a fellow Bavarian here. I really appreciate all the support and kindness I got from you and Nils! **Aron Kahn**, thank you for all the amazing engineering and experimental work on the FLIM system. I could not have finished the final chapter of my thesis without your foundation. Also, you are really fun to work with! **Vojtech Konderla**, I am very glad you continued working in the TP group. I admire your work ethic and positive attitude. It is always fun to have you around! **Jorrit Bleeker**, thank you for your

immeasurable dedication to the group. Your humor and creativity add a lot of joy to the work environment. Thank you for all your help during the last years - you always have interesting new ideas and know the right people to get things done! Finishing the FLIM project would have been impossible without your curiosity and scientific competence! Also, thank your for translating the summary of this thesis to Dutch. **Christel Koopman**, you are a role model of reliability and diligence! Your critical attitude, intelligence, and humility make scientific discussion with you wonderful. It was a great relief that you took over so many teaching and lab (GC!) responsibilities as I was approaching my final year! **Jan-Willem Hurkmans**, thank you for your input on mass transfer correlations. Your down-to-earth character makes for some absurd, but entertaining conversations – very nice! I am glad you decided to do your PhD in the TP group instead of becoming a horse farmer. **Dr. Yu-fan Lee**, it is really fun sharing an office with you. Thank you for many interesting conversations and career advice. **Dr. Kaustub Singh**, your calm presence contributed to a very pleasant working environment. I enjoyed discussing bipolar membranes and gas diffusion electrodes with you. **Dr. Yanyan Liu**, thank you for many cheerful moments and helping with the fluorescence spectroscopy!

It was an enriching experience to work with many other colleagues at TU Delft. **Dr. Robbert van Putten**, thank you for the fun time in Boston and Delft. I really liked all the insightful conversations and great advice. It means a lot that you cooked the purple dye for me! **Joe Blake**, I learned a lot during our joint simulation project. Our project meetings were always a weekly highlight for me during the pandemic. **Katie Lawrence**, I am glad you got the whole experience when I wanted to demonstrate the spray coating process and the airbrush clogged immediately – Thank you for discussion catalyst inks with me. **Isabell Bagemihl**, I was always happy to bump into you on the corridors and chat a bit – perhaps I will even visit Hamburg some day? Thank you for explaining how to run COMSOL on the computational cluster. **Dr. Saeed Saedy**, I always enjoyed chatting with you! Thank you for the interesting discussions about politics, history, and science. I really appreciate your advice and wisdom regarding career choices and life in general. **Mark Sassenburg**, it was nice to meet for coffee and hear what is going on in the MECS group. Thank you for analyzing the formic acid contents for me! **Hugo Iglesias van Montfort**, thank you for the interesting conversations about student supervision and PhD life. **Siddhartha Subramanian**, thank you for discussing spray coater and CO_2 electrolysis issues. **Dr. Erdem Irtem**, I is a bit ironic that you had to leave TU Delft and start at VS Particle so we could finally work on a project together. The GSL (Grip Strength Lorenz) compression level is hilarious – it is a pleasure working with you!

There are also many scientist beyond my research group that contributed to my thesis through discussions and/or collaborations. **Dr. Antoni Forner-Cuenca**, thank you for sharing your knowledge on gas diffusion layers with us. Your advice helped us make a great selection of materials leading to two scientific publications! I really enjoyed chatting with you at conferences and during your visits to TU Delft. **Dr. Tom Burdyny**, you really helped me understand the field of CO_2 electrolysis when I first started. I deeply appreciate discussing gas diffusion electrodes, reactor engineering, and many other things with you. **Dr. Wolter Jager**, thank you for synthesizing a custom-made fluorescent pH-sensor dye for the FLIM electrolysis project. Without this contribution, the project would

have never been possible. **Dr. David Franzen**, I am very happy I attended your presentation at the Durban ISE conference in 2019. At the time, I would have never imagined that this would lead to a collaboration between us with. I would also like to thank **Prof. Thomas Turek** and **Dr. Barbara Ellendorff** at TU Clausthal for their contribution to this project!

During my PhD, I had the opportunity to supervise several bachelor and master student projects. **Werner Kastelein** and **Sophie van't Hoff**, thank you for your patience with me while I was learning gas diffusion layer theory and how to use COMSOL. The begin of COVID was a turbulent time for teaching. I hope you still enjoyed doing simulations although you originally signed up for experimental bachelor projects. **Thomas Hulshof**, thank you for being very resilient while struggling with my leaky flow cell. It took another two or three more design iterations after your project to get it to work properly. You also did great work laying the foundation with our airbrush coating process! **Namrata Shah**, it was an amazing achievement to develop a coating process with our makeshift equipment. I had a lot of fun working with you! **Christel Koopman**, thank you for your diligence, very hard work, and critical scientific thinking. Without your help, it would have never been possible to complete the project so successfully in the middle of the pandemic. **Vojtech Koderla**, thank you for trusting Joe and me to be your supervisors/companions on your COMSOL simulation journey. I really enjoyed our weekly meetings and was very impressed by your work ethic and high level of initiative during this challenging project. Hopefully you were still able to learn something useful from me although you outstripped my modeling capabilities from day one. **Maxime Hoogland**, our combined FLIM imaging and electrolysis research was in many ways the pinnacle of my PhD journey. Thank you for all your hard work and perseverance during this ambitious and complex project!

Many great friends supported me during the last four years. **Rick Vink**, thank you for the fun time in Boston and introducing me to Delft. **Dr. Paul Dichtl**, **Konstantin Huber**, and **Dr. Patrick Haider**, it has been a pleasure to know you for the last 15 years. Thank you for always staying in touch!

Caroline Gutierrez, thank you for coming to Europe and the wonderful moments we got to share.

Edith Baumgartner and **Josef Baumgartner**, thank you for all your hard work and endless support. I am fortunate to be your son. **Matthias Baumgartner** and **Agnes Baumgartner**, I am very grateful to have such wonderful siblings. Thank you for always taking time when it matters!

Lorenz
Delft, June 11, 2023

Curriculum Vitæ

Lorenz Martin Baumgartner

12-11-1992 Born in Munich, Germany

2011 – 2014 **B.Sc. in Chemical engineering**
Department of Chemistry
Technical University of Munich, Germany

2014 – 2017 **M.Sc. in Chemical engineering**
Department of Chemistry
Technical University of Munich, Germany

2016 – 2017 **Visiting student researcher**
Department of Chemical engineering
Massachusetts Institute of Technology, Cambridge, MA, USA

2017 – 2018 **Research engineer**
Department of Chemical engineering
Massachusetts Institute of Technology, Cambridge, MA, USA

2018 – 2023 **Ph.D. in Chemical Engineering**
Transport Phenomena Section
Department of Chemical Engineering
Faculty of Applies Sciences
Delft University of Technology, The Netherlands

Thesis:	Mass transfer and flooding phenomena in carbon dioxide electrolyzers
Promotor:	Prof. Dr.ir. C.R. Kleijn
Promotor:	Dr.ir. D.A. Vermaas

List of Publications

1. **Baumgartner, L.M.**; Koopman, C.I.; Forner-Cuenca, A.; Vermaas, D.A. **Narrow Pressure Stability Window of Gas Diffusion Electrodes Limits the Scale-Up of CO_2 Electrolyzers.** ACS Sust. Chem. & Eng., **10**,(14), 4683-4693 (2022)

2. **Baumgartner, L.M.**; Koopman, C.I.; Forner-Cuenca, A.; Vermaas, D.A. **When Flooding is not Catastrophic – Woven Gas Diffusion Electrodes enable stable CO_2 electrolysis.** ACS Appl. Energy Mater., **5**,(12), 15125-15135 (2022)

3. Petrov, K.V.; Bui, J.B.; **Baumgartner, L.M.**; Weng, L.; Dischinger, S.M.; Larson, D.M.; Miller, D.J.; Weber, A.Z.; Vermaas, D.A. **Anion-exchange membranes with internal microchannels for water control in CO_2 electrolysis.** RSC Sust. Energy & Fuels, **6**, 5077-5088 (2022)

4. Blake, J.W.; Konderla, V.; **Baumgartner, L.M.**; Vermaas, D.A.; Padding, J.T., Haverkort, J.W. **Inhomogeneities in the Catholyte Channel Limit the Upscaling of CO_2 Flow Electrolysers** ACS Sust. Chem. & Eng., **11**,(7), 2840-2852 (2023)

5. Bleeker, J.; Kahn, A.P.; **Baumgartner, L.M.**; Grozema, F.C.; Vermaas, D.A.; Jager, W.F.; **Quinolinium-Based Fluorescent Probes for Dynamic pH Monitoring in Aqueous Media at High pH Using Fluorescence Lifetime Imaging.** ACS Sens. (2023)

6. **Baumgartner, L.M.**; Kahn, A.P. ; Hoogland, M.; Bleeker J.; Jager, W.F. ; Vermaas, D.A. **Direct imaging of local pH reveals bubble-induced mixing in a CO_2 electrolyzer** ACS Sust. Chem. & Eng. (Submitted March 2023)

7. **Baumgartner, L.M.**; Goryachev, A.; Koopman, C.I.; Franzen, D.; Ellendorff, B.; Turek, T.; Vermaas, D.A. **Electrowetting Limits Electrochemical CO_2 Reduction in carbon-free Gas Diffusion Electrodes.** RCS Energy Adv. & Eng. (Submitted June 2023)